

Autonomous Soaring Flight for Unmanned Aerial Vehicles

Nicholas R.J. Lawrance

A thesis submitted in partial fulfilment
of the requirements for the degree of
Doctor of Philosophy



THE UNIVERSITY OF
SYDNEY

Australian Centre for Field Robotics
Faculty of Engineering and Information Technologies
The University of Sydney

March 2011

Declaration

I declare that the work in this thesis has not previously been submitted for a degree nor has it been submitted as part of requirements for a degree except as acknowledged within the text.

I also declare that the thesis has been written by me. Any help that I have received in my research work and the preparation of the thesis itself has been acknowledged. In addition, I declare that all information sources and literature used are indicated in the thesis.

Nicholas R.J. Lawrance

March 31, 2011

Abstract

Nicholas R.J. Lawrance
The University of Sydney

Doctor of Philosophy
March 2011

Autonomous Soaring Flight for Unmanned Aerial Vehicles

Unmanned Aerial Vehicles (UAVs) provide unique capabilities in a range of industrial, scientific and defence applications. A small UAV could extend flight duration without requiring additional propulsive power through the use of soaring. This thesis examines the aerodynamic mechanisms of soaring flight and proposes planning and control algorithms for a UAV to autonomously sense and utilise the wind environment to extend flight duration.

In order to utilise soaring a thorough understanding of the energy interaction between an aircraft and the surrounding atmosphere is required. This thesis presents a mathematical model for a gliding aircraft and examines how wind contributes to the energy change of an aircraft. Conditions for optimal energy efficiency are identified for gliding and soaring flight in linear wind shear.

The proposed path planner takes advantage of the energy equations for a gliding aircraft to plan energy efficient paths over a known wind field. Previous soaring planners have focused on a single type of energy gain such as static soaring. By using the energy equations directly the planner can exploit all energy gain conditions rather than relying on specialised controllers.

The planner requires an adequate estimate of the wind field to plan reliable energy gain paths. A small UAV would typically only have access to direct wind observations taken during flight. Gaussian Process (GP) regression is proposed to generate a wind map from direct wind observations. This model-free approach can account for static and dynamic wind fields and does not restrict the planner to particular types of wind structure.

Maintaining an accurate map requires the planner to ensure efficient map sampling and maintain sufficient energy to continue flight. The path planning algorithm exploits the variance estimate from the GP map to identify regions of the map which require improvement. The planner assesses the aircraft's energy state and current map to determine target regions of the wind field for further exploration or energy exploitation.

Results demonstrate that this architecture is capable of generating energy-gain paths in both static and dynamic wind fields. The mapping algorithm records direct samples of the wind to generate a wind map that is used by the planning algorithm to simultaneously explore and exploit the wind field to extend flight duration without propulsive power.

Acknowledgements

I would firstly like to gratefully acknowledge my supervisor Dr Salah Sukkarieh for his support and guidance.

I would also like to thank my friend and fellow student Alistair Reid. Since the beginning of our candidature his friendship and support have made this time both rewarding and enjoyable. Our conversations may not have always focused on research but I wouldn't have it any other way.

My sincere thanks also goes to my many friends who have helped me get to where I am today. To Calvin, for remaining a great friend and always providing open and ungrudging support. To Lash, Vic, and the whole UAV group thanks for your help, your words and your time. Working with such a great group of people has made my time here more fun than it probably should have been.

To the ACFR as a whole, I have appreciated the social atmosphere and the support provided by the academics, students and staff. It has honestly been a pleasure to work here and I hope it will continue to be a welcoming place for students from Australia and overseas.

I owe thanks to the Government of Australia and to The University of Sydney for allowing students to pursue their research and providing the means and equipment to do it well. Being surrounded by such a wealth of incredibly intelligent people has been a humbling but very rewarding experience.

I would finally and most importantly like to thank my family. Without the care and support of my parents, my sisters and my grandfather I would never have made it here. Their belief in me has been an anchor in rough times.

To my wonderful family.

Contents

Declaration	i
Abstract	ii
Acknowledgements	iv
Contents	vi
List of Publications	x
List of Figures	xi
List of Tables	xv
Nomenclature	xvi
1 Introduction	1
1.1 Motivation	1
1.2 Related Fields	2
1.3 Thesis Contributions	2
1.4 Thesis Structure	3
2 Background	5
2.1 Soaring Background	5
2.1.1 History of gliding aircraft	5
2.1.2 Historical soaring research	9

2.2	Atmospheric Energy Sources	13
2.2.1	Atmospheric conditions for soaring flight	13
2.2.2	Static soaring sources	19
2.2.3	Dynamic soaring sources	26
2.3	Static Soaring	28
2.3.1	Bird static soaring	29
2.3.2	Manned static soaring	30
2.3.3	UAV static soaring	34
2.4	Dynamic Soaring	37
2.4.1	Bird soaring	37
2.4.2	UAV dynamic soaring	39
2.5	Summary	40
3	Soaring and Gliding Flight	42
3.1	Frames of Reference and Definitions of Energy	43
3.2	Longitudinal Gliding	46
3.2.1	Longitudinal gliding aircraft model	46
3.2.2	Energy in longitudinal glider model	51
3.2.3	Longitudinal gliding without wind	53
3.3	Longitudinal Soaring	64
3.3.1	Horizontal linear gradient	66
3.3.2	Vertical linear gradient	69
3.3.3	Horizontal wind shear	72
3.3.4	Vertical wind shear	75
3.3.5	Dynamic power summary	76
3.4	Six Degree of Freedom Gliding	77
3.4.1	Gliding aircraft model	77
3.4.2	Energy in 6DOF glider model	82
3.4.3	Gliding without wind	82
3.5	Six Degree of Freedom Soaring	88
3.6	Summary	90

4 Control of a Soaring Aerial Vehicle	93
4.1 Longitudinal Soaring Control	94
4.1.1 Control for soaring in rising air	94
4.1.2 Control for soaring in horizontal shear	95
4.1.3 Rayleigh cycle dynamic soaring control	99
4.1.4 Results	106
4.2 Soaring Control in Known Wind Fields	119
4.2.1 Path planning in known wind fields	120
4.2.2 Results	123
4.3 Summary	128
5 Mapping a Wind Field from Direct Observations	129
5.1 Mapping a Wind Field	131
5.1.1 Requirements for mapping a wind field	132
5.2 Gaussian Process Regression for Aerial Wind Mapping	135
5.2.1 GP regression	135
5.2.2 GP wind mapping from direct observations	138
5.3 Static Wind Mapping	141
5.3.1 Shared hyperparameter validation	142
5.4 Dynamic Wind Mapping	145
5.4.1 Separable covariance functions	145
5.4.2 Drifting separable covariance	151
5.5 Summary	152
6 Simultaneous Exploration and Exploitation of a Wind Field	153
6.1 System Architecture	153
6.1.1 Mission goals	153
6.1.2 System architecture	155
6.2 Exploration of Static Wind Fields	155

6.2.1	Static wind field mapping	156
6.2.2	Global target assignment	156
6.2.3	Local path planning	158
6.2.4	Simulation setup	163
6.2.5	Results	165
6.3	Exploration of Dynamic Wind Fields	178
6.3.1	Spatio-temporal wind mapping	178
6.3.2	Global target selection	179
6.3.3	Local path planning	181
6.3.4	Simulation	181
6.3.5	Results	182
6.4	Summary	186
7	Conclusion	187
7.1	Summary of Contributions	188
7.2	Future Research	190
A	Toroidal thermal model	194
B	Aircraft models	201
B.1	Point mass model for the SBXC glider	202
B.2	Strip method simulation for the SBXC glider	203
	Bibliography	206

List of Publications

- [1] N. R. Lawrance and S. Sukkarieh. A guidance and control strategy for dynamic soaring with a gliding UAV. In *IEEE International Conference on Robotics and Automation*, pages 3632–3637, Kobe, Japan, 2009.
- [2] N. R. Lawrance and S. Sukkarieh. Wind energy based path planning for a small gliding unmanned aerial vehicle. In *AIAA Guidance, Navigation and Control Conference*, Chicago, Illinois, 2009. AIAA Paper 2009-6112.
- [3] N. R. Lawrance and S. Sukkarieh. Simultaneous exploration and exploitation of a wind field for a small gliding UAV. In *AIAA Guidance, Navigation and Control Conference*, Toronto, Ontario, Canada, 2010. AIAA Paper 2010-8032.
- [4] N. R. Lawrance and S. Sukkarieh. Autonomous exploration of a wind field with a gliding aircraft. *Journal of Guidance, Control, and Dynamics*, 34(3):719–733, 2011.
- [5] N. R. Lawrance and S. Sukkarieh. Autonomous soaring for atmospheric exploration of Titan. In *Proceedings of the 10th Australian Space Science Conference Brisbane 27 – 30 September, 2010*, pages 223–236. National Space Society of Australia Ltd, 2011.
- [6] N. R. Lawrance and S. Sukkarieh. Path planning for autonomous soaring flight in dynamic wind fields. In *IEEE International Conference on Robotics and Automation*, pages 2499 – 2505, Shanghai, China, 2011.

List of Figures

2.1	U.S. Standard Atmosphere 1976	14
2.2	Energy from the sun is absorbed by the surface and atmosphere causing large scale air transport.	16
2.3	Mean sea level pressure chart over Australia for 6 January 2011.	17
2.4	Laminar boundary layer for viscous flow over a fixed surface.	18
2.5	Formation of thermals in stable and mixed conditions.	20
2.6	Toroidal thermal bubble.	21
2.7	Variation of lifting air speed for the Allen thermal model	23
2.8	Velocity vector field and vertical velocity profile sections for a toroidal thermal	24
2.9	Ridge lift from lateral wind being deflected by a ground obstacle.	25
2.10	Ridge shear	27
2.11	Heuristic rules for centring on lifting air	31
2.12	MacCready speed-to-fly theory determines the optimal speed to travel between known thermals.	33
3.1	Inertial and air-relative frames	44
3.2	Air-relative velocity and longitudinal forces on a glider in uniform wind.	46
3.3	Positive linear wind gradients in \mathbf{J}_w	48
3.4	Power loss for a steady glide in no wind	54
3.5	Glide angle for a steady glide in no wind	56
3.6	Lift and drag coefficients and forces for the SBXC model in a steady glide in no wind	56

3.7	Glide ratio for a steady glide in no wind	60
3.8	Dimensionless power as a function of air relative climb angle for flight in linear wind gradients	69
3.9	Energy gain in horizontal wind shear.	73
3.10	Energy gain in vertical wind shear.	76
3.11	Air-relative velocity and applied forces for a gliding aircraft.	78
3.12	Turn rate efficiency during a steady gliding turn	85
3.13	Turn rate efficiency during a gliding turn with physical limitations .	87
3.14	Minimum drag turn conditions	89
3.15	Energy gain cycle in planar wind shear.	91
4.1	Airspeed and energy change for steady climb through linear horizontal wind shear of strength 0.5/s	97
4.2	Airspeed and energy change for steady climb through linear horizontal wind shear of strength 1.0/s	97
4.3	Dynamic soaring in a fixed horizontal shear layer	99
4.4	A Rayleigh dynamic soaring cycle in linear horizontal wind shear. .	100
4.5	Travelling in horizontal shear using Rayleigh dynamic soaring cycles .	102
4.6	Mode switching logic for Rayleigh cycle soaring control.	103
4.7	Trajectory for single dynamic soaring cycle in linear wind shear . .	107
4.8	Energy and body angles for a dynamic soaring cycle in linear wind shear	108
4.9	Top view of trajectories for single dynamic soaring cycles with upwind travel	110
4.10	Diagram of ideal energy transfer during a Rayleigh dynamic soaring cycle.	111
4.11	Energy variation during simulated dynamic soaring cycles	111
4.12	Pohlhausen's quartic boundary layer profile	113
4.13	Pohlhausen's quartic boundary layer estimation	114
4.14	Upwind soaring in an unknown Pohlhausen's quartic profile	115
4.15	Downwind soaring in an unknown Pohlhausen's quartic profile . . .	115
4.16	Effect of minimum flight altitude on upwind soaring.	118

4.17	Path planning tree for gliding flight	121
4.18	Estimation of the navigation reward function in terms of the equivalent energy of travel towards the goal	122
4.19	Path planning through a toroidal thermal with full wind field knowledge	124
4.20	Path planning through horizontal wind shear with full wind field knowledge	125
4.21	Path planning to a goal through a thermal with full wind field knowledge	126
5.1	Structure of GP regression over Cartesian coordinates of wind.	139
5.2	2D toroidal thermal wind field	142
5.3	2D toroidal thermal wind field - separate hyperparameter training . .	144
5.4	2D toroidal thermal wind field - shared hyperparameter training . . .	144
5.5	Spatial and temporal distance matrices for points taken from two cycles around the unit circle.	147
5.6	Covariance contours and covariance matrix for separable covariance functions.	148
5.7	Covariance contours and covariance matrix for non-separable covariance function (Eq. (5.20))	148
5.8	Covariance contours and covariance matrix for non-separable covariance function (Eq. (5.21))	149
6.1	System overview of simultaneous exploration and exploitation path planning architecture for a gliding UAV.	156
6.2	Additional energy in 1σ favourable wind conditions	160
6.3	Energy weighting K_E as a function of the distance to goal d_{goal}	163
6.4	Oblique view of single thermal exploration	167
6.5	Time history of single thermal exploration	168
6.6	Energy and estimated variance during single thermal exploration. . . .	168
6.7	Oblique view of multiple thermal exploration	169
6.8	Time history of multi-thermal exploration	170
6.9	Energy and estimated variance multiple thermal exploration.	170
6.10	Final mean estimate of the wind field from multi-thermal flight	171

6.11	Exploration and exploitation of overlaid wave and thermal wind field	173
6.12	Time history of wave field exploration	174
6.13	Energy and estimated variance during wave and thermal exploration.	174
6.14	Final mean estimate of wind field from wave flight	175
6.15	Sample trajectories for random thermal field trials	176
6.16	Sample trajectory of poor mapping performance	177
6.17	Simulated flight through a drifting wind field	182
6.18	Platform energy during simulated flight.	183
6.19	Global utility heuristic estimate	184
6.20	Simulated flight through dynamic thermals	185
A.1	Balanced vertical volumetric flow for toroidal thermal model	196
A.2	Generating functions and vertical velocity profiles for toroidal thermal model	198
A.3	Velocity profile for an elliptical section with elliptical axis ratio of 2 .	199
A.4	Velocity vector field and vertical velocity profile sections for a toroidal thermal with elliptical axis ratio $k = 3$	200
B.1	The University of Sydney SBXC glider model	201
B.2	Strip method component	203
B.3	Strip model SBXC glider	204
B.4	Glide ratio comparison between strip model and point mass model for the SBXC glider	205

List of Tables

4.1	Dynamic soaring in linear shear. Cycle times and upwind progression speed.	109
4.2	Dynamic soaring with minimum altitude limits.	117
5.1	Training results after 100 runs with separate and shared hyperparameters for traversal of a 2D toroidal thermal	143
5.2	Results comparing separable and non-separable covariance functions for traversal of a 2D drifting toroidal thermal	150
B.1	The aerodynamic and geometric properties of the SB-XC glider model	202

Nomenclature

Acronyms

CBL Convective Boundary Layer

CG Centre of Gravity

DOF Degrees of Freedom

GP Gaussian Process

MSLP Mean Sea Level Pressure

NED North-East-Down

PBL Planetary Boundary Layer

RBF Radial Basis Function

RC Radio Control

RL Reinforcement Learning

RMS Root Mean Square

SBL Stratified Boundary Layer

UAV Unmanned Aerial Vehicle

Greek Symbols

α Angle of incidence, deg

β Angle of sideslip, deg

γ Climb angle, deg

Π Dimensionless power

ρ Air density, kg/m³

ϕ Bank angle, deg

ψ Heading angle, deg

Roman Symbols

\mathcal{A} Wing aspect ratio ($= b^2/S$)

b Wing span, m

\mathbf{C}_a^i Air-relative to inertial frame transformation matrix

C_D Drag coefficient

$C_{D,0}$ Parasitic drag coefficient

$C_{D,i}$ Induced drag coefficient

C_L Lift coefficient

D Drag, N

d_{goal} Distance to the global goal, m

e Oswald's efficiency factor

g Gravitational acceleration, m/s²

\mathbf{J}_w Spatial wind gradients, s⁻¹

k Number of wind observations

L Lift, N

$(\frac{L}{D})_{est}$ Approximate glide ratio

m Vehicle mass, kg

\vec{P} Inertial position vector

R Reward function, J

r_{lift} Thermal lifting radius, m

S Wing area, m²

V Vehicle speed, m/s

V_{core} Thermal maximum core lift velocity, m/s

W Wind speed, m/s

Subscripts

0 Start of planning segment

1 End of planning segment

a Air-relative

b Body

i Inertial

Chapter 1

Introduction

1.1 Motivation

A flying vehicle uses the aerodynamic principles of motion through a fluid to generate enough lift to offset the force of gravity and remain airborne. However, fluids also resist motion in the form of drag. Most flying vehicles balance the force of drag using some sort of propulsion system. Since the energy required for propulsion is carried on-board the aircraft this limits the total amount of propulsive power and hence the flight duration of a powered flight vehicle.

However, certain flight conditions allow an aircraft to extract energy from the atmosphere and remain in flight without propulsive force. This process is known as soaring and allows birds and unpowered aircraft to fly without propulsive power. An Unmanned Aerial Vehicle (UAV) which could autonomously utilise soaring flight for fly for long periods of time without requiring propulsive force or human intervention.

The aim of this thesis, is to provide an understanding of the mechanisms of soaring flight, and to propose a method for a fixed-wing UAV to autonomously soar to increase flight time without requiring additional stored energy.

1.2 Related Fields

The work in this thesis is primarily drawn from two scientific fields. Firstly, an understanding of soaring flight requires an understanding of basic aerodynamic principles. Of particular importance is the energy transfer between an aircraft and the surrounding environment through the aerodynamic forces of lift and drag. This area draws on research conducted on flying vehicles including birds, manned aircraft and UAVs. In this thesis the research focuses on gliding flight and how the wind environment affects the energy gained or lost by an aircraft.

The field of robotics also plays an important part in the development of an autonomous soaring planner. To soar autonomously an aircraft would need to generate a map of the wind environment and take actions to maximise energy gain. The techniques for mapping, planning and control are all drawn from robotics research.

1.3 Thesis Contributions

There are three areas of academic contribution. The first is the analysis of gliding flight in a structured framework. By examining the equations of motion for a gliding aircraft the mechanisms for soaring flight are identified. The conditions required for soaring are examined and analytical expressions are found to calculate the optimum flight conditions to maximise energy capture. These equations provide a useful framework for developing an energy-based soaring controller.

The second contribution is the development of a model-free wind mapping method. Gaussian Process (GP) regression is proposed as a statistically sound, data driven approach to building a wind map. GP regression in this context provides a novel method for taking direct observations of the wind during flight and creating a wind map which can be queried for planning and used to direct future exploration to maintain a useful map for autonomous soaring control.

The final contribution is the development of a path planning architecture for autonomous soaring flight in unknown wind fields. This system and path planning

algorithm utilises the energy information from the soaring analysis and the GP mapping algorithm to simultaneously explore and exploit a wind field. The system is designed to map, identify and utilise energy sources in a wind field to provide extension of mission duration for an autonomous aircraft without requiring additional propulsive power.

1.4 Thesis Structure

This thesis is based on four major chapters. Chapter 2 provides a background for the soaring problem and discusses previous research in soaring and autonomous flight. There is a brief discussion on the history of soaring research as well as an analysis of more recent research into soaring control for autonomous aircraft. The major sources of atmospheric energy are identified and discussed. This chapter provides the background and previous research in autonomous soaring to identify the problem addressed in this thesis and where the current work resides with respect to existing and on-going research in the field.

The aerodynamic mechanisms for soaring flight are discussed in chapter 3. A simple aerodynamic model for a gliding aircraft in wind and wind shear is presented. The conditions for minimizing energy loss in gliding flight are identified and discussed. Through analysis of the energy equations it is also possible to identify the mechanisms of energy gain from wind. Energy gained from wind gradients is isolated and analytic expressions for optimal soaring conditions are found.

Chapter 4 addresses the problem of controlling a fixed-wing aircraft in order to gain energy from a known wind field. A controller for flying energy-gain paths in horizontal wind shear is presented. A path planner for capturing energy from a known wind map is presented. This planner utilises the dynamic equations from chapter 2 to estimate the energy gained across a set of actions and select action sets which maximise the total energy gained.

However, for autonomous flight the vehicle needs to maintain a map of the wind

environment in order to plan energy gain trajectories. Generating a wind map from point observations using Gaussian Process regression is discussed in chapter 5. A method is presented for generating a wind map for static and dynamic wind fields from wind observations taken during flight.

Simultaneously utilising this map and generating energy gain paths to allow further exploration of the field is discussed in chapter 6. A system architecture is presented which takes observation of the field, generates a wind map, and uses the current map to either further explore the field or collect energy. Simulated results are presented for a number of static and dynamic wind fields.

Chapter 7 concludes with a summary of the contributions made in this thesis and suggests areas for future research.

Chapter 2

Background

2.1 Soaring Background

2.1.1 History of gliding aircraft

Flight-capable vertebrates have existed for millions of years, with pterosaurs representing the earliest evidence of vertebrate animals capable of sustained controlled flight [59]. Flying animals continued to evolve utilising flight for travelling and finding food. Modern feathered birds evolved unique features for flight including low-density bone structures and muscular and skeletal arrangements suited to efficient controlled flapping flight [113]. The order of bats (*Chiroptera*) are the only flight-capable mammals and utilise skin-covered wings in place of feathers for flight.

The earliest records of man-made flying machines primarily concern the development of kites and parachutes in Eastern Asia. The earliest use of kites was for military signalling used in China as early as 200 BC [57]. There are earlier records of manned kites in use in China but the stories are often mixed with legend.

European research into flying machines began more recently, with actual flying attempts not beginning until the 10th and 11th centuries. Early flying machines attempted to imitate the shape and flapping of bird wings. As with much medieval

research it was conducted primarily by monks with little understanding or real testing of aerodynamics [107]. These gliders tended to result in failure with a number of early aviators being injured or killed due to inadequate understanding of the principles of flight. However, work with fixed wing gliders continued and with later research more efficient and effective wing shapes began to emerge. It also quickly became apparent that a gliding aircraft continually lost energy, and that birds could only maintain flight through wing flapping.

Some of the earliest scientific study into flight was performed by Sir George Cayley. One of his major contributions to the field was the idea of separating the components of an aircraft responsible for generating lift and thrust. Earlier works had attempted to emulate the propulsion of birds using flapping wings (a feat still being studied for modern flight vehicles). He determined that humans did not possess enough strength to fly by flapping wings but that an engine could provide the propulsion necessary for flight. The most weight efficient engines of the time were steam engines, and Cayley estimated that a 150-160 lb (68-73 kg) Boulton and Watt steam engine was capable of providing the equivalent of the power of six men (550 ft.lbf/s, 746 W) with the weight of only one [18]. He believed, therefore, that this should be able to provide enough energy for a flying vehicle to remain aloft. While he did not make significant further analysis of the power source, this insight was critical in allowing him to study aerodynamics separately from propulsion.

Cayley noted that large birds tended to flap their wings less often than smaller birds, and noted that:

“...they extend their wings, and without waving them, continue to skim for some time in a horizontal path.” [18]

By analysing the forces required for this motion, Cayley discovered that the wings must be supporting the weight through lift generated by the forward motion of the bird. He also noted that there existed a force acting in opposition to the direction of motion;

“... [a] retarding force by which the velocity of the motion, ..., will continually be diminished.” [18]

To offset this force of drag, the path could be tilted downwards so that drag would be countered by some of the weight force and the bird could continue to fly at a constant speed with a loss in altitude. The ratio of forward to vertical motion is known in modern contexts as the glide ratio and remains one of the most important measures of aerodynamic efficiency of an aerial vehicle. Further study lead to an empirical understanding of the dependence of lifting force on the angle of incidence of an inclined plane. Further, he noted the shape of the surface affected its lifting properties, notably that the concave shape of birds’ wings allowed them to generate lift at zero angle of incidence, which is not possible with a flat plate.

However, whilst the general concept of the forces of flight were relatively well understood, this did not translate into flyable aircraft. In particular, it was noted that vehicles shaped like birds were not inherently stable. Careful observation of bird flight showed that birds were not passively stable but required constant control through their tails and wings to continue flying [15]. Development of a manned aircraft would require a similar level of control or the design would need to be passively stable; that is, it would naturally return to a steady flying condition after small deviations.

The stability and control of a flying vehicle was of further interest to Cayley. He made note of the importance of the tail and his designs made use of a cruciform tail to maintain longitudinal and lateral stability. A number of experiments eventually led to Cayley building the first ‘governable parachute’, a rigid-framed kite with a suspended basket capable of lifting a person (a local child) on a tethered flight in 1849. A larger version carried his coachman aloft in 1853 but later crashed [40].

Cayley established the method of studying flying vehicles. The concepts were further studied by a number of others, notably the German brothers Otto and Gustav Lilienthal [40]. Otto designed and flew numerous manned gliders and introduced the concept of flight control through use of weight transfer from the human pilot.

Wilbur and Orville Wright developed the first powered manned aircraft which flew

in North Carolina, USA in December 1903. They took inspiration from Cayley, Lilienthal and other earlier glider designs but they took a more rigorous approach to the design and control of an aircraft. Their earliest work was in the development of a stable design for a gliding aircraft. In 1900-1901 they built and tested a glider which used a canard design for longitudinal stability and wing warping for lateral control. In tethered tests they found the design was stable but difficult to control due to an unmodelled adverse yaw effect of the wing warping. Over the next two years, they made more comprehensive tests into the effect of angle of incidence beginning with results recorded by Lilienthal. Unhappy with Lilienthal's results they built a wind tunnel with a force balance to measure lift and drag and tested a variety of thin cambered aerofoils over a range of aspect ratios. By 1902 they had constructed a glider with full three-axis control weighing just 53 kg. The glider was capable of controlled flight at a glide ratio between 5.7 and 9.5 [72]. The addition of a propulsion system lead to the well-known 1903 powered flight, but most of the control and aerodynamic work was complete in the 1902 glider design.

After the demonstration of the Wright flyer, work on both powered and unpowered aircraft grew rapidly. As knowledge deepened, research split into the disciplines of aircraft design; aerodynamics, propulsion, structure, and stability and control. Gliding aircraft received less interest as the commercial and military applications of powered aircraft drove research in the early 20th century. There was some use of gliders during World War II as near silent flight at night allowed delivery of supplies and troops without alerting the enemy [27].

However, the major driver for the development of high performance sailplanes was the sport of competition gliding. In the 1930s cross-country gliding competitions became popular. Gliders became more efficient through the development of specially designed low-speed aerofoil sections and improvements in materials and construction techniques. The advent of composite materials made a significant difference allowing lightweight and high stiffness construction, specifically allowing increased aspect ratio (longer, shorter chord wings). Modern competition gliders have a glide ratio over 50:1, or a glide angle of less than 1.1° in no wind [29].

2.1.2 Historical soaring research

As Cayley described the forces necessary for flight it became apparent that some birds were flapping less than would seem necessary for continuous flight. This was especially apparent in larger birds, which were capable of continuous flight with increasing altitude without flapping their wings. It was quickly realised that the birds must be capturing energy from motions of the air, and this behaviour became known as soaring.

One of the earliest recorded scientific accounts of soaring flight appeared in Nature in 1880 [73]. S.E. Peal recorded the flight of pelicans, adjutants (storks), vultures and other large birds.

“Firstly they rise by flapping the wings vigorously, and when up some 100 or 200 feet, if there is a breeze, begin to soar in large circular sweeps, rising 10 to 20 feet in each lap, the whole bird being otherwise quite motionless, and the wings extended rigidly.” [73]

He illustrated the soaring pattern of rising in a helix which drifts with the wind and suggested that energy is gained through an exchange of momentum during each cycle.

“I take it the explanation is, that in passing round with the wind, and by slightly falling, great impetus is gained, which is slowed down by turning to meet and rise on the wind like a kite.” [73]

Modern analysis divides soaring into two types; static soaring and dynamic soaring. Static soaring is the use of the vertical component of the wind to gain gravitational potential energy. Dynamic soaring is the use of changes in airspeed from variations in wind to gain air-relative kinetic energy. In Peal’s case, he was likely observing a bird utilising static soaring in rising air. Thus, while his explanation was probably incorrect or at least incomplete in that case, it almost described dynamic soaring and the birds may well have been using a combination of static and dynamic soaring to

gain altitude without flapping. A more principled approach was provided by Lord Rayleigh, who suggested in 1883 that the apparent soaring behaviour of birds could be described by one of three possible cases.

“... a bird without working his wings cannot, either in still air or in a uniform horizontal wind, maintain his level indefinitely. For a short time such maintenance is possible at the expense of an initial relative velocity, but this must soon be exhausted. Whenever therefore a bird pursues his course for some time without working his wings, we must conclude either (1) that the course is not horizontal, (2) that the wind is not horizontal, or (3) that the wind is not uniform.” [84]

This quote illustrates that the energy lost to drag can be overcome in three situations. Firstly, if the path is descending, then the energy from losing gravitational potential can be converted into additional airspeed to maintain flight but steadily lose altitude. If the kinetic energy gained from descent matches that lost to drag then this results in a steady descent at a fixed glide ratio. This is still an energy loss condition relative to the wind, and is the normal flight condition in a fixed static wind field. The remaining two flight conditions are the two most commonly defined soaring flight conditions.

The second option is the case of wind with a vertical component and is usually referred to as static soaring. This describes rising air which offsets the sink speed of the bird. The aerodynamic conditions are the same relative to the surrounding air; the bird still loses altitude with respect to the air but since the air itself is moving upwards with respect to the ground, the bird can continue to gain potential energy if the vertical wind is greater than the normal sink speed. Thermal convection was not well understood at the time and Rayleigh suggests that

“... it does not seem probable that at a moderate distance from the ground there could be a sufficient vertical motion of the air to maintain the birds, ...” [84]

Without sufficient vertical wind Rayleigh went on to describe the possibility of gaining energy by flying through stratum (layers) of air with different horizontal speeds, since it was known that wind speed increased with altitude. He noted that by flying upwards into a higher oncoming wind speed the bird ended up travelling faster with respect to the air. Conserving this energy during a turn left the bird heading downwind. Descending again into the slower oncoming air again resulted in an increase in airspeed due to the bird having reversed direction. He went on to note that although an abrupt change of wind speed with altitude was unlikely, the same principle should apply in a continuous sense. For a bird to maintain flight in a continuous wind gradient

“...it is only necessary for him to descend while moving to leeward [downwind], and to ascend while moving to windward [upwind], the simplest mode of doing which is to describe circles on a plane which is inclined downwards to leeward.” [84]

This action is now known as dynamic soaring and the cycle of climbing and diving through a horizontal wind shear gradient is known as a *Rayleigh cycle*. More generally, dynamic soaring represents energy gained from the wind through use of the spatial or temporal distribution of wind.

Later that year Hubert Airy provided another clear description of soaring flight in Nature [3]. He claimed to have developed his theories in parallel with Lord Rayleigh and drew similar conclusions. He also described many of the wind features required for soaring. He noted that the relatively consistent shape of clouds suggests that features in the wind field may be self-consistent and drift with the average wind. He also suggested that the vortices which are evident in the internal motion of clouds demonstrated circulation of the air which may be present but unobservable at altitudes lower than the cloud base. Finally, he identified the possibility of dynamic soaring if the bird circled across the boundary between regions of varying lateral wind speeds, which is the lateral equivalent of a Rayleigh cycle. Given the relative lack of

hard data both papers provide remarkable insight from the observations and analysis of bird flight.

While bird soaring over land was later shown to be primarily due to vertical motion of the air from thermal columns, the use of dynamic soaring over the sea by albatrosses was confirmed. Idrac [48] used an instrumented kite to identify the lifting air in thermals and also the boundary layer variation of lateral winds over the ocean. He was able to calculate the energy gain of albatrosses and concluded that

“These trajectories of albatrosses are the most advantageous as regards gain of energy.” [48]

In response to Idrac’s experimental work Walkden published a mathematical description of soaring flight and demonstrated the mechanism of energy gain as expressed in the kinetic energy gained from the wind. He also provided an equation to calculate the minimum wind shear required for energy-gain climbing in linear horizontal shear and suggested that dynamic soaring should be possible with a small manned aircraft over a lake or ocean [103].

As glider aircraft developed and knowledge of the structure of the atmosphere improved, gliding aircraft became much more common. However, for modern manned gliders, static soaring is used far more often than dynamic soaring. Despite it being well understood, the conditions for dynamic soaring are not easily exploited by manned vehicles. Boundary layers tend to be close to the ground and flying at high speeds at this altitude represents significant danger. Also, manned aircraft are generally too large to take advantage of the high gradients required for soaring which only occur at low altitude. However, a small UAV is of a comparable size to a large bird and with sufficient planning and control could conceivably take advantage of static and dynamic soaring to extend flight duration.

2.2 Atmospheric Energy Sources

Soaring utilises energy extracted from wind patterns in the atmosphere to provide energy. Energy is collected using either static soaring; extracting energy from rising air, or dynamic soaring; utilising energy from spatial wind distributions. In order to understand these conditions, some information on the basics of air motion in Earth's atmosphere is required. Section 2.2.1 provides a basic description of the atmosphere of Earth and the mechanisms that provide air motions for soaring flight. The following two sections describe the particular conditions required for static and dynamic soaring respectively.

2.2.1 Atmospheric conditions for soaring flight

The atmosphere of Earth is the region of gas trapped by gravity above the Earth's surface. Near the surface, dry air primarily consists of nitrogen (78.1% by volume), oxygen (20.1%), argon (1%) and other trace gases. Water vapour is also present and varies in concentration between 0 and approximately 4% by volume. Both the density and pressure of the air in the atmosphere are highest at the surface and decrease monotonically with altitude. Figure 2.1 illustrates the variation of temperature, pressure and density of Earth's atmosphere for dry air up to 86 km in altitude. Data are drawn from the U.S. 1976 standard atmosphere which is a common atmospheric model for aviation [102].

The atmosphere is generally defined in four layers delineated by variations in atmospheric properties. The maximum altitude of each layer is known as a pause, such that the troposphere extends from the ground to the tropopause, above which is the stratosphere which extends until the stratopause and so on. The effective thickness of each layer and total thickness varies with latitude, with the atmosphere being substantially thicker at the equator than at the poles. The lowest layer is the troposphere which begins at the surface and rises to an altitude of approximately 11 km. At the mean sea level at mid latitude, the standard surface air temperature is 288.2 K, the pressure

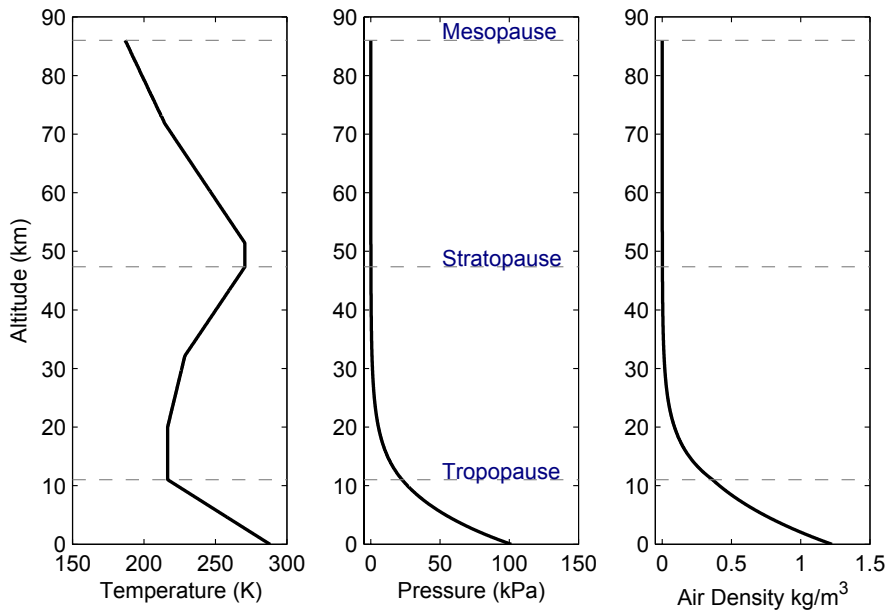


Figure 2.1: U.S. Standard Atmosphere 1976. This atmospheric model is valid for dry air at mid latitudes up to the mesopause at an altitude of 86 km above mean sea level.

is 101.3 kPa and the density is 1.225 kg/m^3 . The troposphere contains around 78% of the mass of air in the atmosphere. As shown in Fig. 2.1 the temperature in the troposphere generally decreases with altitude, at a relatively linear rate known as the *lapse rate*. The troposphere is the most dynamic layer as air is subject to heating from the ground and solar radiation, resulting in considerable variations in pressure and temperature. The top of the troposphere is defined by a temperature inversion known as the tropopause at an altitude of approximately 11 km, above which the temperature starts to increase with altitude, as illustrated in Fig. 2.1.

The layer above the tropopause is the stratosphere, which stretches from the top of the troposphere to an altitude of approximately 47 km. The stratosphere is so named because it tends to be more stable than the troposphere, with very little vertical air motion resulting in ‘stratified’ layers of air. The stratosphere increases in temperature with altitude due to the higher concentration of ozone, which is very effective at absorbing solar radiation. Only 0.1% of the mass of air in the atmosphere is above the stratosphere.

Above the stratosphere is the mesosphere. The mesosphere has low air density, from approximately 1.4×10^{-3} kg/m³ at the stratopause decreasing to approximately 7.0×10^{-6} kg/m³ at the mesopause. The mesosphere is defined by a decrease in temperature with altitude due to the lack of air molecules capable of absorbing solar radiation. The final layer is the thermosphere, which stretches from the mesopause into space. The top of the thermosphere is difficult to define due to the very low concentration of gas molecules. Flight requires sufficient gas pressure and density to maintain enough lift to offset the weight of the vehicle. A commonly used boundary to space is the Kármán Line at 100 km altitude above which a flying vehicle would need a velocity higher than orbital speed to provide sufficient lift for flight. However, the current altitude record for a non rocket-powered aircraft is 37650 m set in 1977 in a jet-powered fighter aircraft [37].

For the small vehicles considered in this work, flight is possible only in the troposphere and lower stratosphere. The troposphere is also of most interest for soaring flight as it contains the most dynamic flow with significant spatial and temporal variations of vertical and lateral wind required for energy-gain soaring flight.

Air motion in the troposphere is driven by a number of factors at a variety of spatial scales. The major source of energy for the atmosphere is solar radiation. Radiant energy from the sun reaches the atmosphere and is directly absorbed by the air, absorbed at the surface, or reflected back into space. The amount of energy in each each of these conditions depends on the air composition and ground materials, but generally approximately 30-50% of the energy is reflected back into space [67]. Energy is stored in the atmosphere as heat, potential and kinetic energy.

Near the equator, more energy is absorbed by the ground and generally the atmosphere is cooler than the ground temperature and tends to absorb energy from the ground. At increased latitudes, the ground tends to be cooler and energy is transferred from the atmosphere back into the surface. Thus the atmosphere acts as an energy transfer system, moving energy from the equator towards the poles (see Fig. 2.2). This air motion is driven by the temperature differences between the equator and poles, resulting in large recirculating cells where air rises up at the equator and out

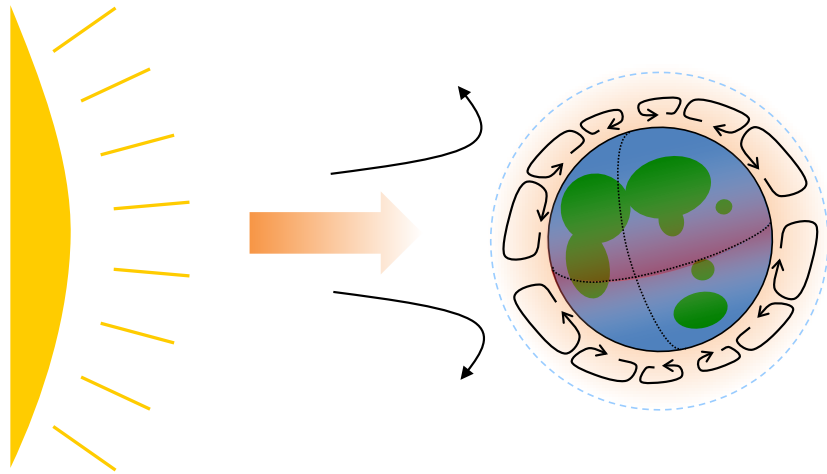


Figure 2.2: Energy from the sun is absorbed by the surface and atmosphere. The equator absorbs more energy which causes air to rise and move towards the poles in large recirculating cells.

towards the poles. This interaction causes large scale effects like light winds and thunderstorms near the equator and high-altitude westerly winds in the hemispheres [67].

At the synoptic scale (order of 1000 km) wind is driven by local pressure variations. Common weather charts show the variation of pressure through isobars (lines of constant pressure) similar to a topographic map of altitude. Air has a general tendency to flow from high pressure to low pressure regions; causing relatively calm weather in high pressure regions and unsettled weather in low pressure regions. The spatial rate of pressure change is known as the *pressure gradient*. The force from a pressure gradient is coupled with Coriolis acceleration due to the rotation of the Earth. This results in winds that tend to circulate pressure regions, with the wind direction running parallel to the isobars. Due to the Coriolis force, air rotates clockwise around low-pressure regions in the southern hemisphere and counter-clockwise in the northern hemisphere. The wind produced by this effect is known as the *geostrophic wind* and allows good estimation of the wind in the upper troposphere. This combination of forces also leads to storm systems such as cyclones, where very low pressure drives a large scale air rotation which draws in air producing strong wind and rain. Figure 2.3 shows a typical mean sea level pressure (MSLP) chart over Australia in January 2011.

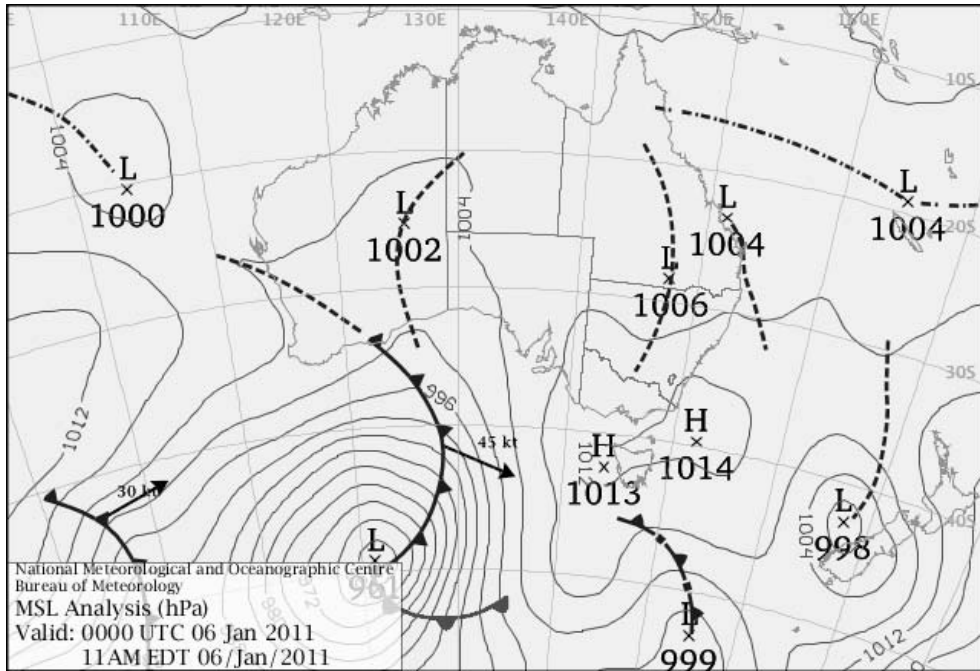


Figure 2.3: Mean sea level pressure chart over Australia for 6 January 2011. Pressure is illustrated by the grey solid lines (isobars) and numbers. H and L illustrate high and low pressure regions respectively. Geostrophic wind is shown by the arrows. Note that the direction is tangential to the isobars and the strength is related to the pressure gradient (relative closeness of the isobars). [Courtesy of the Bureau of Meteorology [16]]

Wind is driven at higher altitudes by air flowing between pressure variations in the atmosphere. At low altitudes, this flow interacts with the surface of the earth in a boundary layer known as the Planetary Boundary Layer (PBL). Boundary layers are defined by the shear gradient that results from a viscous fluid flowing over a fixed surface. Drag from the surface imposes a no-slip condition, meaning that at the surface the fluid must have zero speed. However, at a sufficient distance away from the surface the flow is almost continuous, known as the free-stream condition, as illustrated in Fig. 2.4.

The PBL is the lowest layer of air in the atmosphere. It ranges in thickness and composition depending on the time of day, season, latitude and other meteorological features. Typically, the PBL is one of two common forms; a turbulently mixed convective boundary layer (CBL) which has significant vertical air motion or a more stable stratified boundary layer (SBL) which has reduced vertical air transfer. At

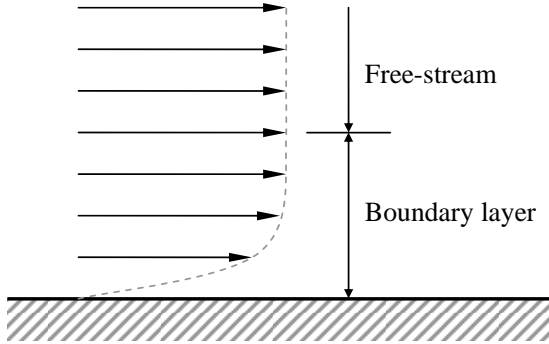


Figure 2.4: Laminar boundary layer for viscous flow over a fixed surface.

tropical to mid-latitudes during the day, the PBL is usually turbulent due to solar heating and forms a CBL capped by a temperature inversion. At night and in higher latitudes the PBL usually has reduced vertical mixing and is a thinner SBL [50].

Generally, lateral wind speed is lower near the surface and increases with altitude. In a CBL the vertical mixing tends to reduce lateral wind variation so that the wind increases with speed quickly near the surface and remains relatively constant to the top of the boundary layer. In a stratified layer the wind tends to increase in speed more gradually with altitude. This also affects the wind direction. At low altitudes, the low speed reduces the effect of the Coriolis acceleration and the wind is directed more towards the direction of decreasing pressure gradient. The angle between the wind and the isobar direction varies between 45° for rough terrain to 10° for smooth terrain. Thus, surface winds can be used to estimate pressure variation and identify local regions of low pressure [20, 95].

Mesoscale features are atmospheric processes in the order of tens to hundreds of kilometre length scales, usually operating for minutes or hours. Examples include thunderstorms and wind-water interactions. Microscale features are the smallest features in meteorological study, and have length scales up to hundreds of metres and time scales in the order of seconds or minutes. This ranges from local turbulence to the small scale convective mixing found in thermals. Microscale effects are driven by local temperature variations, terrain and the interaction of larger mesoscale processes with local features.

Soaring flight requires particular wind features for energy-gain. Static soaring requires vertical air motion and dynamic soaring requires spatial wind gradients. In most cases these both arise from microscale processes. The following two subsections describe some of the more common sources of lifting air for static soaring (§2.2.2) and sufficient wind gradients for dynamic soaring (§2.2.3).

2.2.2 Static soaring sources

Static soaring utilises vertical wind motion. Vertical wind arises from a number of natural sources in the atmosphere. The most common sources are convective mixing of the planetary boundary layer resulting in thermal columns, deflection of lateral winds by geographic obstacles resulting in a vertical wind component, and mixing of the atmosphere from other sources such as storms.

Convective circulation in the lower atmosphere (thermal columns)

Thermals are the vertical mixing features of a convective boundary layer. As the atmosphere warms during the morning and early afternoon, local heating of ground features convects into the atmosphere and causes local temperature variation. The resulting circulation of air causes the PBL to thicken as thermals lift warm air to higher altitudes, forming a mixed CBL. Generally, temperature decreases with altitude, and the top of a CBL is usually defined by a capping inversion where the temperature lapse inverts. Typically the PBL is stable and stratified during the night, resulting in a thin SBL (usually less than 500 m thick). As temperature increases the layer thickens and vertical mixing increases as it transitions into a CBL. Maximum thickness is usually achieved in the mid afternoon and the layer remains convectively mixed until cooling and contracting back into an SBL after sunset [51].

The convection in a CBL is driven by solar radiation heating the Earth's surface and convecting into the surrounding atmosphere. Darker features tend to reach higher temperatures and heat the air to a higher relative temperature than surrounding air.

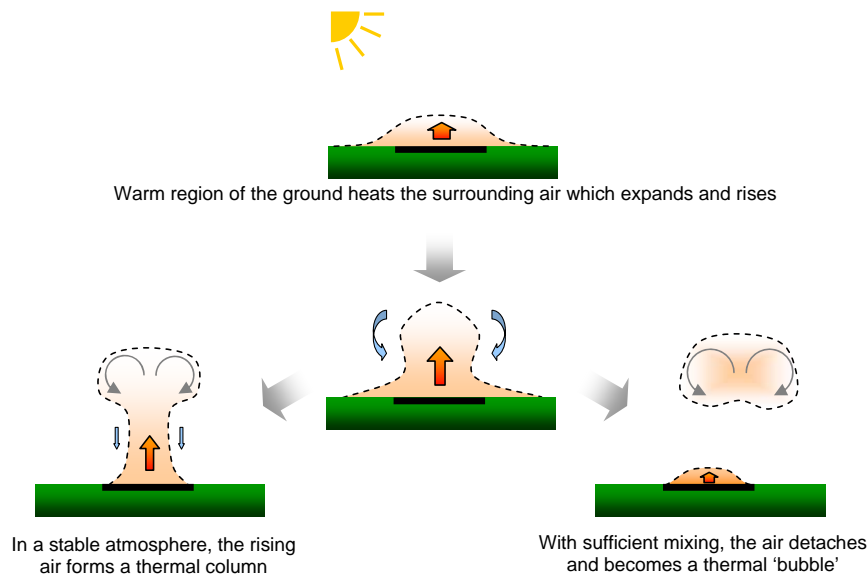


Figure 2.5: Formation of thermals in stable and mixed conditions. The black rectangle represents a ground feature which is radiating heat into the surrounding air. As the air warms it rises. With little wind or mixing a tall thermal column can form, potentially up to the lifting condensation level where a cumulus cloud will form in moist conditions. With enough mixing, the thermal can detach and form a mobile thermal bubble.

The warmer air expands, rises and cools, which draws in air at the base and forms a thermal column of lifting air. Cooler air at higher altitudes is displaced outwards by the rising warm air and is forced downwards. The resulting thermal column tends to have a core of buoyant warm air surrounded by cooler sinking air, known as *convective circulation*. With low-speed lateral winds this can appear as a column with circular cross-section increasing in radius with altitude rising from the ground up to the cloud base, ranging in diameter from 50 to 1000 m [60]. The moisture drawn up by thermals condenses at the lifting condensation level and can form visible clouds. The unique shape and texture of the resulting Cumulus clouds can be used to identify thermal conditions.

More commonly, thermal lift can be moved from the point of formation by lateral winds. This process forms detached thermal ‘bubbles’ of recirculating air in a rough toroidal shape which rise and move with the mean wind as shown in Fig. 2.5. Thermal bubbles are also a product of unstable convection in the atmosphere, but the toroidal shape is relatively common as air is drawn inwards towards the core at the base of

the bubble, and moves outwards away from the core as it cools towards the top of the thermal bubble [82]. This is illustrated in Fig. 2.6.

This form of thermal lift is common over land during the day. The structure of the atmosphere changes significantly at night and becomes more stable and stratified as the ground reaches a temperature equilibrium through heat conduction.

Previous research has developed models for the formation, development and shape of thermals. While detailed models for the convection are not required for the current research, it is worth noting the models developed for meteorological modelling of thermal columns.

Thermals occur throughout the boundary layer. Data collected in autumn (September) 1987 in Boulder, Colorado showed thermals covering between 40 and 50% by area from surface level to the top of the CBL [110]. The relative buoyancy of ther-

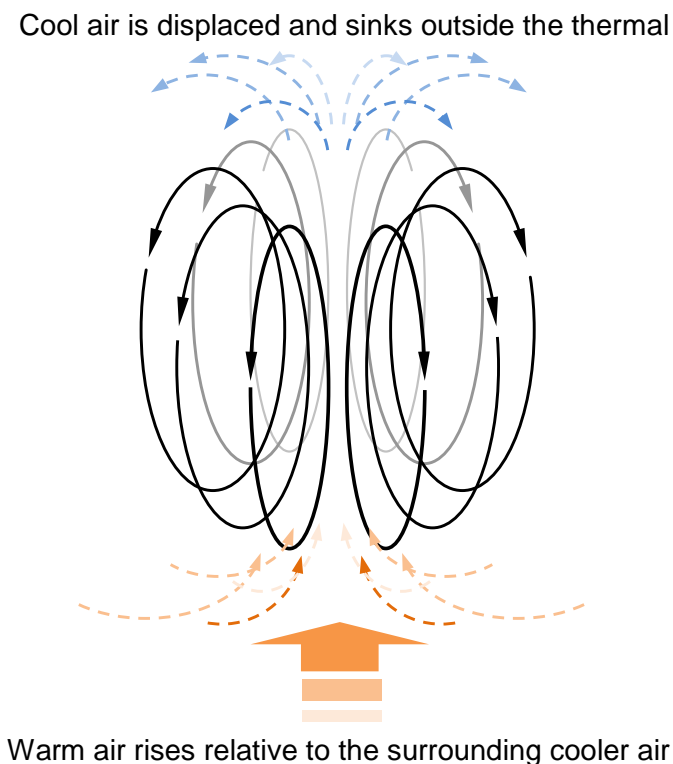


Figure 2.6: Toroidal thermal bubble. The bubble can drift with lateral wind but usually rises and expands until it reaches the upper troposphere.

mals tends to be highest at low altitude and decreases with altitude [60, 110]. Young suggests that the normalized mean vertical velocity of updrafts, \bar{w}_T :

$$\frac{\bar{w}_T}{w_*} = 0.85 \left(\frac{h}{h_i} \right)^{\frac{1}{3}} \left(1.3 - \frac{h}{h_i} \right) \quad (2.1)$$

where h_i is the boundary layer thickness and w_* is the velocity scale. The velocity scale is a further function of the layer thickness h_i , surface temperature flux B and mean potential temperature $\bar{\theta}_v$:

$$w_* = \left(\frac{gh_i B}{\bar{\theta}_v} \right)^{\frac{1}{3}}. \quad (2.2)$$

A similar study by Greenhut and Khalsa [42] showed higher magnitude thermals (up to $w_T/w_* > 1$) but with a different threshold for defining a thermal (Young classed all updrafts as thermals whereas Greenhut and Khalsa used an updraft threshold). These studies used aerial data collected during aircraft flights and measurements from towers and kite balloons. A later study using instrumented American pelicans flying over the Lahontan Valley in Nevada, USA, found that those birds tended to fly in the lower to middle range of the boundary layer (most measurements were recorded between 0.2 and 0.6 h/h_i). The boundary layer thickness was estimated at 2220 m over mountains and 1520 m over valleys. Normalised updraft intensities used by the birds were between 0.7 and 1.2 [91].

While these data give a good understanding of the average prevalence and strength of thermal columns, for most of the research discussed here the interest is in the ability of a UAV to use thermal columns which could be considered typical. Previous studies have used a range of techniques for modelling thermal columns. Wharington uses a Gaussian profile only incorporating updraft [105]. This model was also used by both Allen [8] and Edwards [32] in their soaring controllers.

The thermal model assumes a planar circular normal distribution of lift around a thermal centre point characterised by a maximum lift w_{max} and characteristic radius R . The model accounts for the downwards flowing air often found surrounding the

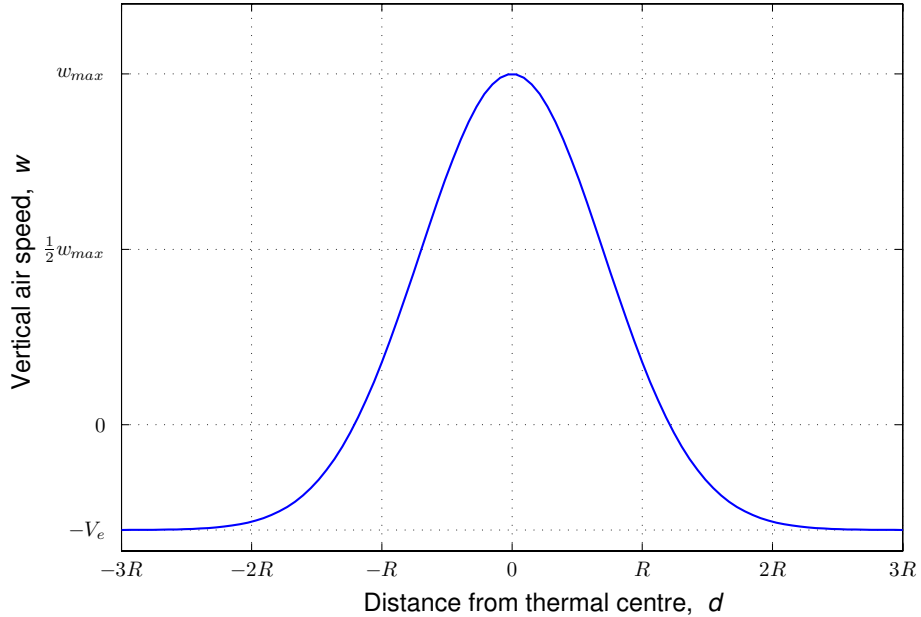


Figure 2.7: Variation of lifting air speed for the Allen thermal model [8]. The maximum lift speed is w_{max} , characteristic radius R and environmental sink V_e .

lifting core of a thermal with an ‘environmental sink rate’ correction V_e . At a distance d from the estimated centre of the thermal the vertical speed w is shown in Eq. (2.3).

$$w = (w_{max} - V_e) e^{-\left(\frac{d}{R}\right)^2} - V_e \quad (2.3)$$

Figure 2.7 illustrates the lift variation in a thermal for this model. Note that the vertical wind does not transition smoothly into the environment unless there is a constant sink rate across the entire environment or $V_e = 0$.

Allen generated a much more comprehensive model in [7]. The reader is referred to that paper to prevent repetition of the equations here. Allen’s model allows estimation of the vertical velocity profile of a thermal as a function of atmospheric parameters based on real data collected during flight tests. However, the author notes that many parameters are dependent on the topography (desert), which makes general modelling difficult.

A limitation of the models presented so far is that they do not model the lateral wind speeds. In stable environments like the desert the thermals tend to have a greater

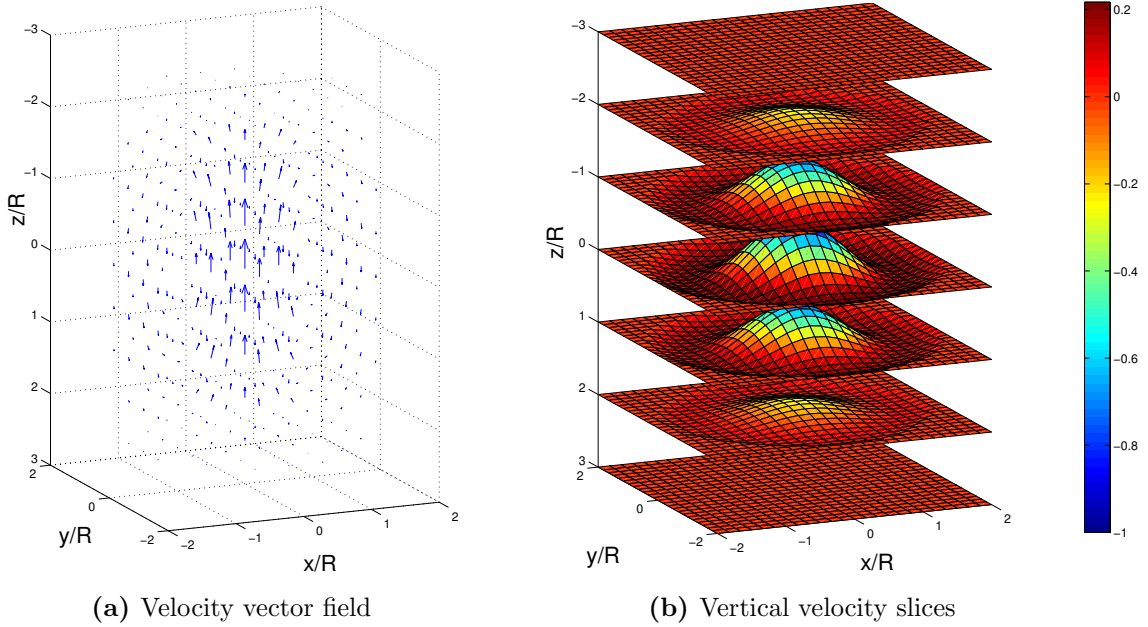


Figure 2.8: Velocity vector field and vertical velocity profile sections for a toroidal thermal. Subfigure (a) shows the velocity vector field. Note the inwards flowing air at the base of the thermal and outwards flowing air at the top. Subfigure (b) shows the vertical velocity at a set of horizontal planes through the thermal. Note the lifting core surrounded by sinking air. The model is conservative so there is no net vertical flow.

continuous vertical extent and less lateral motion. In this thesis a new thermal model which accounts for lateral flow was developed. The model is based on the toroidal shape predicted by some models [7] and observed by glider pilots [82]. Details on the thermal bubble can be seen in Appendix A. A picture of the velocity vector field and vertical profile is provided in Fig. 2.8.

Geographic wind deflection (ridge lift & lee waves)

Low altitude lateral winds can be deflected vertically by ground obstacles such as mountain ridges, where it is known as ridge lift (Fig. 2.9). The amount of lift depends on the wind speed and the size and shape of the ground obstacle. Ridge lift is a common source of atmospheric energy for manned glider aircraft due to the reliability of the lifting wind and the vertical extent of the lifting air.

Another source of lifting air from geographic features are lee waves. Lee waves are a set of consistent atmospheric waves formed running parallel in the lee of a large formation feature such as a mountain range. Wind speed generally increases with altitude so that large obstacles like mountain ranges can result in strong lifting conditions in the lee of the mountains. As in the thermal case, the rising air starts to cool and sink again as it reaches high altitude. Due to the prevailing lateral wind the air continues to move further away to the lee of the obstacle. The sinking air drives more lifting air and the resulting formation is a set of long wavelength standing waves forming behind the obstacle. In moist conditions this can result in cloud formation at the peaks of the waves, on large enough scales to be observed from the ground or space as a set of linear clouds running roughly parallel to the obstacle. Lee waves can rise into the stratosphere and have been used for many of the world's longest distance and duration manned glider flights.

Ridge lift is a popular source of energy for manned gliders due to the reliability of lifting conditions. Since ridge lift is dominated by prevailing wind conditions, it is often possible to estimate the location and strength of the lift with an estimate of wind speed from synoptic scale wind estimates.

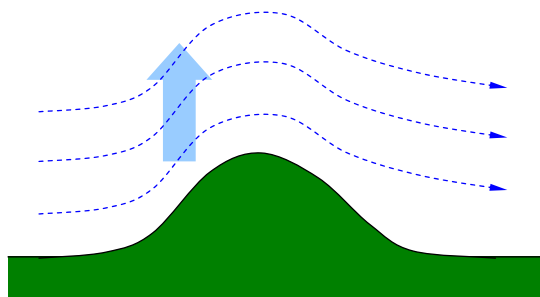


Figure 2.9: Ridge lift from lateral wind being deflected by a ground obstacle. The strength and vertical extent of the lifting air depends on the wind speed and the shape of the obstacle.

Other sources of rising air

Rising air can also be found in other atmospheric phenomena. Storm systems can cause very rapid air transport with lifting winds of over 15 m/s being recorded [36]. However, storm systems are difficult to predict and have a wide range of atmospheric conditions in a relatively small space. This makes them difficult and potentially dangerous for flight and are not intentionally flown by human piloted aircraft. This has led to work attempting to utilise unmanned aerial vehicles to collect data from inside storm systems [34, 35]. Autonomous soaring control and particularly some of the wind mapping techniques described in this thesis could provide significant utility in these situations.

2.2.3 Dynamic soaring sources

Dynamic soaring utilises spatial or temporal distributions of the wind to gain energy. Most wind fields consist of features that vary over a variety of spatial and temporal scales. Short distance and time phenomena are usually classed as turbulence and are assumed to be random motions and not possible to model.

Surface boundary layer

The primary source of reliable wind shear is in the PBL. Wind shear occurs due to the viscosity of the air causing a no-slip condition at the surface of the Earth which transitions into the mean wind at higher altitudes. The PBL can be divided into two main sub-layers, a lower layer where the friction and heat of the Earth's surface dominate the shear stresses and the wind is usually nearly parallel to the surface, and an upper layer where large scale effects like Coriolis forces and temperature variation cause shear stresses in all directions.

Generally, the surface layer is relatively thin, from 10-20m over flat surfaces such as the ocean up to 100m or more over rough or broken terrain [50]. During the night, the PBL is thin and stratified, and usually capped by a fast moving boundary layer

known as the nocturnal jet [95]. During the day the boundary layer grows to 1-2km in thickness with the upper boundary defined by a sharp increase in speed which caps the layer.

For dynamic soaring a relatively steep wind gradient is required. This occurs most reliably very close to the surface. However, other features such as the nocturnal jet and capping inversion layers may have sufficient wind gradient for soaring in some cases. The spatial variation of wind in a mixed CBL would usually be insufficient for dynamic soaring.

Other sources of wind shear

Wind shear can also occur outside the PBL. The jet stream is a high altitude, high speed body of air which moves around the planet at mid latitudes. The significant spatial variation in wind speeds may be sufficient for soaring flight. Grenestedt proposed the idea of jet stream soaring and showed that an efficient glider should be capable of continuous flight using the wind gradients in the jet stream [43].

Another popular source of wind shear is the shear created when high-speed winds pass over a relatively sharply defined obstacle such as a ridge (Fig. 2.10). Generally the wind shears over the top of the ridge but leaves a slower moving recirculating cell in the ridge lee. This can give rise to very significant wind speed changes over short distances. Unlike the boundary layer profiles this is not a smooth transition but the

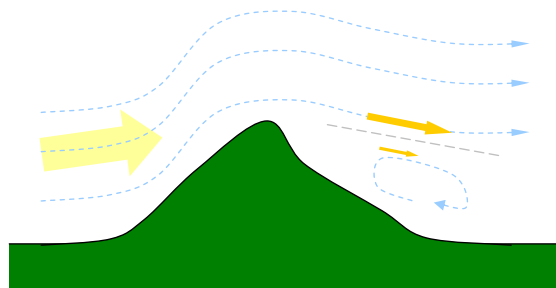


Figure 2.10: Ridge shear. Wind flowing over a sharp ridge can result in a very pronounced shear layer with a mass of high speed wind moving over a relatively slow moving cell of trapped air.

wind can vary by up to 10 m/s across a distance of a few metres or less. Thus, large amounts of energy can be captured in relatively few cycles. Dynamic soaring in ridge shear has become a popular radio control (RC) aircraft hobby. Very high speeds can be achieved as the aircraft accelerates in each successive cycle. Unofficial records of over 400 mph have been claimed with RC aircraft.

2.3 Static Soaring

Static soaring was the earliest identified form of soaring flight. It is also the most commonly observed soaring flight technique in birds. Static soaring only requires a source of air which is rising with respect to the ground. This condition is common during the day over land due to convective mixing of the planetary boundary layer. Essentially, uneven heating of the ground from solar radiation causes changes in local air temperature and density, resulting in convective mixing of the lowest level of the atmosphere (see §2.2.2 for further information). The resulting regions of rising air are exploited by birds to provide continuous flight whilst gliding, resulting in long duration flight without flapping. Static soaring is prevalent among birds of prey which search for and ambush prey from high altitude.

Studies of soaring birds have attempted to analyse both the behaviour of the bird and the conditions required for soaring flight. Early research on bird flight attempted to determine the aerodynamic properties of birds whilst gliding. This was attempted using stuffed bird samples and birds trained to fly in wind tunnels [47, 86, 100]. Since the sink rate represents the altitude loss rate with respect to the wind, a vertical wind which equalled the gliding sink rate would be sufficient for continuous energy-neutral flight.

Static soaring is also commonly used by manned gliders. Research has mainly focused on aircraft design to maximise endurance and modern sailplanes can fly almost indefinitely with sufficient lift sources. The results of manned soaring research have also driven research and demonstration of static soaring for unmanned aerial vehicles [4].

2.3.1 Bird static soaring

The earliest studies of bird soaring focused on the observed behaviour of soaring birds circling in flight and gaining altitude without flapping. This was discovered to be soaring in rising air by the Lilienthal brothers, who were working on the theory of gliding flight as well as their own manned glider attempts [63]. The behaviours were considered biologically interesting as soaring was mostly confined to larger birds such as vultures, condors, albatrosses, eagles and hawks [74, 77, 98–100]. The gliding behaviour was observed in many different regions around the world including both land and ocean flights. Different birds also used soaring for different reasons. Some birds used soaring for migratory flights; some species of migrating cranes were observed to use a combination of flapping and soaring flight to maximise travel efficiency over long distances [78, 79]. Their behaviour seems to roughly agree with modern manned glider efficiency principles for flying between thermals (see §2.3.2) [93]. Bird factors such as weight and wing loading also determine which part of the atmosphere is most used for migratory soaring. Larger birds which used a combination of soaring and flapping flight were observed flying at higher altitudes whereas birds which were also foraging tended to utilise convection circulation at lower altitudes [90]. Birds were observed to utilise both thermal columns and features such as ridge lift [89].

Other birds such as hawks and vultures use very efficient soaring with minimal wing flapping to fly for long periods over shorter ranges for hunting [75, 76]. As bird weight and wingspan increases, flapping flight consumes more energy [46], which is why larger birds tend to favour soaring flight.

This research showed that soaring formed an important part of the development of some bird species, allowing them to travel longer distances and fly for longer periods without requiring additional energy. However, it is difficult to draw too many conclusions about how the behaviour of soaring birds could be imitated by an autonomous vehicle for soaring flight. Birds have access to a much larger knowledge base through their extensive flight experience. Birds also have access to sensors and control that may not be available to an autonomous aircraft. However, the bird studies do show that in many regions there is sufficient energy to considerably extend

the flight duration of a gliding vehicle of a scale similar to a large bird.

2.3.2 Manned static soaring

Flying in lift from thermals poses two main problems. The thermal has to be located and the optimum bank angle has to be determined. This can be a difficult problem as thermals are not uniform and often drift in the wind. Glider pilots largely rely on heuristic rules to attempt to maximise energy gain. The heuristic strategies used by pilots vary with changes in the aircraft, weather conditions and pilot experience. The goal is to maximise the rate of energy capture. Since thermals have roughly circular vertical wind profiles, this is achieved by flying around the thermal centre. The optimum action should then produce relatively consistent energy gain. A simple method is to fly in variable circles when lift is encountered. During a cycle the thermal centre is estimated to be some distance away in the direction of the stronger lift. The next cycle moves towards the side with stronger lift and the process is repeated until the lift is even during the whole circuit. For a smooth circular profile this should be approximately centred around the thermal. A rough illustration is provided in Fig. 2.11.

This can be qualified by a rough set of rules to centre on a thermal. Allen and Lin [8] paraphrase Reichmann [85] to give the set of rules used by glider pilots for determining the optimum bank angle.

1. *As climb improves, flatten the circle (approximately 15 - 20° bank)*
2. *As climb deteriorates, steepen the circle (approximately 50° bank)*
3. *If climb remains constant, keep constant bank (approximately 25 - 30° bank) [8]*

Of course, actual thermal pilots have additional information about the expected lift profile of thermals which allows them to estimate the gains during flight. However, this can become more complicated as thermals drift and vary across their vertical

extent. The drift is actually naturally dealt with in the above algorithm if an air-relative frame is assumed, since there is nothing to link the motion to inertial space.

Manned gliders usually rely on a set of heuristic rules like these for flying in thermals. Generally, they try to locate lifting air by identifying clouds or other aircraft (manned or birds) in lift and when they pass through a thermal sensors such as a total energy variometer or vertical speed indicator will show the energy being gained from the thermal. Thermals also have vertical variation of the flow with air drawn upwards and towards the centre at the base and moving outwards at the top of the thermal. Thus, thermals may ‘appear’ stronger at the base due to the increased lift when banking against the inward flow [82].

Modern research into control of human gliders has mainly focused on competition gliding. There are a number of competitive gliding competitions with a variety of goals. Modern gliders are capable of remaining airborne almost indefinitely in favourable conditions so endurance competitions are uncommon. Cross-country gliding is a competitive sport which usually specifies a course around which competitors attempt to maximise speed. Usually, gliders are divided by limited wing span and mass and an

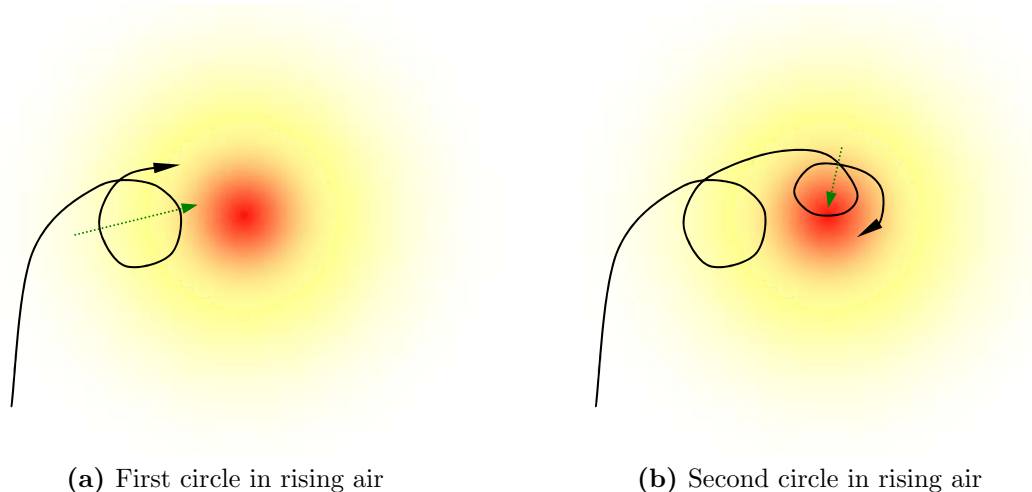


Figure 2.11: Heuristic rules for centring on lifting air. The thermal strength is indicated by the shaded background. The first cycle has high lift on the right side, so the thermal centre is somewhere towards the right (dashed arrow). The second cycle has stronger lift on the lower side, so the thermal centre is re-estimated. This continues until the cycles are consistent all the way around.

open (unlimited span) class. Courses can be as long as 1000 km. During an event the pilot has to balance energy capture (which usually involves circling in thermals) against the goal of completing the course as fast as possible.

There are many competing factors which determine overall performance. The most important is probably average thermal strength, since maximising energy capture rate reduces time spent circling in thermals and allows faster completion of the course. The balance of energy capture and travel is essentially an estimation problem relying on estimation of the average strength of thermals and the likelihood of encountering a thermal on a given path. Human pilots also use knowledge about observed thermal driving features on the ground and in the air. The main control variable in this problem is the flight speed. While it would seem that flying at the maximum lift-to-drag ratio speed would maximise performance this is not always the case. Higher flight speeds result in faster energy loss but in the presence of sufficient thermals the energy capture rate outweighs the energy loss resulting in faster overall performance. This problem was analysed in detail by MacCready [69, 70] and resulted in the common MacCready speed to fly estimation ring in gliders. MacCready showed that the optimal flight speed can be calculated by estimating the expected lift in a thermal.

The problem can be fairly simply explained. In cross-country gliding the goal is to complete a fixed course in the minimum time possible (i.e. maximise average speed). For simplicity consider a single repeatable segment on a linear course. Assume that a glider at the start of the segment has to travel to a thermal at the end of the segment and climb in the thermal to reach the same energy altitude as at the start of the course. The travel airspeed can be selected. At the optimum travel speed it will fly to the thermal and climb to the original altitude in the minimum time possible. At a higher speed, more energy will be lost during the travel which would require longer to climb in the thermal and result in a higher total time. At a slower speed the energy lost during travel is decreased but the time spent during travel is increased, also resulting in increased total time.

A sample trajectory is shown in Fig. 2.12. Let the forward distance be x_t and the vertical distance be z_t . Let W_c be the rate of climb in the thermal, V_x be the forward

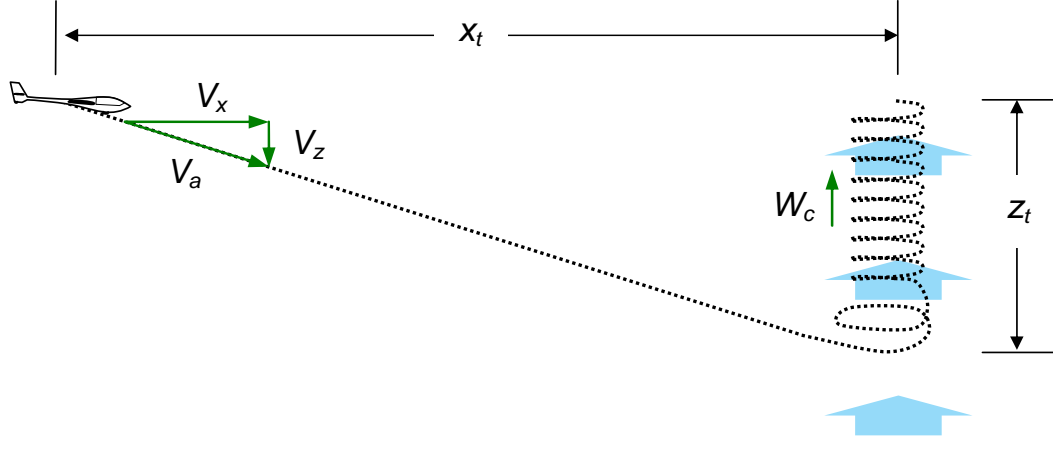


Figure 2.12: MacCready speed-to-fly theory determines the optimal speed to travel between known thermals.

speed during the cruise and V_z be the vertical speed. Both V_x and V_z are functions of the airspeed V_a for a known sink polar. Let t_{cruise} be the time spent in cruise and t_{climb} be the time spent in climb. Then, the goal is to find the average forward speed, $\frac{dx_t}{dt}_{avg}$.

$$\begin{aligned}
 t_{cruise} &= \frac{x_t}{V_x} \\
 t_{climb} &= \frac{z_t}{W_c} \\
 t &= t_{cruise} + t_{climb} \\
 &= t_{cruise} + \frac{z_t}{W_c} \\
 &= t_{cruise} + t_{cruise} \frac{V_z}{W_c} \\
 t &= \frac{x_t}{V_x} \left(1 + \frac{V_z}{W_c} \right)
 \end{aligned}$$

Therefore, the average forward speed is

$$\frac{dx_t}{dt}_{avg} = \frac{V_x W_c}{W_c + V_z}. \quad (2.4)$$

Since the forward and vertical speeds are functions of the airspeed through the sink polar, it is possible to solve for the optimum airspeed which will maximise cross-country travel speed with an estimate of the thermal lift speed. This research led to the development of mechanical speed-ring indicators which are fitted to gliders to allow a pilot to select an estimate of the expected lift and calculate the optimum airspeed. Further adaptations include a generalized version which incorporates calculations for thermals drifting at different speeds to the prevailing weather [94], and a stochastic approach to maximise overall lift in uncertain conditions [21].

Modern competition-grade gliders have well-studied sink polars such that the MacCready theory speed-to-fly estimates are very accurate. This allows pilots to rapidly determine whether a thermal is worth attempting to soar in to maximise speed around a full course. Competition is now mostly based on high-level estimates for the wind conditions.

2.3.3 UAV static soaring

Previous work in autonomous soaring in thermals has used a similar set of heuristic rules. Firstly, a model of the thermal is developed offline which should describe the spatial variation of lifting air around a thermal. This is used online to estimate the centre and lateral drift of the thermal. The controller then attempts to fly (air-relative) circles around the centre of the thermal to gain energy. This approach was pioneered by Michael Allen working at NASA Dryden using an SBXC remote control scale cross country glider [6, 8]. The aircraft was powered by an electric motor driving a nose-mounted collapsible propeller which folds backwards against the fuselage when not in use. Computation and control was performed using a commercial off-the-shelf Piccolo Plus autopilot system with custom closed-loop controllers to identify and utilise thermal lift.

The thermal model assumes a circular normal distribution of lift around a thermal centre point characterised by a maximum lift w_{max} and characteristic radius R and an ‘environmental sink rate’ correction V_e , as described in §2.2.2.

Aircraft total power and power rate were estimated using airspeed, altitude (from a static pressure sensor) and throttle (if the engine was active). The power estimate was used to identify and estimate the thermal centre. The thermal radius was then estimated using the assumed thermal model to model the lift decay rate away from the thermal centre. Finally, these results were used to generate a heading rate command to circle the thermal centre which was sent to the lower-level control loops to generate control surface actuations.

The research culminated in a number of demonstration flights showing significant energy gain from thermal columns. Test flights were performed at the Edwards Air Force Base in Antelope Valley, California, USA, during summer months. Energy gained from thermals resulted in an average altitude gain of 173 m per identified thermal.

Similar research was developed by Edwards and Silverberg [32] in pursuit of developing an autonomous thermal soaring aircraft (named ALOFT) capable of competing against human pilots in cross-country gliding competitions. The general approach was similar to that of Allen's work but with a number of improvements. Edward and Silverberg adopted an active greedy search which uses least squares minimisation to estimate the location of the thermal centre [31]. That research used a lookup table based on the thermal radius to determine the orbit radius rather than optimising over the collected data to determine the actual distribution. The authors acknowledged that this approach is stable but potentially less optimal than a more adaptive data-driven approach.

The soaring control was tested on an RnR SBXC cross-country glider platform. A Piccolo II autopilot performed low-level control. Thermal estimation and high level commands were generated on the ground using an off-board computer which returned guidance commands to the aircraft at a rate of approximately 2 Hz. Data were collected at 2 Hz and stored in a first-in-first-out queue containing a total of 45 s worth of data. Each data point contained time-stamped measurements of inertial location, airspeed, and wind speed. The data were processed on the ground to determine the presence and location of thermal columns. A single thermal column was tracked at

any given time.

The guidance scheme was demonstrated in a competitive remote-control soaring competition; the 2008 Montague Cross-Country Soaring challenge. The ALOFT aircraft was the only autonomous competitor and placed third at the end of the competition. The challenges included both speed challenges, where competitors must complete a predefined course in minimum time, and distance challenges, where competitors must fly as long a distance as possible within a limited course. The aircraft flew up to 63.5 km (39.4 miles) with flight times lasting over 3 hours. The aircraft was especially effective at high altitudes where human piloting is difficult due to lack of visibility. A more recent flight demonstrated autonomous soaring of a 97.2 km round trip flight unofficially setting a new soaring record [32].

Similar research for thermal identification and tracking has been demonstrated by Andersson [10]. Kahveci *et. al.* examined the control strategies in further depth and examine the applicability of LQ control [49].

These methods provide competitive results but are limited to certain types of lift and require considerable hand tuning to operate in variable conditions. These methods are effectively simulating the actions of a human pilot, which combine previous knowledge of thermal flights to build an assumed model of thermals and take actions which have worked in past flights. The autonomous flights of this type are similar but can suffer from a lack of adaptivity. In consistent conditions they perform well but may struggle in varying conditions where human pilots have additional experience and can adapt faster to observed changes.

More adaptive soaring research has also been considered. One of the earliest researchers into autonomous soaring was John Wharington who examined the mechanisms of soaring flight and proposed a number of control solutions. His work focused on utilising reinforcement learning (RL) to develop adaptive controllers during flight. His early work utilised Q-learning which is an RL method in which states and actions are mapped to a value or ‘quality’ function. Learning which actions improve the value function over a large number of trials allows an overall control policy to be determined [96].

Wharington used RL to learn parameters of a heuristic based thermal locator and to estimate speed-to-fly for flights between thermals in cross-country soaring. However, while the learning rate was slow (“several months” of real time learning [106]) the method did converge and was able to learn optimal gains for both thermal soaring and speed-to-fly. Wharington concludes that while the approach shows promise the computing hardware was inadequate at the time for such a method and the solutions prepared were potentially too specific and not general enough for flight application [105].

2.4 Dynamic Soaring

Dynamic soaring is the utilisation of spatial variations of wind to gain energy. Energy is captured by flying into wind which produces an effectively increased forward airspeed. This increases the air-relative kinetic energy of the vehicle. However, unlike static soaring, dynamic soaring is not usually a continuous process. Most wind gradients are spatially limited and dynamic soaring requires complex cycles to realise net energy gain. Also unlike static soaring, a typical dynamic soaring cycle contains both energy loss and energy gain segments. This means that planning and control for dynamic soaring is much more complicated and would require more sophisticated control than for an autonomous vehicle using only static soaring.

2.4.1 Bird soaring

As with static soaring research, early research into dynamic soaring focused largely on birds. Dynamic soaring continues to receive less direct interest for UAV applications due to the difficulty of dynamic soaring planning. Early research noted that as well as the circling behaviour of birds over land, some soaring birds performed repetitive cyclic manoeuvres over the oceans that seemed to allow extended flight with little wing flapping. These cycles appeared to be performed at low altitudes just above the ocean surface where convective mixing would be limited.

Lord Rayleigh first noted the patterns of flight in 1883 and suggested that the birds must be utilising variation in the flow to maintain flight without flapping [84]. Froude estimated the vertical wind speed from waves and determined that it was insufficient for soaring of albatrosses, and that they must instead have been capturing energy through some mechanism other than vertical air motion [38]. The first in-depth study of the flight patterns was by Idrac [48] who noted the soaring flight and attempted to study the wind conditions. He used kites to measure the air properties but determined that the birds must be using rising air rather than true dynamic soaring. However, Walkden [103] showed that a bird could maintain airspeed by climbing through sufficient wind gradient. These seemingly conflicting results made it difficult to determine the common mode of soaring over the oceans and modern analysis has shown that in most cases a combination of static and dynamic soaring is employed by birds in different conditions over the oceans. This was probably the first mathematical analysis of dynamic soaring. Later research found that there can be rising air over the ocean when the air temperature is higher than the ocean temperature. Small convection cells form and are subsequently deformed by the lateral wind into long stretches of alternating rising and falling air known as roll vortices [109]. Further research identified the conditions for soaring flight. Brown provides a very good summary of the knowledge of bird soaring by 1963 [15].

Recent advances in computers have provided numerical solutions for optimisation of the trajectories used by birds for soaring flight and have allowed identification of the gradients required for soaring [87, 108]. These studies show that birds should be able to gain enough energy for continuous travelling flight even in an upwind direction in conditions which are typical over the open ocean. Birds which make the most extensive use of soaring such as albatrosses also use seasonal information to benefit from seasonal winds for migration routes to minimise energy expenditure [104].

2.4.2 UAV dynamic soaring

As in the static case it may be difficult to emulate directly the behaviour of dynamic soaring birds with a soaring UAV. However, the process of dynamic soaring is now well understood and an autonomous system should be able to take advantage of the principles of dynamic soaring flight. This concept has seen some research in recent years due to the increased accessibility of UAVs and increased scientific interest in having long-duration surveys from aerial vehicles.

Early research focused on the requirements for a soaring aircraft in wind shear. There has been considerable research into offline optimisation of dynamic soaring trajectories [65, 104, 108, 111, 112]. However, while these studies show that dynamic soaring is possible, they do not necessarily address the problem of online control of a dynamically soaring UAV. Boslough shows that an optimised segment-based cycle (known as a Rayleigh cycle) could achieve upwind progress using a UAV with similar parameters to an Albatross. He goes on to show that the performance improves by optimising over a full 3D cycle by allowing continuous control throughout each cycle. Finally, he demonstrates remotely controlled dynamic soaring flight in ridge shear [11]. Soaring in ridge shear with remote control gliders has become a popular hobby sport in recent years due to the very high speeds obtainable by repeated dynamic soaring cycles.

To the author's knowledge, as yet there has not been a demonstration of autonomous dynamic soaring control. The problem is made difficult by the relatively demanding flight conditions where most wind shear is found. Strong shear is found close to the Earth's surface and in the lee of objects such as ridges. These make the use of an autonomous vehicle difficult as very reactive control is required to prevent crashes. However shear does occur at higher altitudes but is difficult to identify and utilise with a remotely piloted aircraft. In this respect an autonomous vehicle may have an advantage due to the ability to directly sample the wind and quickly respond. This concept has been studied in the form of utilising turbulence for soaring flight. Lissaman showed that an aircraft with a lift-to-drag ratio of 20 should be able to sustain flight in gusts above 20% of the cruise speed [66]. Langelaan further explores the gust soaring concept using closed-loop LQR control to react to gusts and

attempt to fly at the optimum climb condition to maximise energy gain. He showed a significant reduction in energy loss over a fixed cruise in a random thermal gust field [54, 55]. Depenbusch used a receding horizon control to control both airspeed and air-relative climb and demonstrated positive energy gain in a random Dryden turbulent field [28]. This work is potentially significantly easier to deploy on a UAV as it does not require extensive modelling of the environment and is purely reactive to turbulence as it is experienced by the aircraft. Finally, Kyle's PhD thesis [52] demonstrates analysis of a number of optimisation routines for on-line control of a soaring UAV. He assesses particle swarm, direct shooting and hybrid solvers for energy-based optimisation for control of a soaring aircraft. Of particular interest are the semi-dynamic soaring results utilising receding horizon model predictive control in a combination of shear and a thermal.

2.5 Summary

There has been significant research into soaring with fixed-wing vehicles. Early research focused on the ability of some birds to utilise the wind to minimise energy expenditure. With the introduction of manned aerial vehicles, similar techniques were pursued by pilots to capture energy during flight. Modern sailplanes are very efficient at collecting atmospheric energy and can fly almost indefinitely in sufficient conditions.

Energy is transferred from the atmosphere into a flying vehicle through vertical air motion or spatial wind distributions. These conditions occur commonly in Earth's atmosphere. Rising air is produced through the convective mixing of the lower troposphere due to solar heating, causing 'thermal' columns of rising warm air. Lateral winds caused by pressure variations can also be deflected by ground obstacles resulting in vertical winds. Wind distributions are common in the planetary boundary layer where the wind speed increases from close to zero near the surface of the Earth up to the mean geostrophic wind at high altitude.

Utilising rising air is known as static soaring and is a common method of gaining

energy for birds and manned glider aircraft. UAV control systems have been developed and demonstrated to be able to take advantage of rising air to significantly increase flight duration without requiring more on-board energy storage. Dynamic soaring (using wind gradients) is less common but has been observed in large ocean birds.

Given the current state of understanding of soaring flight and the technical development of small cost-effective UAVs it should be possible to develop autonomous soaring control to extend the mission duration of a UAV without requiring additional propulsive power. Utilising soaring could significantly increase the endurance of a UAV and consequently increase the number of applications of UAV technology for long duration monitoring and surveillance.

Chapter 3

Soaring and Gliding Flight

This chapter presents an analysis and discussion of the equations of motion for a gliding aircraft. The goal is to provide an understanding of the mechanics of gliding and soaring flight and develop strategies based on the analytic model which could be utilised by a soaring controller.

Gliding is defined as flight without applied propulsive force. In still air, gliding is an energy-loss flight condition due to drag. However, in certain conditions energy is transferred from the atmosphere to the dynamic energy of the aircraft. If this atmospheric energy input exceeds the loss due to drag then the aircraft gains dynamic energy. Soaring flight is defined as positive energy gain from the atmosphere. This chapter aims to identify the optimum flight conditions in both energy-loss gliding and energy-gain soaring flight through analysis of the equations of motion for a gliding aircraft.

The analysis focuses on the theoretical equations of motion for a gliding aircraft. Most of the results are applicable to any aircraft with known physical parameters. However, particular results are demonstrated for the parameters of an RnR SBXC cross country remote control scale glider aircraft. This aircraft model is used in most of the simulations in the subsequent chapters. For scale reference, the glider model has a wing span of 4.32 m, a reference wing area of 0.957 m² and a mass of 5.44 kg. Further details of the model are provided in Appendix B.

3.1 Frames of Reference and Definitions of Energy

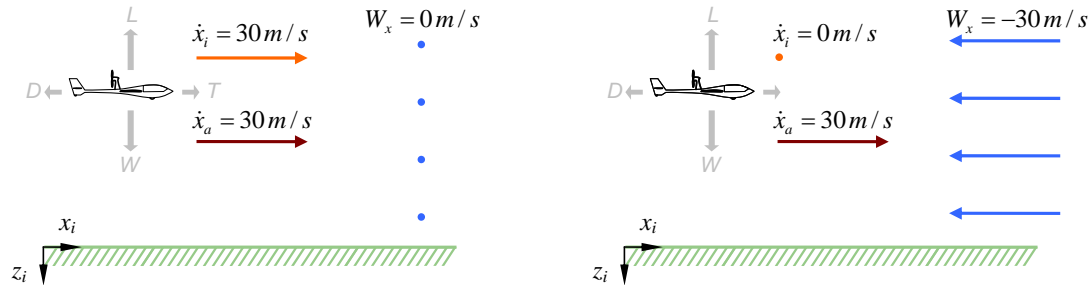
Reference frames are an important consideration for defining the terms of energy for an aerial vehicle. Motion is described in two reference frames. The inertial frame, denoted with subscript i , is an earth-fixed frame. The frame is a standard right-handed frame where the x_i , y_i and z_i axes are aligned north, east and down respectively with the origin at surface level. The aircraft location is described by the vector \vec{P} in inertial space. Assuming a flat-earth model gravity is always aligned in the direction of the positive z_i axis. Also, since the aircraft location is defined with respect to the inertial origin, the altitude above the surface is $-z_i$.

The second reference frame is the air-relative frame, denoted with subscript a . The air-relative frame represents the motion of the aircraft with respect to the air directly surrounding it. Aerodynamic forces are generated by air-relative motion. Consider a powered aircraft flying straight and level with sufficient propulsive force to maintain a constant forward airspeed of 30 m/s (Fig. 3.1). In still air, the aircraft has the same inertial speed and airspeed of 30 m/s. Now assume the same flight condition (same engine power and airspeed, and hence air-relative motion) with a headwind of 30 m/s. In inertial space the aircraft has no forward speed. However, the engine power is the same, and the aerodynamic force generated by motion of the air over the wing surface is the same. Thus, the lift and drag forces are the same as in the original case. From the point of view of the aircraft, the airspeed determines the aerodynamic force generated by the wings.

The wind vector \vec{W} is defined as motion of the air with respect to the Earth-fixed inertial axes. Thus, the air-relative velocity vector of the aircraft \vec{V}_a can be written as function of the inertial speed \vec{V}_i and the wind \vec{W} .

$$\vec{V}_a = \vec{V}_i - \vec{W} \quad (3.1)$$

Wind can vary over inertial space, so momentum is poorly defined in the air-relative frame and it is not a true inertial frame. The difference is because the air itself has



(a) Forward flight in no wind. Assume sufficient thrust is generated to offset drag. The inertial speed is the same as the airspeed.

(b) Forward flight in headwind. The airspeed (and hence aerodynamic force) remains unchanged, but the inertial speed is reduced by the headwind speed.

Figure 3.1: Inertial and air-relative frames. Dynamic energy is defined with respect to the air-relative motion since this determines the aerodynamic force, and hence the energy of the vehicle with respect to the surrounding air. Thus, the dynamic energy is the same in both cases.

inertia with respect to the ground and could be considered a local inertial frame.

It is also important to clearly define the terms of energy used in the subsequent soaring analysis. The energy of a point mass can be described as the sum of gravitational potential and kinetic energy. Gravitational potential energy is the potential energy associated with the gravitational force acting between two bodies. In the case of a vehicle flying in Earth's atmosphere assume that the acceleration due to gravity, g , is a constant value of 9.81 m/s^2 (a valid assumption for altitude changes much smaller than the radius of the Earth). Thus, the gravitational potential energy is then a function of the mass of the vehicle and the distance between the centres of mass of the Earth and the vehicle. The altitude $-z_i$ is defined as the vertical distance of the vehicle above the origin of the inertial frame and the mass of the vehicle is m . The gravitational potential energy (relative to the origin of the inertial frame) is

$$E_{P,i} = -mgz_i. \quad (3.2)$$

Thus, the gravitational potential energy of a vehicle with fixed mass is only dependent on the inertial altitude.

Kinetic energy is the energy associated with velocity. For a particle of mass m trav-

elling at a velocity V the kinetic energy is

$$E_K = \frac{1}{2}mV^2. \quad (3.3)$$

In the case of a flying vehicle this needs to be carefully considered, as there are two important velocities. The inertial velocity is the velocity relative to the ground-fixed inertial frame and the airspeed $V_a = |\vec{V}_a|$ is relative to the local wind frame. As stated earlier, the aerodynamic force is dependent on the airspeed. Thus, the air-relative kinetic energy $E_{K,a}$ represents useful energy in the current air-relative frame.

$$E_{K,a} = \frac{1}{2}mV_a^2 \quad (3.4)$$

For the analysis presented here, air-relative dynamic energy E_a is defined as the sum of the gravitational potential energy and the air-relative kinetic energy. The air-relative energy represents the useful energy for the aircraft relative to the surrounding air at the current instant in time. This measure is therefore dependent on the current wind field.

$$\begin{aligned} E_a &= E_{P,i} + E_{K,a} \\ &= -mgz_i + \frac{1}{2}mV_a^2 \end{aligned} \quad (3.5)$$

This dynamic energy is the energy most commonly referred to in the following analysis. It is not strictly conservative as the energy varies with changes in the local wind. However, it represents the ‘useful’ energy of the aircraft in the current wind field. Dynamic soaring can be considered as exploiting this fact; by taking additional air-relative energy from the wind and retaining it as local air-relative inertia to be used in other wind frames.

3.2 Longitudinal Gliding

3.2.1 Longitudinal gliding aircraft model

The basic principles of soaring flight can be demonstrated using the simplified equations of motion for a gliding platform in three degrees of freedom (3DOF); forward and vertical translation and longitudinal rotation of the lift vector (climb angle). For a point mass model, the forces acting on an airframe are the aerodynamic force (decomposed into lift, L , and drag, D) and the weight force. The aerodynamic force is a function of the physical properties of the aircraft (shape, size, materials, etc.) and the motion of the vehicle relative to the surrounding air. The weight force is the force due to gravity and is directed downwards in inertial space.

The inertial velocity \vec{V}_i , the air-relative velocity \vec{V}_a and the wind \vec{W} are defined in the axes of the inertial frame.

$$\vec{V}_i = \begin{bmatrix} \dot{x}_i \\ \dot{z}_i \end{bmatrix}, \quad \vec{V}_a = \begin{bmatrix} \dot{x}_a \\ \dot{z}_a \end{bmatrix}, \quad \vec{W} = \begin{bmatrix} W_x \\ W_z \end{bmatrix}$$

The air-relative climb-angle γ_a is shown in the figure. This is the angle between the air-relative velocity \vec{V}_a and the inertial x_i -axis. Only non-inverted forward flight is considered such that $\gamma_a \in (-\frac{\pi}{2}, \frac{\pi}{2})$.

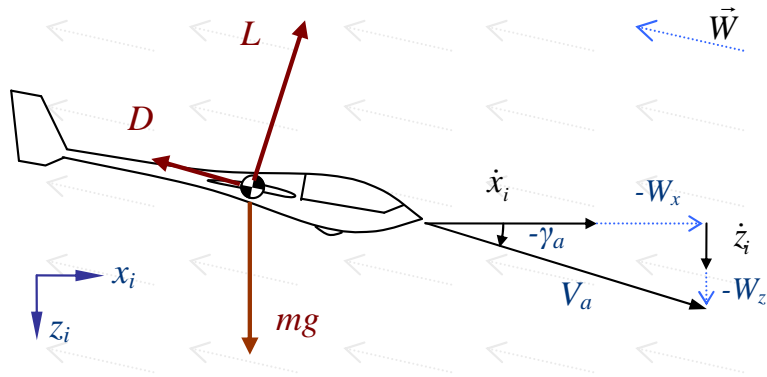


Figure 3.2: Air-relative velocity and longitudinal forces on a glider in uniform wind.

Note that the wind directions appear reversed due to the negative addition of wind. Wind is defined in the inertial axes, thus for an aircraft heading in the direction of positive x_i , a tailwind is defined by a positive W_x and sinking air is defined by positive W_z . However, a tailwind decreases the forward airspeed relative to the forward inertial speed, so the wind is subtracted as shown in Fig. 3.2. Thus for the case shown in Fig. 3.2 the wind has negative W_x and W_z components, that is, a lifting headwind which increases the airspeed relative to the inertial speed as shown in the figure.

Lift is defined as the part of the aerodynamic force acting perpendicularly to the air-relative velocity vector. Thus drag is the aerodynamic force acting against the direction of motion in the fluid. The resulting accelerations in the inertial frame can be expressed in terms of the air-relative climb angle.

$$m\ddot{x}_i = -L \sin \gamma_a - D \cos \gamma_a \quad (3.6)$$

$$m\ddot{z}_i = -L \cos \gamma_a + D \sin \gamma_a + mg \quad (3.7)$$

The air-relative velocity is the inertial velocity minus the contribution due to wind expressed in the inertial frame.

$$\dot{x}_a = \dot{x}_i - W_x(x_i, z_i) = V_a \cos \gamma_a \quad (3.8)$$

$$\dot{z}_a = \dot{z}_i - W_z(x_i, z_i) = -V_a \sin \gamma_a \quad (3.9)$$

So far, the wind has been defined as a wind vector valid at a particular time and place. Now consider the case of a linear spatial variation of wind in the inertial frame. This wind is described by a vector and spatial gradient Jacobian matrix J_w (Eq. (3.10)). For two dimensions there are four gradients. The two linear gradients $\frac{\partial W_x}{\partial x}$ and $\frac{\partial W_z}{\partial z}$ represent acceleration of a flow along a line. While these are relatively uncommon flows in a normal wind field, they can occur on small scales and effective linear gradients can be experienced in some conditions. The cross-gradients $\frac{\partial W_x}{\partial z}$ and

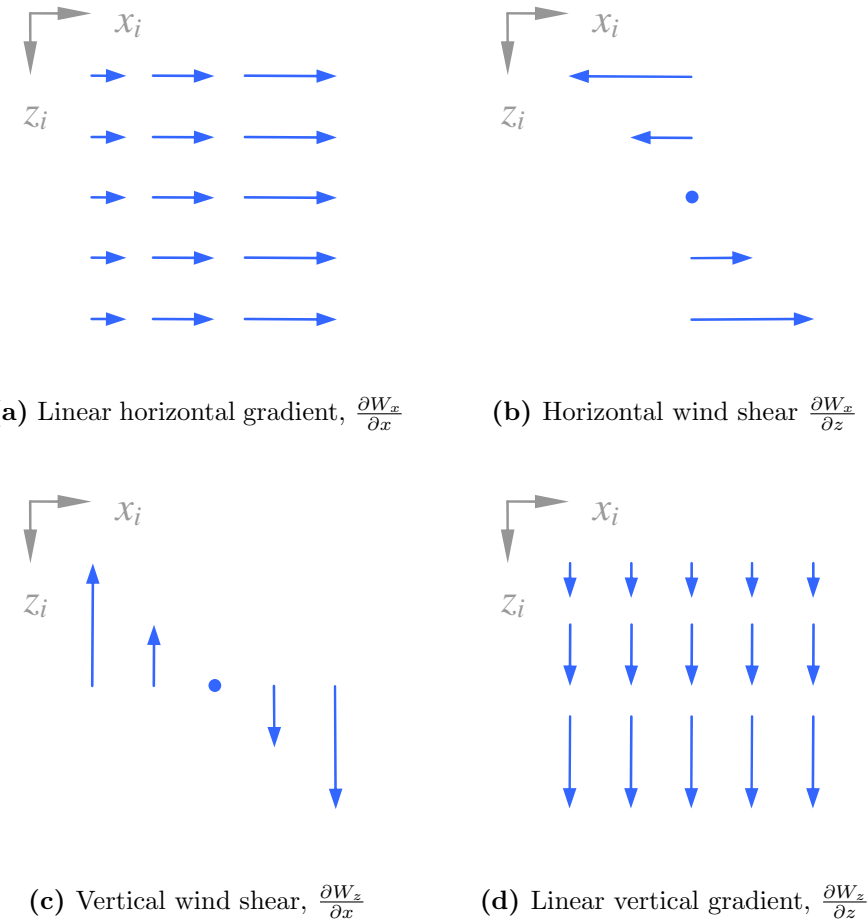


Figure 3.3: Positive linear wind gradients in \mathbf{J}_w .

$\frac{\partial W_z}{\partial x}$ represent variation of wind speed along the other dimension. This type of flow is common for boundary and shear layers. An illustration of the positive gradients is shown in Fig. 3.3.

$$\mathbf{J}_w = \begin{bmatrix} \frac{\partial W_x}{\partial x} & \frac{\partial W_x}{\partial z} \\ \frac{\partial W_z}{\partial x} & \frac{\partial W_z}{\partial z} \end{bmatrix} \quad (3.10)$$

Rearranging and differentiating Eqs. (3.8) & (3.9) yield the accelerations as functions of airspeed, air-relative climb angle and spatial wind gradients.

$$\ddot{x}_i = \frac{dV_a}{dt} \cos \gamma_a - V_a \sin \gamma_a \frac{d\gamma_a}{dt} + \frac{\partial W_x}{\partial x} \dot{x}_i + \frac{\partial W_x}{\partial z} \dot{z}_i \quad (3.11)$$

$$\ddot{z}_i = -\frac{dV_a}{dt} \sin \gamma_a - V_a \cos \gamma_a \frac{d\gamma_a}{dt} + \frac{\partial W_z}{\partial x} \dot{x}_i + \frac{\partial W_z}{\partial z} \dot{z}_i \quad (3.12)$$

Using the standard formulations for lift and drag;

$$L = \frac{1}{2} \rho V_a^2 S C_L, \quad (3.13)$$

$$D = \frac{1}{2} \rho V_a^2 S C_D. \quad (3.14)$$

A common approximation for estimating drag coefficient is the sum of a parasitic drag component and a lift-induced drag component. Parasitic drag is the drag due to the resistance of a fluid to an object moving through it and is a combination of the form drag due to the shape of the object and skin friction. The parasitic drag coefficient can be approximated as a constant value denoted $C_{D,0}$. Lift induced drag is the drag caused by an object which produces lift. This drag is due to the vortices produced between the high and low pressure regions of a lifting surface. Lifting line theory for an ideal (elliptical) lift distribution gives the induced drag coefficient equation in terms of the wing aspect ratio, \mathcal{A} . For non-ideal conditions, the equation is modified using Oswald's efficiency factor, e , which represents the deviation of the real design from the ideal elliptical case [9]. The total drag coefficient is the sum of the parasitic and induced drag coefficients.

$$\begin{aligned} C_D &= C_{D,0} + C_{D,i} \\ &= C_{D,0} + \frac{C_L^2}{\pi \mathcal{A} e} \end{aligned} \quad (3.15)$$

This allows the drag to be described as a function of the lift coefficient, airspeed and known constants. However, in the current set of equations there are still two unknown variables; the climb angle rate ($\frac{d\gamma_a}{dt}$) and the specific lift ($\frac{L}{m}$). The system can only be

solved by introducing another equation or by specifying one of the values as a control input.

Rearranging Eq. (3.6) and Eq. (3.7) to solve for specific drag yields:

$$\frac{D}{m} = \frac{1}{\cos \gamma_a} \left(-\frac{L}{m} \sin \gamma_a - \ddot{x}_i \right), \quad (3.16)$$

$$\frac{D}{m} = \frac{1}{\sin \gamma_a} \left(\frac{L}{m} \cos \gamma_a + \ddot{z}_i - g \right). \quad (3.17)$$

Equating (3.16) and (3.17) and solving for specific lift yields:

$$\frac{L}{m} (\cos^2 \gamma_a + \sin^2 \gamma_a) = g \cos \gamma_a - \ddot{x}_i \sin \gamma_a - \ddot{z}_i \cos \gamma_a. \quad (3.18)$$

Substituting the acceleration equations ((3.11) and (3.12)) gives:

$$\frac{L}{m} = g \cos \gamma_a + V_a \frac{d\gamma_a}{dt} - \sin \gamma_s \left(\frac{\partial W_x}{\partial x} \dot{x}_i + \frac{\partial W_x}{\partial z} \dot{z}_i \right) - \cos \gamma_a \left(\frac{\partial W_z}{\partial x} \dot{x}_i + \frac{\partial W_z}{\partial z} \dot{z}_i \right).$$

Thus, by specifying a climb angle rate, the resulting specific lift can be obtained as a function of the airspeed, climb angle, wind velocity and spatial wind gradients:

$$\frac{L}{m} = g \cos \gamma_a + V_a \frac{d\gamma_a}{dt} - \begin{bmatrix} \sin \gamma_a \\ \cos \gamma_a \end{bmatrix}^T \mathbf{J}_w \begin{bmatrix} \dot{x}_i \\ \dot{z}_i \end{bmatrix}. \quad (3.19)$$

Alternatively, there may be situations where the lift required is unachievable due to maximum lift constraints (such as wing loading limit or maximum lift coefficient). In that case, rearranging to solve for climb angle rate as a function of specific lift yields:

$$\frac{d\gamma_a}{dt} = \frac{1}{V_a} \left(\frac{L}{m} - g \cos \gamma_a + \begin{bmatrix} \sin \gamma_a \\ \cos \gamma_a \end{bmatrix}^T \mathbf{J}_w \begin{bmatrix} \dot{x}_i \\ \dot{z}_i \end{bmatrix} \right). \quad (3.20)$$

The specific drag can be calculated from the specific lift through substitution of Eq. (3.15) into Eq. (3.14).

$$\frac{D}{m} = \frac{1}{2m}\rho V_a^2 S C_{D,0} + \frac{m \left(\frac{L}{m}\right)^2}{\frac{1}{2}\rho V_a^2 S \pi A Re} \quad (3.21)$$

Finally, substitution of Eq. (3.6) & (3.7) into Eq. (3.11) & (3.12) yields the airspeed acceleration.

$$\frac{dV_a}{dt} = -g \sin \gamma_a - \frac{D}{m} - \begin{bmatrix} \cos \gamma_a \\ -\sin \gamma_a \end{bmatrix}^T \mathbf{J}_w \begin{bmatrix} \dot{x}_i \\ \dot{z}_i \end{bmatrix} \quad (3.22)$$

The first term ($-g \sin \gamma_a$) is the transfer of energy from gravitational potential to kinetic energy due to a climb. The second term ($-\frac{D}{m}$) is the loss of airspeed due to drag. The remaining term (considered as a single group) represents the contribution of wind to airspeed.

Equations (3.19–3.22) can be integrated numerically to provide a simulation of a glider flying through a wind field with linear spatial wind gradients. These equations can also act as a first-order approximation of a non-linear wind field by specifying the wind magnitude and gradients at each point with a suitably small integration time step.

3.2.2 Energy in longitudinal glider model

The primary goal of soaring is to maximise the energy extracted from the atmosphere. The longitudinal dynamic equations in the previous section can be examined in terms of the energy gained or lost to give an understanding of how the wind contributes to the overall energy of the platform. This provides understanding of the mechanisms of soaring flight, allowing the controllers presented in later chapters to take advantage of this information in designing control strategies for autonomous soaring.

In Sec. 3.1 the dynamic energy was defined as the sum of gravitational potential energy and air-relative kinetic energy (Eq. (3.5)).

$$E_a = -mgz_i + \frac{1}{2}mV_a^2$$

The air-relative power \dot{E}_a can be calculated by taking the time derivative of the air-relative energy.

$$\begin{aligned}\dot{E}_a &= -mg\dot{z}_i + mV_a \frac{dV_a}{dt} \\ &= mg(V_a \sin \gamma_a - W_z) + mV_a \frac{dV_a}{dt}\end{aligned}\quad (3.23)$$

This value is the current rate of energy being transferred from the environment into the vehicle. Negative power represents energy loss gliding (such as the loss from drag in no wind) while positive power represents soaring flight. This assumes the aircraft is not expending internal energy (no propulsion). Substituting Eq. (3.22) into Eq. (3.23) and dividing by mass yields the air-relative specific power.

$$\frac{\dot{E}_a}{m} = -V_a \frac{D}{m} - gW_z - V_a \begin{bmatrix} \cos \gamma_a \\ -\sin \gamma_a \end{bmatrix}^T [\mathbf{J}_w] \begin{bmatrix} \dot{x}_i \\ \dot{z}_i \end{bmatrix} \quad (3.24)$$

Note that the altitude-airspeed energy transfer terms cancel, and the remaining terms illustrate how a gliding aircraft can gain or lose air-relative energy from a wind field. Also worth noting is that the three terms of Eq. (3.24) are recognisable as the three cases of gliding flight identified by Lord Rayleigh (§2.1.2). The first term is the power loss to drag, and flight in this condition will continue to lose energy in the form of altitude or airspeed. The second term is energy being gained from vertical wind motion, which is also commonly identified as static soaring. The third and final term is the energy being gained from wind gradients, and is commonly identified as dynamic soaring. It is interesting that although Rayleigh did not formulate the gliding problem with these equations the forms of soaring flight are effectively defined in terms of the expressions in the power equation.

The following two subsections discuss the application of the soaring energy equations to gliding flight in no wind and to soaring flight in steady wind and wind gradients.

3.2.3 Longitudinal gliding without wind

The goal of this section is to examine gliding in no wind. The metrics discussed in this section are important for all gliding aircraft as they allow calculation of gliding efficiency and are often used to compare the performance of gliding aircraft. Of further interest is examining the types of control policies which minimise energy loss during gliding flight.

The three terms from the specific power equation (Eq. (3.24)) correspond to three types of energy transfer between an aircraft and the environment. Analysing the terms separately provides information on the optimum action to maximise energy gain or minimise energy loss.

Drag energy

The specific power from drag $\frac{\dot{E}_{a,Drag}}{m}$ is power lost to the atmosphere from the aerodynamic drag force.

$$\begin{aligned}\frac{\dot{E}_{a,Drag}}{m} &= -V_a \frac{D}{m} \\ &= -\frac{1}{2m} \rho S C_{D,0} V_a^3 - \frac{2m}{\rho S \pi A Re} \left(\frac{L}{m}\right)^2\end{aligned}\quad (3.25)$$

Firstly note that for a positive airspeed both terms are strictly negative, thus power is always lost to drag. The two terms correspond to the sources of drag in the drag coefficient equation (Eq. (3.15)). Power lost to parasitic drag monotonically increases with the cube of airspeed for subsonic flight. Specific power lost to induced drag is more complicated due to the dependency on specific lift. In general though, at normal flight speeds power lost to induced drag decreases asymptotically towards zero with increasing airspeed. Figure 3.4 shows the total specific power lost to drag (and corresponding sink rate) as well as the parasitic and induced drag components.

Most gliding flight is analysed during a steady-glide flight condition. A steady glide is when both the air-relative glide angle and the airspeed remain constant. For a

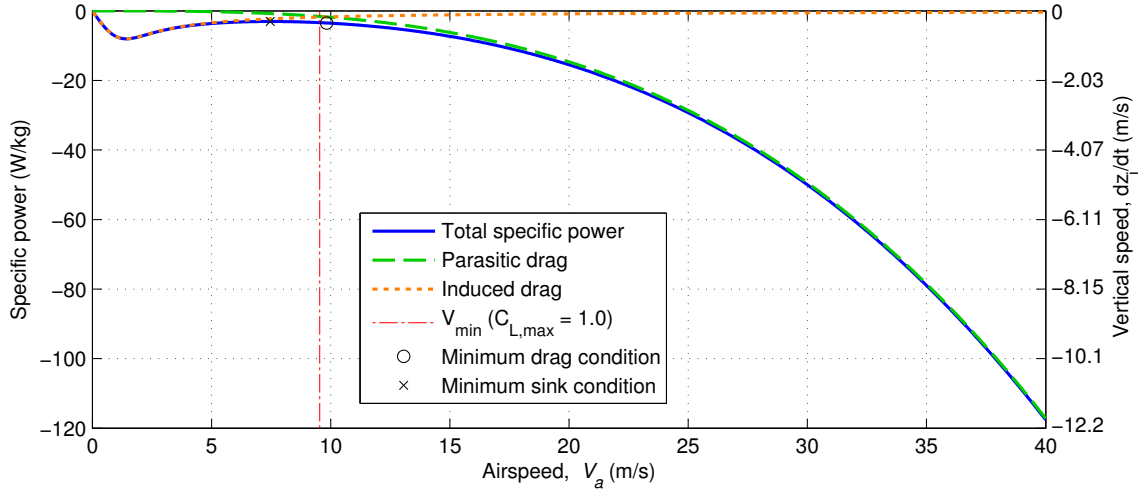


Figure 3.4: Specific power loss and sink rate for a steady glide (no acceleration) in no wind. The dashed line indicates the contribution from parasitic drag and the orange dotted line from lift-induced drag. The dash-dot vertical line illustrates the minimum airspeed limit of 9.54m/s imposed by a maximum lift coefficient of 1.00.

steady glide in still air there is no inertial acceleration since both the airspeed and climb angle are constant. Thus, the forces in Eq. (3.6) & (3.7) must be balanced such that

$$L = mg \cos \gamma_a, \quad (3.26)$$

$$D = -mg \sin \gamma_a. \quad (3.27)$$

Substituting the drag coefficient from Eq. (3.14) into (3.27),

$$mg \cos \gamma_a = \frac{1}{2} \rho V_a^2 S \left(C_{D,0} + \frac{C_L^2}{\pi A Re} \right).$$

Substituting the lift coefficient from Eq. (3.13) with lift specified in (3.27),

$$-mg \sin \gamma_a = \frac{1}{2} \rho V_a^2 S \left(C_{D,0} + \frac{(mg \cos \gamma_a)^2}{\frac{1}{2} \rho V_a^2 S \pi A Re} \right).$$

Making the substitution $(1 - \sin^2 \gamma_a)$ for $\cos^2 \gamma_a$ and rearranging yields

$$mg \sin^2 \gamma_a - \left(\frac{1}{2} \rho V_a^2 S \pi A Re \right) \sin \gamma_a - \frac{\left(\frac{1}{2} \rho V_a^2 S \right)^2 \pi A Re C_{D,0} + m^2 g^2}{mg} = 0.$$

This quadratic equation in $\sin \gamma_a$ can be solved to give the air-relative climb angle as a function of known parameters and the current airspeed. Note that while there are two solutions to the equation, only one will give a real result in γ_a .

$$\sin \gamma_a = \frac{\frac{1}{2} \rho V_a^2 S \pi A Re - \sqrt{\left(\frac{1}{2} \rho V_a^2 S \right)^2 \pi A Re (\pi A Re + 4C_{D,0}) + 4m^2 g^2}}{2mg} \quad (3.28)$$

Thus, for a given airspeed there exists a single climb angle which will result in a steady glide in still air. There is a very weak dependence on air density, so the glide is not perfectly steady as density varies with altitude, but this effect is only apparent over large altitude changes. The author believes this formulation represents a novel description for explicit solution of the glide angle for the described drag model. Figure 3.5 illustrates the range of climb angles for a steady glide in no wind for the SBXC parameters at sea level. A similar derivation can be found in many aerodynamic textbooks [80], but most sources make the assumption that the glide ratio is high enough that lift equals weight, an assumption which is not required and not made here.

While the entire airspeed range from 0m/s is shown, the low airspeed results show a steep increase in the dive due to the rapid increase of induced drag. In reality this is not possible as the aircraft has a maximum lift coefficient and at airspeeds below this limit the wing would stall. The maximum lift coefficient for this case is set at 1.00 based on the wing section, which limits the minimum airspeed to 9.54 m/s as indicated in the figure. The maximum airspeed (for gliding) is limited by the parasitic drag coefficient $C_{D,0}$. When heading straight down, the lift coefficient is zero and the vehicle is travelling at terminal velocity where weight is matched by parasitic drag. Note that in most cases this is far above the practical limit for a glider. For the SBXC the parasitic drag coefficient is 0.017 and the total weight is 5.44kg so the

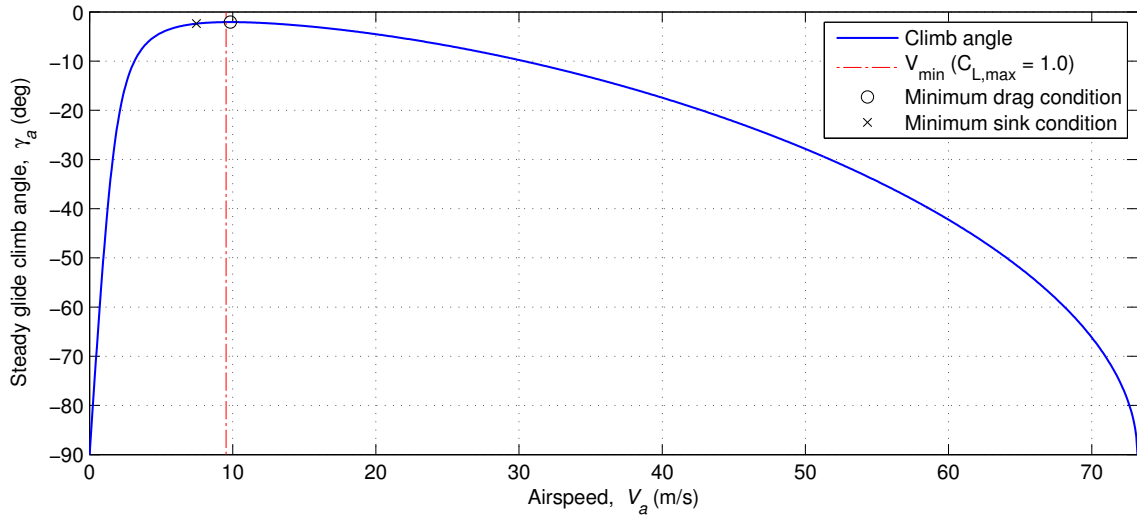


Figure 3.5: Glide angle for a steady glide (no acceleration) in no wind. The dash-dot vertical line illustrates the minimum airspeed limit of 9.54 m/s imposed by a maximum lift coefficient of 1.00. The maximum airspeed is limited to the terminal velocity of 73.2 m/s.

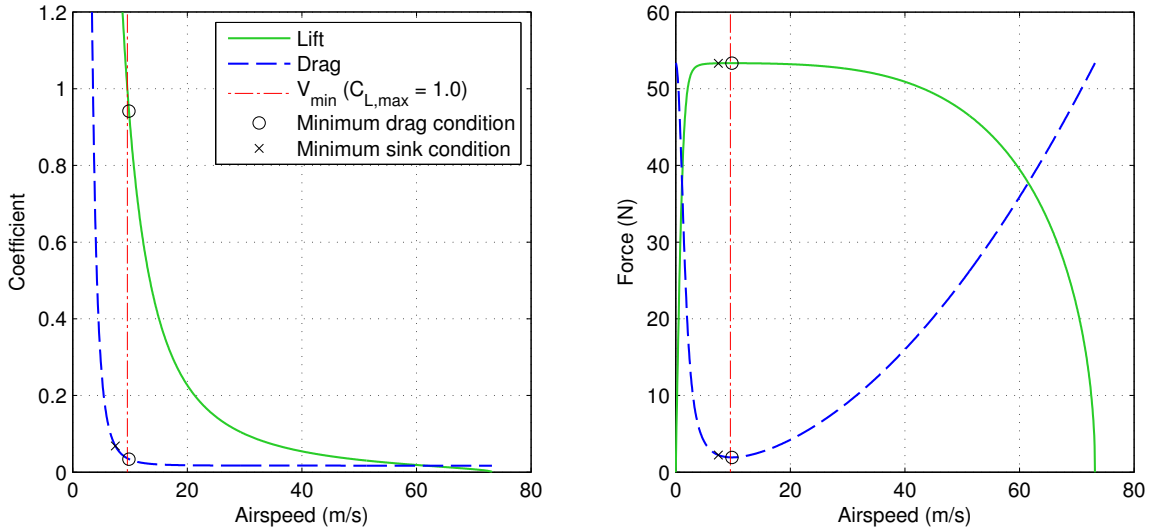


Figure 3.6: Lift and drag coefficients and forces for the SBXC model in a steady glide in no wind.

maximum theoretical airspeed is 73.2 m/s. The lift and drag coefficients and forces are illustrated in Fig. 3.6.

For a gliding aircraft the energy rates during a steady glide are important measures of the efficiency of the flight. There are two important quantities for a steady glide. The

first is the speed at which range is maximised. This airspeed is important for gliding flight as it represents the minimisation of energy used for forward travel. Flying in this condition represents the most efficient travel speed, that is, the furthest forward distance travelled per unit of energy used. Differentiating the air-relative energy (Eq. (3.5)) with respect to forward travel for a steady glide (no accelerations).

$$\begin{aligned}\frac{\partial E_a}{\partial x_i} &= -mg \frac{\partial z_i}{\partial x_i} \\ &= -mg \frac{\partial z_i}{\partial t} \frac{\partial t}{\partial x_i} \\ &= -mg \frac{\dot{z}_i}{\dot{x}_i}\end{aligned}\tag{3.29}$$

Minimising this equation for positive mass and gravity corresponds to maximisation of the ratio of forward distance travelled to vertical distance travelled. This is also commonly known as the lift-to-drag ratio since it is equivalent to the ratio of lift to drag or the corresponding dimensionless coefficients.

$$\frac{\dot{x}_i}{\dot{z}_i} = \frac{-1}{\tan \gamma_a} = \frac{L}{D} = \frac{C_L}{C_D}\tag{3.30}$$

Further, maximisation of the lift-to-drag ratio is also equivalent to minimisation of the drag force. This can be demonstrated through the climb angle. Minimisation of $\tan \gamma_a$ is equivalent to minimisation of $\sin \gamma_a$ since both gradients are positive definite for $\gamma_a \in (-\frac{\pi}{2}, \frac{\pi}{2})$. This can be solved by finding the airspeed which gives minimum steady glide drag across the range of velocities $V_a \in [V_{min}, V_{max}]$. The minimum airspeed is a standard result from solution of the lift equation (Eq. (3.13)) for a specified lift coefficient and the maximum airspeed is equivalent to the terminal velocity for the parasitic drag coefficient $C_{D,0}$.

$$V_{min} = \sqrt{\frac{2mg}{\rho S \sqrt{C_{L,max}^2 + \left(C_{D,0} + \frac{C_{L,max}^2}{\pi A Re}\right)^2}}}\tag{3.31}$$

$$V_{max} = \sqrt{\frac{mg}{\frac{1}{2} \rho S C_{D,0}}}\tag{3.32}$$

Substituting the known solution for $\sin \gamma_a$ from Eq. (3.28) into the drag equation (Eq. (3.27)) yields the drag as a function of airspeed, air density and known constants.

$$\begin{aligned} D &= -mg \sin \gamma_a \\ &= \frac{1}{4}\rho S \pi A Re V_a^2 - \sqrt{\left(\frac{1}{16}\rho^2 S^2 \pi A Re (\pi A Re + 4C_{D,0}) V_a^4 + m^2 g^2\right)}. \end{aligned} \quad (3.33)$$

The stationary points with respect to V_a can be determined by finding the roots of the derivative.

$$\frac{\partial D}{\partial V_a} = \frac{1}{2}\rho S \pi A Re V_a - \frac{\frac{1}{8}\rho^2 S^2 \pi A Re (\pi A Re + 4C_{D,0}) V_a^3}{\sqrt{\frac{1}{16}\rho^2 S^2 \pi A Re (\pi A Re + 4C_{D,0}) V_a^4 + 4m^2 g^2}} = 0$$

Therefore,

$$V_a \sqrt{\frac{1}{16}\rho^2 S^2 \pi A Re (\pi A Re + 4C_{D,0}) V_a^4 + 4m^2 g^2} = \frac{1}{4}\rho S (\pi A Re + 4C_{D,0}) V_a^3.$$

Clearly, $V_a = 0$ is a trivial solution. To find the remaining solutions, assume $V_a \neq 0$ to allow division by V_a , then square both sides to yield:

$$\frac{1}{16}\rho^2 S^2 \pi A Re (\pi A Re + 4C_{D,0}) V_a^4 + 4m^2 g^2 = \frac{1}{16}\rho^2 S^2 (\pi A Re + 4C_{D,0})^2 V_a^4.$$

Thus,

$$V_a^4 = \frac{4m^2 g^2}{\rho^2 S^2 C_{D,0} (\pi A Re + 4C_{D,0})}.$$

There are four solutions to this equation, two imaginary and two real. Of the real positive-negative pair, only the positive root is of interest. Thus, the airspeed of minimum drag (maximum glide ratio) $V_{a,mindrag}$ is

$$V_{a,mindrag} = \sqrt[4]{\frac{4m^2 g^2}{\rho^2 S^2 C_{D,0} (\pi A Re + 4C_{D,0})}}. \quad (3.34)$$

This solution is unique to gliding aircraft in a steady glide condition. Previous work has provided the equivalent equation for powered aircraft [80, p. 264] which could be used with Eq. (3.28) to yield the same result. This equation shows a number of interesting features. The minimum drag airspeed is proportional to the square root of the weight and inversely proportional to the square root of air density and wing area. The drag efficiency variables $\mathcal{A}R$, e and $C_{D,0}$ have a more complicated relationship but are both inversely related to the minimum drag speed.

The result can be substituted back into the original equation for the lift-to-drag ratio to determine the maximum possible L/D for a set of aircraft parameters.

Equation (3.28) gives the glide angle as a function of airspeed. Substituting the minimum drag airspeed (Eq. (3.34)) and letting $k = \pi \mathcal{A}Re$ for convenience yields the climb angle at minimum drag:

$$\begin{aligned}\sin \gamma_a &= \frac{\frac{1}{2} \rho S k \sqrt{\frac{4m^2g^2}{\rho^2 S^2 C_{D,0}(k+4C_{D,0})}} - \sqrt{\frac{4\rho^2 S^2 k(k+4C_{D,0})m^2g^2}{4\rho^2 S^2 C_{D,0}(k+4C_{D,0})} + 4m^2g^2}}{2mg} \\ &= \frac{k}{2\sqrt{C_{D,0}(k+4C_{D,0})}} - \frac{k+4C_{D,0}}{2\sqrt{C_{D,0}(k+4C_{D,0})}}.\end{aligned}$$

The resulting lift-to-drag ratio can be evaluated using Eq. (3.30). Solving for maximum lift-to-drag ratio;

$$\begin{aligned}\left(\frac{L}{D}\right)_{max} &= \frac{-1}{\tan \gamma_a} = \frac{\sqrt{1 - \sin^2 \gamma_a}}{-\sin \gamma_a} \\ &= \frac{\sqrt{C_{D,0}(k+4C_{D,0}) - 4C_{D,0}^2}}{2C_{D,0}} \\ &= \frac{1}{2} \sqrt{\frac{k}{C_{D,0}}}.\end{aligned}$$

Thus,

$$\left(\frac{L}{D}\right)_{max} = \frac{1}{2} \sqrt{\frac{\pi \mathcal{A}Re}{C_{D,0}}}. \quad (3.35)$$

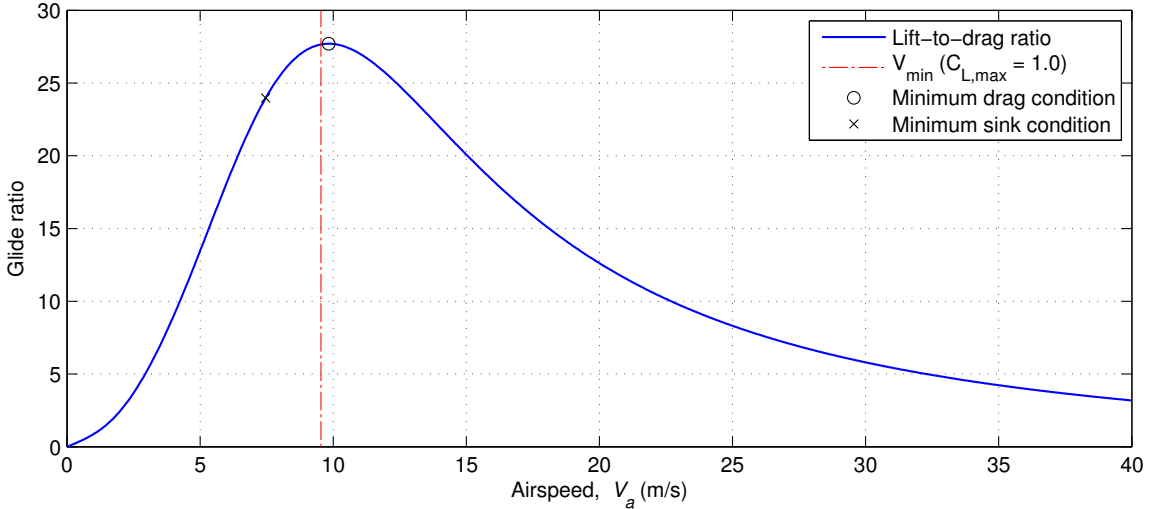


Figure 3.7: Glide ratio for the SBXC model in a steady glide in no wind. The maximum glide ratio is 27.7 at 9.83m/s.

The maximum glide ratio (for a given wing efficiency e) is proportional to the square root of the ratio between the aspect ratio and the parasitic drag coefficient. This is basically a measure of the drag efficiency of the aircraft. Higher aspect ratio wings have lower lift-induced drag which is why most sailplanes aim to maximise aspect ratio. Similarly, the parasitic drag is largely due to the shape of the fuselage which drives the design of the slender fuselage shapes used in most gliders.

Worth noting is that the maximum glide ratio is not a function of weight, but the speed at which it occurs is. This is the reason for ballast in sailplanes; a heavier aircraft can utilise the same lifting air and gain the same specific power, but will travel faster during gliding flight and so can travel faster between thermals. However, the sink rate is a function of mass and will be higher for a heavier aircraft.

For the SBXC model specified the maximum theoretical glide ratio is 27.7 at 9.83m/s, thus, for an altitude of h metres, the vehicle could travel a lateral distance of $27.7h$ metres. The lift-to-drag ratio over a limited airspeed range is shown in Fig. 3.7.

This result is the same as the common definition of glide ratio calculated for a powered aircraft [53, 80]. The powered definition is used to estimate the energy required for propulsion for the Bréguet range equation and assumes that the aircraft is flying

straight and level with lift equal to weight and thrust equal to drag [17]. However, the velocity at which drag is minimised is slightly different from the powered case where zero climb angle is assumed [53].

$$V_{min drag, powered} = \sqrt[4]{\frac{4m^2g^2}{\rho^2 S^2 C_{D,0} \pi A Re}} \quad (3.36)$$

Using the powered approximation results in very small error, but is nevertheless not strictly correct for a gliding aircraft in a steady dive.

The second important steady glide condition is the minimum power loss condition. This is the condition where the aircraft is gliding with the smallest power loss to drag. From the equation for drag power (Eq. (3.25)) and the drag in Eq. (3.27) for a steady glide in no wind,

$$\begin{aligned} \frac{\dot{E}_{a,gliding}}{m} &= -V_a \frac{D}{m} \\ &= gV_a \sin \gamma_a. \end{aligned} \quad (3.37)$$

The minimum power loss condition is also known as ‘minimum sink’ as the downwards vertical speed ($V_a \sin \gamma_a$) is also minimised. Figure 3.4 shows the specific power from drag in a steady glide. The shape is interesting as there are two critical points; a local minimum and local maximum. For the parameters of the current aircraft, both these points are below the minimum airspeed. However, this type of situation is relatively unique to small scale glider aircraft, which are designed to fly at low speeds and have very small induced drag coefficients due to streamlined fuselages and low speed aerofoils. In other aircraft the local maximum is at a higher airspeed, so there is a known fixed speed which will minimise sink, and speeds above and below this will have higher power loss to drag. The minimum sink point (in the range of achievable airspeeds) can be found by substituting the glide angle (Eq. (3.28)) into the power equation (Eq. (3.37)) and differentiating with respect to V_a to determine the point of zero gradient. For convenience of notation let $k = \pi A Re$.

$$\begin{aligned}\frac{\dot{E}_{a,gliding}}{m} &= gV_a \sin \gamma_a \\ &= \frac{gV_a}{4m} \left[\rho SkV_a^2 - \sqrt{\rho^2 S^2 k (k + 4C_{D,0}) V_a^4 + 16m^2 g^2} \right]\end{aligned}$$

$$\begin{aligned}\frac{\partial \frac{\dot{E}_{a,gliding}}{m}}{\partial V_a} &= \frac{g}{4m} \left[\rho SkV_a^2 - \sqrt{\rho^2 S^2 k (k + 4C_{D,0}) V_a^4 + 16m^2 g^2} \dots \right. \\ &\quad \left. + \frac{4\rho^2 S^2 k (k + 4C_{D,0}) V_a^4}{2\rho SkV_a - \frac{1}{2}\sqrt{\rho^2 S^2 k (k + 4C_{D,0})} V_a^4 + 16m^2 g^2} \right]\end{aligned}$$

Stationary points occur when the derivative is zero. Setting the equation to zero and multiplying by the factor $\sqrt{\rho^2 S^2 k (k + 4C_{D,0}) V_a^4 + 16m^2 g^2}$ yields:

$$\begin{aligned}3\rho SkV_a^2 \sqrt{\rho^2 S^2 k (k + 4C_{D,0}) V_a^4 + 16m^2 g^2} - \rho^2 S^2 k (k + 4C_{D,0}) V_a^4 - 16m^2 g^2 \dots \\ - 2\rho^2 S^2 k (k + 4C_{D,0}) V_a^4 = 0.\end{aligned}$$

Simplify and collect terms.

$$3\rho SkV_a^2 \sqrt{\rho^2 S^2 k (k + 4C_{D,0}) V_a^4 + 16m^2 g^2} = 3\rho^2 S^2 k (k + 4C_{D,0}) V_a^4 + 16m^2 g^2$$

Square both sides.

$$\begin{aligned}9\rho^4 S^4 k^3 (k + 4C_{D,0}) V_a^8 + 144\rho^2 S^2 k^2 m^2 g^2 V_a^4 = \\ 9\rho^4 S^4 k^2 (k + 4C_{D,0})^2 V_a^8 + 96\rho^2 S^2 k (k + 4C_{D,0}) m^2 g^2 V_a^4 + 256m^4 g^4 \\ 9\rho^4 S^4 k^2 C_{D,0} (k + 4C_{D,0}) V_a^8 - 12\rho^2 S^2 k (k - 8C_{D,0}) m^2 g^2 V_a^4 + 64m^4 g^4 = 0\end{aligned}$$

This equation is effectively a quadratic in V_a^4 . Thus, it can be solved using the quadratic equation.

$$\begin{aligned}
V_a^4 &= \frac{12\rho^2 S^2 k (k - 8C_{D,0}) m^2 g^2 \pm \sqrt{(12\rho^2 S^2 k (k - 8C_{D,0}) m^2 g^2)^2 - 2304\rho^4 S^4 k^2 C_{D,0} (k + 4C_{D,0}) m^4 g^4}}{18\rho^4 S^4 k^2 C_{D,0} (k + 4C_{D,0})} \\
&= \frac{12\rho^2 S^2 m^2 g^2 k \left(k - 8C_{D,0} \pm \sqrt{(k - 8C_{D,0})^2 - 16C_{D,0}(k + 4C_{D,0})} \right)}{18\rho^4 S^4 k^2 C_{D,0} (k + 4C_{D,0})} \\
&= \frac{2m^2 g^2 \left[k - 8C_{D,0} \pm \sqrt{k(k - 32C_{D,0})} \right]}{3\rho^2 S^2 k C_{D,0} (k + 4C_{D,0})}
\end{aligned}$$

Thus, the gradient of the drag power is zero with respect to airspeed when

$$V_a^4 = \frac{2m^2 g^2 \left[k - 8C_{D,0} \pm \sqrt{k(k - 32C_{D,0})} \right]}{3\rho^2 S^2 k C_{D,0} (k + 4C_{D,0})}.$$

There are a total of 8 solutions to this equation. When $32C_{D,0} < \pi \mathcal{R}e$ (which would be true for all practical aircraft), there are four imaginary and four real roots. The real roots are symmetric, so ignoring the negative roots, the remaining two solutions are real and positive. Both stationary points can be observed in Fig. 3.4. The larger root is the local maximum where the power loss is minimised in the range of allowable flight conditions. The author believes this equation is a novel contribution for expressing the theoretical minimum sink speed for a steady glide condition with the specified drag model.

$$V_{a,\text{minsink}} = \sqrt[4]{\frac{2m^2 g^2 \left[\pi \mathcal{R}e - 8C_{D,0} + \sqrt{\pi \mathcal{R}e(\pi \mathcal{R}e - 32C_{D,0})} \right]}{3\rho^2 S^2 \pi \mathcal{R}e C_{D,0} (\pi \mathcal{R}e + 4C_{D,0})}} \quad (3.38)$$

Also note that this can be written as a function of the minimum drag airspeed, such that

$$V_{a,\text{minsink}} = V_{a,\text{mindrag}} \sqrt[4]{\frac{\pi \mathcal{R}e - 8C_{D,0} + \sqrt{\pi \mathcal{R}e(\pi \mathcal{R}e - 32C_{D,0})}}{6\pi \mathcal{R}e}}.$$

These results can also be used to demonstrate that the minimum sink speed is always less than the minimum drag speed. Assume both velocities are positive (as shown

earlier), then compare the fourth power. A simple proof by contradiction is provided, initially assuming minimum drag speed is less than minimum sink speed.

$$\begin{aligned}
 V_{a,\text{mindrag}} &< V_{a,\text{minsink}} \\
 V_{a,\text{mindrag}}^4 &< V_{a,\text{minsink}}^4 \quad \forall V_a > 0 \\
 \frac{4m^2g^2}{\rho^2S^2C_{D,0}(k + 4C_{D,0})} &< \frac{2m^2g^2 \left[k - 8C_{D,0} + \sqrt{k(k - 32C_{D,0})} \right]}{3\rho^2S^2kC_{D,0}(k + 4C_{D,0})} \\
 2 &< \frac{k - 8C_{D,0} + \sqrt{k(k - 32C_{D,0})}}{3k} \\
 (5k + 8C_{D,0})^2 &< k(k - 32C_{D,0}) \\
 3k^2 + 14kC_{D,0} + 64C_{D,0}^2 &< 0
 \end{aligned}$$

This cannot be true for any values of $k = \pi \mathcal{R}e > 0$ and $C_{D,0} > 0$. Therefore,

$$V_{a,\text{mindrag}} > V_{a,\text{minsink}} \quad \forall C_{D,0} > 0, \pi \mathcal{R}e > 0.$$

3.3 Longitudinal Soaring

While for flight in still air energy is always lost to drag, the specific power equation (Eq. (3.24)) shows that wind can contribute positive power in certain conditions. The second and third term of the power equation both contain wind terms.

The static soaring specific power $\frac{\dot{E}_{a,\text{Static}}}{m}$ is the energy gained or lost from vertical motion of the air relative to the fixed inertial frame (W_z).

$$\frac{\dot{E}_{a,\text{Static}}}{m} = -gW_z \tag{3.39}$$

Assuming constant gravity this term is only affected by the magnitude of the vertical wind; positive values of W_z (downdrafts) result in energy loss and negative values

(updrafts) result in energy gain. Since this term is only a function of the wind magnitude the rate of specific energy gain from lifting air is not affected by the control of the aircraft. Flying at minimum sink will result in the fastest energy gain overall because it minimises power lost to drag, a fact well-known to glider pilots [81]. It is easy to consider vertical wind as transporting the local air-relative frame vertically in the inertial frame. Thus, the conditions of flight for the aircraft are the same, but the whole frame is moving vertically in inertial space resulting in a direct increase or decrease in gravitational potential energy of both the air and the aircraft. This is also the only term which can result in energy gain from a uniform wind field ($\mathbf{J}_w = \mathbf{0}$).

The dynamic soaring specific power is energy gained or lost due to wind gradients. This term corresponds to changes in air-relative kinetic energy, that is, wind effects which change the airspeed of the vehicle.

$$\begin{aligned} \frac{\dot{E}_{a,Dynamic}}{m} &= -V_a \begin{bmatrix} \cos \gamma_a \\ -\sin \gamma_a \end{bmatrix}^T [\mathbf{J}_w] \begin{bmatrix} \dot{x}_i \\ \dot{z}_i \end{bmatrix} \\ &= -\frac{\partial W_x}{\partial x} V_a \cos \gamma_a (V_a \cos \gamma_a + W_x) + \frac{\partial W_z}{\partial z} V_a \sin \gamma_a (-V_a \sin \gamma_a + W_z) \dots \\ &\quad - \frac{\partial W_x}{\partial z} V_a \cos \gamma_a (-V_a \sin \gamma_a + W_z) + \frac{\partial W_z}{\partial x} V_a \sin \gamma_a (V_a \cos \gamma_a + W_x) \quad (3.40) \end{aligned}$$

Expanding this term illustrates the effect of each gradient on the air-relative power. It is not immediately apparent what behaviour (selection of airspeed and climb angles) maximises power gain from wind gradients. This equation is an extension of an equation previously demonstrated in the literature for the shear gradient $\frac{\partial W_x}{\partial z}$ [108] to include all linear longitudinal gradients.

Breaking the power into the contributions from each gradient demonstrates the mechanism of dynamic soaring. Essentially, all terms represent the increase in air-relative kinetic energy through airspeed acceleration. Each term is the projection of the wind gradient in the direction of travel to represent the rate at which airspeed is increasing. This allows us to determine the airspeed and climb angle which maximise energy

capture from each component of the wind gradient. An important point to note for all gradients is that the power gained is proportional to the airspeed, thus energy is gained (or lost) faster at higher airspeeds. This is interesting as it means that higher airspeeds can actually increase energy gain rate, but this is limited by the cubic increase in parasitic drag. Each gradient is explained below and power gain conditions are illustrated in Fig. 3.10. The conditions of power gain in each gradient are identified and in each case an equation for the dimensionless power is provided. Also note that the analysis only includes power directly from the wind gradient, so total power must also include power lost to drag and any static soaring power.

3.3.1 Horizontal linear gradient

The first gradient is the horizontal linear gradient $\frac{\partial W_x}{\partial x}$. This represents the horizontal wind which increases or decreases along the x -axis. Isolating the specific power (\bar{P}) contribution for this gradient from the dynamic energy equation,

$$\bar{P}_{\frac{\partial W_x}{\partial x}} = -\frac{\partial W_x}{\partial x} V_a \cos \gamma_a (V_a \cos \gamma_a + W_x). \quad (3.41)$$

shows that the energy gained is effectively the projection of the gradient in the direction of travel. Recall that the gradients are defined in inertial space. Then, the $V_a \cos \gamma_a + W_x$ term is the inertial speed of the aircraft in the x -direction (the direction of the gradient). Multiplying this by the magnitude of the gradient gives the effective magnitude in air-relative space. The component in the direction of travel ($\cos \gamma_a$) is the airspeed acceleration, which, multiplied by the airspeed yields the resulting air-relative specific power. This is true for all gradients; the power from a wind gradient is the airspeed acceleration multiplied by the airspeed itself. This can be seen in the calculation of the wind power, where the dynamic soaring term is due to differentiation of the kinetic energy (Eq. (3.24)).

For a horizontal linear gradient, power will be gained when $\bar{P}_{\frac{\partial W_x}{\partial x}} > 0$. Note that $\cos \gamma_a > 0 \forall \gamma_a \in (-\frac{\pi}{2}, \frac{\pi}{2})$ which means that the power function is symmetrical in γ_a . Then, a negative gradient ($\frac{\partial W_x}{\partial x} < 0$, increasing headwind) will result in energy gain

as long as the aircraft is still moving forward in inertial space ($V_a \cos \gamma_a + W_x > 0$). Conversely, power is gained by moving backwards in inertial space (high negative wind speed) if the gradient is positive (though this is relatively unlikely to occur in a typical wind field).

For power gain:

$$\bar{P}_{\frac{\partial W_x}{\partial x}} > 0 \text{ if } \begin{cases} \frac{\partial W_x}{\partial x} > 0, & V_a \cos \gamma_a + W_x < 0 \\ \frac{\partial W_x}{\partial x} < 0, & V_a \cos \gamma_a + W_x > 0 \end{cases} \quad (3.42)$$

Generally, linear gradients are relatively uncommon over large distances in most wind fields as it requires linear acceleration of the air. This can happen over short distances due to turbulent mixing and is possible over larger distances when air accelerates as it passes through narrow obstacles. A horizontal linear gradient could be caused by a geographic funnel such as a canyon.

Power from a linear horizontal gradient (and all wind gradients) increases in magnitude with increasing airspeed. Maximum power with respect to climb angle can be determined by finding the stationary points of the power function with respect to climb angle γ_a . The stationary points are where the derivative of Eq. (3.41) are zero.

$$\frac{\partial \bar{P}_{\frac{\partial W_x}{\partial x}}}{\partial \gamma_a} = \frac{\partial W_x}{\partial x} V_a \sin \gamma_a (2V_a \cos \gamma_a + W_x) \quad (3.43)$$

The roots are $\gamma_a = 0$ and $\cos \gamma_a = -\frac{W_x}{2V_a}$. The second root is real only for $|W_x| < |2V_a|$ and since $\gamma_a \in (-\frac{\pi}{2}, \frac{\pi}{2})$, this root only exists when $W_x < 0$. This is an interesting condition as it applies regardless of the direction of the gradient. The points can be determined as local maxima or minima by examining the second derivative.

$$\frac{\partial^2 \bar{P}_{\frac{\partial W_x}{\partial x}}}{\partial \gamma_a^2} = \frac{\partial W_x}{\partial x} V_a (4V_a \cos^2 \gamma_a + W_x \cos \gamma_a - 2V_a) \quad (3.44)$$

If $\gamma = 0$,

$$\frac{\partial^2 \bar{P}_{\frac{\partial W_x}{\partial x}}}{\partial \gamma_a^2} = \frac{\partial W_x}{\partial x} V_a (2V_a + W_x). \quad (3.45)$$

This point will be a local maximum if $\frac{\partial W_x}{\partial x} > 0$ and $W_x < -2V_a$ or if $\frac{\partial W_x}{\partial x} < 0$ and $W_x > -2V_a$. Conversely, it is a minimum if $\frac{\partial W_x}{\partial x} < 0$ and $W_x < -2V_a$ or if $\frac{\partial W_x}{\partial x} > 0$ and $W_x > -2V_a$.

At the $\cos \gamma_a = -\frac{W_x}{2V_a}$ root,

$$\frac{\partial^2 \bar{P}_{\frac{\partial W_x}{\partial x}}}{\partial \gamma_a^2} = \frac{1}{2} \frac{\partial W_x}{\partial x} (W_x^2 - 4V_a^2). \quad (3.46)$$

From the earlier condition that $|W_x| < |2V_a|$ (for real roots), this point will be a local maximum if $\frac{\partial W_x}{\partial x} > 0$ and a minimum if $\frac{\partial W_x}{\partial x} < 0$.

This case is interesting because the energy is dependent on the horizontal wind, which is defined as changing in the lateral gradient. Thus, continuous energy gain in a linear gradient is not possible, as the wind changes with inertial motion. Consider forward flight in an increasing headwind (negative gradient) from a zero wind position. While energy is gained initially, the inertial speed continually slows as the aircraft moves forward in inertial space and the headwind increases until the wind matches the airspeed and the vehicle has no forward inertial speed and hence receives no energy from the gradient. At this point the best action is a steady glide condition which will result in steady sink as in still air. This means that energy gain from a linear gradient requires other types of gradients to provide useful energy.

An illustration of the power from a horizontal linear gradient is shown in Fig. 3.8a. The vertical axis is the dimensionless power Π_{XX} obtained by dividing the specific power by the wind gradient and the square of the airspeed.

$$\Pi_{XX} = \frac{\bar{P}_{\frac{\partial W_x}{\partial x}}}{\frac{\partial W_x}{\partial x} V_a^2} \quad (3.47)$$

Then, the actual power from the gradient is the dimensionless power multiplied by

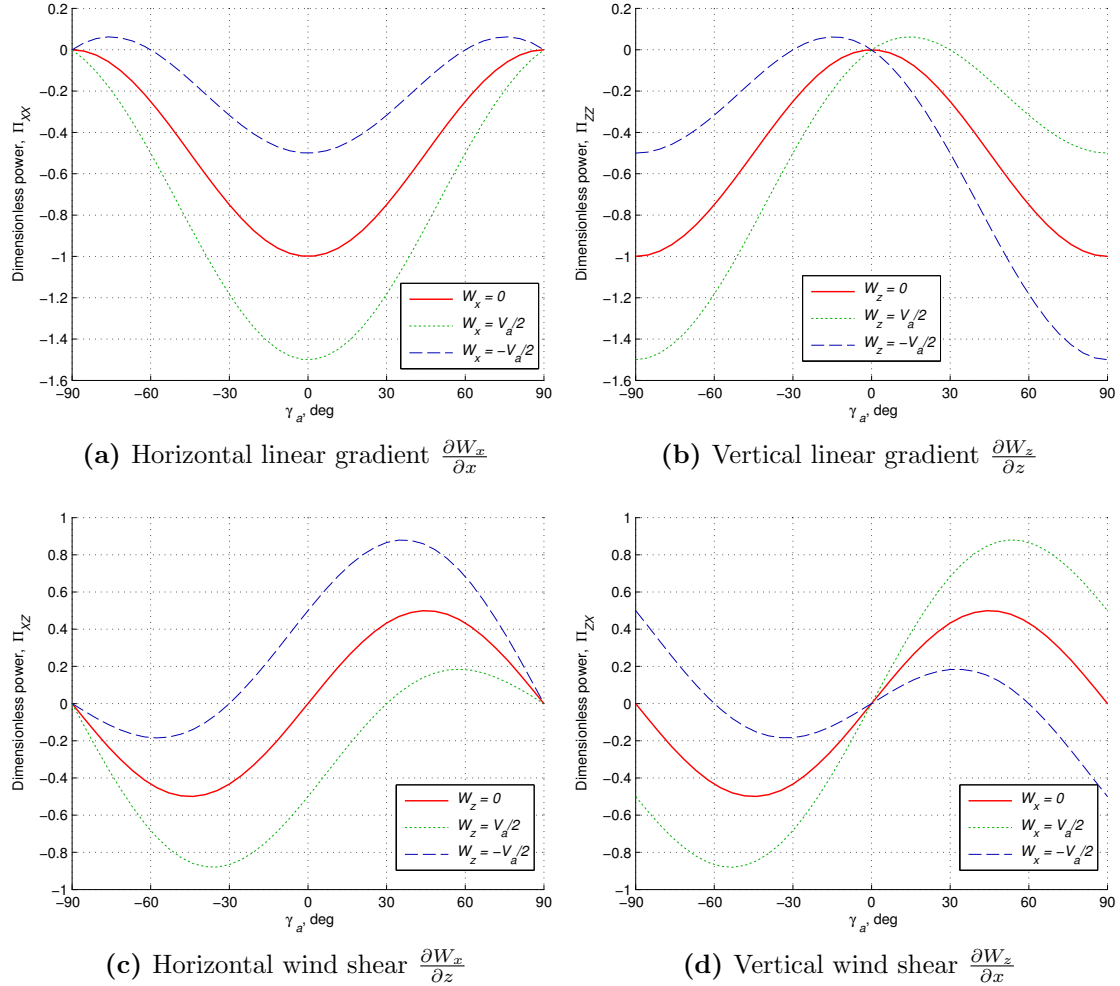


Figure 3.8: Dimensionless power as a function of air relative climb angle for flight in linear wind gradients. Specific power can be calculated by multiplying the dimensionless power by the wind gradient and the square of the airspeed (Eq. (3.47)).

the gradient, the airspeed squared and the mass of the vehicle.

3.3.2 Vertical linear gradient

A vertical linear gradient ($\frac{\partial W_z}{\partial z}$) is the variation of vertical wind speed with altitude. This gradient has a more complicated effect because the $\sin \gamma_a$ component is not positive definite. Thus, the optimum climb angle depends on the airspeed, gradient strength and vertical wind speed. Let the dynamic specific power from a vertical

linear gradient be $\bar{P}_{\frac{\partial W_z}{\partial z}}$. From Eq. (3.40),

$$\bar{P}_{\frac{\partial W_z}{\partial z}} = -\frac{\partial W_z}{\partial z} V_a \sin \gamma_a (V_a \sin \gamma_a - W_z). \quad (3.48)$$

There are four distinct solutions for positive power assuming that $\frac{\partial W_z}{\partial z}$, V_a and γ_a are non-zero (in which cases the power would be zero).

$$\bar{P}_{\frac{\partial W_z}{\partial z}} > 0 \text{ if } \begin{cases} \frac{\partial W_z}{\partial z} > 0, & V_a \sin \gamma_a > 0, & V_a \sin \gamma_a - W_z < 0 \\ \frac{\partial W_z}{\partial z} > 0, & V_a \sin \gamma_a < 0, & V_a \sin \gamma_a - W_z > 0 \\ \frac{\partial W_z}{\partial z} < 0, & V_a \sin \gamma_a > 0, & V_a \sin \gamma_a - W_z > 0 \\ \frac{\partial W_z}{\partial z} < 0, & V_a \sin \gamma_a < 0, & V_a \sin \gamma_a - W_z < 0 \end{cases} \quad (3.49)$$

Recalling that the air-relative sink speed \dot{z}_a is $V_a \sin \gamma_a$ and the inertial sink speed \dot{z}_i is $W_z - V_a \sin \gamma_a$, these cases correspond to:

1. Climbing into a positive gradient with a downdraft greater than the air-relative rate of climb (moving downwards in inertial space), or
2. Diving into a positive gradient with an updraft greater than the air-relative sink speed (moving upwards in inertial space), or
3. Climbing into a negative gradient with a downdraft less than the air-relative rate of climb (moving upwards in inertial space), or
4. Diving into a negative gradient with an updraft less than the air-relative sink speed (moving downwards in inertial space).

As with the horizontal linear gradients, vertical linear gradients are relatively uncommon in a normal wind field. The gradients require acceleration of the air in a linear direction. This can happen over short distances and time scales, but a significantly powerful linear gradient over a long distance is unlikely to be encountered in most tropospheric wind fields. A vertical linear gradient would be possible in some thermal

and storm systems. However, the magnitude of the vertical component contributing to static soaring would usually provide a much more significant power change than the dynamic component.

To determine the maximum power obtainable by selection of climb angle, the power equation can be differentiated with respect to climb angle to determine the stationary points of the function, to yield

$$\frac{\partial \bar{P}_{\frac{\partial W_z}{\partial z}}}{\partial \gamma_a} = -\frac{\partial W_z}{\partial z} V_a^2 (2 \sin \gamma_a \cos \gamma_a) + \frac{\partial W_z}{\partial z} V_a \cos \gamma_a W_z. \quad (3.50)$$

The roots of Eq. (3.50) represent stationary points in the function. Firstly, $\cos \gamma_a = 0$ gives the roots $\gamma_a = \pm \frac{\pi}{2}$. The other solution solves to $\sin \gamma_a = \frac{W_z}{2V_a}$ which is valid for $|W_z| \leq 2V_a$. The second derivative of the power function can be used to determine whether these stationary points are local maxima or minima.

$$\begin{aligned} \frac{\partial^2 \bar{P}_{\frac{\partial W_z}{\partial z}}}{\partial \gamma_a^2} &= -2 \frac{\partial W_z}{\partial z} V_a^2 \cos 2\gamma_a - \frac{\partial W_z}{\partial z} V_a \sin \gamma_a W_z \\ &= -2 \frac{\partial W_z}{\partial z} V_a^2 (1 - \sin^2 \gamma_a) - \frac{\partial W_z}{\partial z} V_a \sin \gamma_a W_z \end{aligned}$$

Substituting the stationary points (for $|W_z| \leq 2V_a$) yields:

$$\begin{aligned} \left. \frac{\partial^2 \bar{P}_{\frac{\partial W_z}{\partial z}}}{\partial \gamma_a^2} \right|_{\sin \gamma_a = \frac{W_z}{2V_a}} &= -2 \frac{\partial W_z}{\partial z} V_a^2 \left(1 - \frac{W_z^2}{4V_a^2} \right) - \frac{\partial W_z}{\partial z} V_a \frac{W_z}{2V_a} W_z \\ &= -2 \frac{\partial W_z}{\partial z} V_a^2. \end{aligned}$$

Thus, the stationary point is a local minimum if the gradient is negative and a local maximum if the gradient is positive. Since there is at most one stationary point for $\gamma_a \in (-\frac{\pi}{2}, \frac{\pi}{2})$, the stationary points are global maxima or minima across the domain of γ_a .

The solution can also be substituted back into Eq. (3.48) to determine the actual power gained,

$$\bar{P}_{\frac{\partial W_z}{\partial z}} \Big|_{\sin \gamma_a = \frac{W_z}{2V_a}} = \frac{\partial W_z}{\partial z} \frac{W_z^2}{4}. \quad (3.51)$$

Interestingly, the specific power is not a function of the airspeed, so for a particular (positive) gradient strength, all airspeeds will result in the same power gain with optimal selection of the climb angle. Also, the power is independent of the direction of the wind. It is still important to note that this only applies to the dynamic energy and power is still transferred through the static soaring term for vertical wind.

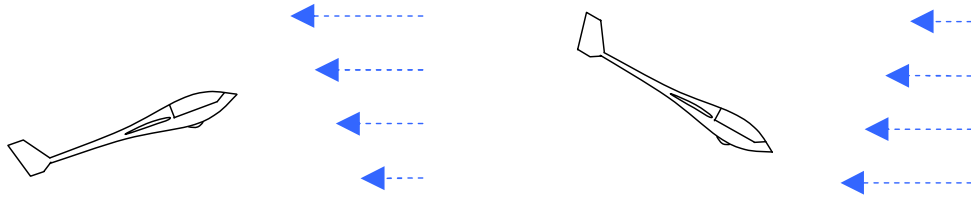
This information can be summarised to the optimal strategy in a vertical linear gradient.

- For a positive gradient, the optimum action is to have an air-relative climb angle $\gamma_a = \sin^{-1} \frac{W_z}{2V_a}$. The amount of energy gained is $\frac{\partial W_z}{\partial z} \frac{W_z^2}{4}$. This strategy will gain energy if the wind speed is greater magnitude and opposite direction to the air-relative vertical speed. Otherwise energy will be lost at all climb angles except 0° .
- For a negative gradient, the optimum action is to maximise climb angle. If there is an updraft, maximum power is obtained in the steepest possible climb, if there is a downdraft maximum power is obtained in the steepest possible dive.

3.3.3 Horizontal wind shear

The remaining gradients are the cross-gradients. Horizontal wind gradient is defined as variation of the horizontal wind in the vertical direction ($\frac{\partial W_x}{\partial z}$). This type of wind gradient is common for boundary layers, where it is often known as horizontal wind shear. The specific dynamic power for a horizontal wind shear is

$$\bar{P}_{\frac{\partial W_x}{\partial z}} = -\frac{\partial W_x}{\partial z} V_a \cos \gamma_a (-V_a \sin \gamma_a + W_z). \quad (3.52)$$



(a) Positive power climb in a positive horizontal wind shear (b) Positive power dive in a negative horizontal wind shear

Figure 3.9: Energy gain in horizontal wind shear. Maximum power is obtained by climbing at an air-relative angle of $\gamma_a = \pm 45^\circ$ if there is no vertical wind ($W_z = 0$).

The positive power cases are shown in Eq. (3.53) and illustrated in Fig. 3.9.

$$\bar{P}_{\frac{\partial W_x}{\partial z}} > 0 \text{ if } \begin{cases} \frac{\partial W_x}{\partial z} > 0, & -V_a \sin \gamma_a + W_z < 0 \\ \frac{\partial W_x}{\partial z} < 0, & -V_a \sin \gamma_a + W_z > 0 \end{cases} \quad (3.53)$$

Thus, positive dynamic power is gained when:

1. Flying into a positive gradient with increasing inertial altitude (downdraft less than air-relative rate of climb or updraft greater than air-relative sink), or
2. Flying into a negative gradient with decreasing inertial altitude (updraft less than air-relative sink or downdraft greater than air-relative rate of climb).

The maximum power climb angle can be calculated by finding the stationary points with respect to γ_a . Differentiating the specific power equation gives

$$\frac{\partial \bar{P}_{\frac{\partial W_x}{\partial z}}}{\partial \gamma_a} = -\frac{\partial W_x}{\partial z} V_a (2V_a \sin^2 \gamma_a - W_z \sin \gamma_a - V_a). \quad (3.54)$$

For non-zero gradient and airspeed, the roots of the quadratic equation in $\sin \gamma_a$ can be solved to find the stationary points.

$$\sin \gamma_a = \left\{ \frac{W_z + \sqrt{W_z^2 + 8V_a^2}}{4V_a}, \frac{W_z - \sqrt{W_z^2 + 8V_a^2}}{4V_a} \right\} \quad (3.55)$$

Evaluating the specific power at the stationary points yields

$$\begin{aligned} \bar{P}_{\frac{\partial W_x}{\partial z}} \Bigg|_{\sin \gamma_a = \frac{W_z + \sqrt{W_z^2 + 8V_a^2}}{4V_a}} &= \\ -\frac{\sqrt{2}}{16} \frac{\partial W_x}{\partial z} \sqrt{4V_a^2 - 2W_z^2 + 2W_z \sqrt{W_z^2 + 8V_a^2}} \left(3W_z + \sqrt{W_z^2 + 8V_a^2} \right) \end{aligned} \quad (3.56)$$

or,

$$\begin{aligned} \bar{P}_{\frac{\partial W_x}{\partial z}} \Bigg|_{\sin \gamma_a = \frac{-W_z - \sqrt{W_z^2 + 8V_a^2}}{4V_a}} &= \\ -\frac{1}{16} \frac{\partial W_x}{\partial z} \sqrt{8V_a^2 - 2W_z^2 - 2W_z \sqrt{W_z^2 + 8V_a^2}} \left(3W_z - \sqrt{W_z^2 + 8V_a^2} \right). \end{aligned} \quad (3.57)$$

Note that when $W_z = 0$ the optimal climb angle is $\pm 45^\circ$. Also, since for most flights the magnitude of vertical wind is significantly less than the airspeed, the solutions are usually close to 45° . From the second derivative and observation of the original power function, it can be noted that energy is gained by solving for the first root in a positive gradient and the second root in a negative gradient. The energy rate increases in magnitude with increased airspeed. This applies to both cases; if energy is being lost it will be lost faster at a higher airspeed and if energy is being gained it will be gained at a higher rate at higher airspeed. This information can be summarised to the optimal strategy in a horizontal wind shear.

- For a positive gradient, the optimum action to maximise air-relative dynamic power is to have an air-relative climb angle $\gamma_a = \sin^{-1} \frac{W_z + \sqrt{W_z^2 + 8V_a^2}}{4V_a}$. The amount of energy gained is shown in Eq. (3.57). This strategy will gain energy if $W_z < V_a$.
- For a negative gradient, the optimum action to maximise air-relative dynamic power is to have an air-relative climb angle $\gamma_a = \sin^{-1} \frac{W_z - \sqrt{W_z^2 + 8V_a^2}}{4V_a}$. The amount of energy gained is shown in Eq. (3.56). This strategy will gain energy if $W_z > -V_a$.

3.3.4 Vertical wind shear

Vertical wind gradients are variation of the vertical wind in a lateral direction ($\frac{\partial W_z}{\partial x}$). The specific dynamic power for vertical wind shear is

$$\bar{P}_{\frac{\partial W_z}{\partial x}} = \frac{\partial W_z}{\partial x} V_a \sin \gamma_a (V_a \cos \gamma_a + W_x). \quad (3.58)$$

Firstly, notice that the function is odd for γ_a such that $\bar{P}_{\frac{\partial W_z}{\partial x}}(-\gamma_a) = -\bar{P}_{\frac{\partial W_z}{\partial x}}(\gamma_a)$. Air-relative dynamic power will be positive in the following cases.

$$\bar{P}_{\frac{\partial W_z}{\partial x}} > 0 \text{ if } \begin{cases} \frac{\partial W_z}{\partial x} > 0, & V_a \sin \gamma_a > 0, & V_a \cos \gamma_a + W_x > 0 \\ \frac{\partial W_z}{\partial x} > 0, & V_a \sin \gamma_a < 0, & V_a \cos \gamma_a + W_x < 0 \\ \frac{\partial W_z}{\partial x} < 0, & V_a \sin \gamma_a > 0, & V_a \cos \gamma_a + W_x < 0 \\ \frac{\partial W_z}{\partial x} < 0, & V_a \sin \gamma_a < 0, & V_a \cos \gamma_a + W_x > 0 \end{cases} \quad (3.59)$$

Thus, positive dynamic power is gained when

1. Climbing into a positive gradient with forward inertial speed (headwind less than air-relative forward speed), or
2. Diving into a positive gradient with backward inertial speed (headwind greater than air-relative forward speed), or
3. Climbing into a negative gradient with backward inertial speed (headwind greater than air-relative forward speed), or
4. Diving into a negative gradient with forward inertial speed (headwind less than air-relative forward speed).

The common cases (1 & 4) where the horizontal wind is less than the forward airspeed are illustrated in Fig. 3.10. The maximum power climb angle can be calculated by

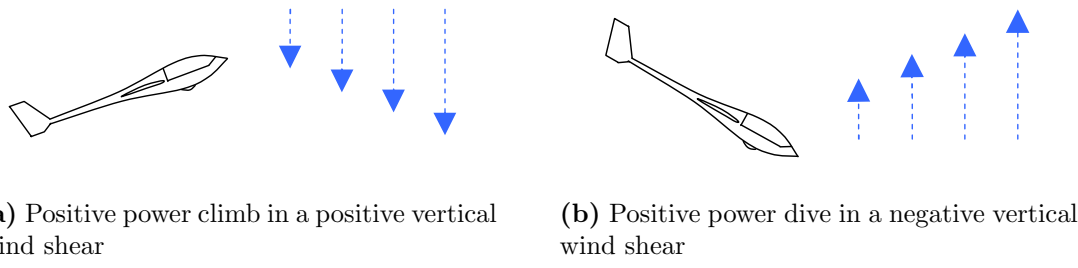


Figure 3.10: Energy gain in vertical wind shear. Maximum power is obtained by flying at an air-relative angle of $\gamma_a = \pm 45^\circ$ if there is no horizontal wind ($W_x = 0$).

finding the stationary points with respect to γ_a . Taking the derivative;

$$\frac{\partial \bar{P}_{\partial W_z}}{\partial \gamma_a} = \frac{\partial W_z}{\partial x} V_a (2V_a \cos^2 \gamma_a + W_x \cos \gamma_a - V_a). \quad (3.60)$$

For non-zero gradient and airspeed, the roots of the quadratic equation in $\sin \gamma_a$ can be solved to find the stationary points. The two required solutions are shown below assuming \cos^{-1} returns the first-quadrant solution and we need the solutions in the range $\gamma_a \in [-\frac{\pi}{2}, \frac{\pi}{2}]$.

$$\gamma_a = \left\{ \cos^{-1} \left(\frac{W_x + \sqrt{W_x^2 + 8V_a^2}}{4V_a} \right), -\cos^{-1} \left(\frac{W_x + \sqrt{W_x^2 + 8V_a^2}}{4V_a} \right) \right\} \quad (3.61)$$

Assuming the headwind is less than the forward airspeed, the positive solution yields a maximum for a positive gradient and the negative solution yields the maximum power for a negative gradient. As in the previous case, with zero horizontal wind the maximum power is achieved at 45° into the gradient.

3.3.5 Dynamic power summary

Dynamic power is the rate of energy capture from wind gradients. As shown in the cases above, the amount of power gained is essentially proportional to the projection of the gradient into the flight direction. This is not surprising since the dynamic

energy is due to acceleration of the airspeed. Of further note is that the power is proportional to the square of the airspeed, so power capture increases significantly with increased airspeed. This is important for a controller but should be considered with respect to physical and structural limitations of an aircraft.

It is also important to note that the analysis provided here has assumed that the optimum action is taken to maximise the power collected. While this maximises the time rate of energy capture, this may not always be the optimum action for different missions. Alternatively, it may be of interest to consider the analogue of the glide ratio for soaring flight in a wind gradient. As discussed earlier, minimum sink is the conditions which minimises energy loss per unit of time. Maximum glide ratio, on the other hand, represents the minimum energy loss per unit of forward travel. For a soaring case, it is common that the wind gradients only exist in a limited spatial region. A common example is that the horizontal wind shear from a boundary layer typically has a limited vertical extant. In such conditions it would make sense to maximise the energy collected over the whole layer thickness rather than maximising the rate of energy capture. This problem is considered and discussed in chapter 4. This also motivates the need for solutions which consider longer duration energy capture rather than instantaneous power. For dynamic soaring, for example, a single soaring cycle will contain both energy loss and energy gain segments. Thus, maximising instantaneous power is not a suitable solution for this type of soaring. To consider these more complicated solutions, a six-degree of freedom model is required, which can more closely simulate the flight of an aerial vehicle.

3.4 Six Degree of Freedom Gliding

3.4.1 Gliding aircraft model

While most of the important soaring mechanisms can be identified from the longitudinal model, the practical applicability is limited. In particular, the longitudinal equations are limited to forward motion, so the aircraft is present at each x location

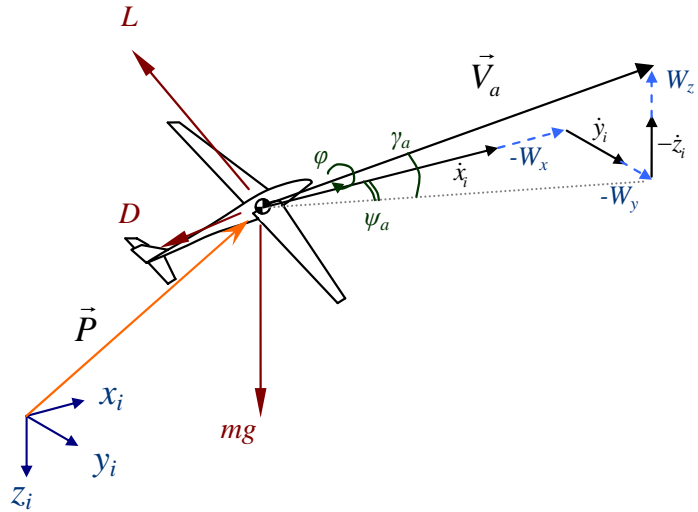


Figure 3.11: Air-relative velocity and applied forces for a gliding aircraft.

only once; it cannot revisit areas of high lift and it cannot travel laterally to a goal. A more complicated model is required to simulate behaviours such as circling in thermal lift and full dynamic soaring cycles. A major focus of this research was to be able to develop control and planning methods capable of utilising static and dynamic soaring in the same framework. This meant extending the longitudinal dynamics into six degrees of freedom.

The 6DOF dynamic model, like the longitudinal model, is an aerodynamic point mass model. The applied forces are the aerodynamic force (decomposed into lift, L , and drag, D) and the weight force (mg). Body force due to sideslip is not considered. The inertial and air-relative frames of reference are the same as in the longitudinal case with the addition of the lateral y -axis and two air-relative angles; ϕ and ψ_a . The bank angle, ϕ , is the rotation of the lift vector around the velocity vector. It is not directly affected by wind which is why it does not have a subscript a . The air-relative heading angle ψ_a represents the direction of the airspeed relative to the inertial x -axis. Figure 3.11 illustrates the forces acting on a gliding aircraft in wind and the angle and axis conventions used in the subsequent analysis.

The air-relative to inertial transformation matrix is denoted \mathbf{C}_a^i and is shown made

up of the standard rotation transformation matrices denoted \mathbf{L}_x , \mathbf{L}_y & \mathbf{L}_z :

$$\mathbf{C}_a^i = \mathbf{L}_z(\psi_a) \mathbf{L}_y(\gamma_a) \mathbf{L}_x(\phi). \quad (3.62)$$

The inertial position is denoted \vec{P} :

$$\vec{P} = \begin{bmatrix} x_i \\ y_i \\ z_i \end{bmatrix} \quad (3.63)$$

The air-relative velocity can be described in terms of the airspeed, V_a , and the heading and climb angles.

$$\vec{V}_a = \mathbf{C}_a^i \begin{bmatrix} V_a \\ 0 \\ 0 \end{bmatrix} = \begin{bmatrix} V_a \cos \gamma_a \cos \psi_a \\ V_a \cos \gamma_a \sin \psi_a \\ -V_a \sin \gamma_a \end{bmatrix} \quad (3.64)$$

As in the longitudinal case, the air-relative velocity, \vec{V}_a , is the difference between the inertial velocity, \vec{V}_i and the wind component, \vec{W} , all expressed in the inertial frame.

$$\vec{V}_a = \vec{V}_i - \vec{W} \quad (3.65)$$

The applied forces acting on the vehicle are lift, weight and drag. Note that the vehicle is assumed to be aligned with the velocity vector; sideslip and lateral forces are ignored. The resulting force sum

$$\vec{F} = \vec{L} + \vec{D} + m\vec{g}. \quad (3.66)$$

Any acceleration of the aircraft must result from applied forces,

$$\begin{aligned} \vec{F} &= m\ddot{\vec{P}} \\ &= m\frac{d\vec{P}}{dt}. \end{aligned} \quad (3.67)$$

Rearranging for the inertial velocity in Eq. (3.65) and substituting Eq. (3.66) into Eq. (3.67),

$$\ddot{\vec{P}} = \frac{1}{m} (\vec{L} + \vec{D} + m\vec{g}) = \frac{d}{dt} (\vec{V}_a + \vec{W}). \quad (3.68)$$

Consider the case of locally spatially-fixed linear wind gradients. Let \mathbf{J}_w be the spatial wind gradients at a particular location.

$$\mathbf{J}_w = \begin{bmatrix} \frac{\partial W_x}{\partial x} & \frac{\partial W_x}{\partial y} & \frac{\partial W_x}{\partial z} \\ \frac{\partial W_y}{\partial x} & \frac{\partial W_y}{\partial y} & \frac{\partial W_y}{\partial z} \\ \frac{\partial W_z}{\partial x} & \frac{\partial W_z}{\partial y} & \frac{\partial W_z}{\partial z} \end{bmatrix} \quad (3.69)$$

Evaluating the derivatives in Eq. (3.68),

$$\frac{1}{m} \left(\mathbf{C}_a^i \begin{bmatrix} -D \\ 0 \\ -L \end{bmatrix} + \begin{bmatrix} 0 \\ 0 \\ mg \end{bmatrix} \right) = \frac{d\mathbf{C}_a^i}{dt} \vec{V}_a + \mathbf{C}_a^i \frac{d\vec{V}_a}{dt} + \mathbf{J}_w \dot{\vec{P}}. \quad (3.70)$$

This can be expanded into a set of three simultaneous equations with unknown variables $L, D, \frac{d\phi}{dt}, \frac{d\gamma_a}{dt}, \frac{d\psi_a}{dt}$ and $\frac{dV_a}{dt}$. Adding the relationship between lift and drag as in Eq. (3.15) leaves three free variables. If it is assumed that the roll rate is directly controlled (as a control input to the system) then the two remaining variables are the pitch rate and lift. As in the longitudinal case, the equations can be resolved to give the lift required for a certain pitch rate (Eq. (3.72)) or the pitch rate produced for a given lift constraint (Eq. (3.73)). The resulting equations for the full 6DOF system are shown in Eqs. (3.71)–(3.75). A similar derivation and model with slight notation differences can also be found in [52].

$$D = \frac{1}{2} \rho V_a^2 S C_{D,0} + \frac{L^2}{\frac{1}{2} \rho V_a^2 S \pi Re} \quad (3.71)$$

$$L = \frac{m}{\cos \phi} \left(V_a \frac{d\gamma_a}{dt} + g \cos \gamma_a - \begin{bmatrix} \cos \psi_a \sin \gamma_a \\ \sin \psi_a \sin \gamma_a \\ \cos \gamma_a \end{bmatrix}^T \mathbf{J}_w \dot{\vec{P}} \right) \quad (3.72)$$

$$\frac{d\gamma_a}{dt} = \frac{1}{V_a} \left(\frac{L}{m} \cos \phi - g \cos \gamma_a + \begin{bmatrix} \cos \psi_a \sin \gamma_a \\ \sin \psi_a \sin \gamma_a \\ \cos \gamma_a \end{bmatrix}^T \mathbf{J}_w \dot{\vec{P}} \right) \quad (3.73)$$

$$\frac{dV_a}{dt} = \frac{-D}{m} - g \sin \gamma_a - \begin{bmatrix} \cos \psi_a \cos \gamma_a \\ \sin \psi_a \cos \gamma_a \\ -\sin \gamma_a \end{bmatrix}^T \mathbf{J}_w \dot{\vec{P}} \quad (3.74)$$

$$\frac{d\psi_a}{dt} = \frac{1}{V_a \cos \gamma_a} \left(\frac{L}{m} \sin \phi + \begin{bmatrix} \sin \psi_a \\ -\cos \psi_a \\ 0 \end{bmatrix}^T \mathbf{J}_w \dot{\vec{P}} \right) \quad (3.75)$$

In general, these equations are similar to the ones obtained for the longitudinal-only case. For simulation of a glider in 6DOF these equations can be integrated numerically with specified roll rate and either lift or pitch rate functions. In the simulations presented in this thesis, the pitch rate is specified in all cases but rejected if the lift required would violate either a pre determined maximum lift coefficient or a load factor limit. In that case, the lift is specified and the resulting pitch rate is determined. This effectively models stall prevention and limit loading. However, it does assume that a controller exists and is able to command and track a specified roll rate and either pitch rate or lift coefficient.

3.4.2 Energy in 6DOF glider model

The energy equations for the 6DOF case are similar to the longitudinal case. The air-relative energy is the sum of kinetic and gravitational potential energy (Eq. (3.5)).

The air-relative specific power is

$$\frac{\dot{E}_a}{m} = -V_a \frac{D}{m} - gW_z - V_a \begin{bmatrix} \cos \psi_a \cos \gamma_a \\ \sin \psi_a \cos \gamma_a \\ -\sin \gamma_a \end{bmatrix}^T \mathbf{J}_w \dot{\vec{P}}. \quad (3.76)$$

As in the longitudinal case there are three sources of energy loss or gain; energy lost to drag, energy from vertical wind (static soaring component) and energy from wind gradients (dynamic soaring component). Both the drag loss and static soaring power are identical to the longitudinal case. The dynamic energy is different due to the inclusion of the air-relative heading ψ_a and the additional wind gradients in the wind Jacobian. The primary effect is the projection of gradients in the lateral xy plane into the air-relative direction of travel through ψ_a . Note that the results are exactly equivalent to the longitudinal case if $\psi_a = 0$.

3.4.3 Gliding without wind

The additional parameters introduced in the 6DOF model are the lateral position y and the heading and bank angles ψ_a and ϕ . The longitudinal gliding analysis covers gliding flight when $\phi = 0$. Thus, the new gliding condition introduced in the 6DOF model is for banked turns. Consider the case of a steady descent banked turn, where the aircraft has constant bank angle, climb angle , and airspeed V_a . Thus, a steady turn will give a constant turn rate $\dot{\psi}_a$ and a constant descent rate \dot{z}_i . This is similar to the steady gliding dive (and in fact a steady dive can be considered a special case of a steady turn with zero bank angle and zero turn rate).

Firstly, the conditions for a steady turn need to be determined. Assuming no wind $\vec{W} = \mathbf{0}$ and $\mathbf{J}_w = \mathbf{0}$. For a steady turn, the airspeed should be constant, such that

$\frac{dV_a}{dt} = 0$. Then, the solution is to solve for γ_a as a function of the airspeed V_a and bank angle ϕ . From Eq. (3.74),

$$\begin{aligned}\frac{dV_a}{dt} &= \frac{-D}{m} - g \sin \gamma_a = 0 \\ \Rightarrow D &= -mg \sin \gamma_a.\end{aligned}\quad (3.77)$$

Similarly, the climb angle should be constant, so from Eq. (3.72),

$$L = \frac{mg \cos \gamma_a}{\cos \phi}. \quad (3.78)$$

Let

$$q = \frac{1}{2} \rho V_a^2, \quad (3.79)$$

$$k = \pi Re. \quad (3.80)$$

Substituting into the drag equation (3.71),

$$\begin{aligned}qSC_{D,0} + \frac{m^2 g^2 \cos^2 \gamma_a}{qSk \cos^2 \phi} &= -mg \sin \gamma_a \\ \cos^2 \phi q^2 S^2 k C_{D,0} + m^2 g^2 (1 - \sin^2 \gamma_a) + mg \cos^2 \phi q Sk \sin \gamma_a &= 0 \\ m^2 g^2 \sin^2 \gamma_a - mg \cos^2 \phi q Sk \sin \gamma_a - (m^2 g^2 + \cos^2 \phi q^2 S^2 k C_{D,0}) &= 0.\end{aligned}$$

This equation is a quadratic in $\sin \gamma_a$ which can be solved to yield

$$\sin \gamma_a = \frac{\cos^2 \phi q Sk - \sqrt{4m^2 g^2 + \cos^2 \phi q^2 S^2 k (\cos^2 \phi k + 4C_{D,0})}}{2mg}. \quad (3.81)$$

Note that one of the roots has been eliminated as it would always result in an imaginary solution (since the discriminant would be greater than or equal to $2mg$ so the magnitude of the denominator will be larger than the numerator in all but the degenerate $\phi = \frac{\pi}{2}$ case and the inverse sine operation would require an imaginary γ_a). Thus, Eq. (3.81) allows calculation of the air-relative climb angle which would result

in a steady gliding turn at a given airspeed and bank angle. Also note that in the no bank case ($\phi = 0$), this is equivalent to the longitudinal solution Eq. (3.28).

As in the steady dive case, a turn efficiency measure needs to be defined which expresses the utility of a steady banked turn. Turn efficiency is defined as $-\frac{\partial \psi_a}{\partial E}$ which is the heading change per energy used. The negative sign is included because the energy rate will be negative. Thus, maximising this turn efficiency represents the minimum amount of energy used to make a certain heading change in that flight condition. Note that this assumes a steady condition and does not account for the time taken or energy lost to transition from a steady dive to a steady turn. The turn energy can be calculated as the quotient of the turn rate and the power.

$$\begin{aligned} -\frac{\partial \psi_a}{\partial E} &= -\frac{\partial \psi_a}{\partial t} \frac{\partial t}{\partial E} \\ &= \frac{-\tan \phi}{mV_a^2 \sin \gamma_a} \end{aligned} \quad (3.82)$$

The power, turn rate, drag force and turn efficiency are illustrated across a range of speed bank angles in Fig. 3.12. Note that the turn efficiency plot is relatively complicated, with multiple stationary points in ϕ . Ideally, the equation would be solved analytically for the stationary points in the turn efficiency with respect to the bank angle ϕ . This would allow calculation of the optimal bank angle for a given airspeed. However, this is a complicated analytic expression of a 10th order (symmetrical) polynomial in $\cos \phi$ and analytic roots are not solvable, requiring a numerical approximation.

It is also worth considering that there are limitations on the airframe which would preclude some of these flight conditions. Specifically, conditions which require a lift coefficient above the previously defined maximum $C_{L,max}$ should be removed. The maximum bank angle for a given airspeed can be found by solving for the condition

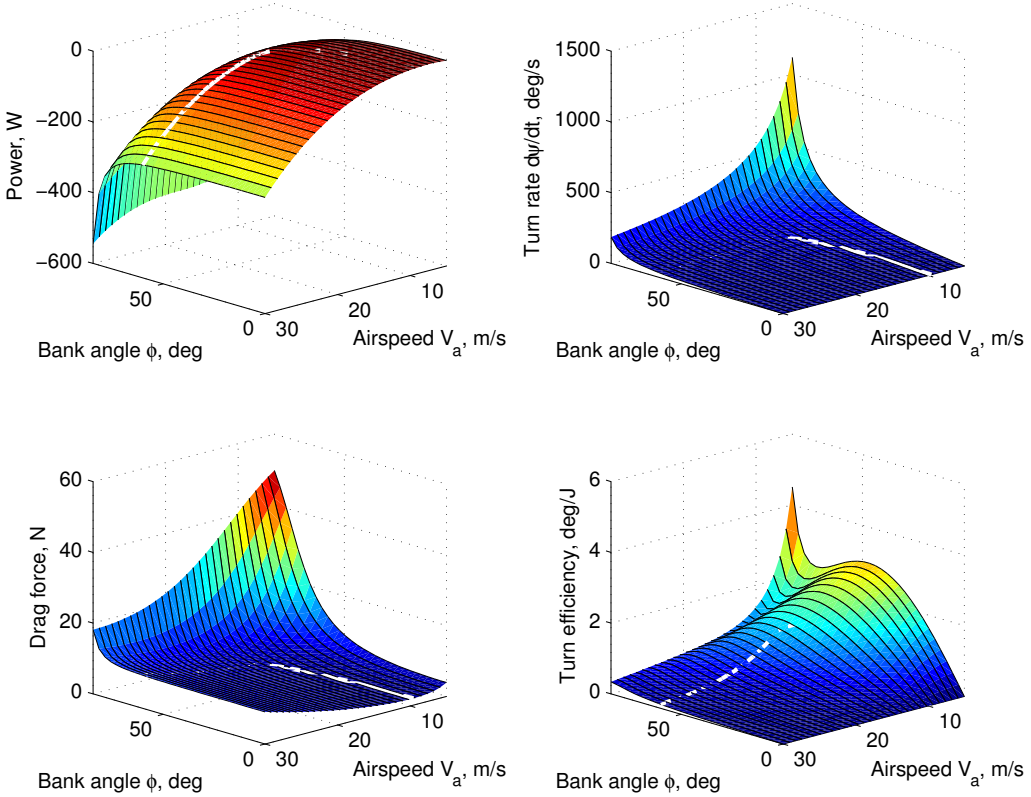


Figure 3.12: Turn rate efficiency during a steady gliding turn. The white line illustrates the limits imposed by physical limitations ($C_{L,max} = 1.0$ and $n_{max} = 2$).

of maximum lift. From Eq. (3.71) and (3.77)

$$-mg \sin \gamma_a = qS \left(C_{D,0} + \frac{C_{L,max}^2}{k} \right).$$

Substituting the climb angle from Eq. (3.81)

$$\begin{aligned} \cos^2 \phi qSk - \sqrt{4m^2g^2 + \cos^2 \phi q^2 S^2 k (\cos^2 \phi k + 4C_{D,0})} &= \\ \frac{-qS}{mg} \left(C_{D,0} + \frac{C_{L,max}^2}{k} \right) & \\ q^2 S^2 \left(k \cos^2 \phi + 2 \left(C_{D,0} + \frac{C_{L,max}^2}{k} \right)^2 \right) &= 4m^2 g^2 + \cos^2 \phi q^2 S^2 k (\cos^2 \phi k + 4C_{D,0}). \end{aligned}$$

Then, the maximum bank angle ϕ_{max} for a given airspeed V_a and maximum lift

coefficient $C_{L,max}$ is limited to

$$\cos \phi_{max} = \frac{\sqrt{m^2 g^2 - \left(\frac{1}{2}\rho V_a^2 S \left(C_{D,0} + \frac{C_{L,max}^2}{k}\right)\right)^2}}{\frac{1}{2}\rho V_a^2 S C_{L,max}}. \quad (3.83)$$

Equation (3.83) is a relatively common definition and can be found in most flight mechanics texts ([9, 80]).

In addition to the lift coefficient limit, most aircraft have limit load factors, n , which limit the lift as a multiple of the weight (there are usually positive and negative load limits).

$$n = \frac{L}{mg} \quad (3.84)$$

For a high aspect ratio glider the limit loads are usually due to the high bending moments on the (relatively) slender wings. Figure 3.13 shows the same results as Fig. 3.12 with maximum lift coefficient $C_{L,max} = 1.0$ and maximum load $n_{max} = 2$. The maximum load effectively imparts a bank angle limit of approximately 60° .

Figure 3.13 shows that in the case of the current glider configuration, the physical limitations remove the stationary points and the turn efficiency monotonically increases with bank angle in the allowable domain. Thus, at a given speed the optimum bank angle is actually the maximum bank angle limited by the lift coefficient or load factor. However, these safety limits are usually defined with some margin of safety included and a controller would require relatively strict limits near the edge of the flight envelope to prevent stall or overloading the wing. It is also important to note that this simplified model assumes uniform lift over the entire wing. In reality, the lift can vary significantly and part of the wing may stall near the $C_{L,max}$ limit leading to an adverse flight condition such as a spin.

A further condition of interest may be the minimum drag bank angle for a given airspeed or vice-versa in a steady turn. The solution method is similar to the longitudinal case, except that in the turn case $\pi A Re$ is effectively replaced by $\pi A Re \cos^2 \phi$.

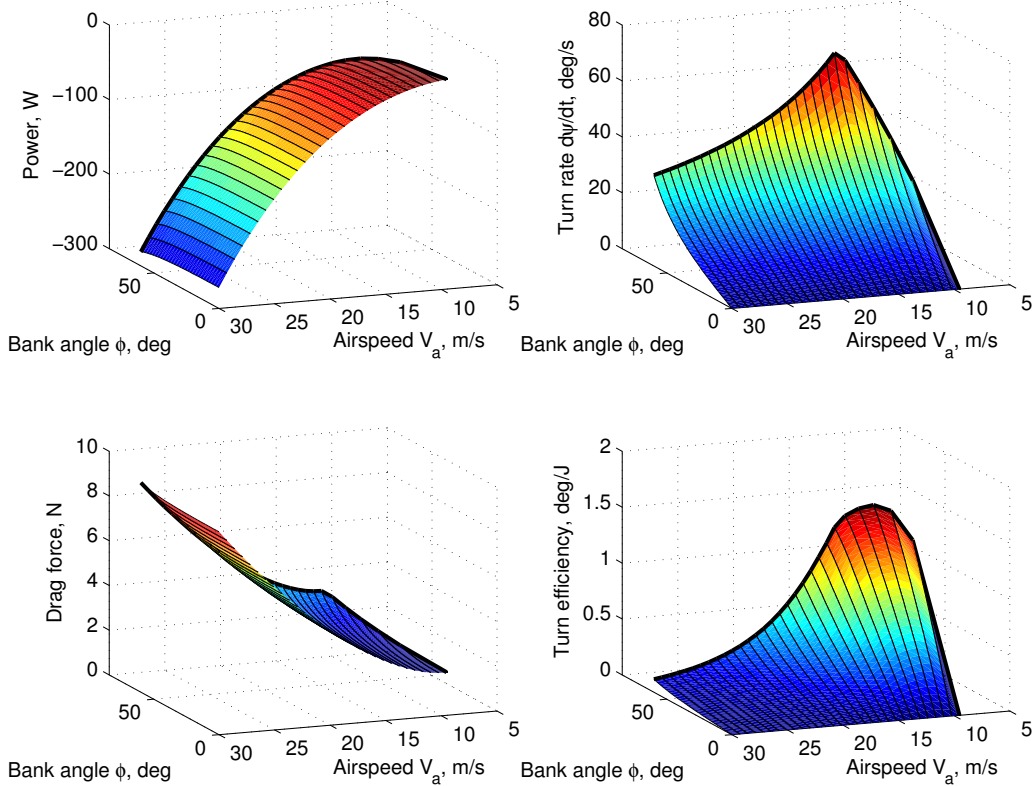


Figure 3.13: Turn rate efficiency during a steady gliding turn. The lift coefficient is limited to $C_{L,max} = 1.0$ and there is a maximum positive load factor of $n_{max} = 2$.

Thus, the steady turn minimum drag speed is

$$V_{a,mindrag} = \sqrt[4]{\frac{4m^2g^2}{\rho^2S^2C_{D,0}(\pi\mathcal{R}e\cos^2\phi + 4C_{D,0})}}. \quad (3.85)$$

Note that in the no turn condition this is equivalent to the longitudinal solution (Eq. (3.34)). Conversely, solving for the minimum drag bank angle at a given airspeed gives

$$\cos\phi_{mindrag} = \sqrt{\frac{4m^2g^2 - \rho V_a^4 S^2 C_{D,0}^2}{\rho^2 V_a^4 S^2 \pi \mathcal{R}e C_{D,0}}}.$$
 (3.86)

3.5 Six Degree of Freedom Soaring

The additional gradients not covered in the longitudinal model are $\frac{\partial W_x}{\partial y}$, $\frac{\partial W_z}{\partial y}$, $\frac{\partial W_y}{\partial x}$, $\frac{\partial W_y}{\partial y}$ and $\frac{\partial W_y}{\partial z}$. Since the lateral y dimension can be considered equivalent to x dimension projected through the heading angle, some of the new gradients have direct equivalence to the longitudinal solutions. The vertical wind shear $\frac{\partial W_z}{\partial y}$ and horizontal wind shear $\frac{\partial W_y}{\partial z}$ can be treated similarly to $\frac{\partial W_z}{\partial x}$ and $\frac{\partial W_x}{\partial z}$ respectively. Similarly, the linear gradient $\frac{\partial W_y}{\partial y}$ is equivalent to the lateral linear gradient $\frac{\partial W_x}{\partial x}$.

There is a new situation for the 6DOF model in static soaring which is circling in lift. In most cases, lifting air occurs in spatially limited regions such as a thermal column. Manned gliders and birds tend to fly (air-relative) circling paths inside lifting air resulting in ascending spirals. Although the gliding section discussed the optimal action for turn efficiency, gliding in lift is a different problem as the turning flight is only performed to stay within the limits of the lifting air rather than to change heading. Thus, selecting optimum turning conditions in a thermal requires a more complicated set of control rules. Finding an analytic solution is only possible for a known wind field. However, the results from the gliding analysis can determine the radius of the circle which would result from a steady gliding turn at the minimum drag conditions.

The turn radius can be found through calculating the cycle time from the heading rate $\frac{d\psi_a}{dt}$ and the resulting circle diameter from the forward airspeed. The turn radius is

$$r = \frac{V_a^2 \cos \gamma_a}{\tan \phi}. \quad (3.87)$$

The result is familiar to powered aircraft where the climb angle is zero. As in many of the cases discussed here, making the small angle assumption on the climb angle $\cos \gamma_a \approx 1$ would result in a relatively small error. Figure 3.14 shows the minimum drag bank angle, turn radius and vertical speed for a range of airspeeds. Note that the lifting load limit n_{max} limits the allowable bank angle above a certain velocity, which limits the turn radius significantly. In the case for SBXC parameters, the bank is limited above 15m/s to approximately 60° .

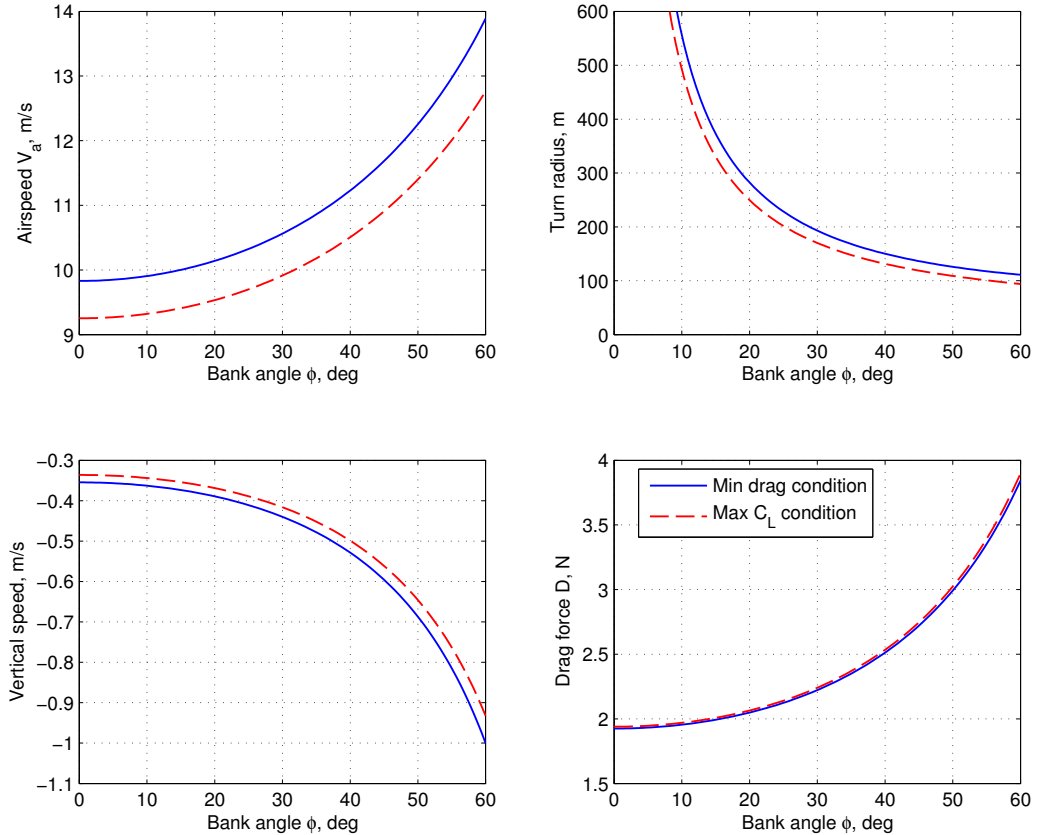


Figure 3.14: Minimum drag and maximum lift coefficient flight conditions for steady turns. $C_{L,max} = 1.0$, $n_{max} = 2.0$ limiting the bank angle to $\sim 60^\circ$.

These results show that for a gliding aircraft the minimum sink usually occurs at the maximum lift coefficient. Thus, to minimise energy loss in a limited circle radius, the best action is to fly at maximum lift coefficient. Although the minimum drag case may travel a longer total distance for the same energy loss, it will be at a higher turn radius. These results are important for gliding in thermals, where selecting a suitable bank angle is possible by determining the size of the lifting air and hence the minimum sink possible for a circle of that size.

Also for the 6DOF system there are additional unique wind gradients which have no equivalent in the longitudinal analysis. The unique results in the 6DOF case are the planar horizontal wind gradients $\frac{\partial W_x}{\partial y}$ and $\frac{\partial W_y}{\partial x}$, representing lateral wind variation across the lateral plane. This type of gradient could occur in a natural environment as a result of a wind shear layer from a vertical obstacle (such as a cliff or wall) or

from variation of lateral winds resulting in local lateral shear.

Note that these gradients are equivalent to each other in the lateral plane through a 90° rotation of the heading ψ_a . The contribution to specific power of the lateral gradient $\frac{\partial W_x}{\partial y}$ is

$$\bar{P}_{\frac{\partial W_x}{\partial y}} = \frac{\partial W_x}{\partial y} V_a \cos \psi_a \cos \gamma_a (V_a \sin \psi_a \cos \gamma_a + W_y). \quad (3.88)$$

Again, assuming inverted flight is not permitted ($\gamma_a \in [-\frac{\pi}{2}, \frac{\pi}{2}]$), then $\cos \gamma_a > 0$ and dynamic power will be gained,

$$\bar{P}_{\frac{\partial W_x}{\partial y}} > 0 \text{ if } \begin{cases} \frac{\partial W_x}{\partial y} > 0, & V_a \cos \psi_a > 0, & V_a \sin \psi_a \cos \gamma_a + W_y < 0, \\ \frac{\partial W_x}{\partial y} > 0, & V_a \cos \psi_a < 0, & V_a \sin \psi_a \cos \gamma_a + W_y > 0, \\ \frac{\partial W_x}{\partial y} < 0, & V_a \cos \psi_a > 0, & V_a \sin \psi_a \cos \gamma_a + W_y > 0, \\ \frac{\partial W_x}{\partial y} < 0, & V_a \cos \psi_a < 0, & V_a \sin \psi_a \cos \gamma_a + W_y < 0. \end{cases} \quad (3.89)$$

Interestingly, this could be used to gain energy in the horizontal equivalent of a Rayleigh cycle. Gaining energy by heading into the gradient is possible in two opposing directions, with energy-loss turns in between (see Fig. 3.15). The turns could also be performed vertically if inverted flight is permitted.

3.6 Summary

A simple mathematical model for a gliding aircraft can be used to identify the conditions of minimum energy loss gliding and energy gain soaring flight. These equations allow a good background understanding of the mechanisms of soaring flight; the conditions required for soaring and the actions that maximise the energy captured in each condition.

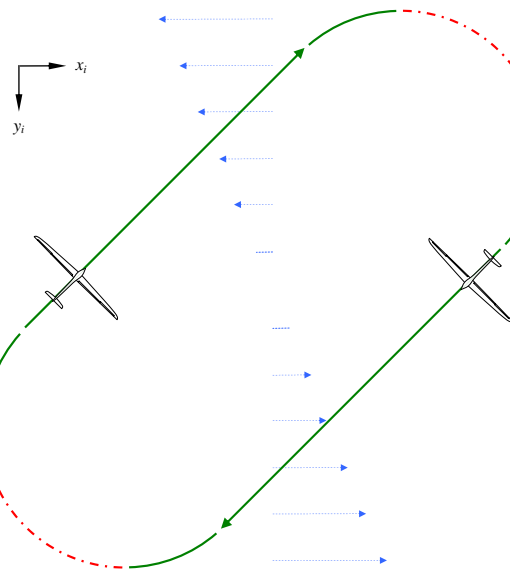


Figure 3.15: A piecewise energy gain cycle in planar wind shear. The wind is indicated with blue dashed arrows and the cycle trajectory is indicated with solid green and dash-dot red arrows. The solid green lines indicate energy gain segments while the dash-dot red lines are energy loss.

For gliding flight, it is important to understand and quantify the flight conditions which minimise energy loss. The analysis presented here identified two important conditions for gliding in a steady glide. Minimum sink is the airspeed at which a steady glide will have the slowest rate of energy loss. Flying at minimum drag (a higher airspeed) minimises the energy lost per unit of forward travel; that is, minimising drag maximises the range of a gliding aircraft. Equations to calculate both the minimum sink and minimum drag airspeed were found. During steady turns, the optimum action to minimise energy loss for a certain heading change is to fly at minimum drag airspeed and at the maximum allowable bank angle. In thermal gliding, the optimal bank angle depends on the power profile of the thermal but can be solved analytically using the turn radius and sink rate equations found in §3.4.3.

Energy-gain soaring requires either a vertical wind or a sufficient wind gradient. Static soaring is the energy gained from flying in vertical wind. This is equivalent to translating the whole wind field upwards in inertial space, so the same energy loss rules apply to static soaring and the no-wind gliding conditions. The rate of energy cap-

ture from rising air is independent of the aircraft actions. Dynamic soaring is the capture of energy from wind gradients. The actions which maximise energy capture are highly dependent on the gradient itself. However, in general power from linear gradients is gained due to acceleration of the airspeed, so the action which maximises energy capture is the orientation which maximises the rate of effective airspeed acceleration. The power from a linear wind gradient is proportional to the square of the airspeed and the strength of the gradient.

This information can be utilised by all gliding aircraft to minimise energy loss during gliding flight and maximise energy gain in suitable conditions. The analytic solutions also allow fast calculation of optimal flight conditions which could be used to control an autonomous soaring vehicle to maximise capture of energy during flight.

Chapter 4

Control of a Soaring Aerial Vehicle

Chapter 3 focused on determining the mechanisms of energy gain flight for a simplified aircraft model. The focus in this chapter is to determine control strategies which could utilise the soaring mechanisms determined in the previous chapter to identify regions of possible energy gain and exploit them. The goal here is to identify situations where energy gain is possible and utilise control strategies that produce energy-gain trajectories.

The first soaring control presented is control for utilising a single type of energy gain flight. Static soaring controllers have shown to be capable of collecting energy from thermals in flight with minimal requirement on sensors and relatively simple heuristic controls. A similar type of control for dynamic soaring in linear shear is presented. Results demonstrate that with simple wind estimation this type of control is capable of generating energy gain paths in wind shear.

However, these types of controllers suffer from a lack of flexibility. Since they are designed for a single type of soaring they cannot easily be adapted to utilise other types of soaring. While a group of complimentary controllers could be used, the planner would also need to identify each wind condition as it is encountered and select the appropriate controller. Section 4.2 addresses the problem of designing a flexible controller capable of generating energy-gain paths or minimising energy loss in all wind conditions.

4.1 Longitudinal Soaring Control

The most commonly encountered energy features in a wind field are rising air and horizontal shear layers. The following sections discuss control strategies for soaring flight in these conditions. Most results are drawn from the equations for the dynamic model of the previous chapter. This analytic approach allows open-loop estimation of actions to maximise energy capture.

4.1.1 Control for soaring in rising air

Rising air is relatively common in mixed wind fields in the troposphere. Convective mixing causes vertical circulation of air and the rising regions can be used for soaring flight. In the simplest case, rising air is just a vertical component of the wind. As noted in the previous chapter, during level cruise energy gain from rising air is independent of aircraft speed. Thus, minimising drag power loss (flying at minimum sink) will maximise total power gain and maximising glide ratio will yield the maximum travelling performance (most distance travelled for the rate of energy captured).

Generally though, rising air occurs in limited regions of a wind field such that level flight through thermal columns does not provide enough energy to maintain flight. The most common behaviour is circling inside lifting air. While banked flight is less efficient than level flight small aircraft can circle completely within the limits of thermal columns to provide continuous power. Recall that flying in lifting air is equivalent to flying in still air and moving the frame of reference vertically in inertial space which results in potential energy gain. As demonstrated in §3.4.3 for most aircraft the minimum sink condition is achieved by flying at minimum speed (maximum lift coefficient) and selecting the maximum bank angle to allow tight enough turning to remain within the lifting air. Previous research has demonstrated flight testing of static soaring controllers [8, 10, 31, 32]. These mostly rely on predefined thermal models which are fit to data collected in-flight. This allows estimation of the thermal centre and optimal circling radius.

4.1.2 Control for soaring in horizontal shear

Horizontal wind shear is vertical variation of horizontal wind. This type of dynamic soaring was the earliest observed form of dynamic soaring as it is commonly used by birds. Horizontal wind shear is a relatively common wind structure which forms in windy conditions over the Earth's surface where the wind and surface are relatively stable (such as over the ocean).

In §3.3 it was noted that maximum power is gained from horizontal wind shear by climbing at an air-relative climb angle of 45° . However, this is not necessarily the most useful measure of utility for wind gradients. Most shear layers have a limited 'thickness' or altitude range where the gradient is sufficient to continue energy gain flight. Thus while maximising power provides the highest time rate of energy gain, a more appropriate measure may be to maximise the energy captured from a limited thickness layer. Thus, maximising the rate of energy capture with respect to altitude gained will maximise the energy captured over the vertical extent of a shear layer. This is roughly analogous to the speed of minimum sink (minimum energy loss per unit of time) compared to the maximum glide ratio (minimum energy loss per unit of forward travel).

Determining the climb angle for maximum energy gain is achieved by determining the rate of energy change with respect to inertial altitude. This value is called the energy altitude gradient, $\frac{\partial E_a}{\partial z_i}$. Differentiating dynamic energy (Eq. (3.5)) with respect to inertial altitude yields

$$\frac{\partial E_a}{\partial z_i} = -mg + mV_a \frac{\partial V_a}{\partial t} \frac{\partial t}{\partial z_i}. \quad (4.1)$$

Consider the case where the only wind is due to the horizontal shear $\frac{\partial W_x}{\partial z}$. With no vertical wind the vertical inertial speed is equal to the air-relative vertical speed ($\dot{z}_i = -V_a \sin \gamma_a$). Then, substituting the airspeed acceleration from Eq. (3.22),

$$\begin{aligned}\frac{\partial E_a}{\partial z_i} &= -mg - \frac{m}{\sin \gamma_a} \left(-\frac{D}{m} - g \sin \gamma_a - \cos \gamma_a \frac{\partial W_x}{\partial z} V_a \sin \gamma_a \right) \\ &= \frac{D}{\sin \gamma_a} - mV_a \cos \gamma_a \frac{\partial W_x}{\partial z}.\end{aligned}$$

This can be further expanded from the drag equation (Eq. (3.21)).

$$\begin{aligned}\frac{\partial E_a}{\partial z_i} &= \frac{\rho V_a^2 S C_{D,0}}{2 \sin \gamma_a} + \frac{2m^2 g^2 \cos^2 \gamma_a}{\pi A \rho V_a^2 S \sin \gamma_a} + \frac{2 \sin^3 \gamma_a \frac{\partial W_x}{\partial z}^2}{\pi A \rho S} + \\ &\quad \frac{4mg \cos \gamma_a \sin \gamma_a \frac{\partial W_x}{\partial z}}{\pi A \rho V_a S} - mV_a \cos \gamma_a \frac{\partial W_x}{\partial z} \quad (4.2)\end{aligned}$$

Figures 4.1 and 4.2 illustrate the airspeed acceleration $\frac{\partial V_a}{\partial t}$, power $\frac{\partial E_a}{\partial t}$ and energy altitude gradient $\frac{\partial E_a}{\partial z_i}$ for horizontal wind shear of 0.5s^{-1} and 1.0s^{-1} respectively. From these figures, it is clear that higher airspeed increases airspeed acceleration, power and energy altitude gradient. Also interesting is that in some conditions (low wind gradient and low airspeed) it would be possible to gain energy but steadily lose airspeed. This would be unsustainable over a certain height as eventually the airspeed would drop below stall even though total energy is increasing. Conversely, above this limit the aircraft accelerates as it climbs and increases the time and altitude rate of energy capture.

For limited thickness shear, the goal would be to maximise the energy captured during a climb through the layer. As noted, increasing airspeed increases the energy captured. Ideally, a controller would be able to calculate the optimal climb angle as a function of the current airspeed and wind gradient. An analytic solution would find the maximum by determining stationary points of Eq. (4.2) with respect to air-relative climb as shown for the power calculations in Chapter 3. However, in this case a general analytic solution does not exist due to the inclusion of the drag term. A numerical solver could be used to optimise for energy altitude gradient. Alternatively a lookup table could be generated off-line for a range of gradient and airspeed combinations and the results stored either as a regressed function or a look up table.

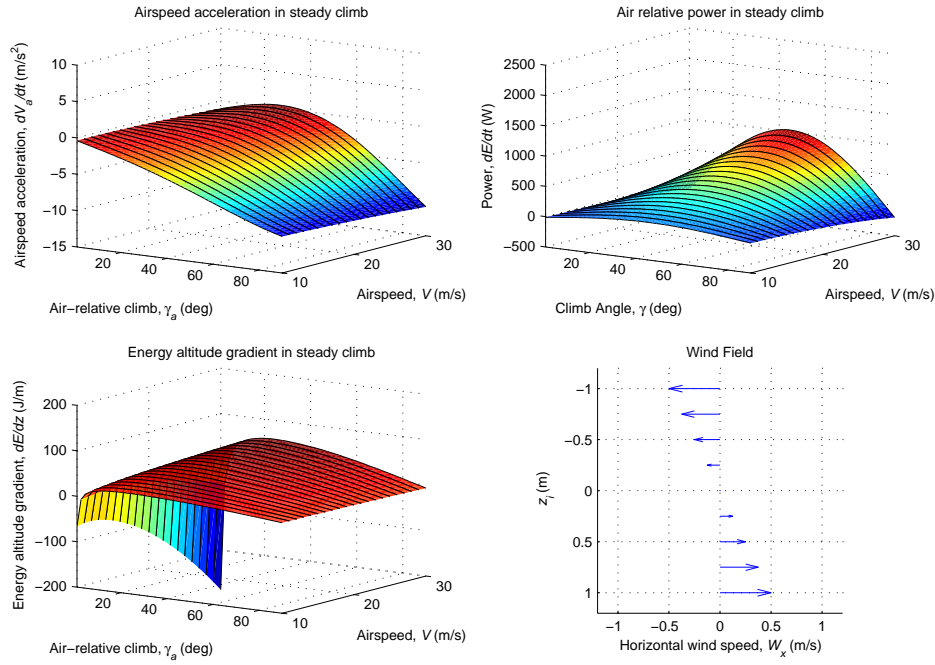


Figure 4.1: Airspeed and energy change for steady climb through linear horizontal wind shear of strength 0.5/s

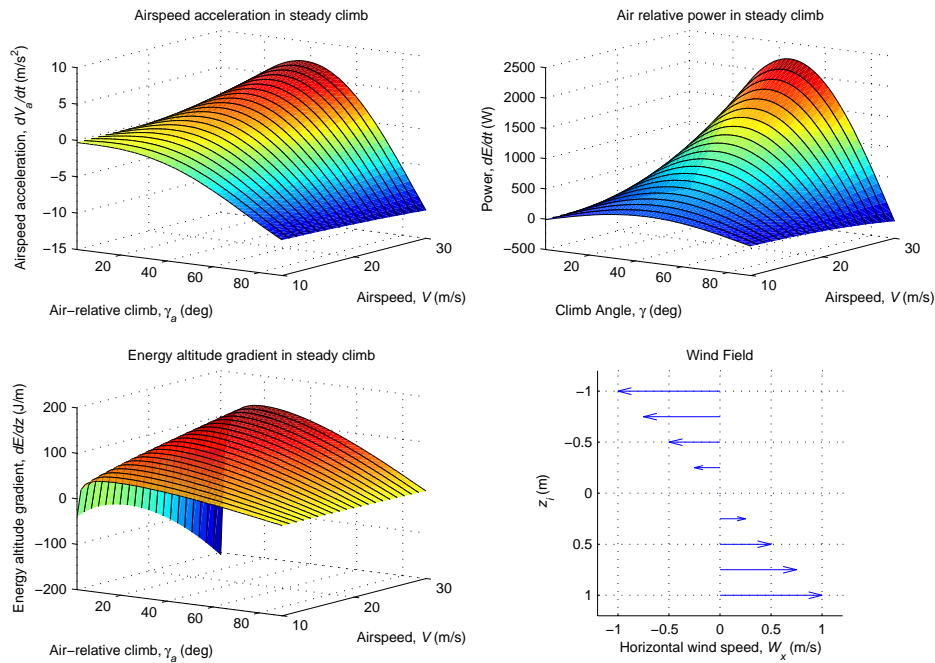


Figure 4.2: Airspeed and energy change for steady climb through linear horizontal wind shear of strength 1.0/s

Note that the energy altitude curve is relatively smooth for variation of the climb angle around the optimum, so deviation from the optimal angle would not result in very significant reduction in energy gain. Previous work by Wood [108] performed similar calculations and determined that a fixed climb angle of 20° would be a sufficient approximation of the maximum energy gradient climb angle. The results in this thesis largely agree with this conclusion but it is suggested that a pre-generated lookup table or even an on-line numerical solver would yield improved results with increased flexibility.

The analysis presented for energy gain in shear so far has assumed that the goal is to maximise energy capture from a single traversal of a limited thickness linear shear layer. However, the energy from a single traversal of a shear layer would be insufficient for long-term flight. Traversals cannot be immediately repeated due to physical displacement of climbing through a shear layer; the energy gained in a climb leaves the aircraft at the top of the shear layer in constant wind. Diving into the shear in the same direction presents an adverse shear and energy loss. It is simple to show that continuous energy gain forward flight in a shear layer is impossible due to the energy loss from drag. Any energy gained during the climb through a shear layer is stored as either kinetic or potential energy.

Of further interest is the possibility that energy could be stored internally but not as either airspeed or altitude. This mechanism would allow exploitation of the effect of airspeed on energy. Travelling at higher speed upwards through the gradient, then descending slowly could yield a net energy gain if energy is stored at the top of a cycle to reduce airspeed and used to accelerate at the bottom of the cycle. This type of mechanism would require capture and storage of flight energy through an energy storage device such as a Ram Air Turbine (RAT) used in commercial aircraft for emergency power. Ideally, the same system would be used for propulsion. This concept does not have a natural equivalent since birds cannot recapture airspeed energy for internal storage. Exploration of this concept remains for future consideration.

4.1.3 Rayleigh cycle dynamic soaring control

Where energy storage is not possible, energy can still be gained in a horizontal shear layer through cyclic trajectories. This concept takes advantage of the fact that energy is gained climbing upwards through an increasing headwind or diving through a decreasing tailwind. This is possible in a fixed shear layer by reversing the direction of the aircraft, as shown in Fig. 4.3. A Rayleigh cycle is the simplest trajectory to include both these energy gain segments in a single flight cycle.

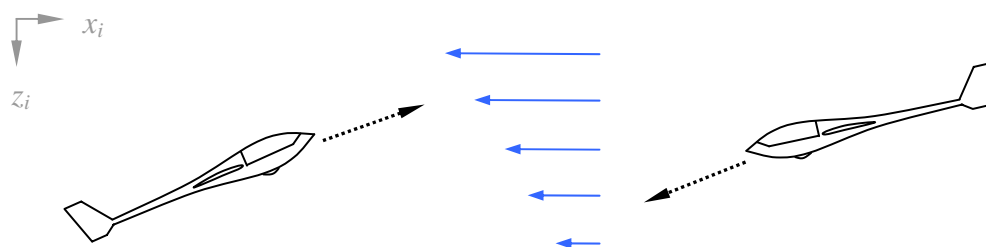


Figure 4.3: Dynamic soaring in a fixed horizontal shear layer

A Rayleigh cycle is generally defined in four segments. Consider starting at the low altitude of a headwind shear layer heading into the wind. Climbing upwards through the shear layer is an energy-gain condition (subject to the requirements detailed in §3.3). In most shear layers, the gradient decreases with altitude and above the shear the wind is nearly constant. Since there is a minimum shear required for energy gain, the useful ‘top’ of a shear layer can be defined as the altitude at which climbing through the gradient no longer returns useful energy. The second segment is a downwind turn where the aircraft stays at a relatively constant altitude and makes a 180° turn to head downwind. This retains the airspeed such that at the end of the turn the aircraft is heading downwind with a strong tailwind and consequently high ground speed. The turn will result in energy loss.

Diving into the gradient is another energy gain segment as the tailwind decreases with altitude, effectively resulting in increasing airspeed. Also, the potential energy is converted into kinetic energy so the aircraft has high airspeed at the base of the

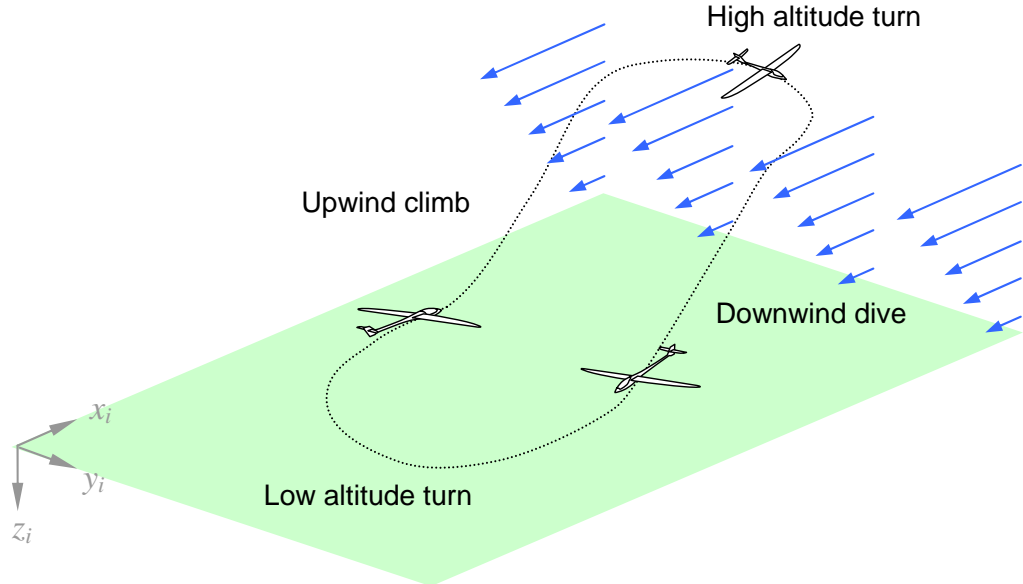


Figure 4.4: A Rayleigh dynamic soaring cycle in linear horizontal wind shear.

shear layer. The minimum altitude is usually defined by a safety limit since shear layers usually have maximum gradient at the surface.

The final segment is a low altitude turn where the aircraft turns upwind to return to the flight conditions at the start of the cycle. The climb and dive phases will result in net energy gain in sufficient wind gradient and the two turns will result in energy loss. If more energy is gained than lost, then the aircraft will end the cycle with a higher airspeed than it started. The additional energy can be stored as kinetic energy by repeating the cycle with increasing airspeed but this can only increase up to a structural limit of the airframe load during the high speed low altitude turn. Alternatively, excess energy can be utilised to travel such that each cycle has the same start and end conditions but the aircraft can move laterally without expending net energy.

Previous research has examined the conditions required for net energy gain cycles for soaring birds. The Rayleigh cycle is named after original research from Lord Rayleigh [84] who identified the flight pattern in ocean birds. While he demonstrated the mechanism of dynamic soaring, it was not until recent developments in computers

that a soaring cycle could be adequately simulated and optimised. Wood [108] estimated that for an albatross model in conditions expected over the ocean a Rayleigh cycle could be performed resulting in significant energy gain allowing upwind travel. More recent analysis by Sachs [87] examined the minimum wind gradient required for energy gain cycles. That research was not restricted to fixed-phase cycles and allowed continuously variable bank and lift coefficient control to determine optimum cycles. Sachs also allowed open cycles where the turns are in opposite directions so that cycles end with some lateral travel. It was found that this type of cycle is more common in birds and simulation suggests it is more efficient. Sachs finds that for a logarithmic profile from 0 m/s at the surface (which is common in boundary layers), a reference wind speed of 8.6 m/s is required at 10 m altitude. Both studies note that performance can be dependent on how close to the surface the bird is allowed to fly, since the gradient tends to be steepest there. While birds have sufficient control to fly very close to the surface this may not be possible with autonomous aircraft.

Since most UAV missions would require some sort of travel rather than energy storage, consideration is made for a mission requiring a horizontal shear controller capable of heading towards an arbitrary target at the same altitude as the shear layer without using energy. The controller should be able to identify conditions where soaring would yield sufficient energy to travel towards the goal and take actions which maximise the energy captured to travel to the goal as quickly as possible.

The simplest solution is a mode-based control that uses the normal phases of Rayleigh cycle dynamic soaring combined with a controller to enable travel towards a goal. Suitable conditions are identified by utilising the equations generated in the previous section to estimate the energy gained and determine if net energy gain is possible in the current conditions. A higher level mode controller simply selects the four segments in order; upwind climb, high altitude turn, downwind dive and low altitude turn.

The travel segment requires more careful consideration as travel is defined in inertial space, and the best time to use excess energy depends on the wind. For example, if the target is downwind, travel at the top of the shear layer is much more efficient as the wind allows significantly further travel in inertial space at the same air-relative

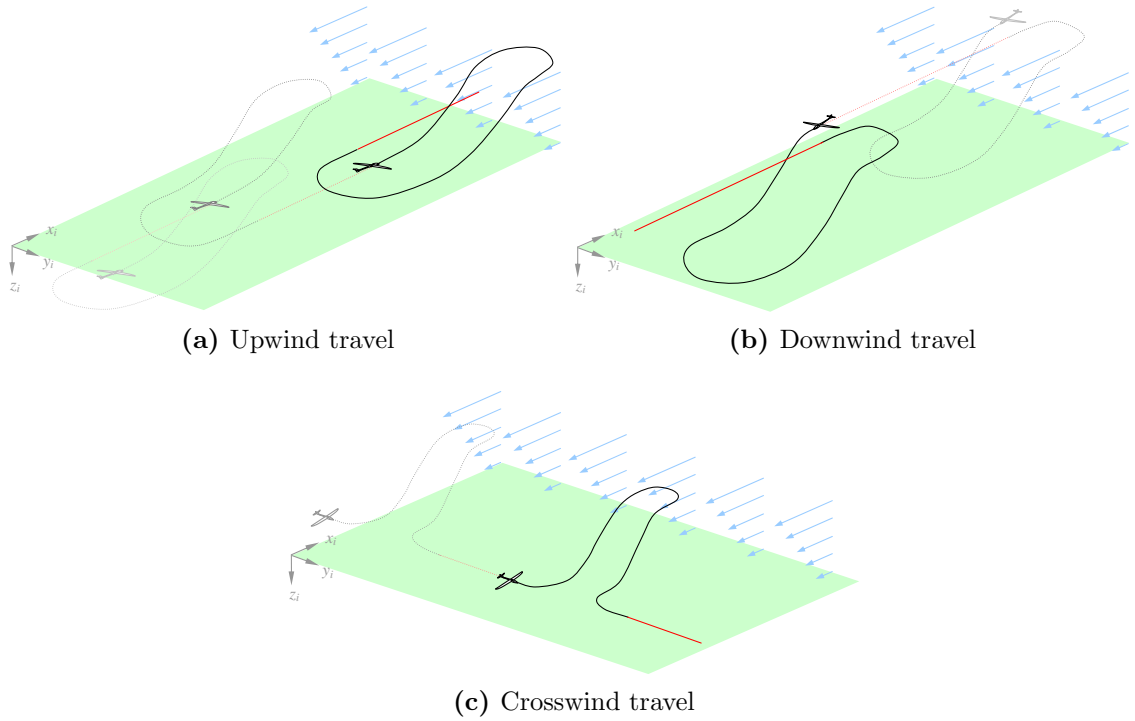


Figure 4.5: Travelling in horizontal shear using Rayleigh dynamic soaring cycles. The Rayleigh cycles are illustrated in black and the travelling sections in red.

conditions. Conversely, upwind travel is the most difficult as it must be performed at the altitude of minimum wind (usually the base of the shear layer) to maximise the energy used to move in inertial space. Also worth considering is that the turn directions are variable since the energy cost is the same but the inertial movement is different. Thus, the turn direction should also be selected depending on the travel direction. Figure 4.5 illustrates travelling flight with Rayleigh dynamic soaring cycles in linear horizontal wind shear.

Starting at the base of a shear layer heading into a (relatively) positive gradient, climb upwards into a headwind gradient, make a constant altitude 180° turn at the top of the gradient, dive downwards through the gradient and make a low altitude turn to head upwind again (illustrated in Fig. 4.4). In a sufficient gradient, energy will be gained during the climb and dive phases and lost during the turns. If excess energy remains at the end of a cycle it can be used to travel or stored (to a limit) as kinetic energy with increasing speed in each cycle.

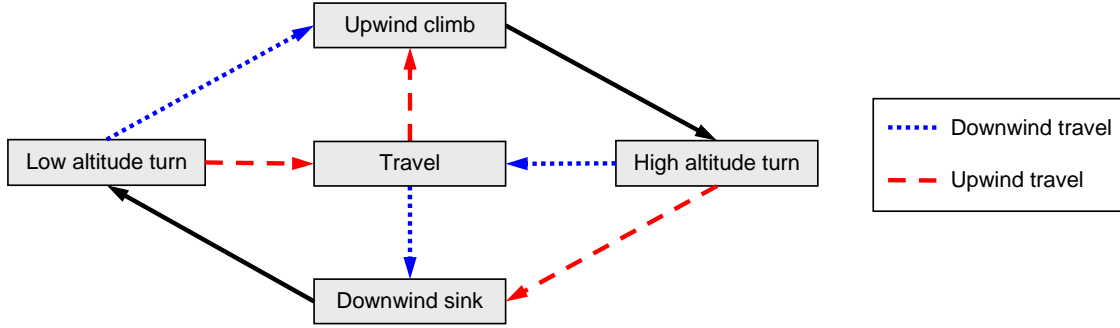


Figure 4.6: Mode switching logic for Rayleigh cycle soaring control. If the travel direction is upwind, the logic follows the dashed and solid arrows (travel at low altitude). If the travel direction is downwind, the logic follows the dotted and solid arrows (travel at high altitude). This assumes a wind gradient where the wind speed is low close to the ground and increases with altitude but remains the same direction.

While previous research has largely focused on off-line optimization, this work aims to examine whether a simple control strategy would be sufficient for dynamic soaring in horizontal shear. The simplest approach is to directly adopt the piecewise trajectory of the Rayleigh cycle and design a controller based on this. The basic piecewise trajectory consists of five flight phases; upwind climb, high altitude turn, downwind sink, low altitude turn and travel.

Designing a control strategy for each phase and cycling through them should allow the aircraft to gain energy in a sufficient wind gradient. The control structure implemented in this work has two layers. The lowest level controllers are the slip, bank and climb angle controllers, actuated by the rudder, ailerons and elevator respectively. These are hand-tuned PID controllers. The heading controller is an additional low-level guidance loop which commands slip and bank angles to achieve steady turns and tracking of a heading angle. The bank angle commands are limited by a load factor specification to prevent excess wing loading during turns.

Above the low-level control is the piecewise trajectory based mode control. There are five control modes corresponding to each trajectory section. Modes are switched when conditions for the current mode are complete. The guidance logic is shown in Fig. 4.6. Each flight section has a goal and termination conditions, at which point the controller moves to the next flight segment.

Upwind climb

The upwind climb is an energy gain section. In this section, the climb angle is commanded by the upwind climb controller based on current airspeed and wind gradient estimates to maximise the energy altitude gradient using interpolation from a table of lookup values generated using Eq. (4.2). The heading is tracked into the wind to maximize airspeed acceleration. The upwind climb is terminated when the maximum altitude is reached. Altitude limits are calculated by determining the minimum wind gradient required for energy-gain flight. Wind gradient is assumed to be known or estimated online as described in the wind estimation section.

High altitude turn

The high altitude turn involves turning downwind whilst minimizing altitude loss. The aircraft should stay above the profile to maximize energy gain in the downwind dive. As shown earlier, power loss is reduced when turning at lower speeds. Thus, in some cases it may be beneficial to climb to a higher altitude and make the turn at a lower speed. The efficacy of this action depends on the speed difference and the drag cost of climbing to slow down. Also worth considering is the extent of the shear layer since most shear layers decrease gradually. An optimal solution could only be found through continuous optimisation so it is difficult to draw general conclusions for the optimum action here. However, in most cases a climbing turn at maximum bank will probably result in near-optimal performance. The high turn is complete when the aircraft is heading downwind at the high extent of the wind shear profile.

Downwind dive

During the dive, the aircraft exchanges altitude for kinetic energy, and additional air-relative kinetic energy is obtained from the reduction in tailwind while diving through the wind profile. Thus the airspeed increases significantly during the downwind dive. As in the climb phase, the dive angle is tracked to the optimum using the climb

angle controller from a lookup table based on a range of aircraft parameters and wind gradients. The heading is commanded in the downwind direction to maximise energy capture from the gradient. The airspeed is usually highest at the terminal state of this mode. The phase is completed when the minimum altitude is reached; either a mission limit minimum or the altitude where the gradient no longer yields additional power.

Low altitude turn

During the low turn the aircraft performs a level turn at low altitude to head upwind. This turn is at high airspeed and consequently usually represents the largest energy loss component of the cycle. Ideally, this turn would be performed at a lower airspeed to minimise energy loss. However, the energy stored as kinetic energy is only available at that altitude, converting the energy into potential energy would require climbing in inertial space. However, climbing would be in an adverse wind gradient and result in the loss of the dynamic energy gained by diving through the gradient. Thus, the turn must be performed at as close to a level altitude as possible with minimum energy loss at the current airspeed. Consequently, this turn usually has a larger radius than the high altitude turn.

During the low altitude turn there is a constant commanded altitude (the lower limit of the shear layer or a minimum safe altitude) and the heading is commanded in the upwind direction or towards the target vector (for crosswind flights).

Travel

The travel component is where the aircraft uses additional energy gained in the cycle to travel towards a specified goal. The travel controller is invoked based on wind direction estimates and a bearing to the target. If the target bearing has a downwind component the travel phase is at high altitude to take advantage of the wind. If the target bearing is upwind the travel phase is at low altitude. Travelling uses all excess energy to travel in the target direction at a fixed altitude.

In the current system, the travel phase is implemented using a target pursuit algorithm where the target point is defined as a point on the target vector. The true path settles asymptotically onto the target vector. The stage is terminated when the current energy is within a small threshold of the energy at the start of the cycle.

4.1.4 Results

Simulated results are presented to demonstrate the validity of the control architecture for soaring in horizontal shear. The results are simulated using a high-fidelity strip-method simulation of the aircraft. The aerodynamic model used in the simulation is described in detail in appendix B.2. Essentially, the strip method divides the aerodynamic components of the aircraft (wings, horizontal and vertical stabilisers) into individual strips which are solved as sections and the resulting forces and moments applied to give the accelerations and rotation rates. The advantage of this type of simulation over coefficient models is the ability to handle variation of wind across the aircraft and even partial wing stall. A further advantage is the direct modelling of control surfaces as surface deflections are modelled as variation of the wing shape with lookup tables generated offline across the range of surface deflections.

However, strip methods usually use relatively simple corrections to account for tip vortices and downwash which can simulate overall dynamics well but do not necessarily provide an accurate model for the actual flow, notably near the wing tips [88]. This can affect the control surface effectiveness but with the very high aspect ratio wings of glider models the effect will be less significant.

Dynamic soaring control in known linear wind gradients

The first set of results show a single dynamic soaring cycle in linear wind shear. The wind is 0 m/s at 100 m altitude and increases linearly to 15 m/s at 115 m altitude such that the wind gradient is 1.0 s^{-1} . The controller has perfect knowledge of the shear layer and so the altitude limits and optimum climb angles are known and fixed

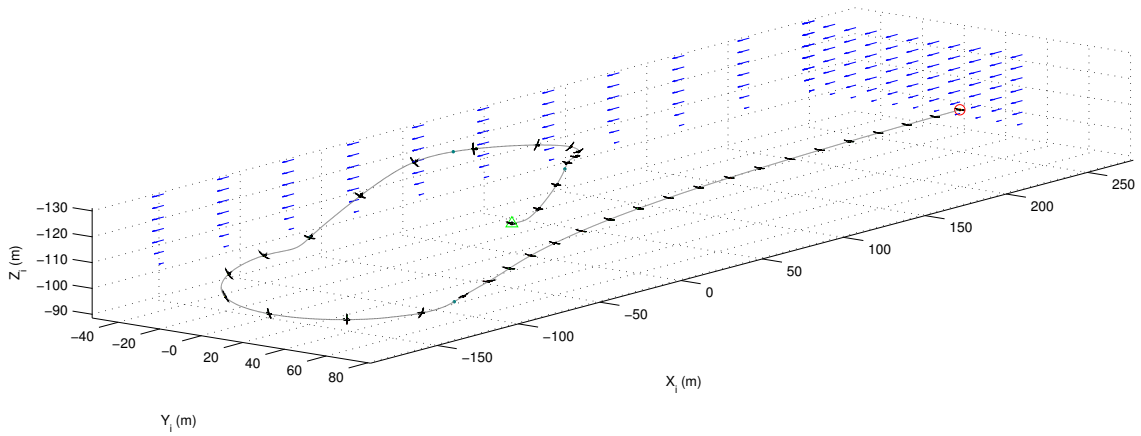


Figure 4.7: Trajectory for single dynamic soaring cycle in linear wind shear. The shear layer is 15 m thick with a gradient of 1 s^{-1} . The aircraft starts at an airspeed of 17.5 m/s. The travel section is not shown.

throughout the flight. The resulting path is shown in Fig. 4.7 and the corresponding energy change in Fig. 4.8.

While the turns are energy loss segments of the flight, the controller should attempt to minimise the energy lost in turns. Each turn requires the aircraft to turn at a near constant altitude and minimise energy lost. As demonstrated in Sec. 3.4.3, the most efficient turn (minimising energy lost over heading change) is to fly at the maximum bank angle defined by the limit load n_{max} . This means that the turn radius increases at high speeds, so the low altitude turn is generally much larger than the high altitude turn. This usually results in a small lateral motion in each cycle which can be offset during the travel phases or used for lateral travel.

The first set of results illustrate the control scheme in a single dynamic soaring cycle in known shear. The aircraft starts heading upwind into the gradient at an airspeed of 15 m/s. While an isolated linear shear layer of this strength is relatively unlikely to occur in a realistic wind environment these results are provided to demonstrate the control scheme.

Figure 4.7 illustrates the path taken during the cycle. Changes in flight phase are illustrated as filled circles. The climb phase uses a lookup table based on airspeed and wind strength to determine a target climb angle. Bank angle has a maximum

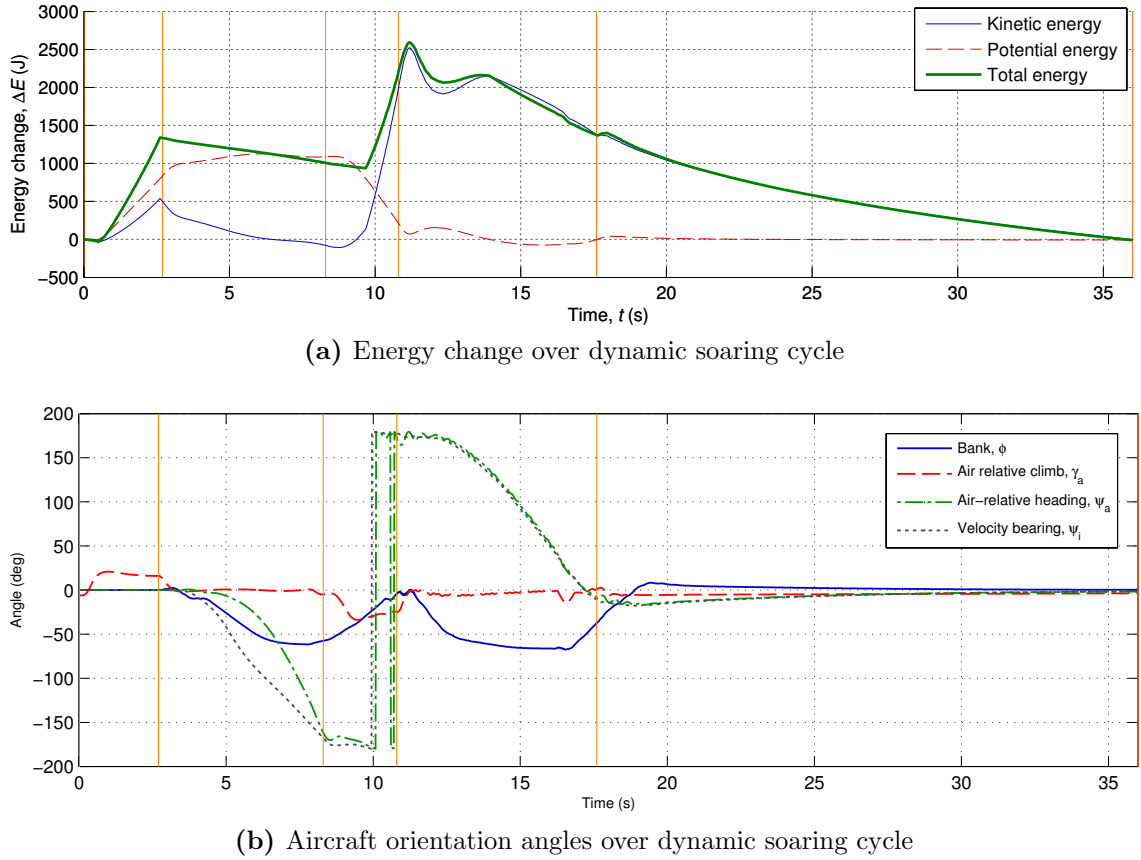


Figure 4.8: Energy and aerodynamic angles for a single dynamic soaring cycle in linear wind shear. The vertical lines indicate the mode time changes in the sequence climb, high altitude turn, dive, low altitude turn, travel. The travel direction is in the positive x -direction (upwind).

commanded value of 60° but this is breached by about 3° during the low altitude turn due to overshoot of the controller. Given that the $n_{max} = 2$ limit is probably a conservative limit the bank overshoot is not particularly significant. Note that the turn radius for the high-altitude turn is smaller than the low altitude turn due to the much lower kinetic energy. The accompanying video *RayleighCycle.mpg* shows the full dynamic soaring cycle.

Also shown for these results are the time history of the energy and body angles for the soaring cycle (Fig. 4.8). The travel segment of the flight is also shown for an upwind travel section. The climb starts at $t = 0$, the high altitude turn at $t = 2.7\text{s}$, the dive at $t = 8.3\text{s}$, the low altitude turn at $t = 10.8\text{s}$ and the travel phase at $t = 17.6\text{s}$.

The cycle finishes when the total energy drops below the starting energy so that the cycles should be repeatable in the same wind conditions. The complete cycle lasts 36.0s and the net upwind travel distance is 272.4m.

Earlier analysis showed that both the rate of energy capture and the total energy capture achievable from a linear shear layer increases with airspeed. However, it was also shown that power loss increases with airspeed during the turn and travel phases. Thus, a reasonable expectation is that an airspeed exists at which total energy gain is maximised. For the current problem the goal is upwind travel progress. Low speed cycles often have high travel distance per cycle since they are undergoing the travel phase at speeds closer to the minimum drag ratio speed. However, the cycle time is correspondingly longer so the net upwind progress may be reduced. Table 4.1 shows the total upwind progress, cycle time and resulting average upwind travel speed for cycles which start and end at 15, 17.5, 20 and 25 m/s respectively. The corresponding trajectories are shown in Fig. 4.9. Note that the 25m/s cycle overshoots the low altitude turn due to poor tuning of the linear controllers. The turn is at a much higher airspeed than would be common for this type of aircraft.

Generally, cycle time decreases with airspeed. However, the upwind travel performance varies across the range of speeds tested with a peak around 20m/s. This is complicated by the fact that controllers are tuned for optimum performance across the speed range of 15-20m/s which would be more common for this aircraft. In a real implementation it is suggested that the target cycle airspeed would be defined by other factors such as safety and control limits. From these simulations it is difficult to draw a solid conclusion about the optimum speed for overall cycle performance, but, in general, increasing airspeed increases cycle performance in strong wind shear.

Table 4.1: Dynamic soaring in linear shear. Cycle times and upwind progression speed.

Initial airspeed	Cycle time	Upwind travel	Mean upwind speed
15.0 m/s	42.3 s	298.6 m	7.06 m/s
17.5 m/s	36.0 s	272.4 m	7.57 m/s
20.0 m/s	33.5 s	283.1 m	8.45 m/s
25.0 m/s	27.4 s	221.1 m	8.07 m/s

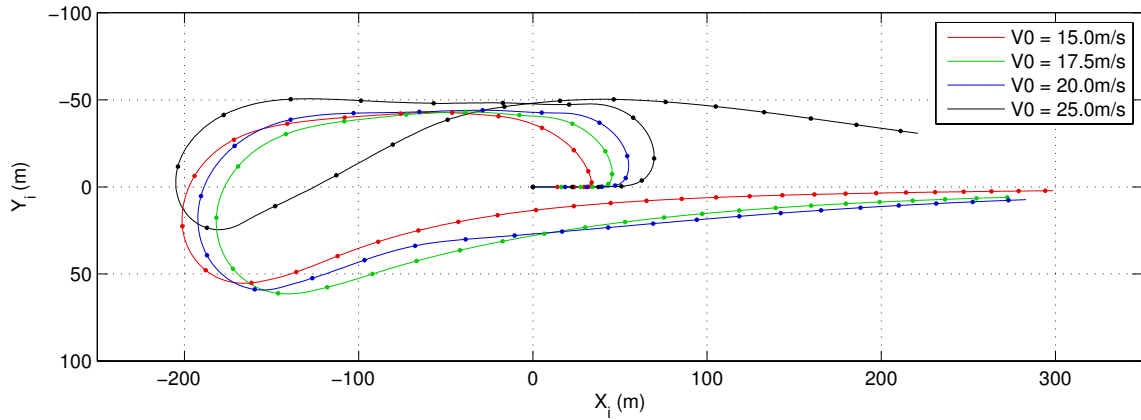


Figure 4.9: Top view of trajectories for single dynamic soaring cycles with upwind travel

Of further interest is the energy transfer that occurs during the cycles. Figure 4.10 shows the ideal energy transfer for a cycle in linear shear. Note that lines of constant energy run diagonally parallel to $x = -y$. Therefore, the climb and dive phases both result in energy gain while the turn and travel phases result in energy loss. The climb phase should ideally increase both air-relative kinetic and potential energy simultaneously. The high altitude turn should be at a fixed altitude and result in a loss of kinetic energy only. The dive should significantly increase kinetic energy and lose potential energy. The large increase in air-relative kinetic energy is due to the energy transferred from altitude into airspeed as well as the increase due to the wind gradient. The low altitude turn should be at almost constant altitude. If there is more kinetic energy at this stage (further to the right on the plot) than at the start of the cycle, then it is a net energy gain cycle and the additional energy can be used for travel or the following cycle can be at increased airspeed. For an upwind travel phase there should be consistently decreasing kinetic energy loss at constant altitude until the energy matches the initial energy. A closed cycle (which ends with the same energy as it started) is repeatable in the same wind conditions.

Figure 4.11 shows the energy transfer for the four simulated cycles. Each cycle is closed by a travel phase which attempts to travel directly upwind at constant altitude such that it ends with the same energy as it started. Also note that the cycles are offset to show the energy change during the cycle; the higher energy cycles actually

start with more total energy than the lower speed cycles. Note that higher speed cycles gain energy faster in the climb and dive but lose more energy during the turns.

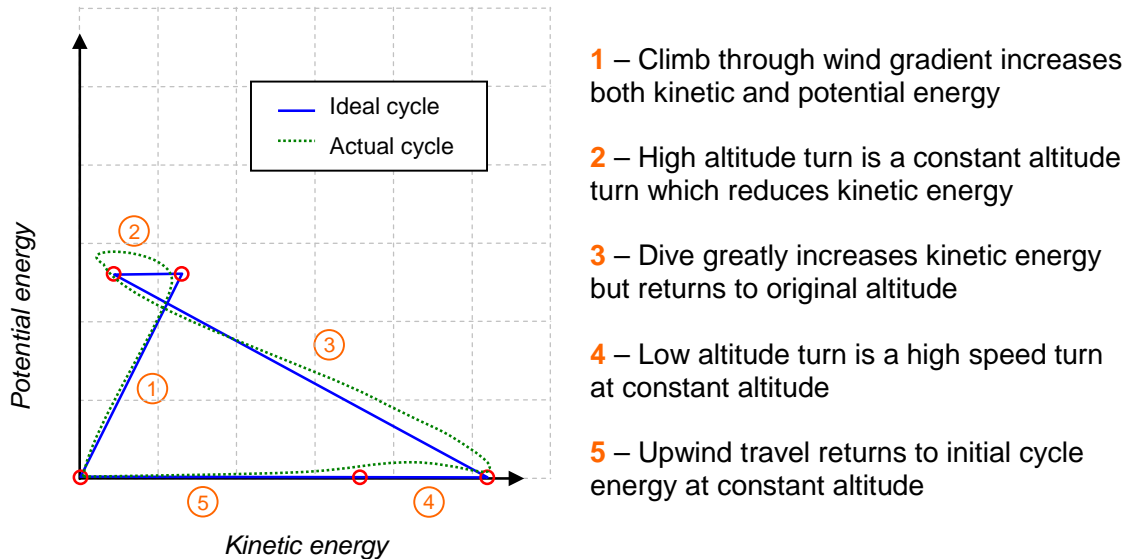


Figure 4.10: Diagram of ideal energy transfer during a Rayleigh dynamic soaring cycle.

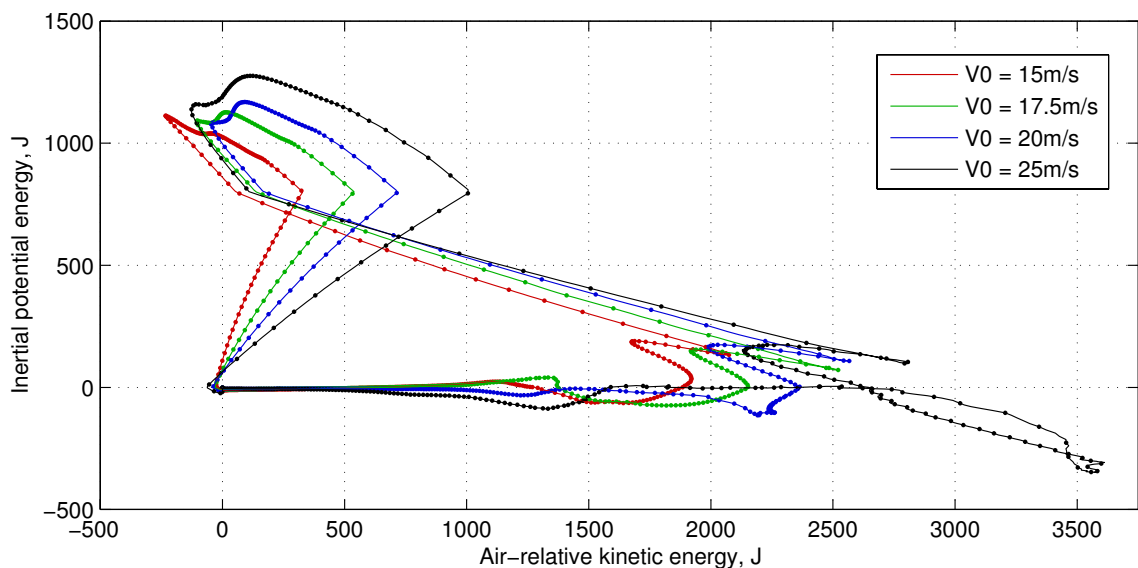


Figure 4.11: Energy variation during simulated dynamic soaring cycles. The dots are spaced 0.1s apart to show the rate of energy variation during the cycles. Energy is shown relative to the starting condition and the wind conditions are the same for all cycles.

Dynamic soaring control in an unknown wind gradient

While the linear profile results show that the controller is capable of collecting energy from a sufficient wind gradient this is not a particularly realistic scenario as isolated linear shear is uncommon in natural wind fields. Most birds use the planetary boundary layer wind shear for dynamic soaring flight. This shear is produced close to the ground and usually has a smoother profile. The goal of this section is to determine how sensitive the controller is to variation in the profile and whether a simple wind estimation to determine altitude limits is sufficient to plan energy-gain paths. Note that this still assumes the aircraft is in an area where wind shear is expected but the exact profile is unknown.

In this analysis the Pohlhausen's quartic wind profile is used, a common profile for turbulent boundary layers which is continuous and differentiable over a shear layer extent [41]. The layer shape is defined by a thickness δ , mean wind u_{max} (which is constant above the shear layer) and a shape parameter λ which is usually set to 1. The wind speed u as a function of the height above the shear layer base z is shown in Eq. (4.3). The distribution of wind speed with altitude is shown in Fig. 4.12.

$$u = u_{max} \left(2\eta - 2\eta^3 + \eta^4 + \frac{\lambda(1-\eta)^3}{6\eta} \right), \quad \text{where} \quad (4.3)$$

$$\eta = \frac{z}{\delta}.$$

It does not seem feasible to assume that a UAV would have full knowledge of the surrounding wind field. It may be feasible to expect a wind gradient given certain geographical and meteorological conditions, but given that the wind speed and direction can change and are difficult to predict, it would be unreasonable to expect an aircraft to be able to predict the wind field *a-priori*. Thus, some estimation of wind may be required on-line. Given the limited payload of a small UAV any wind estimation should rely on simple sensor data. The simplest method to estimate wind is to compare the aircraft airspeed (from pitot static data) with an inertial speed estimated from GPS and/or INS readings. Angle of attack and sideslip wind vanes

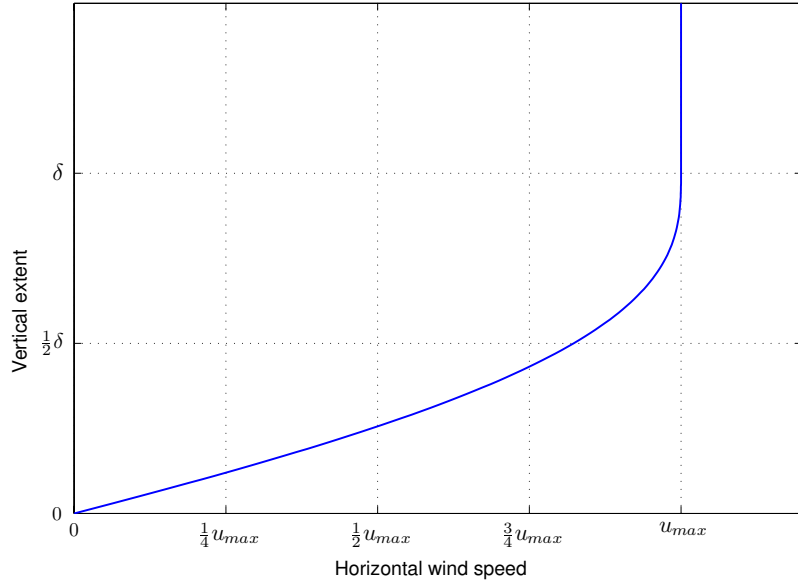


Figure 4.12: Pohlhausen's quartic boundary layer profile. Shape parameter $\lambda = 1$.

are simulated from the true angle data and injected with artificial noise to simulate wind direction sensors. Similarly, the true airspeed is injected with artificial noise to simulate pitot-static airspeed measurements. This is converted to earth frame wind using body orientation estimates. Wind measurements are performed at 10Hz in the following simulations. Up to 100 wind estimates are stored. Old data is replaced with new data based on a fitness measurement which estimates the value of new data as it is recorded.

The critical parameters which need to be estimated are the wind bearing and the variation of wind speed with altitude. Vertical components of wind are ignored. Wind bearing is estimated using a simple mean of all recorded data, with newer readings weighted higher than older readings. Wind bearing is assumed to be constant everywhere, due to prevailing wind conditions. Since wind is largely driven by pressure gradients this is a reasonable assumption over large surfaces with few obstacles (such as the ocean) [95]. A variety of regression methods from the sampled data could be used to estimate the wind profile. In this case, Gaussian Process (GP) regression with a squared exponential kernel is used, though least square regression would perform equally well. A data driven approach is suggested here rather than parametric

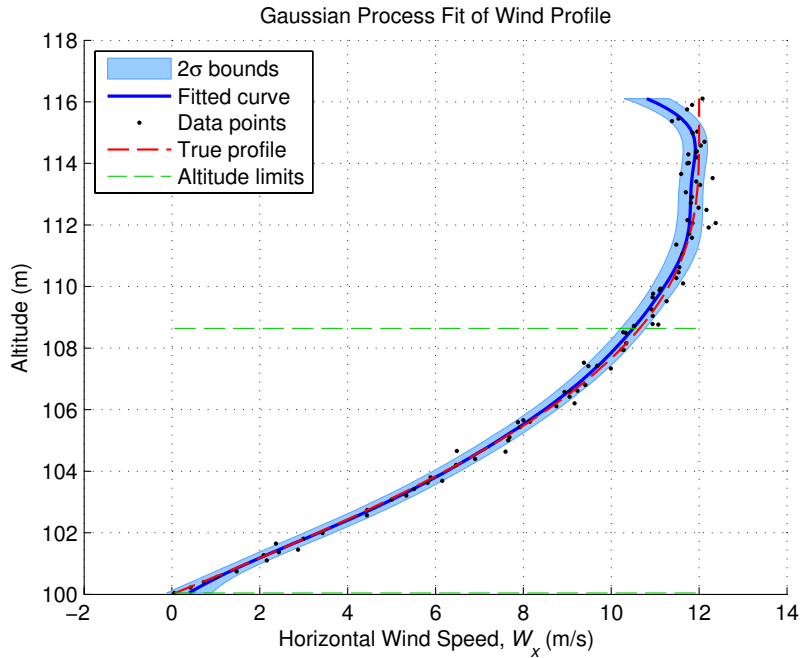


Figure 4.13: Pohlhausen’s quartic boundary layer estimation using Gaussian Processes

estimation of known equations to allow mapping of a variety of wind profiles. Further information on GP regression can be found in Chapter 5. The soaring altitude limits are determined by comparing the gradient of the regressed wind profile with the minimum required soaring gradient. Feasible soaring regions are defined by minimum and maximum altitude limits which are used by the soaring controller. Figure 4.13 shows a typical estimation performed during flight for the Pohlhausen’s quartic wind profile.

Simulated flights through a Pohlhausen’s quartic profile with upwind travel are provided in Fig. 4.14. The profile has thickness $\delta = 15$ m, maximum wind speed $u_{max} = 12$ m/s and shape parameter $\lambda = 1$. The vehicle begins the flight at an airspeed of 17.5 m/s heading into the wind. The first action is a climb to collect data and determine if there is a sufficient gradient for soaring flight. Once a gradient is found the controller uses the same architecture as for the previous results but the altitude limits are determined dynamically from regression of the wind data. The results show that the first cycle is larger and deviates further from the target vector

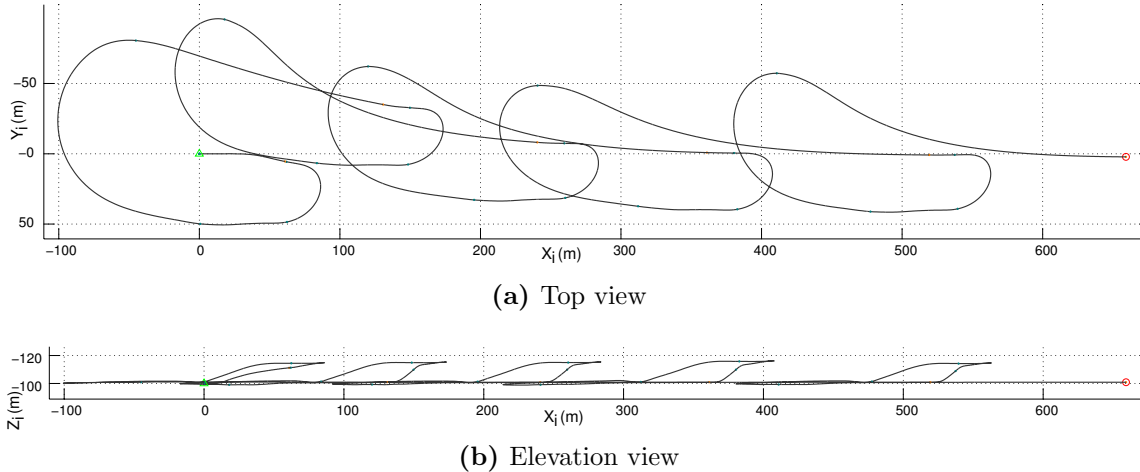


Figure 4.14: Dynamic soaring in an (initially) unknown Pohlhausen’s quartic profile with upwind travel. The blue dots indicate mode change times and the orange dots indicate cycle changes.

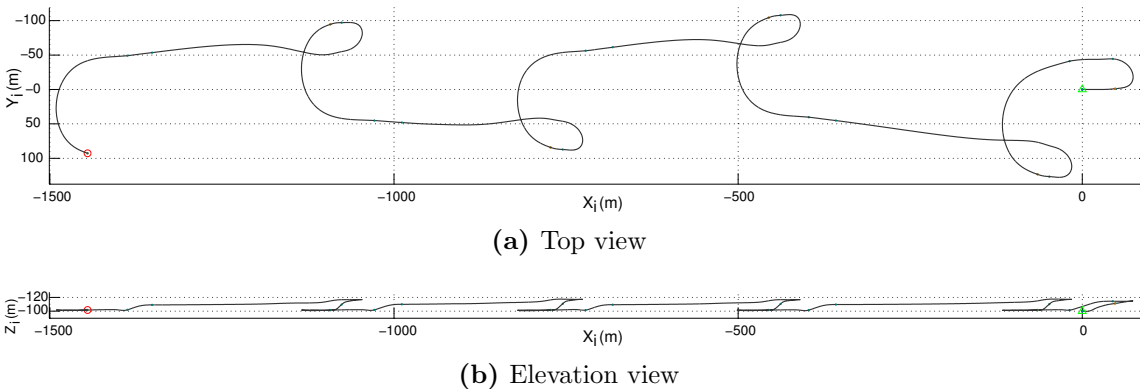


Figure 4.15: Dynamic soaring in an (initially) unknown Pohlhausen’s quartic profile with downwind travel. The blue dots indicate mode change times and the orange dots indicate cycle changes.

(upwind). Once the altitude limits settle to nearly constant values the later cycles are more similar. Consistent upwind progress is demonstrated with an average upwind speed of 5.09 m/s. This is considerably reduced from the linear case which had a stronger, consistent gradient.

Similar results can be demonstrated for downwind flight. In the downwind case, the travel is completed at high altitude to take advantage of the additional wind speed. Figure 4.15 shows the same wind scenario for downwind commanded travel.

These results demonstrate that a customised soaring controller can generate soaring trajectories with very limited wind estimation. However, this system is specific to one type of wind and one type of soaring control. It can only soar in horizontal wind shear and must start in a favourable location for soaring.

However, this type of control is sensitive to variations of the wind field. In particular, there may be practical limits that prevent the controller from using the entire wind shear. As noted earlier, horizontal wind shear primarily forms in layers over fixed surfaces (such as the ground). Also noted earlier was the fact that, in general, collected power is proportional to the magnitude of the wind gradient. Due to the nature of viscosity in shear layers the most rapid spatial change in wind speed (the maximum wind gradient) occurs closest to the surface and decreases with altitude (see Fig. 4.13). For safety reasons it is common to specify a minimum flight altitude for an aircraft. Thus, increasing the minimum flight altitude can significantly decrease performance during dynamic soaring in shear.

To examine these effects a number of simulations were performed with increasing minimum flight altitude. The wind, starting conditions and controller are the same in each simulation, but with a specified minimum altitude. All simulations use the Pohlhausen's quartic profile starting at altitude 100 m with total depth 15 m and maximum wind speed 12 m/s. In all cases the aircraft begins the simulation at 100 m altitude with airspeed 20 m/s (note that this is below the minimum altitude threshold for most of the simulations but is retained to provide some consistency of starting conditions across the simulations). The goal is to maximise upwind travel. Three simulations are performed with minimum altitudes of 100, 101, 102 and 103 metres each. The average results for mean upwind travel are shown in Table 4.2 and sample paths are shown in Fig. 4.16. The mean wind gradient is the mean gradient over the usable shear layer (from the minimum altitude to the top of the layer at 115 m altitude). *Note that the 103 m solution fails with insufficient energy after two full cycles, the mean upwind speed result is averaged over two cycles.

Clearly the minimum altitude limit has a significant effect on the upwind travel performance. Note that there are two effects at play in these simulations. Firstly,

Table 4.2: Dynamic soaring with minimum altitude limits.

Min. altitude	Min. wind speed	Mean gradient	Mean upwind speed
100 m	0.00 m/s	0.800 s ⁻¹	5.90 m/s
101 m	1.59 m/s	0.743 s ⁻¹	5.38 m/s
102 m	3.15 m/s	0.681 s ⁻¹	-1.96 m/s
103 m	4.63 m/s	0.614 s ⁻¹	-3.54* m/s

reducing the minimum altitude reduces the energy available for capture from the wind gradient. This effect is significant because, as demonstrated in §3.3, the power is proportional to the magnitude of the wind gradient. Thus, the integral of the gradient gives a measure of the total energy available from a wind gradient, such that the total energy is proportional to the total wind magnitude change between the two altitudes. For most shear layers the gradient is maximum near the surface (as in the sample Pohlhausen's profile), so that increasing the minimum altitude quickly reduces the total energy available in the wind gradient. From Table 4.2 a minimum altitude of 101, 102 and 103 m corresponds to a total energy reduction of 14.2%, 27.7% and 40.3% respectively from the full thickness. This is an important point, as the shape of the layer is in some cases not particularly important but rather determining the altitude limits which maximise the mean gradient and total energy. However, this is overly simplified as the energy lost in during the turns and travel phases depends on many factors including the aircraft and control parameters. Thus it is difficult to determine an analytic solution for the minimum required wind gradient. The qualitative results shown here illustrate the relative effect of reducing the available wind gradient.

The second effect is the downwind motion due to the wind at the low turn altitude. While this does not reduce the total energy captured, it can result in considerable downwind travel since the low altitude turn takes up a relatively high proportion of the cycle. The combination of these two effects can dramatically decrease upwind progression.

As shown in the results, relatively small increases in minimum altitude can significantly decrease upwind progression. With a minimum altitude of 102 m the aircraft can no longer make upwind progress. At 103 m continuous flight is not possible,

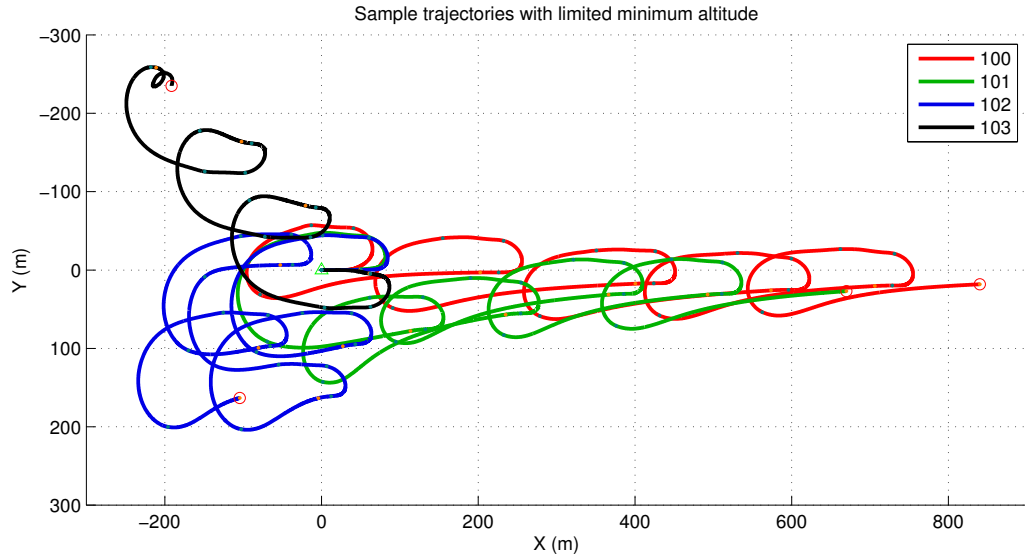


Figure 4.16: Effect of minimum flight altitude on upwind soaring.

and the controller fails with insufficient energy after three cycles. This is important for dynamic soaring in shear as shear layers usually occur over a fixed surface which represents a flight hazard. These results show that this control scheme is sensitive to limitations on the energy available for capture.

4.2 Soaring Control in Known Wind Fields

Ideally, a soaring control should be able to use many types of energy source. This could be possible by identifying types of wind flow in flight and then selecting between predefined guidance controllers defined for each energy source. However, this approach offers limited flexibility as it would need to have guidance routines for all types of encountered wind. Chapter 3 showed that static and dynamic energy are simply terms in the aircraft dynamic energy equation. Thus a controller which utilises the energy equation directly should be able to plan energy gain paths that utilise all sources of energy by only working from the total energy gain. Such an approach would offer improved flexibility and allow use of all encountered energy sources.

Static soaring can be relatively well solved with a locally greedy approach (remain flying in rising air for as long as possible while minimising drag loss). However, dynamic soaring cycles are generally more complicated. Dynamic soaring cannot be performed by a local greedy method since within a dynamic soaring cycle there are usually segments that result in local energy loss. An effective path planner would need a sufficient planning horizon to develop plans which could utilise both static and dynamic soaring.

Ideally a planner should meet the following criteria:

1. **Be capable of generating energy-gain paths utilising static and dynamic soaring.** As shown previously, by attempting to maximise the energy component directly, a planner should be able to use static and dynamic soaring to maximise energy gain.
2. **Produce achievable flight paths given vehicle constraints.** Flight vehicles are dynamic systems and have constraints on their motion. A path planner should be able to account for this and generate achievable paths.
3. **Use limited wind field information available from direct observations.** Wind fields are often unpredictable, and even static fields are usually overlaid with a random gust pattern. Given that it may prove difficult to characterise a

field with only direct observations a path planner should be able to plan energy gain paths based on recent, local knowledge.

4. **Be simple enough to run on-board a UAV.** Most small UAVs have limited computational resources and a practical planner would have to account for this.

4.2.1 Path planning in known wind fields

In Chapter 3 a set of equations were developed which approximate the response of a fixed-wing vehicle in wind. Numerically integrating these equations from a known starting position with a set of control functions produces an estimated path of the vehicle. Varying the input control functions produces alternative paths. A simple and computationally efficient method to generate paths is to define a set of control input functions and forward simulate over the set to estimate the resulting paths. This expanding tree structure is similar to a state lattice [62], but based on control inputs for a fixed time horizon rather than target positions (which may be unreachable).

Segments are ranked using a heuristic energy-based reward function. The best performing branches are propagated with a new set of control inputs, and the resulting path segments are again ranked using the same reward function. This process repeats for a pre-defined tree depth as illustrated in Fig. 4.17. While this method is sub-optimal, it generates achievable paths and allows exploration of the field within reachable states.

Of particular importance is the selection of the reward or cost function. An energy-based reward function is proposed to attempt to maximise the estimated total energy gained from the planned path. The simplest reward function is a greedy energy function. This evaluates the energy difference between the start (subscript 0) and end (subscript 1) of a path segment, R_E , where

$$R_E = -mg(z_{i,1} - z_{i,0}) + \frac{1}{2}m(V_{a,1}^2 - V_{a,0}^2). \quad (4.4)$$

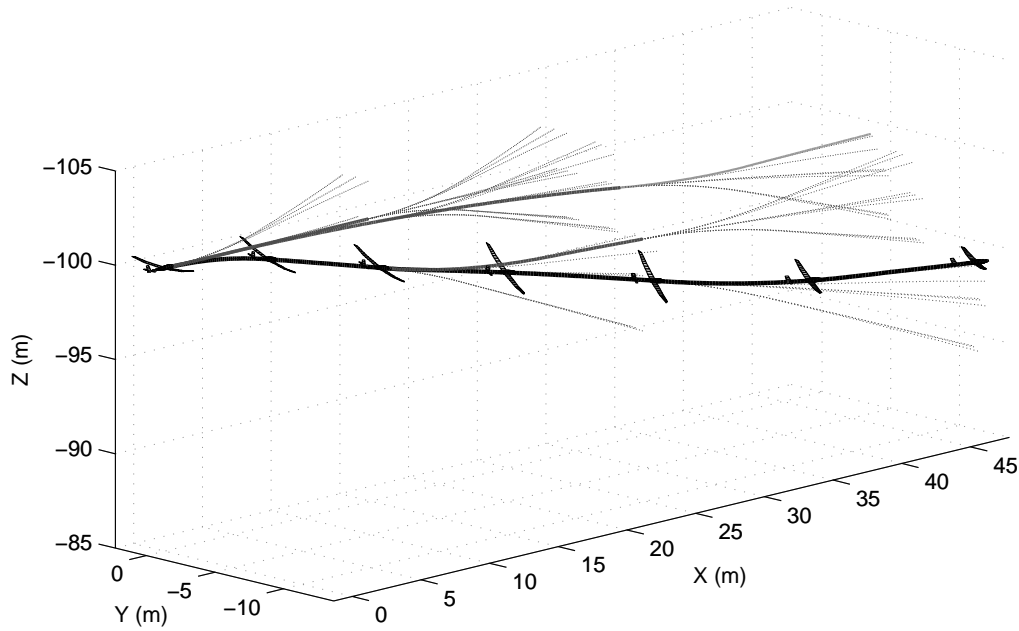
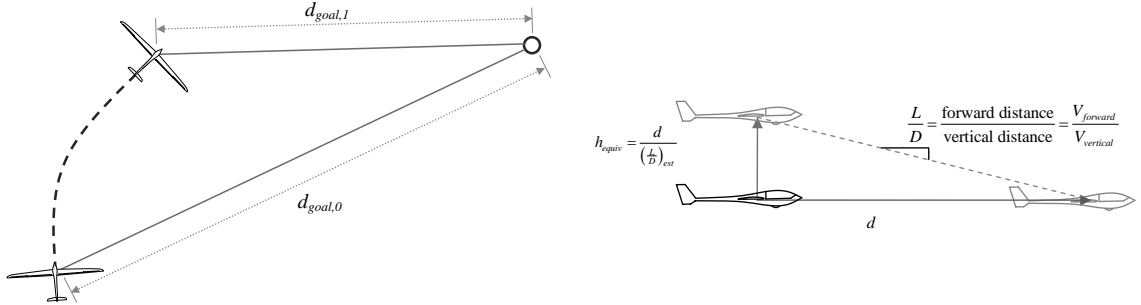


Figure 4.17: Path planning tree for gliding flight

This type of approach maximises the energy gained in each segment but ignores the conditions at the end of the segment which may result in greater future gains. For example, one path selection may maximise energy collected by flying through the core of a thermal but terminate the path in sinking air. This maximises local gain but at the cost of future power.

Considering this, a second fitness function was tested which takes into account the power at the endpoint of the segment based on the wind estimate. Equation (3.76) gives the power at a particular point given the wind estimate at that point. This can be used to estimate the potential energy gain of the next segment. The second fitness function tested incorporates this information with the overall energy gains in that segment. The energy potential is estimated by multiplying the power at the final state by the time step (Δt) with a weighting of $K_{\dot{E}}$. This rewards segments which result in high energy gain and terminate in high power regions. This is referred to as the power reward function R_P , where

$$R_P = -mg(z_{i,1} - z_{i,0}) + \frac{1}{2}m(V_{a,1}^2 - V_{a,0}^2) + K_{\dot{E}}\dot{E}_1\Delta t. \quad (4.5)$$



(a) The distance travelled towards the goal is the difference between the distance to the goal at the beginning and end of the segment ($d_{goal,0} - d_{goal,1}$).

(b) The equivalent altitude h_{equiv} represents the altitude that would be required to travel horizontal distance d at glide ratio $(\frac{L}{D})_{est}$.

Figure 4.18: Estimation of the navigation reward function in terms of the equivalent energy of travel towards the goal

Most practical UAV missions would have goals other than pure energy gain. A simple example is navigating to a goal point. If the vehicle has enough energy to reach the goal it should travel directly there. If not, it should attempt to capture enough energy to make it to the goal. To do this, a navigation reward R_{nav} is defined based on distance travelled towards the mission goal.

To be compatible with the previously defined energy rewards, the navigation reward must also be expressed in terms of energy. The distance travelled towards the goal d is the difference between the distance to the goal at the start and end of the flight segment ($d_{goal,0} - d_{goal,1}$), as shown in Fig. 4.18a. This can be converted to an energy by estimating the amount of energy that would be required to travel that distance towards the goal.

The approximate lift-to-drag ratio $(\frac{L}{D})_{est}$ provides the ratio of vertical to lateral distance travelled at nominal conditions. Given the distance travelled towards the goal d , the equivalent altitude h_{equiv} can be calculated which represents the altitude that would be required to travel horizontal distance d at glide ratio $(\frac{L}{D})_{est}$;

$$h_{equiv} = \frac{d}{(\frac{L}{D})_{est}}, \quad (4.6)$$

as shown in Fig. 4.18b. Note that the glide ratio varies with airspeed, but an average

fixed value is used for a stable approximation. Since a gain in altitude is effectively an increase in gravitational potential energy, multiplying the equivalent altitude by the vehicle mass and the acceleration due to gravity yields the equivalent energy of travelling distance d towards the goal at the nominal glide ratio. This is defined as the navigation reward,

$$R_{nav} = mg \frac{d_{goal,0} - d_{goal,1}}{\left(\frac{L}{D}\right)_{est}}. \quad (4.7)$$

However, it is only worth travelling towards the goal if there is enough energy to reach the goal or if there is no energy available. The energy required to reach the goal can be estimated in the same way as the navigation reward function; the energy required to travel the distance to the goal at the nominal glide ratio.

A proposed method of combining the two reward functions is to use a switch mechanism which selects a reward function favouring the energy reward if the aircraft has insufficient energy to reach the goal and favouring the navigation reward if the aircraft has sufficient energy. Let $E_{current}$ be the current platform energy and E_{goal} be the energy required at the goal location. Then,

$$R = \begin{cases} (1 - K_{nav}) R_P + K_{nav} R_{nav} & \text{if } E_{current} > E_{goal} + mg|\vec{b}|/\left(\frac{L}{D}\right)_{est}, \\ K_{nav} R_P + (1 - K_{nav}) R_{nav} & \text{if } E_{current} \leq E_{goal} + mg|\vec{b}|/\left(\frac{L}{D}\right)_{est}. \end{cases} \quad (4.8)$$

Note that for a $K_{nav} < 1$ there are energy and navigation components in both cases. This favours progress towards the goal when there is no energy available and utilises energy efficient paths when navigating to the goal.

4.2.2 Results

The first set of results shows the ability of the path planner to generate energy-gain paths with full field knowledge. In this case, the planner has access to the real wind field at every iteration. The results are presented to compare the greedy final energy reward function, R_E , against the power reward function, R_P .

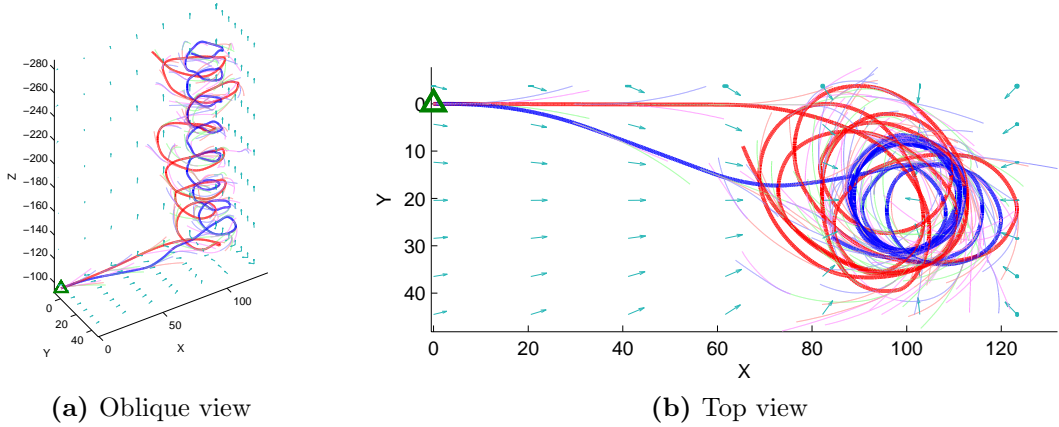


Figure 4.19: Path planning through a toroidal thermal with full wind field knowledge. The thermal is centred at (100, 20, -200). The solid red line indicates the path generated using the greedy R_E reward function. The blue solid line is the path generated using the R_P reward function. Light coloured paths indicate alternative branches generated during planning and the wind field is shown by blue arrows.

Results are presented for flights through a thermal and a vertical wind gradient. The thermal results presented in Fig. 4.19 show the typical pattern of circling near the core of a thermal. The videos *thermal_Rgreedy.wmv* and *thermal_Rpower.wmv* animate the flight path selection for the pure energy and power rewards functions respectively. In the 80 second simulation, the greedy reward function results in 9045 J of energy gain, and the power function results in 9275 J of energy gain. This is a good result given that the controller has no information about the structure of the thermal. Both reward functions produce acceptable results, though the power reward function has slightly better performance and produces a neater spiral path. The greedy energy reward function tends to move further from the core to obtain more energy in single sections, whereas the power reward places additional value on the power at the end of the segment, which means it tends to stay nearer the core.

Results for full field knowledge in horizontal shear are presented in Fig. 4.20 and videos *shear_Rgreedy.wmv* and *shear_Rpower.wmv*. Again, the controller is capable of generating an energy gain trajectory with both reward functions. At the end of the simulation, the greedy reward function version gained 1292 J and the power reward function gained 1649 J. In this case, the power reward is much more effective than

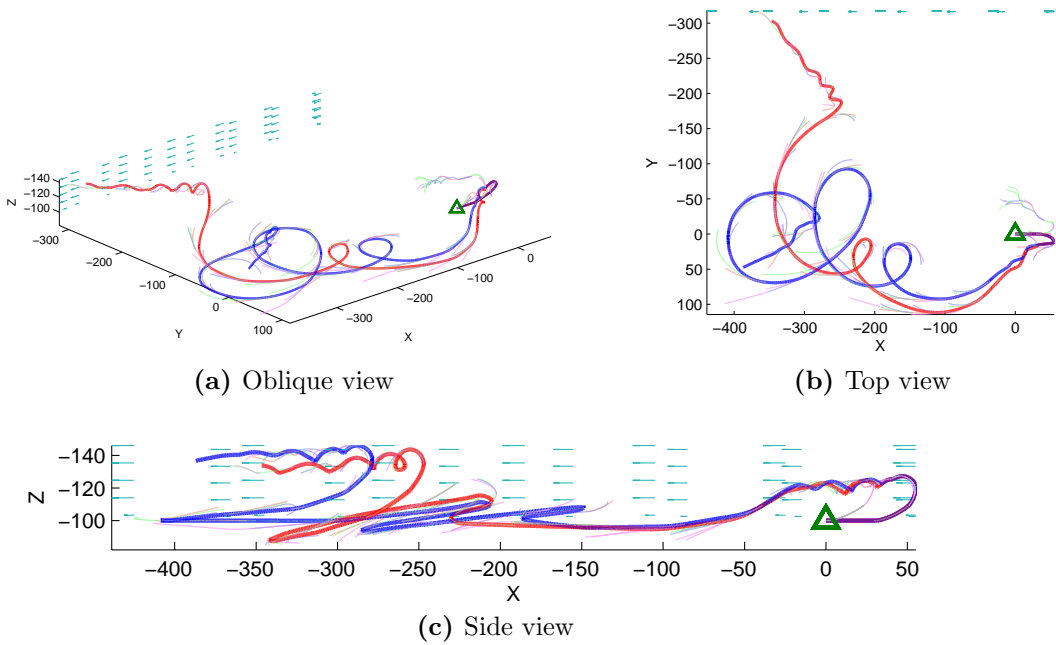


Figure 4.20: Path planning through horizontal wind shear with full wind field knowledge. The shear layer base is at 100 m altitude and is 15 m thick. The solid red line indicates the path generated using the greedy R_E reward function. The blue solid line is the path generated using the R_P reward function. Light coloured paths indicate alternative branches generated during planning and the wind field is shown by blue arrows.

the greedy reward function. The greedy function makes a tight loop across the shear layer, but extends well above and below the shear altitudes. After the second loop it climbs above and out of the profile. Once it is above the profile, the minimum power loss is yielded by slowing to the minimum sink speed, which means climbing higher. The aircraft continues to climb until it reaches the minimum sink speed, then cruises at minimum sink until it enters the profile again much later in the flight (not shown). The power reward begins circling earlier and completes three full cycles before climbing out of the profile, which results in higher energy gain than the greedy version. Also worth noticing is that the power reward result stays much closer to the altitude limits of the profile; not climbing as high or descending as low as the greedy function.

In both flight cases both reward functions are capable of generating energy gain trajectories. The power reward function shows improved performance over the greedy

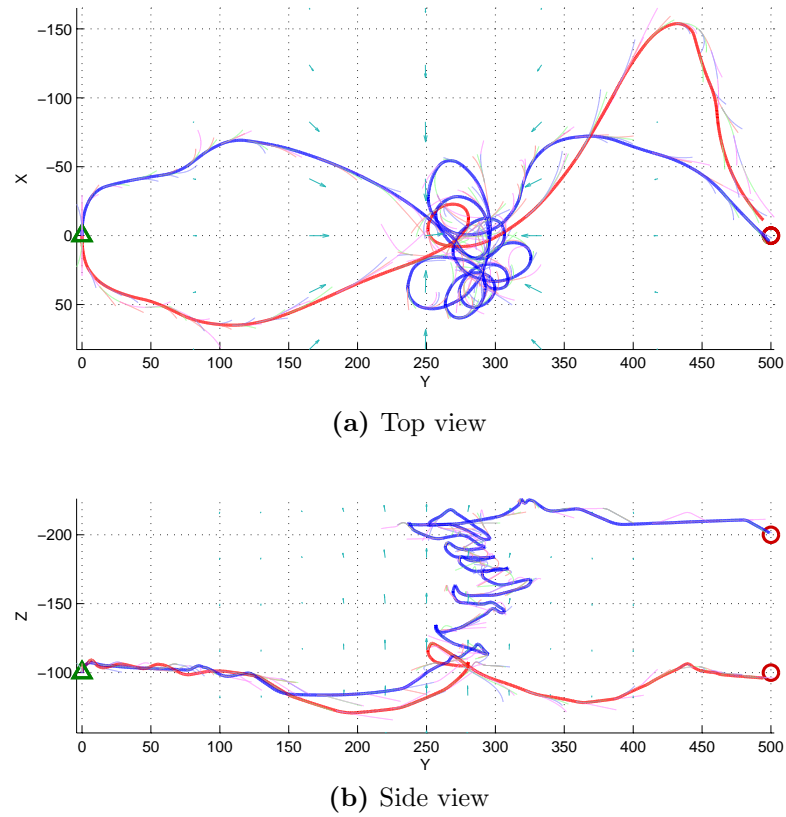


Figure 4.21: Path planning to a goal through a thermal with full wind field knowledge. There is one thermal centred at $(0, 250, -150)$. Aircraft starts at $(0, 0, -100)$ indicated by the green triangle. The red path shows the planned path for a goal at $(0, 500, -100)$. The blue path shows the planned path for a goal at $(0, 500, -200)$. The aircraft start heading is reversed in the second case for path clarity.

energy reward function. This suggests that the use of an energy-based reward function is plausible and could potentially be used to generate energy-gain paths for both static and dynamic soaring.

The final set of full-field knowledge results are shown in Fig. 4.21 and the videos *same_level_target.wmv* and *climb_to_target.wmv*. In these results the path planner uses the power reward function R_P but also considers a goal location using the navigation reward functions described in Eq. (4.7) & (4.8). Two simulations are presented. In both cases, the aircraft starts at an altitude of 100 m (co-ordinate $(0, 0, -100)$) and is attempting to reach a goal located 500 m away along the y axis. There is a single

thermal bubble centred at (0, 250, -150) with a core vertical wind speed of 3 m/s. In the first case, the goal is at the same altitude as the starting position, so the aircraft should end the path with the same energy as it began (red path, starting heading along the positive x -axis). In the second simulation (blue path, starting heading along the negative x -axis), the goal altitude is 100 m higher than the starting position, so the aircraft needs to gain enough energy from the thermal to reach the higher energy state of the goal. In both cases the aircraft uses energy available in the thermal to reach the goal. These results demonstrate the ability of the navigation reward function to reach a goal energy state and spatial location. In both cases, the controller is attempting to gain sufficient energy during the first part of the flight to reach the goal. This is demonstrated by the circling behaviour inside the thermal. Once sufficient energy is obtained the controller switches to favour navigation rewards and travels towards the goal.

While the goal position is reached in both cases, the results also demonstrate some of the shortcomings of the planning method. The red path shows poor navigation towards the goal, with a large detour which results in insufficient energy to reach the goal altitude (path terminates 3.9 m below the goal). This is due to the high speed exit from the thermal. After one circle inside the thermal, the controller estimates that it has enough energy to reach the goal, so it switches to navigation. However, at this point it is travelling at high speed and heading away from the goal. Though it favours the navigation reward, there is still some weight on the energy reward which means that the aircraft does not pull-up or turn rapidly due the high estimated energy loss from such manoeuvres. As it loses airspeed, the energy cost reduces and the planner turns towards the goal. However, by this time the large excursion has cost more energy than was estimated, and the planner cannot reach the goal energy state. The total energy loss is 460 J.

The blue path shows improved performance. It circles inside the thermal gaining energy until the goal energy state is met and the planner can switch to navigation. In this case, the exit from the thermal is at a lower speed, and the aircraft turns faster toward the goal. It reaches the goal with a small amount of excess energy in the form

of airspeed. The total energy gain is 5632 J, 295 J higher than the goal energy.

These results demonstrate that an energy based planner should be capable of utilising both static and dynamic soaring. By including a navigation reward the planner is able to collect energy and travel to a goal location. However, the planner relies on an accurate wind map. In the simulations presented here, the planner had direct access to the wind and hence could make perfect predictions about the energy cost of each action.

4.3 Summary

Analysis of the mechanisms of gliding flight in wind allowed identification of the conditions required for energy-gain soaring. By identifying and taking appropriate actions an autonomous aircraft should be capable of soaring flight. This chapter demonstrated two alternative methods for controlling a gliding aircraft to soar in known wind fields.

The first controller showed that a relatively simple mode-based controller should be capable of collecting energy from horizontal wind shear with a small UAV. Given relatively little information, such as the shear layer altitude limits, the controller was demonstrated to be capable of using a typical PBL shear layer to generate sufficient energy for upwind travel.

The second controller presents a more flexible approach to planning gliding paths. Previous controllers have largely focused on exploiting known wind features with pre-defined soaring strategies. The planner proposed in this thesis uses the energy equations directly to determine which actions maximise total energy benefit, from any source. This framework permits more flexible planning in known wind. Results demonstrate the ability of the planner to generate energy gain paths utilising both static and dynamic soaring.

Chapter 5

Mapping a Wind Field from Direct Observations

One of the major difficulties for a soaring unmanned aerial vehicle is the requirement to measure and estimate the wind. Wind fields on Earth are often highly dynamic and vary over a wide range of spatial and temporal scales. The motion of air in a natural environment is driven by many factors, and modelling all factors to make long-term future predictions on the small scale is almost impossible. Finally, air is transparent to most sensors so remote observation of air motion is difficult. This makes estimation of wind fields a complicated problem.

Birds have good natural wind estimation and fuse information from many sources. Birds can sense temperature and turbulence through their feathers and skin. They also use vision to provide ground-relative position estimation. Finally, birds have proprioceptive information; that is, they have good knowledge of their own flight models and can predict what events should occur under their own actions and consequently infer externally driven events such as changes in flight motion due to wind. Combining these information sources with long-term learning and training through imitation of expert flyers allows some birds to be very proficient at soaring flight.

A small UAV would not typically have access to the same level of sensing available to a bird. Generally, a UAV would only be able to make direct *in-situ* measurements

of the wind, which are only valid at the time and place the measurement was taken. Due to the low viscosity of air, wind speeds can change rapidly over low distances and time scales. However, the wind at small scales tends to be mostly driven by conditions such as mean wind flow and altitude as well as time of day and seasonal conditions. Thus, some wind modelling is possible. These factors have driven soaring research in two directions.

Firstly, while wind may be difficult to predict, there are still local actions which can maximise energy capture from wind as it is encountered in a wind field. As shown in Chapter 3 the equations of motion for a soaring aircraft can be utilised to determine actions which maximise local energy gain. Some research has focused on utilising these situations to gain energy from local air motion such as turbulence [25, 28, 55, 56, 66]. Further information can be found in §2.4.2. Research in this area focuses on determining the correct actions to exploit local wind conditions rather than attempting to model larger scale wind effects.

An alternative to local energy gain is long term planning based on prior estimation of a wind field. This can cover planning with full or limited prior knowledge of a wind field [54, 65]. Long term planning is a different type of problem from the one addressed in this work. For long-term planning, it is important to be able to use information that is not collected during the flight, such as weather, topography, or information collected on previous flights. Glider pilots exploit prior knowledge of an area to predict where favourable winds will occur. This can be further broken down into prediction of features which do not move and prediction of general conditions. For example, ridge lift can be relatively well predicted without even being at a site in some regions. Prevailing weather and static ground features are good examples of prior information which can be used to predict conditions. Alternatively, there are methods to predict average conditions but not specific features. For example, certain weather patterns are conducive to the formation of thermal fields. This can be aided by remote observation of cloud patterns and wind, but it does not generally allow the remote prediction of specific thermals in the field.

Model based mapping lies somewhere between the prior information mapping and

the direct learning mapping presented here. Wind fields contain many wind features but only some are reliably useful for soaring control, so it makes sense to attempt to identify and utilise the known features and ignore other features. Model based mapping involves defining a set of wind feature models before flight and attempting to fit observations made during the flight to one of the prior models. This can also simplify the planning problem as strategies for known features can be defined off-line then applied on-line as features are identified during the flight. This approach is similar to the operation of glider pilots in manned glider flights. Thermals are the most common use for this type of guidance approach, since energy gain strategies in thermals are already well-known the goal becomes identification and characterisation of thermals in-flight. This is probably the most technologically mature guidance strategy with numerous demonstration flights of controllers which identify, track and utilise thermal columns only [6, 8, 10, 12, 31, 32].

This thesis aims to explore the possibility of non model-based wind estimation and utilisation by an unmanned aerial vehicle. This requires *in-situ* measurement, estimation and modelling of a wind field from direct observations taken during a flight. This chapter presents the use of Gaussian Process (GP) regression for mapping a wind field. The next chapter (Chapter 6) combines the previous work on soaring control with the mapping presented here to generate a guidance and control scheme to simultaneously explore and utilise a wind field.

5.1 Mapping a Wind Field

The goal of the mapping task is to generate a wind map which can be used by a path planner to generate energy gain paths for a gliding autonomous aircraft. This section discusses the requirements for the mapping system and the sensor data used to build a map.

5.1.1 Requirements for mapping a wind field

For this work assume that the aircraft is capable of measuring the wind velocity at the aircraft's current position. On a real aircraft this would usually be through measurements of air-relative and inertial velocity vectors. The air-relative velocity vector can be estimated through measurements of airspeed and angles of attack and sideslip. Airspeed can be accurately measured using a pitot-static system which calculates the airspeed through differences between static and dynamic pressure measurements. This is a common feature on almost all manned and unmanned aircraft. Measurement systems for aerodynamic angles are less common on small aircraft and UAVs. One possible method of measuring air angles is to use a multi-hole pressure system which takes measurements of dynamic pressure at multiple orientations to the wind field and calculates the resulting air-relative vector [61]. A second option is the use of wind vanes – low-friction vanes which rotate into the direction of the air around a fixed axis [19]. Wind vanes arguably require less calibration and are responsive enough to measure winds even on high speed aircraft [1, 44].

It is also assumed that an Earth-fixed inertial measurement system is available; such as GPS/INS, which estimates inertial position and speed. The difference between the air data and inertial solutions is due to wind, such that it should be possible to estimate wind whenever there are two coincident measurements from the air data and inertial systems. Equations (5.1)–(5.5) allow calculation of the wind vector \vec{W} as a function of measured airspeed V_a , aerodynamic angles α & β and inertial velocity \vec{V}_i . Subscript b denotes a body-relative velocity and \mathbf{C}_b^i is the body to inertial transformation matrix.

$$V_{b,x} = V_a \sqrt{\frac{1 - \sin \beta^2}{1 + \tan \alpha^2}} \quad (5.1)$$

$$V_{b,y} = V_a \sin \beta \quad (5.2)$$

$$V_{b,z} = V_{b,x} \tan \alpha \quad (5.3)$$

$$\vec{V}_b = [V_{b,x}, V_{b,y}, V_{b,z}]^T \quad (5.4)$$

$$\vec{W} = \vec{V}_i - \mathbf{C}_b^i \vec{V}_b \quad (5.5)$$

Each data point consists of the inertial spatial location where the sample was taken as well as the estimate of the wind vector. The mapping routine should take this data and produce a wind map which can be queried at any point across a pre-defined target domain. Most sample data would be expected to be taken inside the target domain but ideally the mapping method should also be able to consider data taken outside the target domain.

One of the contributions of this work is in developing soaring guidance routines based on non model-based wind mapping. This is to eliminate reliance on pre-defined models of wind features to increase flexibility and allow a planner to utilise all sources of energy during flight. Thus, the wind mapping method should be data driven and rely primarily on wind observations taken during the flight. It may be able to take into account previous rough predictions of the wind field based on observations of wind conditions.

The mapping problem is complicated by the fact that there is not often a static underlying wind field. Most wind fields are the result of a number of driving components; such as geostrophic pressure-driven wind at high altitude, shear layers and boundary mixing at lower altitudes. There is additional short length scale turbulence from factors such as ground features and random air motion (gusts). The mapping method should be able to map changes in the wind field at scales much smaller than the scale of the target domain. Combining this with the high dimensionality of the problem limits the applicability of grid-based methods which would require large computational storage or careful adaptive meshing.

Previous research has examined many methods of mapping and predicting wind fields. The meteorological community has worked on complicated atmospheric models mostly for the prediction of weather. These methods are usually cell or grid based and use quantities such as moisture and heat transport between cells to model or predict future weather events [2]. Generally these models need to be on much larger scales than are being used for this research, and consequently require significant computational resources. Similarly, computational fluid dynamics (CFD) solvers could be used in the current work. CFD uses meshed regions of fluid flow to solve the

Navier-Stokes equations in discrete cells and can be used to solve very complicated flow systems. However, CFD methods are sensitive to mesh size. Solutions are found by iterative calculations across the mesh to a certain threshold and would be too computationally intensive for online wind mapping.

There have been attempts by other researchers to model wind flows at smaller scales. Spatial modelling of winds in the planetary boundary layer is of interest for wind power and methods such as neural networks [5] and genetic algorithm learning of a fuzzy model [26] have been used to predict the spatial and temporal variation of wind.

However, currently there is a general lack of small-scale wind field data. Since this is a relatively new problem, there have been, to our knowledge, no attempts to actively map a wind field from a flying vehicle. Thus, it is currently difficult to justify the selection of any particular mapping method over alternative methods. In this work we propose the use of a model-free data driven approach to estimating wind fields for simulated flights. This type of method was selected because, given the lack of real data, a model-based approach might be biased by the selection of simulated models for generating the wind fields. Using a model-free approach allows more flexibility in modelling different types of wind features and is less reliant on the simulated data being a close match to the parametric model. The data driven approach also reduces the impact of simulated wind modelling errors. However, purely data driven approaches suffer from a considerable weakness in that they do not exploit any of the large volume of information which is already known about how air behaves. The author of this work believes that future work which leverages this information would likely improve prediction capability considerably. The area of wind modelling will almost certainly require further research and the methods presented in this chapter are an attempt to provide a feasible wind modelling method given current knowledge and data.

5.2 Gaussian Process Regression for Aerial Wind Mapping

For this research Gaussian process (GP) regression was selected to perform the map estimation. GP regression is a data driven approach which has been used by other researchers to model wind fields on meteorological scales from satellite data, where the method is often known as kriging or best linear unbiased prediction (BLUP) [22, 45, 71].

5.2.1 GP regression

Gaussian process (GP) regression is a non-parametric Bayesian machine learning method of regression analysis. The following provides a brief explanation of GP regression for wind mapping. The notation used is generally consistent with that used by Rasmussen [83], and further information can be found there. As in most regression techniques, the goal is to characterise the underlying function from a finite set of observations, $\mathbf{y} = \{y_i\}_{i=1}^n$ taken at locations in the input space $X = \{\mathbf{x}_i\}_{i=1}^n$ where $y_i \in \mathbb{R}$ and $\mathbf{x}_i \in \mathbb{R}^d$. The observations are assumed to be drawn from the set of actual function values $f(\mathbf{x})$ with additive zero-mean Gaussian noise with variance σ_n^2 .

$$y = f(\mathbf{x}) + \epsilon \quad (5.6)$$

$$\epsilon \sim \mathcal{N}(0, \sigma_n^2) \quad (5.7)$$

The goal of the GP regression analysis is to learn a function f which is the underlying function drawn from the input data. However, GP regression does not return an analytic function, but rather returns a distribution of functions from which estimates of the function value are drawn at any selected test point \mathbf{x}_* .

The covariance function $k(\mathbf{x}, \mathbf{x}')$ defines the covariance between two input points. A covariance function must be a positive semi-definite function. There is a large range

of common covariance functions which determine the properties (such as smoothness, periodicity and stationarity) of the function set generated by the GP. A common set of covariance functions are radial basis functions (RBF), which are based only on the distance between the two input points. In the case of a Euclidean space and distance measurement this is also often an isotropic distance (input dimensions have equal weight) such that $k(\mathbf{x}, \mathbf{x}')$ is a function of r where $r = |\mathbf{x} - \mathbf{x}'|$. In this case, the covariance is high (they are strongly correlated) for points close together and low (weakly correlated) for points far apart. The covariance function is used to generate a symmetric positive semi-definite covariance matrix $K(X, X)$ which represents the covariance relationship between all pairs of points in the input space, such that $K_{i,j} = k(\mathbf{x}_i, \mathbf{x}_j)$. To include observation noise as specified in Eq. (5.6) the final covariance is

$$\text{cov}(X, X) = K(X, X) + \sigma_n^2 I. \quad (5.8)$$

Gaussian process regression uses the information expressed in the covariance matrix to generate a Gaussian distribution of functions. Any point in the function space can be tested and the return is a Gaussian distribution output at that point defined by a mean value and covariance. The mean value at a sample location is actually a weighted sum of the training points, with the weightings determined by the inverse covariance matrix. Without covering the mathematics in-depth, the estimated mean value \bar{f}_* and covariance $\text{cov}(f_*)$ for a set of test points X_* , training points X , observations \mathbf{y} and covariance function k are shown below.

$$\begin{aligned} \bar{f}_* &= \mathbb{E}[f(X_*)|X, \mathbf{y}, X_*] \\ &= K(X_*, X)[K(X, X) + \sigma_n^2 I]^{-1}\mathbf{y} \end{aligned} \quad (5.9)$$

$$\text{cov}(f_*) = K(X_*, X_*) - K(X_*, X)[K(X, X) + \sigma_n^2 I]^{-1}K(X, X_*) \quad (5.10)$$

Selection of an appropriate covariance function is critical as it determines the set of basis functions from which the solution set is drawn. This thesis makes extensive use of the *squared exponential* covariance (Eq. (5.11)), a radial basis function. It is a commonly used covariance function which generates smooth outputs and in this

case has zero mean, is isotropic (input dimensions are equally weighted), stationary (function only of relative displacement, not of the absolute values of the input points) and non-degenerate (infinitely differentiable).

$$k(\mathbf{x}, \mathbf{x}') = \sigma_f^2 \exp\left(\frac{-|\mathbf{x} - \mathbf{x}'|^2}{2l^2}\right) \quad (5.11)$$

As can be seen from the equation, there are a number of variable parameters that affect the values returned by the covariance function. This set of variables is called the set of hyperparameters, θ , and training the model is the process of learning the most appropriate set of hyperparameters from the training data. In the case of a squared exponential covariance function the set of hyperparameters is the length scale, l , the signal variance, σ_f^2 , and sensor noise variance, σ_n^2 .

Selection of the hyperparameters affects the output mean and variance estimates. Since the effect of the hyperparameters on the resulting estimate is not always intuitive some measure of determining whether the selected hyperparameters result in a ‘good’ fit is required. A common method of estimating the fitness of a candidate set of hyperparameters is the marginal likelihood. In a Bayesian model comparison, the marginal likelihood represents the probability of obtaining the training observations \mathbf{y} , given the training points X , the set of hyperparameters θ , and the current model M . The weights \mathbf{w} are marginalised out to give the marginal likelihood

$$p(\mathbf{y} | X, \theta, M) = \int p(\mathbf{y} | X, \mathbf{w}, M) p(\mathbf{w} | \theta, M) d\mathbf{w} \quad (5.12)$$

This integral can be evaluated over a Gaussian model set, meaning that (the log of) the marginal likelihood is relatively easy to calculate. Maximising the marginal likelihood represents a fit based on a balance of minimum model complexity and remaining near the training data. Very complex models tend to fit the data well near the training points but are poor predictors away from the training data (overfitting) whereas simple models may not be capable of capturing the information in the training data and consequently assume a simple underlying function and very noisy observations (underfitting).

In the current application, the GP is trained using an optimisation routine (in this case Matlab's `fminunc` or a simple gradient descent function) which varies the hyperparameters to minimise the negative log of the marginal likelihood. The log marginal likelihood is shown in Eq. (5.13). Each term can be associated with a penalty on the model. The first term represents a measure of the deviation of the model from the observed data \mathbf{y} . Decreasing the magnitude of this term increases the marginal likelihood. The second term is a complexity penalty from the determinant of the covariance matrix which represents a measure of the variance across the data set. The final term is constant with respect to the hyperparameters so is not strictly required for minimisation of the marginal likelihood.

$$\log(p(\mathbf{y} | X, \theta, M)) = -\frac{1}{2}\mathbf{y}^T(K + \sigma_n^2 I)^{-1}\mathbf{y} - \frac{1}{2}\log|K + \sigma_n^2 I| - \frac{k}{2}\log 2\pi \quad (5.13)$$

5.2.2 GP wind mapping from direct observations

In the case of the wind data, the training set is the set of observed wind data. The training inputs are the set of observation locations in inertial space (and in the temporal case time). The data are the observed components of wind velocity, in this case the projection of the wind vector in 3D Cartesian space in the inertial frame. An alternative representation was considered (such as spherical or cylindrical coordinates) because in some cases the continuity is possibly better preserved over an alternative set of dimensions. However, the singularity in angular direction that occurs at zero velocity can cause significant problems if the inputs are uncoupled.

Thus, a separate GP process is used to model wind changes over each Cartesian dimension. However, by sharing common hyperparameters over the three models they end up sharing the same covariance matrix. This reduces computational complexity to the equivalent of a one-dimensional case rather than the number of output dimensions. This effectively links the variation parameters across the three dimensions, that is, all three output dimensions are expected to have the same length scale and noise, so the output estimation is independent of axis orientation (output space is isotropic). This

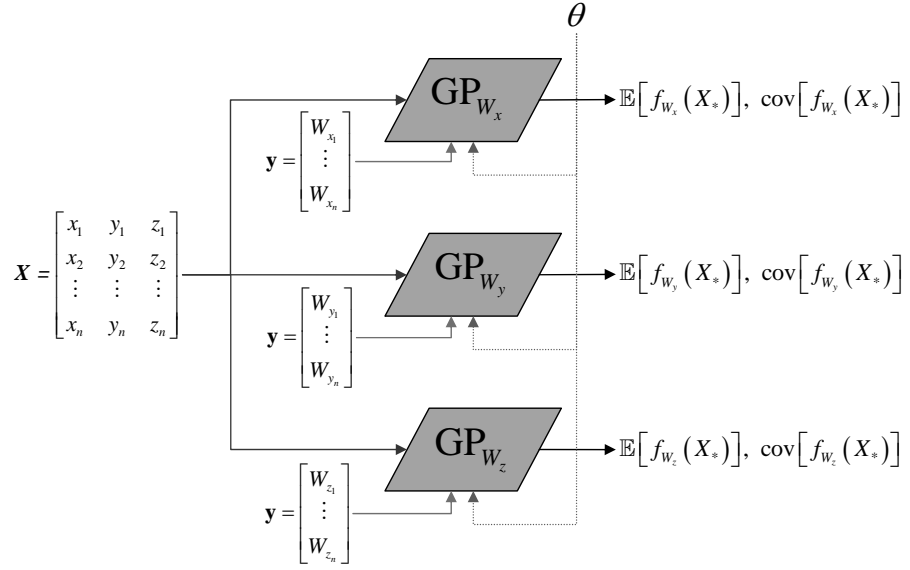


Figure 5.1: Structure of GP regression over Cartesian coordinates of wind.

is a justifiable decision since the variation of a wind field should not depend on the axis selection. There is a weak dependence in the field on the alignment of gravity due to pressure and density changes with altitude but it is considered insignificant given relatively small altitude changes this should not affect the variation length scale of wind flows. This does not mean that the output functions have to vary together since they are independent in their y data sets.

It would be possible to use a unified model across all three dimensions using a co-varying GP commonly known as cokriging [13]. However, this arrangement is more suited to when dimensions of the input data are not recorded concurrently. Cokriging allows prediction of one of the output dimensions based on estimation of the variation of the missing dimension with a dimension which does have data. In the case of the aircraft wind measurements the sensor arrangement would likely return either the full wind vector or none at all. In this case the co-varying model would provide limited improvement at increased computational cost.

Then, the input data X is a common set of input locations and time stamps (in the temporal case).

$$X = \begin{bmatrix} x_{i,1} & y_{i,1} & z_{i,1} & (t_1) \\ x_{i,2} & y_{i,2} & z_{i,2} & (t_2) \\ \vdots & & & \vdots \\ x_{i,k} & y_{i,k} & z_{i,k} & (t_k) \end{bmatrix}$$

The training data are the wind vector components. There are three GP models, as shown in Fig. 5.1, each modelling one projection of the wind data (W_x, W_y, W_z) but sharing input points and hyperparameters.

$$\begin{aligned}\mathbf{y}_x &= [W_{x,1}, W_{x,2}, \dots, W_{x,k}]^T \\ \mathbf{y}_y &= [W_{y,1}, W_{y,2}, \dots, W_{y,k}]^T \\ \mathbf{y}_z &= [W_{z,1}, W_{z,2}, \dots, W_{z,k}]^T\end{aligned}$$

Predictions of the wind are made in each dimension by sampling the model and covariance as shown in Eq. (5.9) and (5.10).

GP regression was selected for this application for a number of reasons. Firstly, it is a model-free method which allows queries of the model at any position in the input space. The regression is an attempt to find an underlying model which minimises some measure of error between the observed data and the predicted model. The resulting model is a Gaussian model defined by the data points, a covariance function and a set of variable hyperparameters. Querying a GP returns an estimate of the model in the form of a mean and covariance. This covariance estimate is one of the main reasons GP regression was selected as it provides a measure of uncertainty when querying the model. This can be used to direct searches of the input space to improve future model prediction. GP regression also allows relatively simple integration of a temporal component allowing for spatially and temporally varying maps.

However, this comes at the cost of computational complexity, which may be significant depending on the operations required. Learning the hyperparameters of a GP can be a relatively computationally expensive operation, as each iteration of the optimisation requires re-evaluation and inversion of the covariance matrix ($\mathcal{O}(k^3)$, where k is the

number of observations). Querying the model for estimates is usually simpler as it requires only a single inversion of the covariance matrix which can be stored inverted for fast retrieval of additional test points. With a stored inverted covariance matrix, generating a mean and covariance estimate is a matrix multiplication operation of $\mathcal{O}(k^2)$. However, the covariance matrix also needs to be updated as new observations arrive, though there are existing methods to update the inverted version directly to reduce computational complexity [24, 92]. This would allow on-line operation with limited computational power and storage, but for the current desktop simulation, this was considered unnecessary and should not affect performance significantly. Computational performance was not a primary consideration for the current research, but the authors believe that the use of GP regression with limited sample points could feasibly be used on an on-board computer with relatively minor changes that should not affect functionality or performance.

5.3 Static Wind Mapping

The simplest mapping would be to assume a static wind field; a field made up of static features which do not move with respect to the inertial space (or equivalently that the whole field moves at a constant speed). In fact, it is a relatively common assumption that features move together at a near constant rate determined by the mean wind [95]. The mean wind is assumed to be estimated before autonomous flight and remains constant during the flight. In this case the input dimensions are only the inertial position estimates.

In the current application the wind field is assumed to be smooth through use of the common squared exponential radial basis function (Eq. (5.11)) as the kernel function with a single fixed length scale l such that the input dimensions are considered isotropic (displacements in all axes are treated equally). Thus, the covariance is only a function of square distance across all dimensions in the input space. This effectively means that the input space is also considered isotropic, again to be invariant of axis orientation.

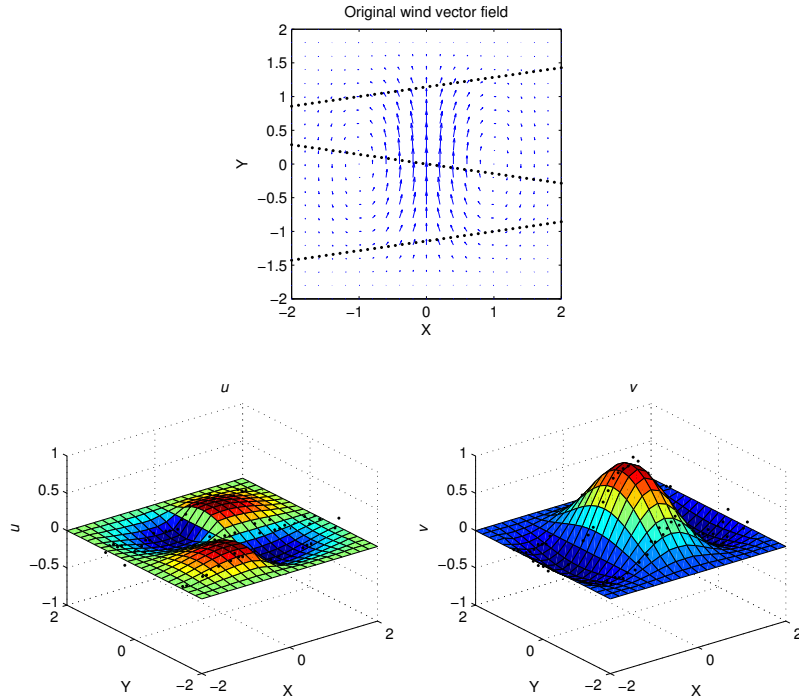


Figure 5.2: 2D toroidal thermal wind field. The lower figures show the lateral u and vertical v wind components. Black dots indicate the sample observations.

5.3.1 Shared hyperparameter validation

To demonstrate the validity of using a single set of shared hyperparameters results are provided comparing estimation of the hyperparameters separately across the output dimensions against sharing the hyperparameters. Hyperparameters are trained to minimise the log marginal likelihood using gradient descent from the same initial starting conditions.

The first set of results is for a two dimensional wind vector data set for three linear traversals through a vertical slice of the toroidal thermal model. The model is as defined in Appendix A with $R = 1$, $k = 2$ and $V_{core} = 1$ with additional Gaussian noise with standard deviation 0.05 on wind observations. The total number of observations is 120 (40 in each linear traversal of the field). The output dimensions are the wind vector directions u and v . The initial model and a set of sample points is shown in Fig. 5.2. Note that in this case there is a noticeable difference in the apparent length scale between the two data output dimensions. The models are first trained

separately across each dimension and then by sharing hyperparameters and using the sum of the log marginal likelihood from the two results. Table 5.1 shows the resulting average parameters after 100 training sessions of the same experiment with different (random) noise. Root mean square (RMS) error is calculated by drawing points from a regular grid (all points shown in the figure) and calculating the RMS error between the predictions and the actual field. Generally, the learned hyperparameters for the shared solution are close to the average solution between the individual models. The noise is well estimated in all cases.

Table 5.1: Training results after 100 runs with separate and shared hyperparameters for traversal of a 2D toroidal thermal

Method	l	σ_f	σ_n	$\log(ML)$	RMS Error
u (alone)	0.5216	0.0775	0.05021	162.4	0.03882
v (alone)	0.8266	0.3243	0.04958	145.33	0.02992
uv (separate)	-	-	-	307.7	0.04911
uv (shared)	0.7649	0.2262	0.05057	296.46	0.05317

The shared hyperparameter solution is only slightly worse than the separate solution, with a 3.65% lower log marginal likelihood and 7.64% increase in RMS error. The average training time was 2.54s for the separate case and 1.53s for the shared case. The significant reduction in training time is due to the requirement of the shared hyperparameter case to only evaluate the inverse covariance matrix once as opposed to once per dimension. The corresponding estimates for a single sample with separate hyperparameter training are shown in Fig. 5.3 and for the shared hyperparameters case in Fig. 5.4.

The figures show that both methods capture the overall shape of the thermal well from the limited sampling. Even unsampled regions are relatively well predicted. The separate solution has a much lower variance estimate on predictions made for the u component whereas the shared solution necessarily has the same variance for both output dimensions. Results for three-dimensional tests were similar with improved relative computational performance for the shared hyperparameter training, but results are much more difficult to visualise than in the 2D case.

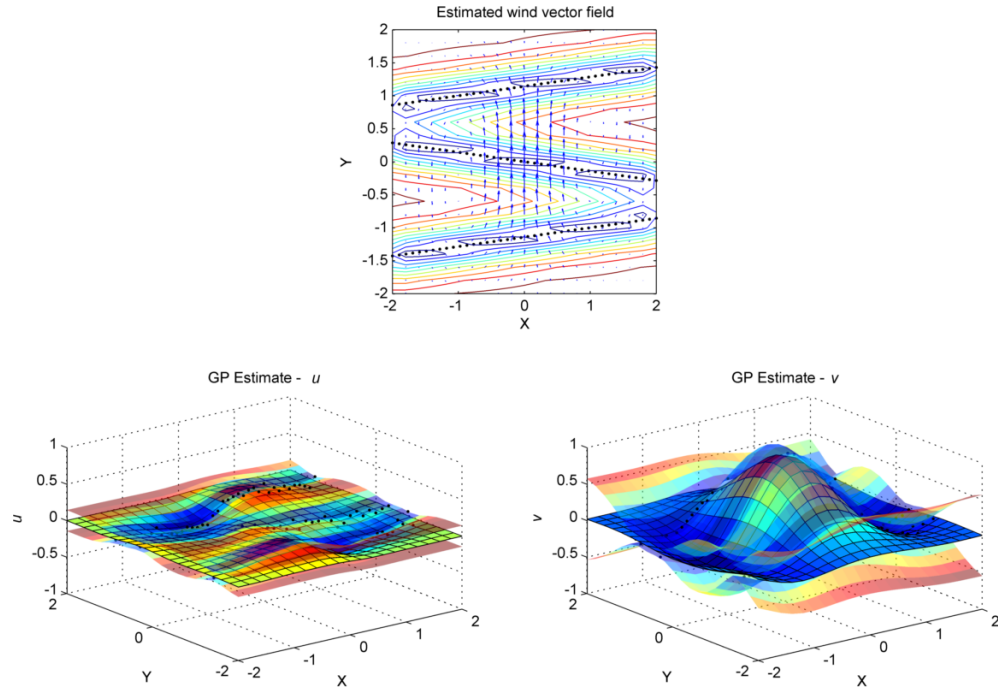


Figure 5.3: 2D toroidal thermal wind field - separate hyperparameter training. The relative confidence in the predictions are shown by the contours on the vector prediction. The 2σ boundaries for the GP prediction are shown by the transparent layers in the output estimates.

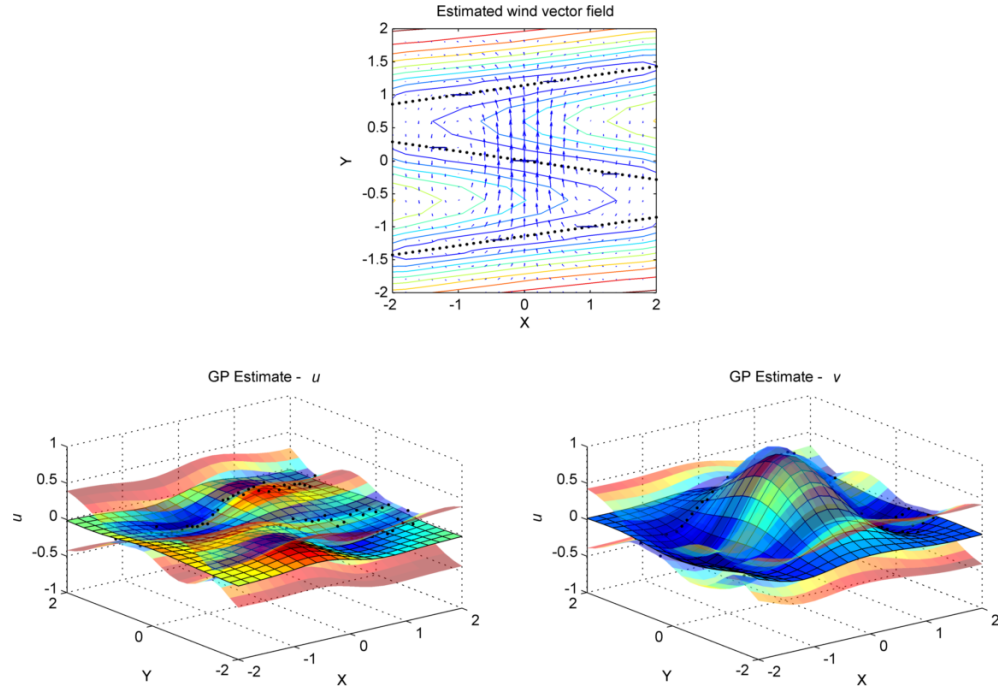


Figure 5.4: 2D toroidal thermal wind field - shared hyperparameter training.

For the modest reduction in performance against the significant computational cost reduction the shared hyperparameter model provides fast training and model queries for a wind GP mapping algorithm. There are also reasonable arguments for the physical interpretation of a common length scale since the viscosity (which limits the rate of change of velocity) is equal in all dimensions.

5.4 Dynamic Wind Mapping

5.4.1 Separable covariance functions

While the spatial results show that GP regression could provide a model-free method for mapping a static wind field, it remains to be shown whether this method remains valid for a dynamic wind field. To provide a dynamic map the GP regression needs to incorporate time into the covariance function. The simplest way to do this is to include time in the same way as the spatial dimensions and create a temporal distance measure which can be combined with the previous spatial distance. A separable covariance function combines these two measures in such a way that the covariance functions can be written as the product of a purely temporal and purely spatial covariance function. For the square exponential case this becomes

$$k(\mathbf{x}, t, \mathbf{x}', t') = \sigma_f^2 \exp\left(-\frac{|\mathbf{x} - \mathbf{x}'|^2}{2l_x^2}\right) \exp\left(-\frac{|t - t'|^2}{2l_t^2}\right). \quad (5.14)$$

where l_x is a spatial length scale and l_t is a temporal length scale, introducing one additional hyperparameter from the spatial case. This separable type has a clear effect from the temporal component. This also means that the reduction in covariance between two points decays within boundaries determined by their spatial and temporal distance.

However, a separable covariance function can be limiting as it does not allow mixing of the spatial and temporal components. Some processes may be related in space and time such that the covariance depends on both the spatial displacement and

the temporal displacement. This introduces a new class of spatio-temporal covariance function known as non-separable functions. A non-separable function cannot be written as the product of a purely spatial and purely temporal covariance function. Cressie and Huang [23] provide a mathematical description of the requirements for generating stationary non-separable covariance functions and propose a number of examples. Let $\mathbf{h} \in \mathbb{R}^d$ be a measure of spatial distance (such as the common 2-norm distance) and u be a measure of temporal distance. The covariance function can be written as $C(\mathbf{h}, u)$.

A relatively simple way to illustrate the effect of some non-separable functions is to plot the variation of covariance with the spatial and temporal distances $\|\mathbf{h}\|$ and $|u|$. A simple example is shown where sample points are drawn around the unit circle in the xy -plane. Assume ζ is a linear vector of 101 evenly spaced points from 0 to 4π . Let,

$$t = [0, 0.02, \dots, 2.00], \quad (5.15)$$

$$\zeta = 2\pi t, \quad (5.16)$$

$$x = \cos \zeta, \quad (5.17)$$

$$y = \sin \zeta. \quad (5.18)$$

This corresponds to two cycles around the unit circle in two units of time. Figure 5.5 shows the matrices for spatial square distance and time square distance. The distance matrices illustrate the relative distance between points in that space. The (1,1) element represents the distance from the first point to itself (the diagonal is always zero distance). The (1,2) element represents the distance from the first point to the second point. Thus, the i -th row represents the distance from the i -th point to the ordered set of all points. Thus, the distance matrices are symmetrical for commutative distance functions. Warm colours (red) represent (relatively) short distances and cool colours (blue) represent long distances. From the figure the two cycles are evident in the spatial distance matrix illustrated by the three diagonals (as the points circle back to the start position twice). The time displacement increases monotonically for our

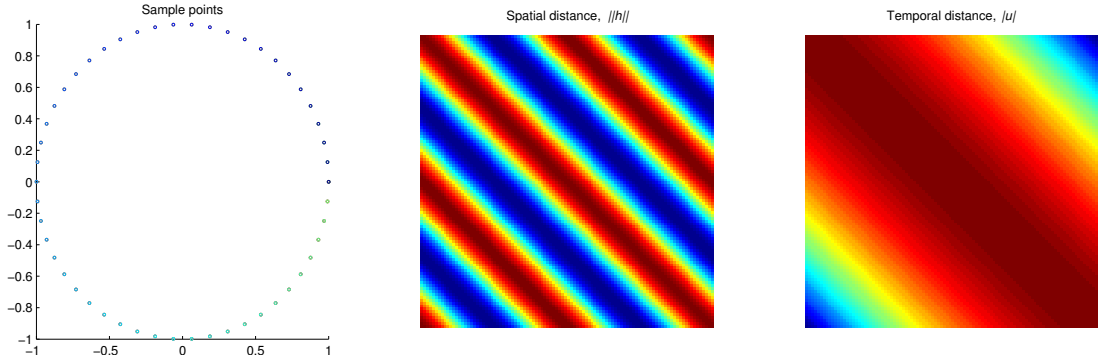


Figure 5.5: Spatial and temporal distance matrices for points taken from two cycles around the unit circle.

ordered sample points, such that the first and last points are the furthest (temporal) distance away from each other as shown by the colour changing from red to blue with increasing distance from the main diagonal.

A spatio-temporal covariance function combines these two metrics to give some measure of ‘total’ distance between each pair of points. The separable covariance function (Eq. (5.14)) can be written in terms of the spatial distance $\|\mathbf{h}\|$ and temporal distance $|u|$ as

$$C(\mathbf{h}, u | \theta) = \sigma_f^2 \exp\left(-\frac{\|\mathbf{h}\|^2}{2l_x^2}\right) \exp\left(-\frac{|u|^2}{2l_t^2}\right), \quad (5.19)$$

where $\theta = [\sigma_f, l_x, l_t]$.

To visualize this, the covariance contours and resulting covariance matrix are shown in Fig. 5.6.

Note that in this case both the spatial and temporal length scales and σ_f were set to 1. The resulting covariance matrix looks like the product of the inverse distance matrices, so that it appears similar to the spatial distance but ‘whitened’ by the increasing temporal separation during the second rotation. The covariance contour plot for the separable function has elliptical contours with axis lengths defined by the relative temporal and spatial length scales (in this case circular as the length scales are the same).

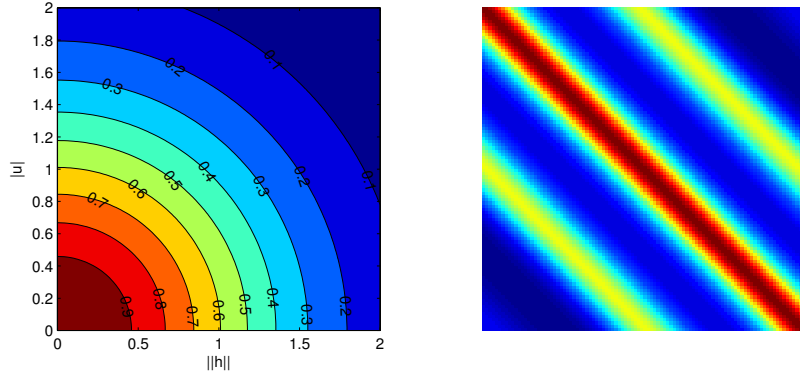


Figure 5.6: Covariance contours and covariance matrix for separable covariance functions. Cool colours (blue) represent low covariance and warm colours (red) represent high covariance.

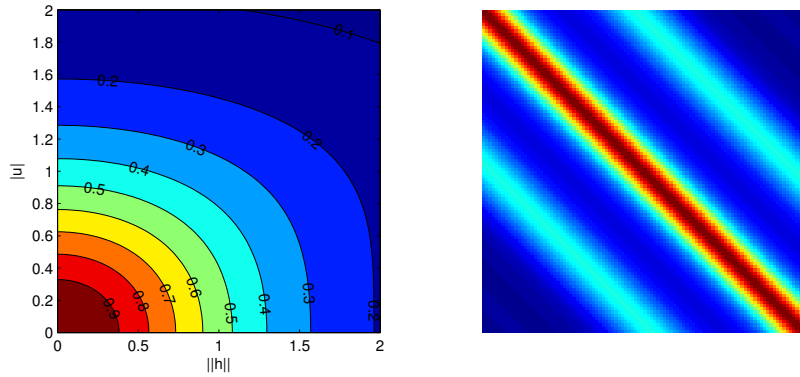


Figure 5.7: Covariance contours and covariance matrix for non-separable covariance function (Eq. (5.20)).

A non-separable function cannot be written as a product of two separate covariance functions. An example of a non-separable covariance function from [23] is

$$C(\mathbf{h}, u | \theta) = \sigma_f^2 \left(\frac{|u|^2}{2l_t^2} + 1 \right) \left[\left(\frac{|u|^2}{2l_t^2} + 1 \right) + \frac{\|\mathbf{h}\|^2}{2l_x^2} \right]^{-\frac{d+1}{2}}, \quad (5.20)$$

where $\theta = [\sigma_f, l_x, l_t]$.

The corresponding covariance contours and matrix are shown in Fig. 5.7.

In this case there is some variation from the separable case. However, a very similar result could be obtained from the separable case by tuning the length scales to yield a similar elliptical shape in the high covariance regions where the contours are almost

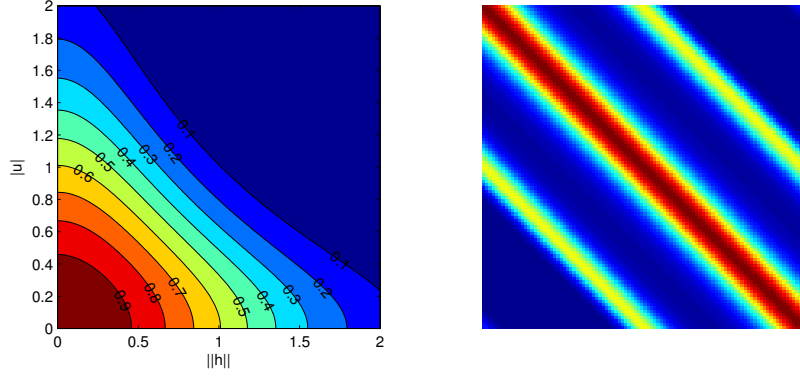


Figure 5.8: Covariance contours and covariance matrix for non-separable covariance function (Eq. (5.21))

elliptical. The shape of this non-separable function is fully defined by the same number of hyperparameters as the non-separable case. For this reason, unless there is a good physical reason in the problem itself to select a non-separable covariance function with known shapes the suggestion is that there is no reason that a non-separable function would perform worse than an arbitrary separable one. Obviously some data does have dependencies which may not be obvious which makes selection of a covariance function difficult. Of more interest is the non-separable type which introduces an additional parameter controlling the spatio-temporal dependencies. For example,

$$C(\mathbf{h}, u | \theta) = \sigma_f^2 \exp \left(\frac{-|u|^2}{2l_t^2} - \frac{||\mathbf{h}||^2}{2l_x^2} - a|u|^2||\mathbf{h}||^2 \right), \quad (5.21)$$

where $\theta = [\sigma_f, l_x, l_t, a]$.

This introduces an additional parameter a which controls the coupled term in the equation. The separable case is a special case of this function for $a = 0$. Increasing a decreases the cross-covariance between time and space, so that high covariance is possible only with low spatial *or* temporal lag but not both. A sample with $a = 5$ is illustrated in Fig. 5.8.

While this can improve flexibility it comes at the cost of an additional hyperparameter dimension for training. It is difficult to provide a direct comparison as the training

performance is dependent on the training method used and the initial estimate of the hyperparameters. However, in comparing methods for this thesis it was noted that the separable function was more stable in training and required consistently less computational time.

A basic comparison was to compare the performance for the thermal data set used earlier to compare the shared hyperparameter models. However, the data set was made into a dynamic field by allowing the thermal to drift over time and having data collected along a different path. The path is evenly spaced samples in time over a total of 80 s. The resulting estimation can be seen in the supplementary video *SeparableCovariance.mpg* provided with the thesis. For reference, in this example the separable covariance took 13.5 s to train and the non-separable 27.5 s. The resulting parameters are shown in Table 5.2. The spatial length scales are very consistent, but the separable function has a higher temporal length scale and lower noise, resulting in significantly lower variance estimates. However, the resulting marginal likelihood values are relatively similar. Finally, note that the low value of a suggests moderate coupling between time and spatial dimensions, so that the result is relatively similar to the separable case anyway.

Table 5.2: Results comparing separable and non-separable covariance functions for traversal of a 2D drifting toroidal thermal

Covariance	l_x	l_t	σ_f	σ_n	a	$\log(ML)$
Separable	0.7538	32.171	0.2040	0.0493	-	363.92
Non-separable	0.7497	11.904	0.2100	1.017	0.4750	350.80

Other non-separable covariance functions were tested in a number of other situations. However, trials suggested that the simpler separable function tended to be more stable and provide equivalent mapping performance to the non-separable versions. For a problem such as the one being analysed here it makes sense to use the simplest solution which requires the least computational resources and provides robust results. Thus a separable covariance function unless prior additional knowledge allows selection of a specific non-separable functions and good initialisation of the hyperparameters.

5.4.2 Drifting separable covariance

A common assumption for large scale wind features in relatively calm winds is that the features tend to drift at a relatively constant rate with the mean wind [95]. It makes sense to incorporate this feature into a dynamic wind estimate. This can be done relatively simply in a separable covariance function by including a drifted distance estimate d_w . The wind is assumed to be moving the wind features in the inertial space at a wind speed of W_d . Note that by including the wind estimate as a hyperparameter it is possible to continuously estimate the wind during the flight as part of the covariance retraining. This means that the wind can be tracked continuously. The drift also separates the estimate from the actual wind, so that the features can drift at a different speed than the mean wind and this model will still be capable of modelling the flow.

$$d_w^2(\mathbf{x}, t, \mathbf{x}', t') = [\mathbf{x} + W_d(t' - t) - \mathbf{x}']^2 \quad (5.22)$$

The distance metric is commutative and stationary with respect to the inputs. The drift velocity in each dimension is modelled by a hyperparameter of the covariance function. This allows estimation of the field drift within the hyperparameter estimation. Also included is a standard isotropic square distance in inertial space. The two distance measures are combined through a weighting $\epsilon \in (0, 1)$. The resulting covariance function (Eq. (5.23)) is a function of the set of hyperparameters $\theta = (\sigma_f, l_x, l_t, l_d, \eta, \mathbf{W})$. The weighting ϵ is calculated through the logistic function $\epsilon = (1 + e^{-\eta})^{-1}$.

$$k(\mathbf{x}, t, \mathbf{x}', t') = \sigma_f^2 \exp \left(-\frac{|t - t'|^2}{2l_t^2} - \epsilon \frac{|\mathbf{x} - \mathbf{x}'|^2}{2l_x^2} - (1 - \epsilon) \frac{d_w^2}{2l_d^2} \right) \quad (5.23)$$

The weight ϵ provides flexibility in estimating drift. If a good drift estimation is found then the model can decrease ϵ towards zero and rely solely on the drifted estimates with a higher temporal length scale. Alternatively, if features seem to be drifting at different rates then the model will revert to a purely spatial estimate with reduced

length scales. An additional advantage of this covariance function is the fact that the wind gradient \mathbf{J}_w can be calculated analytically by differentiating the covariance function with respect to the target locations. Wind gradients are used by both the target finding and path planning algorithms.

The drifting covariance is demonstrated in Section 6.3 for a flight through a dynamic wind field with drifting thermals.

5.5 Summary

Planning soaring paths in wind requires an adequate estimate of the wind field. Since air is transparent to most sensors, aircraft are usually only capable of directly sensing a wind field. Gaussian process regression is proposed as a method to generate a model-free wind map from data collected during flight.

GP regression is a non-parametric Bayesian machine learning method of regression analysis. Applied in a wind mapping context it provides a continuous and differentiable map which can be queried at any point in the input domain. The mapping also returns a confidence estimate in the form of a variance which can be used by a planner to guide future map exploration for improving the map.

Firstly, the basic concept of GP regression was presented. The advantages and limitations for applying GP regression to wind mapping were discussed. A stationary covariance function with shared hyperparameters was demonstrated to provide consistent mapping combined with stable training and good computational performance. It was also shown that extending GP mapping for temporal variation is relatively straightforward and allows flexible modelling of dynamic wind fields from data collected during a flight. To model dynamic wind fields a drifted distance separable covariance function is proposed to provide modelling capability for dynamic features such as thermals which tend to drift in inertial space but remain relatively self-consistent.

Chapter 6

Simultaneous Exploration and Exploitation of a Wind Field

This chapter draws on the concepts covered in earlier chapters to present a unified system architecture for an autonomous aircraft to simultaneously explore and exploit a wind field. The goal of the system is defined as exploration and mapping of an unknown wind field with a gliding aircraft. The system should be able to control a gliding aircraft to explore and generate a map of a wind field and use that map to generate energy-gain paths to allow further exploration of the field.

6.1 System Architecture

6.1.1 Mission goals

The overall goal of the system is to generate a map of the wind environment within a predefined spatial region. However, the aircraft used to explore the field is assumed to have no propulsion and insufficient initial energy to explore the field. Thus, the system should explore the region to find available energy sources and utilise those sources to allow further exploration.

Map improvement is measured through a variance estimate returned by the GP regression mapping module. The goal is to reduce the overall variance across the entire field. In this definition there is no defined termination condition, though in most cases a threshold on the mean or maximum map variance would be sufficient. During flight, the relative variance measures are more important, as these guide the exploration to regions which have higher variance than other regions of the map.

There are also limitations on the ability of the aircraft. The guidance system should not breach certain physical limitations and should comply with safety limits such as minimum and/or maximum altitude or spatial limits. Some of these are defined by the platform (such as airspeed and load limits) and some are mission specific.

Finally, the completion time is considered a secondary design driver. The guidance system should explore the field as quickly as possible but remain within the other mission limits at all times. In most cases the maintenance of sufficient flight energy would be considered the primary goal. Map exploration is largely facilitated to allow more efficient energy capture. In the case of temporal field variation it would be difficult to define an exploration goal since the field is assumed to be constantly varying and hence map improvement has a minimum limit which can be maintained but not consistently reduced. In this case the goal is to provide consistent energy capture for continuous flight within the region of interest.

Inside these limitations the controller is relatively free to plan paths within the wind field. There are no physical obstacles and the aircraft is assumed to be flying without other vehicles in the region. The only exception is unfavourable wind conditions which might lead to stall or otherwise break safety limits. These flight conditions should be automatically avoided by the controller where possible rather than being defined specifically as hazardous regions.

The aircraft is assumed to have limited or no initial knowledge of the field. Thus, the guidance system should not ‘expect’ sufficient energy sources, but use known energy sources wherever possible to maintain exploration. If there is insufficient energy within the region of interest for continuous flight the guidance system should be able to terminate.

6.1.2 System architecture

The system architecture is based on a modular design with separate modules for generating a wind map, planning energy gain paths, and low-level control of a gliding aerial vehicle. This modular design was selected to allow flexibility in the methods used in each module. Each module has specific goals and data requirements which mean that it should be possible to replace modules with alternative algorithms or methods and retain the same structure.

A system defined by three major components is proposed; a mapping module, a high level global target planner and a low level guidance and control system. The mapping module takes sensor data and constructs a map of the wind field. The high level planner is responsible for energy maintenance and identifies regions of energy gain and unexplored regions of the map and selects between these targets to maintain platform energy and continue exploration of the field. The low level guidance controller generates paths which capture local energy in energy gain regions and travel towards the global target. A system overview is illustrated in Fig. 6.1 and the following subsections detail the individual modules. Results are presented for two forms of the system; a version for exploring static wind fields and a version for exploring dynamic wind fields. There are minor differences in the global target exploration modules as explained in each section.

6.2 Exploration of Static Wind Fields

The first set of results present an exploration and exploitation guidance controller for static wind fields. A static wind field is defined as one which does not change with time (though the entire field could translate through inertial space at a constant rate with no loss of generality). The wind field is defined by a number of wind features overlaid with random turbulence.

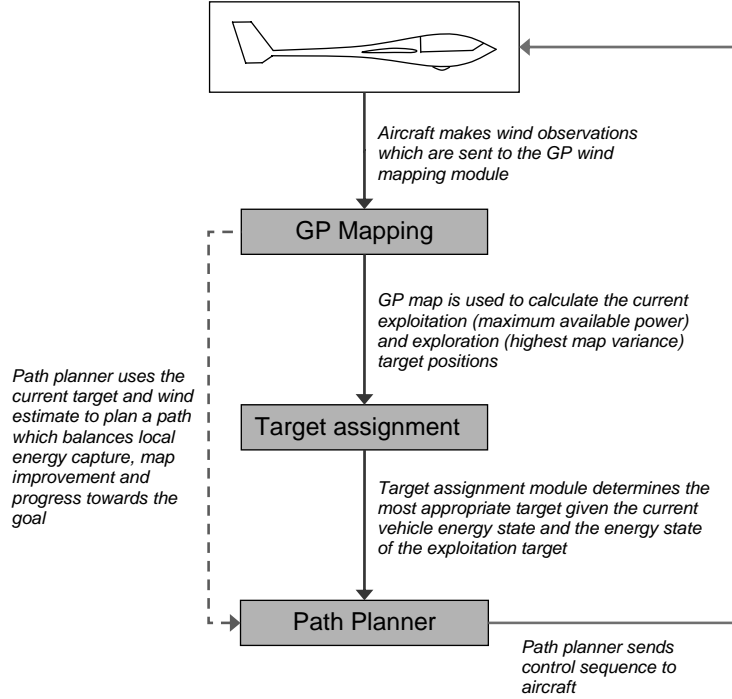


Figure 6.1: System overview of simultaneous exploration and exploitation path planning architecture for a gliding UAV.

6.2.1 Static wind field mapping

Mapping a static wind field is performed using the static Gaussian process regression described in §5.2. The total number of recorded data points is limited to 150 to prevent excessive computational load.

6.2.2 Global target assignment

The global target assignment algorithm manages the aircraft energy by using the map and knowledge of the current energy status to determine whether to pursue an exploitation (energy-gain) or exploration (map improvement) goal. Each planning cycle, two goal points are defined. The exploration goal, $\vec{P}_{explore}$, is defined as the point of maximum estimated uncertainty drawn from a regular three dimensional grid of the target region. This point represents the most uncertain region of the current map, but visiting this point is not necessarily equivalent to maximising field informa-

Algorithm 1 Global target assignment algorithm

Each replanning cycle:

$$E_{travel} = mgd_{explore} / \left(\frac{L}{D}\right)_{est}$$

$$E_{explore} = -mgz_{i,explore} + \frac{1}{2}mV_{cruise}^2$$

$$E_{current} = -mgz_{i,current} + \frac{1}{2}mV_{current}^2$$

if $E_{current} \geq (E_{explore} + E_{travel})$ **then**

$$\vec{P}_{target} \leftarrow \vec{P}_{explore}$$

else

$$\vec{P}_{target} \leftarrow \vec{P}_{exploit}$$

end if

tion. However, given the hierarchical system architecture and continuous GP wind map this point is a suitable target for exploration without requiring continuous path optimisation. The energy goal, $\vec{P}_{exploit}$, is defined as the point on the previous trajectory where maximum power gain was recorded. The target assignment algorithm selects between these goals each planning cycle.

The goal of the mission is to reduce total map uncertainty over the entire region. However, depending on the energy state of the vehicle the current exploration goal may be unreachable. An estimate of the energy required to reach the exploration goal, E_{travel} , is made by taking the distance to the goal ($d_{explore}$) and an estimate of the lift-to-drag ratio to determine the equivalent height and resulting gravitational potential energy required to travel that distance (as in the navigation reward for the known wind planner Eq. (4.7)). The energy required at the exploration goal, $E_{explore}$, is defined at the altitude of the target $-z_{i,explore}$ and a fixed speed (usually the cruise airspeed, V_{cruise}). If the aircraft currently has more energy than the sum of the target energy and the travel energy then the aircraft should be able to reach the exploration goal and the current goal is defined as the exploration goal. Otherwise, the current goal is defined as the exploitation goal, as summarised in algorithm 1.

In this way, the aircraft either has enough energy to attempt to explore the most uncertain region of the map or returns to the previously best known energy source to collect enough energy until exploration is possible. There are limits on the exploitation goal to prevent energy gain attempts from insufficient sources (less than the sink speed) and the target rises in altitude with the aircraft to continue energy gain flight.

6.2.3 Local path planning

The local planner should take the global target information and the current wind map to plan paths which collect energy and travel towards the global target. This problem is similar to the known wind map control discussed in §4.2. However, in that case full knowledge of the wind was required. In the current case the wind map is being updated on-line as new data is collected. The planner generates paths based on the current wind map and a lower-level controller carries out the plans. Over regular planning cycles the planner generates new plans as the map is updated.

For local planning in static wind fields, the planner uses an adaptation of the heuristic reward function R discussed in §4.2. The reward function is a linear sum of three energy-based components quantifying the estimated energy change, the progress towards the global goal and a reward for travelling through unexplored regions. All components are expressed in terms of energy to maintain consistency.

The first component, R_{energy} , estimates the energy change and power available during a segment (Eq. (6.1)). This is equivalent to the power reward function R_P (Eq. (4.5)), which was demonstrated to perform better than total energy change alone in §4.2.2. The total energy change is a sum of the potential and air-relative kinetic energy changes between the initial and final conditions (denoted with subscripts 0 and 1 respectively). An energy estimate based on the instantaneous power at the end of the segment \dot{E}_1 is also included with a fixed weight $K_{\dot{E}}$.

$$R_{energy} = -mg(z_{i,1} - z_{i,0}) + \frac{1}{2}m(V_{a,1}^2 - V_{a,0}^2) + K_{\dot{E}}\dot{E}_1\Delta t \quad (6.1)$$

Also considered is the navigation reward function, which rewards progress made towards a goal point determined by a higher-level planner. Again, this is equivalent to the R_{nav} reward function described in §4.2.1. The navigation reward is a discount on energy used to travel towards the goal.

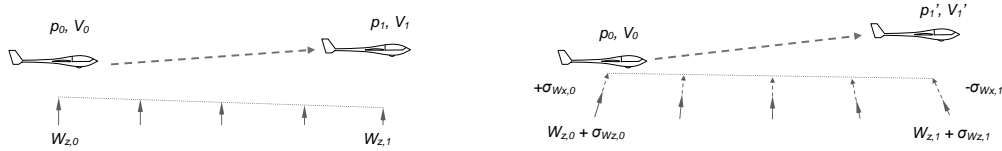
$$R_{nav} = mg \frac{d_{goal,0} - d_{goal,1}}{\left(\frac{L}{D}\right)_{est}} \quad (6.2)$$

While exploration of the entire field is facilitated by the global planner, the local planner can also take into account improvement of the local map by collecting sample points which minimise total variance. In smooth wind conditions there are often path alternatives which are predicted to result in similar performance in terms of progress to the goal and energy efficiency, but differ in the value of new information collected. Since the GP estimate of the current map variance is readily available, this information should be used to select paths which pass through high variance regions to maximise the value of collected sample points. This effectively leverages the GP uncertainty estimate to favour paths which collect samples in high variance regions to maximise the benefit of collecting new sample points.

To be compatible with the energy and navigation rewards presented thus far, the sampling reward function should be expressed in terms of the energy collected. However, the energy reward already estimates the energy that would be gained or lost given the current mean estimate of the wind field. The proposed solution is an energy heuristic based on the ‘possible energy’ of a path segment; how much additional energy could be gained with favourable wind conditions over the mean estimate conditions. The possible additional energy is estimated by calculating the most favourable wind conditions within one standard deviation (1σ) of the mean estimate. This utilises the GP variance to reward exploration in poorly mapped (high variance) regions but in well mapped (low variance) regions the sampling reward becomes insignificant and the total reward is dominated by the energy and navigation components.

Calculating the correct gradient alignments and using the full set of dynamic equations to simulate each segment is computationally expensive. A faster alternative is to estimate the energy difference along the entire segment compared to the mean estimate case. From the aircraft dynamic energy equation (Eq. (3.5)) additional wind energy must come from an increase in altitude and/or a change in effective airspeed. Thus, a reasonable method of estimating the possible energy gain would be to calculate the vertical displacement and airspeed changes along the length of the segment under favourable conditions. A simple longitudinal example is illustrated in Fig. 6.2.

Consider a path estimate generated with the mean wind from point $p_0 = [x_0, y_0, z_0]^T$



(a) The original forward simulated path based on the mean wind estimate.

(b) Favourable wind conditions based on one standard deviation from the mean.

Figure 6.2: The additional energy in favourable wind conditions is estimated by calculating the additional altitude and airspeed gains along the segment. In this case the extra vertical wind results in an increase in altitude and the horizontal wind shear results in additional kinetic energy.

to point $p_1 = [x_1, y_1, z_1]^T$. The corresponding airspeeds V_0 and V_1 are also known. Additionally, the wind variances at the start $[\sigma_{Wx,0}^2, \sigma_{Wy,0}^2, \sigma_{Wz,0}^2]^T$ and end points $[\sigma_{Wx,1}^2, \sigma_{Wy,1}^2, \sigma_{Wz,1}^2]^T$ are calculated from the GP map. Now consider the 1σ best case favourable wind. In the z -direction this is always a lifting wind, so the best case is the mean wind plus $1\sigma_{Wz}$ vertical wind. The net effect is an increase of $\frac{1}{2}(\sigma_{Wz,0} + \sigma_{Wz,1})$ along the length of the segment. Increasing the total mean wind in the other directions does not increase energy; it only induces lateral motion. The maximum shear energy is always due to a maximum shear gradient, which will be opposing estimates at either end of the segment (with the direction determined by the heading of the aircraft) which results in a total variation of $\sigma_{Wx,0} + \sigma_{Wx,1}$ in the x -direction and $\sigma_{Wy,0} + \sigma_{Wy,1}$ in the y -direction along the length of the path segment. Thus, the most favourable 1σ wind change along the entire segment is:

$$\Delta \vec{W} = \begin{bmatrix} \pm(\sigma_{Wx,0} + \sigma_{Wx,1}) \\ \pm(\sigma_{Wy,0} + \sigma_{Wy,1}) \\ \pm(\sigma_{Wz,0} - \sigma_{Wz,1}) \end{bmatrix}. \quad (6.3)$$

Only the component of wind in the direction of flight will change the effective airspeed. This component can be calculated by taking the scalar projection of the wind vector in the flight direction. Let the airspeed at the end of the segment with favourable wind be V'_1 .

$$\begin{aligned}
\Delta V &= V'_1 - V_1 \\
&= \Delta \vec{W} \cdot \hat{\vec{x}}' \\
&= \frac{\begin{bmatrix} \sigma_{Wx,0} + \sigma_{Wx,1} \\ \sigma_{Wy,0} + \sigma_{Wy,1} \\ |\sigma_{Wz,0} - \sigma_{Wz,1}| \end{bmatrix} \cdot \begin{bmatrix} |x'_1 - x_0| \\ |y'_1 - y_0| \\ |z'_1 - z_0| \end{bmatrix}}{\sqrt{(x'_1 - x_0)^2 + (y'_1 - y_0)^2 + (z'_1 - z_0)^2}}. \tag{6.4}
\end{aligned}$$

The additional airspeed results in an increase in total energy and is a function of the current airspeed. Letting the mean original airspeed along the segment be $\bar{V} = \frac{1}{2}(V_0 + V_1)$, the total kinetic energy increase is

$$\begin{aligned}
\Delta E_k &= E_{k,1\sigma favourable} - E_{k,mean} \\
&\approx \frac{1}{2}m(\bar{V} + \Delta V)^2 - \frac{1}{2}m\bar{V}^2 \\
&= \frac{1}{2}m(2\bar{V}\Delta V + \Delta V^2). \tag{6.5}
\end{aligned}$$

Gravitational potential energy is gained through the increased vertical component leading to additional altitude at the end of the segment,

$$\begin{aligned}
\Delta E_p &= E_{p,1\sigma favourable} - E_{p,mean} \\
&\approx \frac{1}{2}(\sigma_{Wz,0} + \sigma_{Wz,1})mg\Delta t. \tag{6.6}
\end{aligned}$$

The corresponding total energy change is defined as the sampling reward function,

$$\begin{aligned}
R_{sampling} &= \Delta E_k + \Delta E_p \\
&= \frac{1}{2}(\sigma_{Wz,0} + \sigma_{Wz,1})mg\Delta t + \frac{1}{2}m(2\bar{V}\Delta V + \Delta V^2). \tag{6.7}
\end{aligned}$$

Note that this form of reward assumes an optimistic estimate of the wind. However, it is equally likely that the opposite case occurs, with 1σ opposing wind (downdraft, adverse wind gradient) resulting in a poorer energy performance than predicted. In

this case, the exploration still provides utility, as improvement in the map and a consequent reduction in variance limits future exploration of that area. Also, the length scale of wind features is usually higher than the length of a planning segment so the mapping component primarily acts in tie-break situations where there is similar energy performance but alternative paths could improve local mapping.

A weighted sum of the three specified reward functions is used to balance local energy capture, progress towards the goal and local field exploration. In general, the goal points are approximations of a target area rather than specific points which need to be flown to. Near the goal, the capture of energy and new information is most important. Further from the goal, it is more important to travel towards the goal. A variable weighting is used between energy and navigation rewards. The sampling reward weighting is fixed as it has equal significance throughout the flight. The variable weighting is $K_E \in [0, 1]$; lower K_E values give precedence to progress towards the goal, higher K_E values favour local energy gains. The resulting reward function is

$$R = K_E R_{energy} + (1 - K_E) R_{nav} + K_{sampling} R_{sampling}. \quad (6.8)$$

The value of K_E is determined by an exponential decay function, which assesses how near the goal the aircraft is and adjusts the gain accordingly.

$$K_E(d_{goal}) = K_{E,min} + (1 - K_{E,min}) \exp\left(\frac{d_{goal}}{100} \log\left(\frac{K_{E,100} - K_{E,min}}{1 - K_{E,min}}\right)\right) \quad (6.9)$$

The value of K_E approaches a constant minimum value $K_{E,min}$ at a distance far from the goal. As it approaches the goal, K_E increases, favouring energy gain over progress towards the goal. When the aircraft is at the goal, K_E is at its maximum value of 1 and the navigation reward is neglected. To determine the decay rate, a second variable is introduced, $K_{E,100}$ which is the value of K_E at a distance of 100 m from the goal. In the current work this value was selected off-line at 0.6 but could be determined by estimating the size of thermals on-line. An illustration of the behaviour of K_E as a function of distance to the goal d_{goal} is shown in Fig. 6.3.

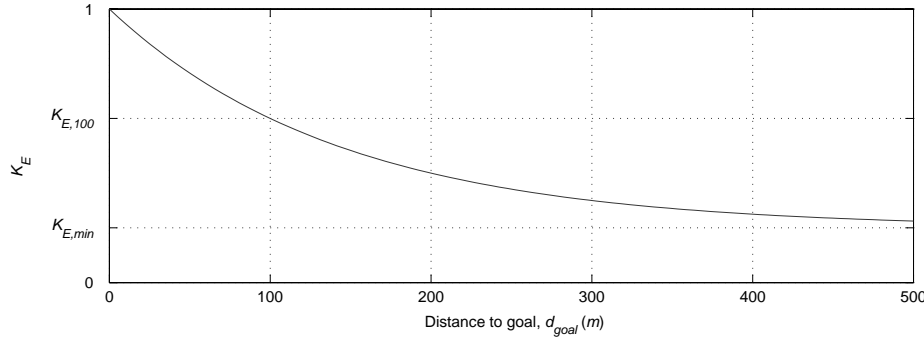


Figure 6.3: Energy weighting K_E as a function of the distance to goal d_{goal} (Eq. (6.9)). Higher K_E values result in higher rewards for local energy collection whereas lower K_E values result in higher rewards for travelling towards the goal.

The automatic balancing of the reward function allows the goal point to be set at an energy source or other target whilst retaining the same path planning structure. In this way, the path planning module acts as the low level guidance controller; given a goal location and the number of branches to search it will return the control sequence required to produce an efficient path to the goal based on the current wind field estimate. In the current work, the path planning algorithm uses the GP map estimate to generate control sequences which are carried out open-loop by the simulated aircraft.

6.2.4 Simulation setup

The aircraft is simulated by numerical integration of the dynamic equations from §3.4. Aircraft parameters are derived from an RnR SBXC remote controlled cross-country glider model (the aircraft model and relevant parameters are in Appendix B.1).

The wind is represented by a static field consisting of a number of thermal bubbles of various strengths and sizes as described for each simulation in the results section. The thermals are instances of the toroidal thermal model described in Appendix A. For each thermal the maximum core lift speed V_{core} and lifting radius r_{lift} are specified. The mean lift across the lifting disk is $\frac{4}{\pi^2}V_{core} \approx 0.41V_{core}$. Note that the flow is conservative such that the lifting volume of air for $r \in [0, r_{lift}]$ is the same as the sinking volume of air for $r \in [r_{lift}, 2r_{lift}]$.

The GP mapping uses observation data collected during the flight by a simulated air data system. This system is simulated by taking the actual wind data from the simulation and adding unbiased Gaussian noise with standard deviation 0.1 m/s to represent measurement error. As explained further in §5.2 the GP regression uses a square exponential covariance function with three hyperparameters: process length scale l , process variance σ_f^2 and noise variance σ_n^2 . The GP hyperparameters were determined by flying 10 simulated trajectories through static wind fields with a random set of up to three thermal columns ranging in size from 25-100 m radius and core strength from 0-7 m/s. Each flight collected 300 data points and the hyperparameters were trained using the Matlab minimisation routine `fminunc` to minimise the negative log marginal likelihood. The mean of the resulting hyperparameters was $l = 45$ m, $\sigma_f = 0.5$ m/s and $\sigma_n = 0.09$ m/s. These values are used and remain fixed in the following simulations.

During each simulation presented in the results, at most 150 data points are stored and used for regression to limit computational load. The simulated sensor system collects data at high frequency (2 Hz) so the maximum number of observations is reached relatively early in the flight. Observations must be discarded to maintain a database of the most useful observations. In the current implementation the observations are ranked by the minimum distance to other observations in the set. The square distance is already calculated as part of the covariance function, so the results are sorted and the oldest entry in the minimum distance pairs are discarded and replaced with new observations. This results in a natural spatial sparsity of the data set representing the best coverage of the target space with the limited number of observations made along the flight trajectory.

The path planner uses the current wind field estimate generated by the GP mapping module to plan paths. Each planned segment is one second with a total tree depth of five and replanning every three seconds. There are three scaled roll rate commands up to a maximum bank of 45° and three pitch rate commands (with load limit and maximum lift coefficient constraints) for a total of nine control options for each branch. The control sequence returned by the path planner is a series of roll

rate and air-relative climb angle commands carried out open-loop by the simulated aircraft with wind data drawn from the simulated wind field. Note that this means that in poorly mapped regions the resulting path can be different from the planned path. The controller does not track the commanded path in space but follows the commanded control sequence.

Target assignment is based on two targets returned from the GP map. The exploration target is the point of maximum variance based on a regular $8 \times 8 \times 5$ grid drawn from the target exploration region. The energy target is defined as the point at which the aircraft gained maximum power during the flight so far. The energy target altitude varies with the altitude of the aircraft to allow climbing in a thermal but will not rise above or drop below altitudes where there was no recorded power gain to prevent attempted energy gain above or below the extent of a thermal bubble.

Also included in the final set of results is a gust model to simulate turbulence. The Dryden continuous turbulence model is used with specifications from MIL-F-8785C [39, 101]. The turbulence is generated for a ‘moderate’ level of turbulence at low altitude (<1000 ft) with mean wind speed at 20 feet altitude, u_{20} , of 15.23 m/s (30 kts). The turbulence is calculated at each time step for the current airspeed and altitude using Gaussian noise.

6.2.5 Results

The simultaneous exploration and exploitation strategy is demonstrated in three simulated trajectories. Each simulation consists of a static wind field with a region of exploration defined. The aircraft begins the simulation with a small set of data already collected; this represents manual or autonomous flight before the autonomous soaring control is activated. This data provides a repeatable exploration path at the start of each simulation but is not necessary for autonomous soaring and the control architecture does not require initial data.

This first simulation illustrates exploration of a region containing a single thermal. The thermal bubble is centred at (350, 50, -200) with maximum vertical wind strength

3 m/s and lifting radius 100 m. The exploration box is defined by the limits $x \in [0, 400]$, $y \in [-100, 100]$, & $z \in [-250, -150]$. The aircraft starts autonomous soaring at (0, 60, -200) heading in the direction of the positive x -axis and the simulation runs for 500 s. The resulting path is shown in Fig. 6.4 and the accompanying videos are *single_thermal.mpg* and *single_thermal_variance.mpg*. The ‘*_variance*’ videos show isosurfaces of the variance estimate to provide an indication of how the map confidence estimate changes during the flight. Spatial dimensions are in metres.

Figure 6.5 shows the progress of the simulation from a top-down view. The straight path with a semi-circular curve terminating at (0, 60, -200) indicates flight before autonomous soaring. Current sample points are indicated by plus symbols. The soaring controller is capable of utilising the energy in the thermal bubble to effectively explore the region. Initially, the aircraft does not pass through the thermal. During early exploration of the region the thermal is discovered, and utilised for the remainder of the flight. The general pattern of motion is to capture energy from the thermal then utilise that energy to explore new regions. However, the energy reward limits the ability of the planner to use path segments which result in excessive local energy loss. While this is often beneficial, it can occasionally cause excessive detours as seen in some of the longer loops extending outside the region of interest. In these cases the airspeed is usually relatively high after exiting the thermal. A sharp turn at high speed would result in rapid energy loss, so the planner continues to select segments which move further from the goal but are locally energy efficient. Eventually, the navigation reward becomes more significant and/or the aircraft slows down enough so that a turn can be made efficiently. This highlights a limitation of the local planning strategy which could be improved with an increased planning horizon. Similarly, large changes in commanded altitude often occur as the exploration goal is moved to a new target. Since lower altitude necessarily means a loss in energy, the planned paths tend to traverse longer distances to minimise energy loss rate rather than diving towards the target with rapid energy loss. This is generally favourable and allows the sampling reward to have a more significant effect to maximise the benefit of data points collected between exploration targets.

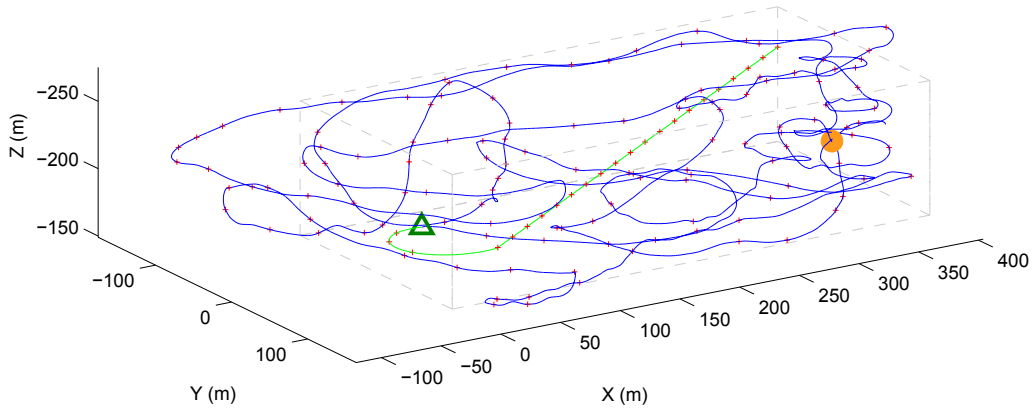


Figure 6.4: Oblique view of single thermal exploration. Autonomous soaring flight starts at the triangle. There is a single thermal bubble centred at (350, 50, -200) with a maximum core vertical wind speed of 3 m/s illustrated by a filled circle. The goal is to reduce maximum uncertainty of the wind field estimate inside the target region defined by the grey dashed box, whilst simultaneously utilising energy captured from the thermal.

The mean field variance is the mean of the variance estimates taken at grid points throughout the region of interest. Both the energy change and the change in mean variance are shown in Fig. 6.6. The energy variation illustrates the planner alternating between capturing energy and exploring the region. This can be seen in the correlation between the two plots. Initially, the aircraft is mostly flying in unexplored regions, resulting in a rapid reduction in variance. However, as the aircraft returns to the energy source to capture more energy ($t = 200 - 300$ s) the new observations are close to previous ones and do not result in significant reduction of the field variance. After enough energy is captured, the aircraft continues to explore the field resulting in further reduction of the variance.

In general, the variance shows an asymptotic decline in overall variance towards a minimum value. This represents the fact that there are a limited number of sample points and due to the nature of GP regression there is necessarily some uncertainty in the regions between the sample points. Overall uncertainty could be further reduced by increasing the number of sample points and allowing additional time for further exploration.

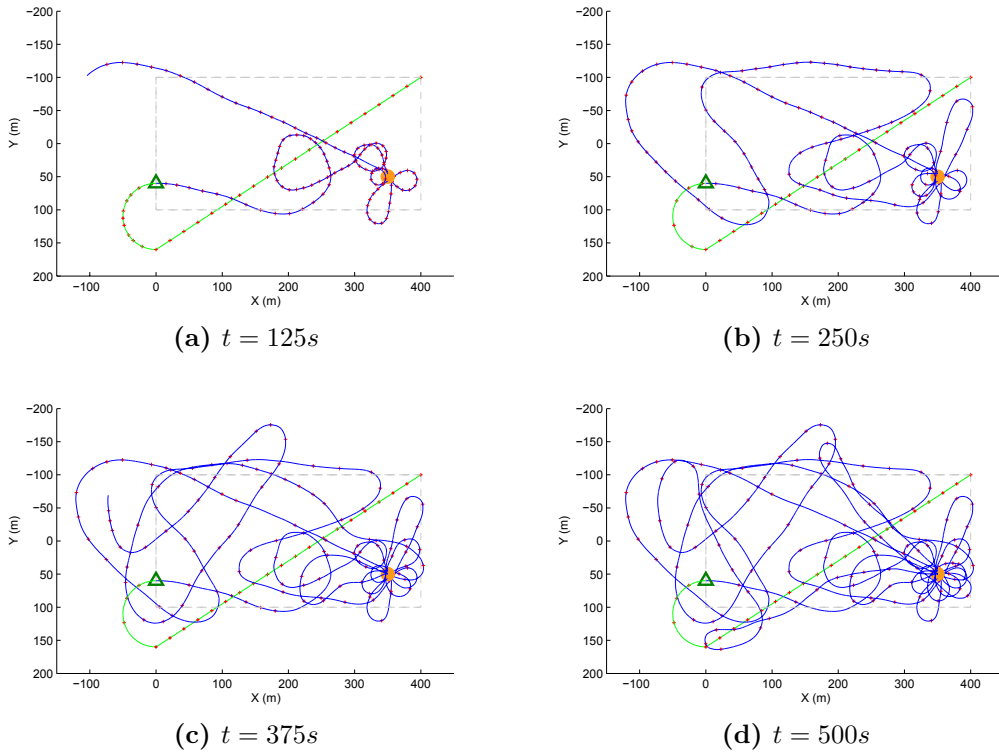


Figure 6.5: Time history of single thermal exploration. Autonomous flight starts at the triangle and continues along the line, initially heading in the positive x -direction. There is a single thermal centred at $(350, 50, -200)$. Stored sample positions are indicated by ‘+’ symbols.

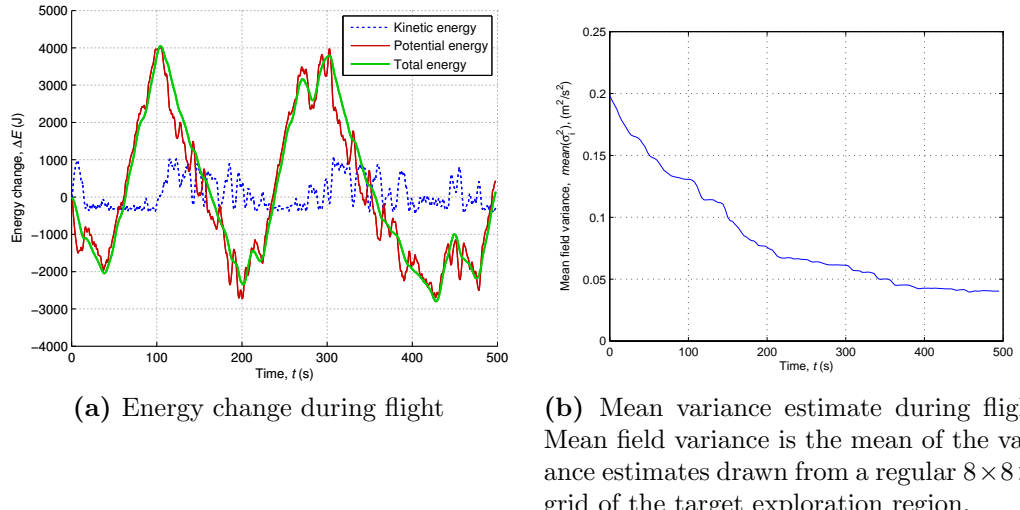


Figure 6.6: Energy and estimated variance during single thermal exploration.

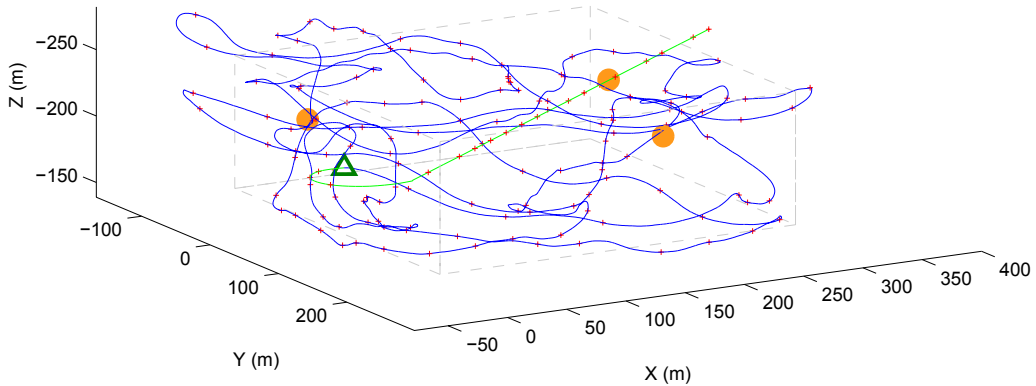


Figure 6.7: Oblique view of multiple thermal exploration. There are three thermal bubbles centred at $(200, 100, -250)$, $(350, -80, -150)$ and $(50, -80, -200)$ with V_{core} of 2 m/s , 3 m/s and 5 m/s respectively.

The second simulation result demonstrates autonomous soaring and mapping over a larger region with three thermal bubbles. In this case, there are two small thermals located at $(200, 100, -250)$ and $(350, -80, -150)$ with V_{core} of 2 and 3 m/s and $r_{lift} = 50$ and 75 m respectively. There is also a larger, more powerful thermal with $r_{lift} = 100 \text{ m}$ and $V_{core} = 5 \text{ m/s}$ located at $(50, -80, -200)$. The exploration box is $x \in [0, 300]$, $y \in [-100, 200]$, & $z \in [-250, -150]$. The simulation time is 500 s and the resulting path is shown in Fig. 6.7 and 6.8 and the videos *multi_thermal.mpg* and *multi_thermal_variance.mpg*.

These results demonstrate the ability to handle multiple energy sources. When autonomous control begins the only known energy source is the 3 m/s thermal. This is used during the first two traversals of the field. At $t \approx 130 \text{ s}$ the larger thermal is found. For the remainder of the flight the planner can gain enough energy from short traversals through the strong thermal to continue exploration (see Fig. 6.9). This demonstrates that the method can utilise different strength energy sources, with considerably less circling required in the strong thermal than the smaller thermals.

A similar pattern in energy use and variance reduction is shown in the multiple thermal case as in the single thermal case. Again, the controller cycles through energy collection and exploration phases. The later cycles are shorter due to the high power available from the large thermal. The results show a fairly steady reduction in overall

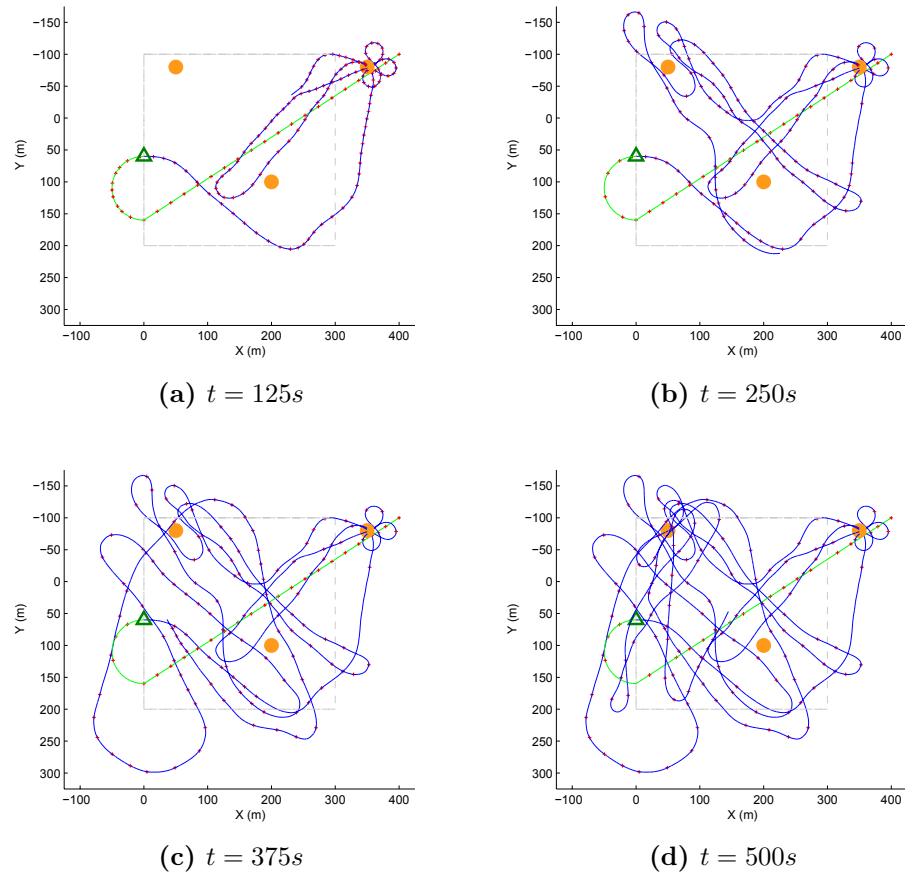


Figure 6.8: Time history of multi-thermal exploration. The thermals are centred at (200, 100, -250), (350, -80, -150) and (50, -80, -200) with maximum lifting airspeeds of 2 m/s, 3 m/s and 5 m/s respectively.

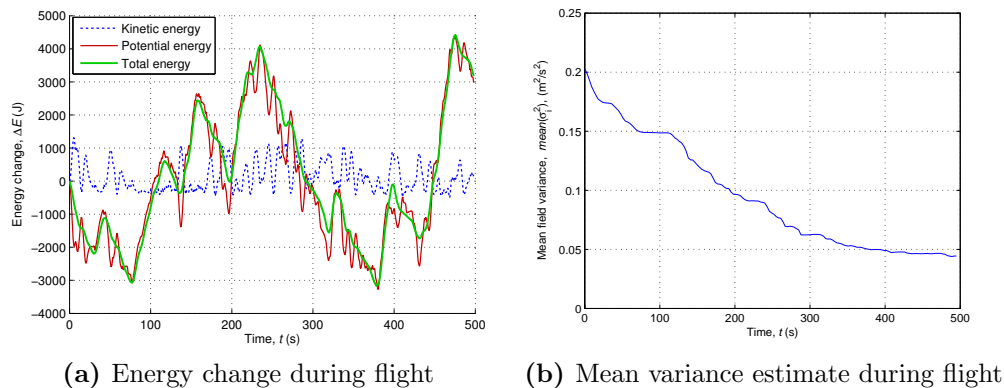


Figure 6.9: Energy and estimated variance multiple thermal exploration.

variance to a similar level seen in the single thermal case. This is a good result given the larger size of the exploration region. Also worth noting is the use of the smallest thermal during flights through that region. Despite the smallest thermal never acting as an energy target, the low-level controller still makes use of the available energy for paths crossing through or near the thermal bubble. This demonstrates the utility of the reward function in generating local paths which utilise any available energy.

Figure 6.10 illustrates the estimate of the wind field at the end of the multi-thermal simulation. This is provided to demonstrate that the exploration is effective at mapping the complete wind field. The GP regression estimates for the thermal core velocities are 1.22, 2.57 and 5.26 m/s for the 2, 3 and 5 m/s thermals respectively. Also captured is the toroidal shape of the thermals and good estimation of the inflow and outflow in the smaller thermals (the larger thermal is too tall for this to be noticeable). This represents an accurate estimate of the wind field and demonstrates the ability of the GP mapping to account for a number of structures simultaneously, which can be difficult for model-based methods that have to separately identify each structure. Of further note is that retraining the model with the final observation set yields optimal hyperparameters of $l = 45.05$ m, $\sigma_f = 0.489$, $\sigma_n = 0.055$, very similar to the values used in simulation. This suggests that retraining should be possible

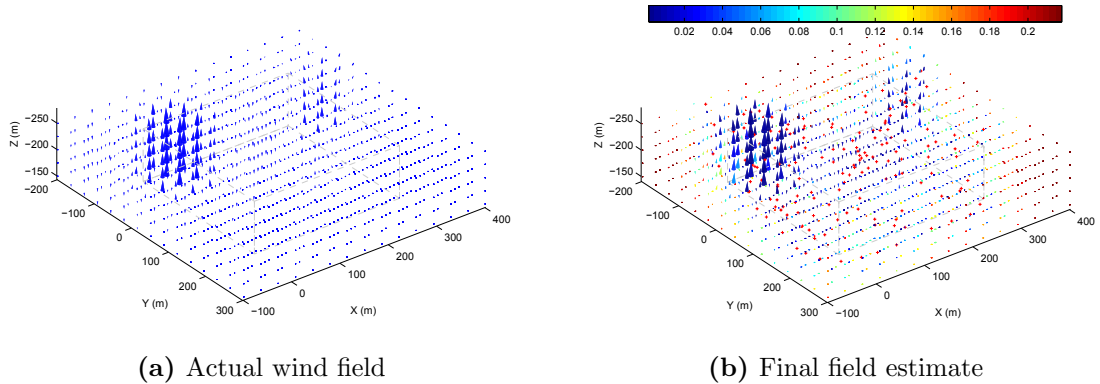


Figure 6.10: Final mean estimate of the wind field from multi-thermal flight. All three thermals are well placed and close to their actual size and strength from an observation set of only 150 points (illustrated as ‘+’ symbols). The cone shading in (b) represents the wind variance estimate at each sample point, σ_W^2 in $(\text{m/s})^2$.

during flight, since a gradient descent would be able to track the optimal solution as the hyperparameters vary slowly from a good initial estimate.

The final results present a more difficult soaring case to demonstrate some of the limitations of the current method. In the final scenario, the wind field is made up of a sinusoidal wave and a single thermal. The wave field is generated using a sinusoidal variation along the x axis.

$$W_x = -V_{wave} \cos\left(\frac{\pi}{4} \cos\left(\frac{2\pi x}{\lambda}\right)\right) \quad (6.10)$$

$$W_z = -V_{wave} \sin\left(\frac{\pi}{4} \cos\left(\frac{2\pi x}{\lambda}\right)\right) \quad (6.11)$$

The wind strength V_{wave} is 2 m/s and the wavelength λ is 200 m. The maximum lift is 1.41 m/s which is enough for energy gain flight (minimum sink is ~ 0.60 m/s straight and level at $V = 15$ m/s) but in a relatively narrow region. The thermal is centred at (350, 50, -200) as in the first set of results but with $V_{core} = 2.5$ m/s and a reduced lifting radius of $r_{lift} = 75$ m (the field is illustrated in Fig. 6.10a). The resulting path is shown in Fig. 6.11 and the videos *wave_field.mpg* and *wave_field_variance.mpg*. In this scenario, the thermal is not found until late in the exploration ($t \approx 400$ s). Although exploration of the field initially heads towards the thermal, energy is lost in travel due to relatively poor estimation of the (initially) unknown sinusoidal field. However, it travels close enough such that the (0, -100, -250) corner of the box becomes the next exploration target. Also, there is just enough energy in the rising regions of the sinusoidal oscillation to gain altitude. However, the constant flow in the negative x direction makes energy gain difficult and relatively slow. Thus, the planner spends a significant amount of time attempting to gain energy from the rising air in the sinusoid (see subfigure 6.12a). During this time there is no reduction in field variance as the aircraft is outside the exploration region (see Fig. 6.13). Eventually, it recovers enough to explore the region around the $x = 0$ face and the information target moves to the opposing ($x = 400$) face. However, the energy lost during exploration needs to be recovered again, and the planner spends more time recovering energy from the rising areas of the wave flow. Finally, at $t \approx 400$ s the thermal is found with

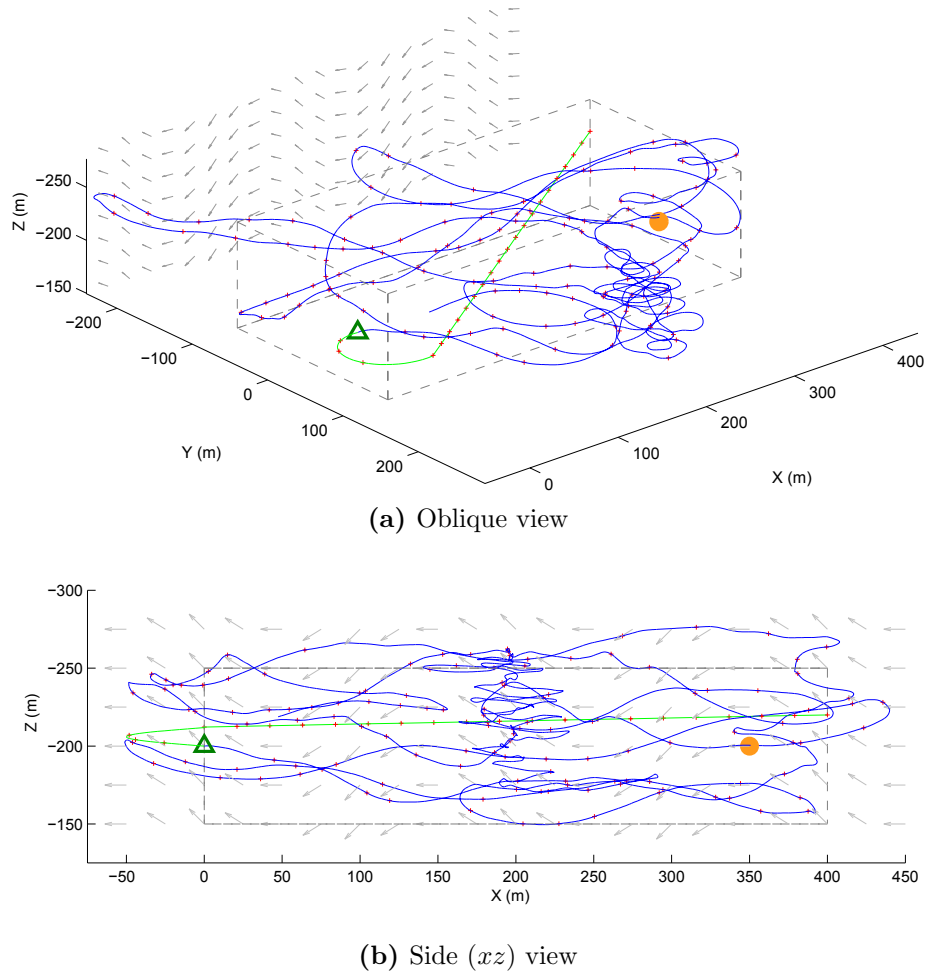


Figure 6.11: Exploration and exploitation of overlaid wave and thermal wind field. The wave is a sinusoidal variation of a 2 m/s wind in the negative x direction with wavelength 200 m, shown by the vector field projected onto the xz -plane. There is a single thermal bubble centred at (350, 50, -200) with a maximum core vertical wind speed of 2.5 m/s illustrated by a filled circle.

significantly higher lift and becomes the new energy target. During the last 100 s further exploration is possible due to the increased energy capture from the thermal.

These results demonstrate the limitations of the current method. In the final scenario, the aircraft does not carry out the mission particularly efficiently. This is largely due to the nature of the target assignment, where the exploration target is defined as the single point which will yield the most information but is not necessarily the most useful one in terms of continuous field exploration. Similarly, the energy target is initially

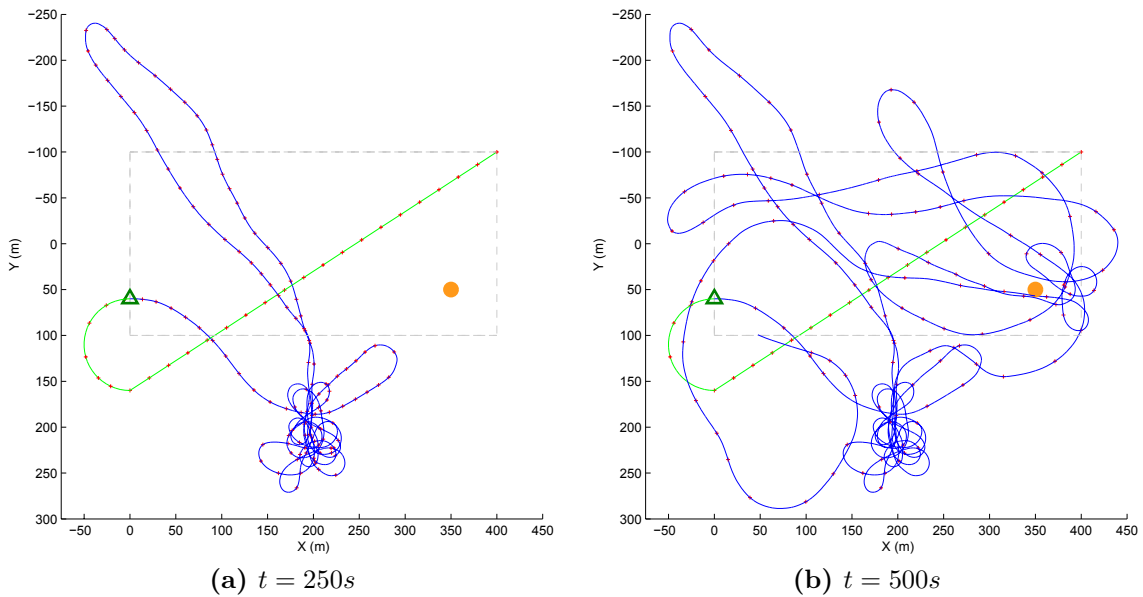


Figure 6.12: Time history of wave field exploration. The wave is a sinusoidal variation of a 2 m/s wind in the negative x direction with wavelength 200 m. There is a single thermal bubble centred at (350, 50, -200) with $V_{core} = 2.5$ m/s illustrated by a filled circle.

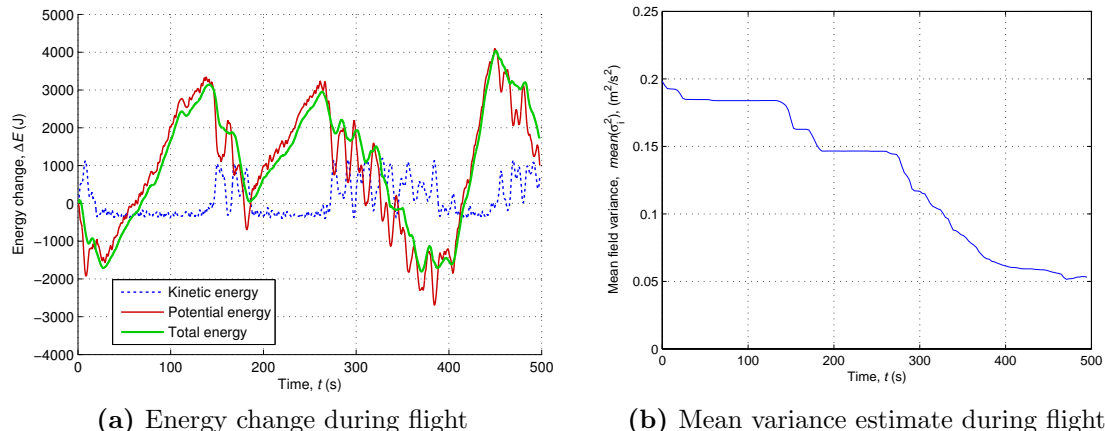


Figure 6.13: Energy and estimated variance during wave and thermal exploration.

outside the target exploration region due to a noisy sample which yielded the highest estimated lift there, despite there being equal energy regions inside the exploration box. In the illustrated scenario, the planner selects a high energy target at the top corner of the region early in the exploration, requiring significant energy capture from the relatively limited energy available from the wave flow. Collecting sufficient energy

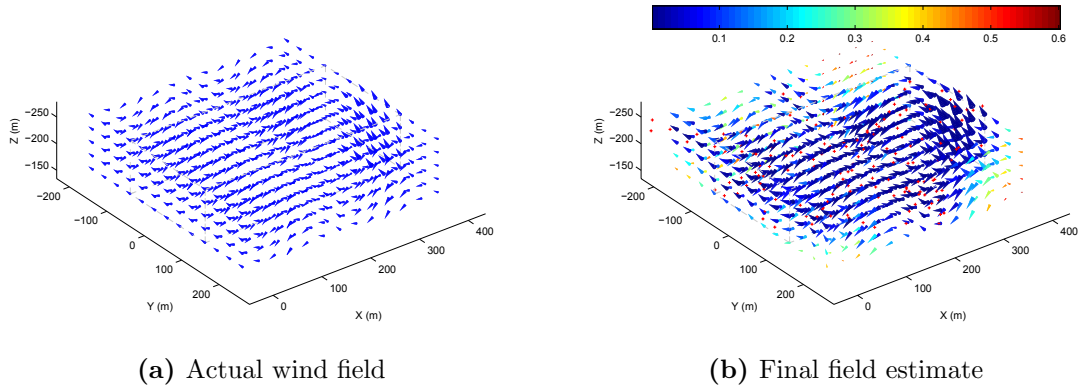


Figure 6.14: Final mean estimate of the wind field from wave & thermal flight. The cone shading in (b) represents the wind variance estimate at each sample point, σ_W^2 in $(m/s)^2$.

to travel to the target takes a long time with very little exploration performed. Both the energy target and information target are single points, and their selection can be biased by poor sampling or noisy observations, leading to a reduction in exploration performance. The resulting wind map at $t = 500$ s (Fig. 6.14) has unexplored regions and significantly higher variance than in the previous cases.

To demonstrate the robustness of the method a set of 100 randomised trials was performed. Each trial is a 500 s simulation for a flight through a random thermal field. The thermal volumetric flow rate $Q_{thermal}$ is defined as the volume of air moving upwards through a horizontal plane through the centre of a thermal. The volumetric flow is dependent on the core vertical speed V_{core} and lifting radius r_{lift} as shown in Eq. (6.12). Note that the thermal model used is conservative, so there is an equal volume of air moving downwards through the same plane in the sinking air region outside the thermal core.

$$Q_{thermal} = \frac{4}{\pi} r_{lift}^2 V_{core} \quad (6.12)$$

For the randomised simulations there are between 2 and 4 thermal bubbles placed randomly in the exploration region with a total volumetric flow equivalent to a single thermal bubble of 2.5 m/s vertical wind and 100 m lifting radius (total $Q_{thermal} = 3.18 \times 10^4$ m³/s). The core speeds range from 0 to 7 m/s and lifting radii range from 40 to 100 m. The resulting time history of the mapping variance estimate and

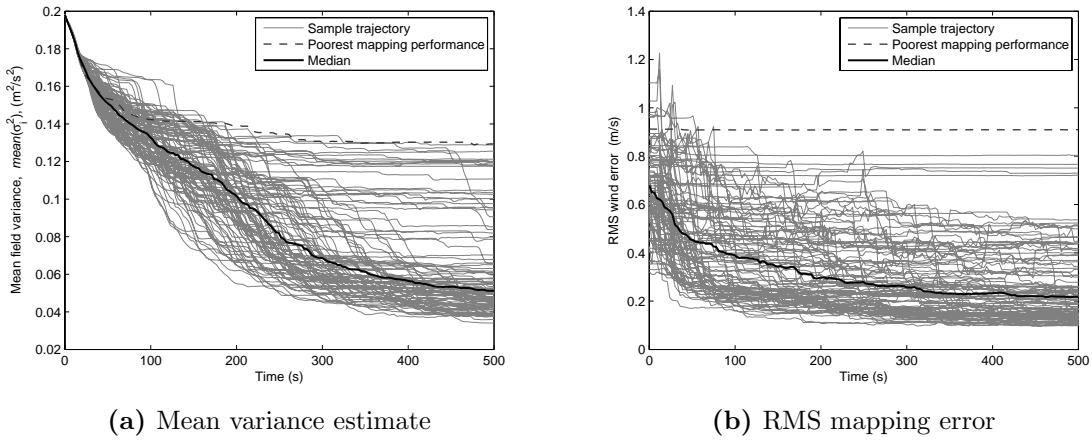


Figure 6.15: Time history of variance estimate and mapping error over 100 simulated flights of 500 s each. Each trial has a random set of thermals with a fixed total lifting volumetric flow rate. The heavy line shows the median across all trials at each time step and the dashed line illustrates the worst performing case.

mapping accuracy are shown in Fig. 6.15. The accuracy is the root mean squared (RMS) map error taken by comparing the wind estimate with the actual wind field at each time step over the regular $8 \times 8 \times 5$ grid used for target assignment. The median field variance at $t = 500$ s across 100 trials was 0.051 (m/s)^2 and the median RMS error was 0.218 m/s .

The simulation was completed in all cases such that the planner never had to cancel the mission due to lack of energy. While most trials significantly reduced the RMS map error, some did not complete the mapping task adequately. The poorest performing case (shown by the dashed line in Fig. 6.15) consisted of two thermals with core speed 1.05 and 6.91 m/s and lifting radii 54.7 and 64.1 m respectively. The path is illustrated in Fig. 6.16. The weak thermal was near the pre-sampled path and consequently already relatively well mapped at the start of autonomous flight. After initial exploration the aircraft spent the remaining flight attempting to collect enough energy from the known small thermal to continue exploration. However, due to the low lift and small radius, the aircraft gained energy very slowly and often lost energy when it left the lifting core and made turns in the surrounding sinking air attempting to return to lifting air. This meant that there was limited improvement

in mapping accuracy due to mapping error being dominated by the unmapped second thermal. This demonstrates the conservative approach of the current control scheme, given that no prior information on the wind field is available. An improved target assignment algorithm may need to be more flexible in selecting exploration targets to prevent extended attempts at utilising weak energy sources to reach a high-energy exploration target.

In some cases there will be insufficient energy for continuous gliding flight. In this case, the planner continues to attempt to explore the region until it reaches the minimum allowable energy level; the minimum altitude and airspeed. At this point the planner would have to notify a higher level mission controller that soaring is not possible with the current information from the wind field. In a practical implementation this would mean that either a propulsion source is required (if available) or the aircraft would have to cancel the mission. Alternatively the planner could reduce the lower altitude limit to allow further exploration at lower altitudes to attempt to find a sufficient energy source. This type of higher level control is not considered here but would form part of future work for implementing this type of system.

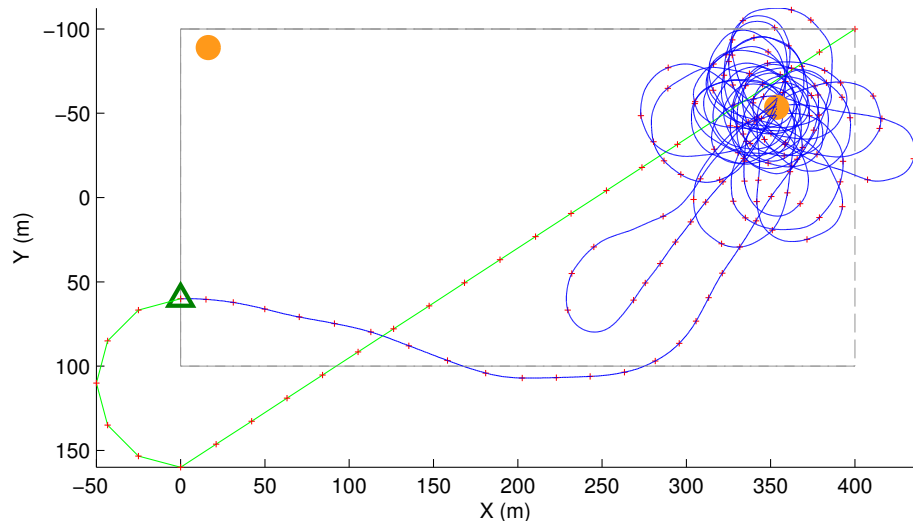


Figure 6.16: Sample trajectory of poor mapping performance due to insufficient energy. The thermal in the top right corner is relatively weak and small. However, the planner estimates that there is sufficient energy for soaring. It spends the rest of the flight attempting to gain enough energy to continue exploration. If the simulation was allowed to proceed the aircraft would eventually collect enough energy to continue exploration.

6.3 Exploration of Dynamic Wind Fields

6.3.1 Spatio-temporal wind mapping

While a constant drift estimate is sufficient in some wind fields, in dynamic fields the features both drift and change with time. In the static wind field cases it was assumed that the field dynamics were much slower than than the length of the mission.

GP regression allows consideration of temporal variation by including a temporal component in the covariance function. Section 5.4 details spatio-temporal wind field mapping. In this section a stationary separable covariance function of spatial distance, time and a drifted distance estimate is demonstrated. From §5.4.2 the covariance function incorporating drift is

$$k(\mathbf{x}, t, \mathbf{x}', t') = \sigma_f^2 \exp \left(-\frac{|\mathbf{x} - \mathbf{x}'|^2}{2l_x^2} - \alpha \frac{|t - t'|^2}{2l_t^2} - (1 - \alpha) \frac{d_W^2}{2l_d^2} \right). \quad (6.13)$$

A stationary function is selected as air properties should be consistent across inertial space. Note that due to the GP formulation this still permits local modelling of (drifting) features, but the expected rate of spatial and temporal variation is the same across inertial space. A separable function is preferred as it represents the simplest combination of spatial, temporal and drift distance estimates. A non-linear combination of these factors would require either additional hyperparameters or a restrictive function which may not offer additional benefit over a separable combination. The separable function also allows easier maintenance of the observation set as reduction in covariance with time is bounded, so that old observations will have a known limited effect on future estimation and can be confidently discarded based on a simple time threshold.

The model is trained using a modified version of the log marginal likelihood as shown in Eq. (6.14). An additional term is included as a penalty on variation of the hyperparameters. This represents a Gaussian prior estimate of the hyperparameters $\mathcal{N}(\theta_0, \Sigma)$ and penalises variation from θ_0 . This improves stability and prevents excessive deviation from initial parameter estimates.

$$\begin{aligned} \log p(\mathbf{y} | X, \theta, M) = \\ -\frac{1}{2}\mathbf{y}^T(K + \sigma_n^2 I)^{-1}\mathbf{y} - \frac{1}{2}\log|K + \sigma_n^2 I| - \frac{n}{2}\log 2\pi - (\theta_0 - \theta)^T\Sigma^{-1}(\theta_0 - \theta) \end{aligned} \quad (6.14)$$

6.3.2 Global target selection

As in the static case, the goal of the global target planner is to maintain energy to allow continuous exploration of the field. However, in the dynamic case the hyperparameters are trained on-line, and the temporal component of the covariance function means that future predictions degrade unless new data is continually collected.

The global planner determines the current target through a heuristic utility measure based on knowledge of the aircraft and wind field. The utility maps goal locations into ‘potential’ power estimates, P , which represent the expected average power available by visiting that goal location from the current location based on map uncertainty, energy required to travel to, and energy available for capture at the target.

Exploration is required to maintain a good map estimate. Thus, the global planner should identify targets which will yield more information about the current wind map. However, depending on the vehicle’s energy state, it may be better to explore or exploit at the current time. In the previous tests, the system targeted the exploration goal if it had sufficient energy and the exploitation goal if it had insufficient energy. While this approach steadily reduces map uncertainty, it would seem that to maximise energy capture regions with potential energy sources should be more attractive for exploration than regions with the same uncertainty but a lower likelihood of containing energy. Thus, the utility function was adapted to determine targets which are beneficial to the aircraft at the current time. When the aircraft has low energy it should favour a more conservative strategy of attempting to capture energy from well-mapped energy sources. When the aircraft has excess energy it should favour a more aggressive approach and attempt to explore uncertain regions with high energy potential to attempt to maximise the future reward of total energy gain.

This is accounted for in the utility function by estimating the amount of excess energy the vehicle would have if it travelled to the target. The excess energy e_{excess} is the current energy, $e_{current}$, minus the target energy e_{target} and an estimate of the energy required to travel to the target e_{travel} . The travel energy is estimated by assuming direct travel to the target for a distance d_{target} at a nominal glide ratio $(\frac{L}{D})_{est}$.

$$e_{travel} = mgd_{target} \left(\frac{L}{D}\right)_{est}^{-1} \quad (6.15)$$

$$e_{excess} = e_{current} - e_{target} - e_{travel} \quad (6.16)$$

The GP regression returns a normal distribution defined by a mean, \bar{W} , and variance, σ_W^2 , estimate for the wind velocity. This feature is exploited by the utility heuristic by assuming an optimistic estimate of the wind in unexplored regions. The wind is estimated using the mean estimate from the current map plus a multiple of the standard deviation (to a maximum of $2\sigma_W$), weighted by the excess energy e_{excess} .

Thus, when the UAV has extra energy the wind is optimistically estimated and higher power is predicted from high variance regions. When the current energy is less than the target, the variance bonus is negative, so the power estimates are pessimistic and the global planner will tend towards the nearest high-power region with low variance. The resulting wind estimate is shown in Eq. (6.17) where e_{max} and e_{min} are the energy limits at the highest and lowest altitude of the exploration region respectively.

$$W_{target} = \bar{W} + 2\sigma_W \frac{e_{excess}}{e_{max} - e_{min}} \quad (6.17)$$

The power available in a target region can be estimated from the adjusted wind and gradient estimates using Eq. (3.76). Dynamic soaring power is calculated by solving for the optimum orientation to maximise power from the estimated wind gradient. However, the average power over the length of a dynamic soaring cycle is less than the maximum instantaneous power (due to energy loss in turns). From the results in gradient soaring demonstrated in §4.1.3 the actual power over a cycle is approximately 1/3 of the maximum instantaneous power (above a minimum gradient cut-off).

6.3.3 Local path planning

The local path planning is the same system as described for the static case (§6.2.3). The temporal component does not change the local path planner as the map can still be queried (though it is now time dependent) and there is still a global target defined for each planning cycle. Thus, the same reward function is still applicable.

6.3.4 Simulation

The aircraft simulation is the same as the previous static case. However, in the dynamic case the GP hyperparameters are trained in-flight using a limited number of gradient descent steps for minimisation of the log marginal likelihood during each planning cycle. This would ideally be a parallel computation but in this simulation the gradient descent is run as a serial process with up to four gradient descent steps allowed after each planning stage.

The hyperparameter values are initialised at $\sigma_f = 0.5$ m/s, $l_x = 50$ m, $l_t = 80$ s, $l_d = 80$ m, $\eta = 0$, $\vec{W}_d = [0, 0, 0]$ m/s and $\sigma_n = 0.1$ m/s, based on estimates of the sensor noise and an approximate scale of features expected to be useful for soaring in a wind field.

During the flights, the maximum number of stored training points is fixed at 150 to prevent excessive computational load. The simulated sensor system collects data at frequency 2 Hz. The relevance of the data is effectively calculated as part of the covariance function for prediction, so observations that are too close together or too old are removed and replaced with new observations. Assuming that only future predictions of the map are required the covariance of existing data increases at a known rate defined by the temporal length scale. This can be translated into a simple threshold on old data since the minimum covariance will be limited by the time difference between the earliest required prediction (now) and the time that the data was recorded. Combining this with the drifted spatial covariance allows old and/or tightly packed data to be reliably discarded.

As in the static case, the local planner plans for a total horizon of 5 seconds, but only the first 3 seconds of the plan are used before replanning. There are three roll rate and three pitch rate commands for a total of nine control options for each branch.

The wind is represented by a dynamic field consisting of features which can move and change strength during simulation. The field is overlaid with the same Dryden continuous turbulence model as in the previous results.

6.3.5 Results

Results are presented for a simulated flight of 500 s in a dynamic wind field. The target exploration region is defined by the box $x \in [0, 400]$, $y \in [-100, 100]$ & $z \in [-250, -150]$. The aircraft begins the simulation with a small set of data already collected; this represents manual or autonomous flight before autonomous soaring control is activated.

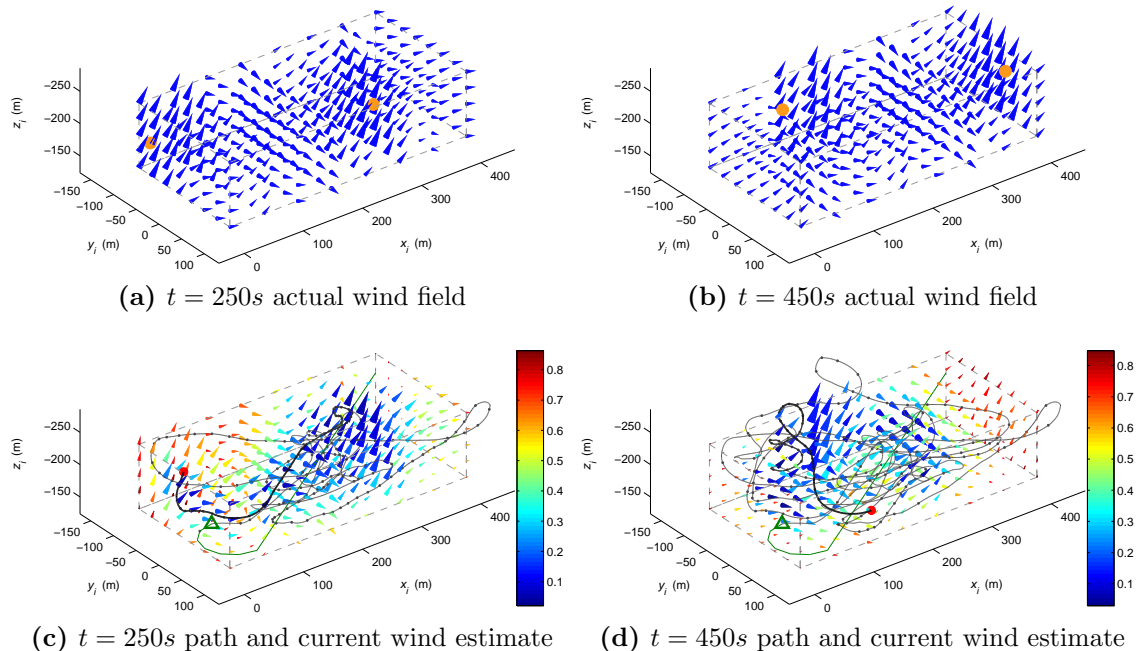


Figure 6.17: Simulated flight through a drifting wind field. Autonomous soaring begins at the green triangle heading in the positive x-direction. The path taken is indicated by the grey line, the current position is the red circle and the heavy line is the previous 40 s of flight. Cone colours represent the variance estimate in $(\text{m}/\text{s})^2$.

The mean wind field is a sinusoidal wave heading in the positive x -direction with a wind speed of 2 m/s and wavelength 200 m. The maximum vertical contribution from the wave is ± 1.41 m/s. Overlaid are two thermal bubbles, both with a core lift of 3m/s which reduces to zero lift at 50m radius. The thermal model is a toroidal recirculating model with conservative vertical and horizontal flow so that the inner lifting core is surrounded by sinking air with a maximum sink of 0.65 m/s. The two thermals start centred at (150, 50, -200) and (-150, -50, -200) respectively. The entire field drifts through inertial space at a constant speed of $W_{drift} = (0.6, -0.1, 0)$ m/s. This means that one thermal starts near the centre of the field and drifts outside the $+x$ boundary by the end of the simulation. The second thermal starts outside the region and drifts into the region by the end of the simulation. This scenario was selected to highlight the ability of the planner to utilise a number of energy sources, and show that continuous exploration is necessary to utilise all available energy sources.

The resulting path is demonstrated in the attached video *drifting_thermals.mp4* and following figures. The coloured boundaries on the lower half of the video illustrate the wind utility estimate. Figure 6.17 shows the progress of the simulation at $t = 250$ s and $t = 450$ s. The actual wind is also shown to compare against the estimate. Figure 6.18 illustrates the energy change during the flight. Of particular note here is

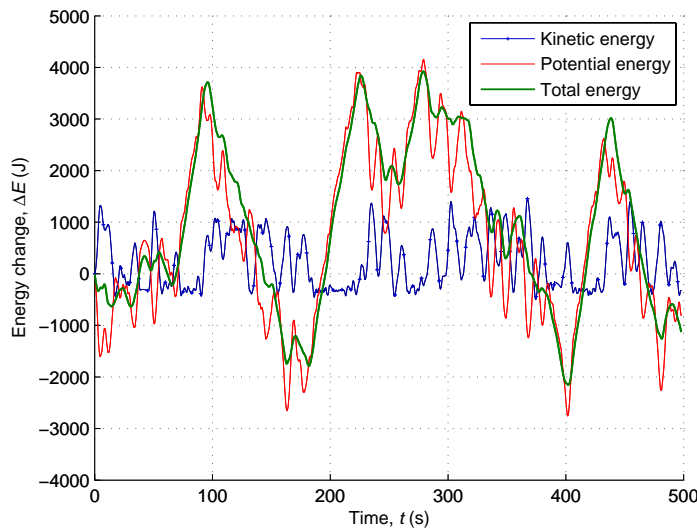


Figure 6.18: Platform energy during simulated flight.

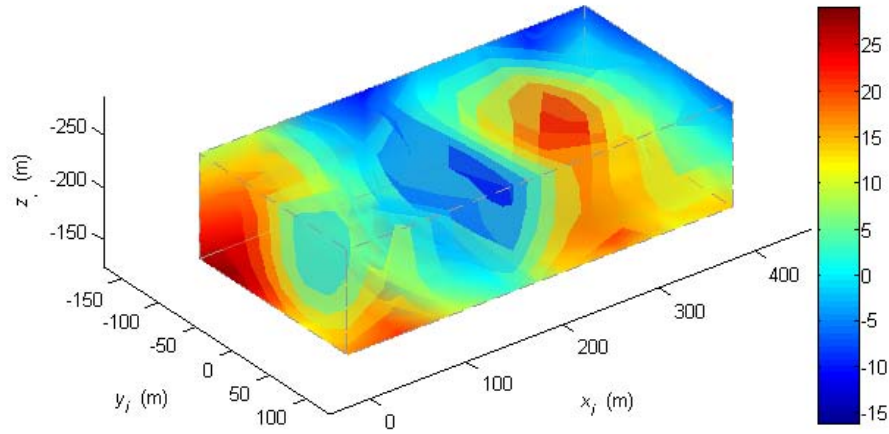


Figure 6.19: Global utility heuristic estimate at $t = 250$ s in terms of specific power (W/kg). Both thermals are of similar estimated strength, but the incoming thermal near $(0, -100, -200)$ has a higher utility because the aircraft is in a high energy state and favours exploration over exploitation.

the overall energy control and particularly the use of semi-dynamic dolphin soaring in the sinusoidal field early in the flight demonstrating the ability of the planner to utilise both static and dynamic soaring strategies in the same framework.

Figure 6.19 illustrates the global utility at $t = 250$ s. In this instance, there is a well mapped thermal near the middle of the field, and a new thermal entering the region of interest through the $x = 0$ plane. At 250 s the aircraft is in a relatively high energy state flying at mid altitude and high speed ($V_a = 25$ m/s). Thus, the global planner favours exploration of regions with high estimated energy and high uncertainty. The fewer number of recent sample points near the incoming thermal increases the estimated power utility of targets in that region. In the remaining flight, the two thermals are alternately tracked as the planner attempts to maintain low uncertainty estimates of both high-energy features.

The hyperparameters at the end of the simulation also provide information on how well the field has been estimated. At $t = 500$ s the hyperparameter estimates were: $\sigma_f = 1.04$ m/s, $l_x = 50.2$ m, $l_t = 121.8$ s, $l_d = 65.0$ m, $\eta = -6.49$, $\sigma_n = 0.0535$ m/s and $\vec{W}_d = [0.599, -0.141, 0.164]$ m/s. The negative η (corresponding to $\epsilon = 0.0015$) indicates that the prediction was relying almost solely on the drifted estimate, and that the wind drift was relatively well estimated, especially in the x -direction. Other

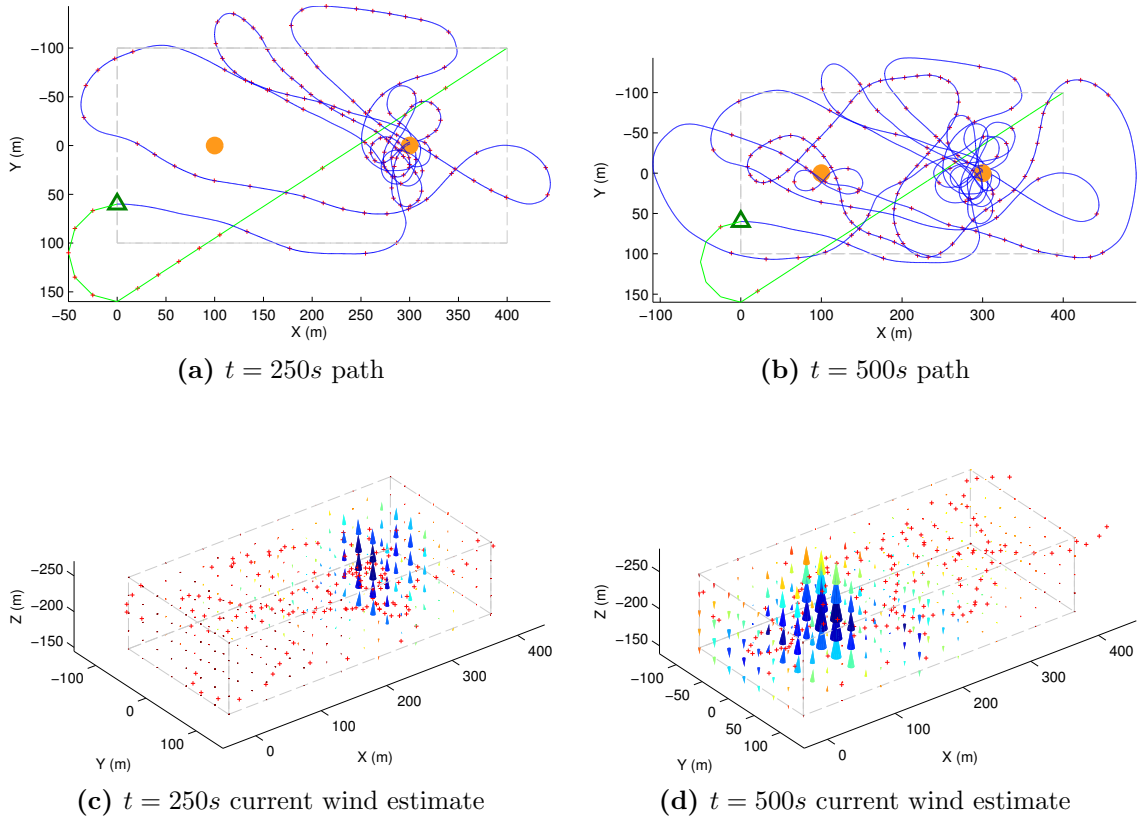


Figure 6.20: Simulated flight through dynamic thermals. The left thermal starts with a core speed of 0 m/s which linearly increases to 5 m/s at 500 s. The right thermal starts with a core speed of 5 m/s which linearly decreases to 0 m/s at 500 s.

simulations not presented here showed similar results, with most simulations ending with a good drift estimate and low η values. For very low drift however, the two length scales tend to converge and η becomes insignificant.

The final set of results show the ability of the system to handle temporal variation of the field. In this case, there are two thermal columns located at $(100, 0, -200)$ and $(300, 0, -200)$ both with lifting radii 75m. Initially the first thermal has a core speed of zero but it linearly increases to 5 m/s over 500 s. The second thermal starts with a maximum core speed of 5 m/s which decreases linearly to 0 m/s over 500 s. Thus, the planner has to constantly track the changing dynamics of the thermals. The resulting path and map estimate at the middle and end of the simulation is shown in Fig. 6.20. The attached video *double_thermal.mpg* provides a clearer illustration of the variation of the field and wind map estimate over the simulation.

The planner is capable of utilising one thermal until it is exhausted and then exploring to find and exploit the other thermal for the rest of the flight. The covariance function and planning routine are identical to the previous simulation. The system estimated the field drift as $\vec{W}_d = [-0.029, -0.020, -0.020]$ m/s and a time length scale of 75.3 s.

6.4 Summary

An autonomous soaring aircraft would need to collect wind data in flight, organise the data into a useful form, and then use the data to take actions to collect energy. This chapter proposed a system architecture for collecting wind data in flight, generating a wind map from the data, and then using an energy based planning and control system to simultaneously explore and exploit the wind. The system is data driven and does not require pre-existing models for the wind or pre-defined energy gain flight patterns. Using GP regression for the wind mapping also allows a planner to incorporate exploration of the map so that the planner can balance the tasks of maintaining an accurate wind map with collecting sufficient energy to continue exploration. By drawing directly from estimations of the energy effect of different control actions, the path planning scheme can make flexible use of energy-gain wind features allowing a combination of static and dynamic soaring.

The system was demonstrated in simulation with a flight model based on a small gliding UAV. It proved to be capable of exploring and exploiting both static and dynamic wind fields with a range of wind features. The system was capable of building a useful wind map even in the presence of turbulence and demonstrated robust performance when sufficient energy was available for soaring.

Chapter 7

Conclusion

Unmanned aerial vehicles typically carry out flight missions using energy stored on-board to provide propulsive power. Energy storage such as batteries and fuel provide a limited energy density; they can carry a fixed amount of energy per unit of mass. Since aircraft are limited in the mass they can carry, they are limited in the amount of energy stored on-board the aircraft. This limits flight duration as they cannot continue to fly after the energy required for propulsion is exhausted. By utilising soaring flight, however, a UAV could fly for periods of time without using propulsive power and extend mission duration without requiring additional stored energy.

This thesis presented the mechanisms of gliding flight in wind and proposed a method for a fixed-wing UAV to autonomously soar to increase flight time without requiring additional stored energy. The proposed system takes wind data collected in flight and generates a wind map using GP regression. A global planner uses the current aircraft energy and the GP map to determine targets which will improve the current map estimate or collect energy. An energy-based planning and control system uses the wind map and the mathematical gliding model to estimate the energy to be gained or lost and uses the information to plan efficient paths to the global target. The system is capable of creating and using a wind map to explore and exploit a wind field to provide extended flight without propulsive power. Section 7.1 summarises the contributions made in this thesis and §7.2 provides directions for future research.

7.1 Summary of Contributions

This thesis presents a number of novel contributions to the field of autonomous soaring control.

Analysis of the mechanisms of gliding and soaring flight

The first contribution is a clear and principled description and model for gliding flight in wind. Analysis of the model allows calculation of the optimum energy gain conditions for soaring flight. These equations provide a background understanding of the mechanisms of soaring flight; the conditions required for soaring and the actions that maximise the energy captured in each condition.

Control for dynamic soaring in horizontal wind shear

A mode-based controller for soaring in horizontal wind shear was presented. Using the mathematical soaring model the conditions for maximising energy gain from a limited thickness shear layer were identified. The controller exploits this knowledge to maximise energy gain during the climb and dive phases of a dynamic soaring cycle. By combining these phases with turn and travel phases the controller is capable of utilising energy gain dynamic soaring cycles and to travel towards a goal. Results showed that with predefined or estimated altitude limits the controller is capable of upwind travel in typical shear layer conditions with a small UAV.

Flexible energy-based planning

The third contribution is an energy-based control scheme which can plan energy-efficient paths in known wind fields. Using the mathematical energy model the planner estimates the energy cost of actions. A reward function is proposed which combines energy cost, power available and a progress towards a global goal in a flight energy framework. The resulting planner is demonstrated to be capable of planning paths

utilising both static and dynamic soaring. This negates the requirement for specialised control strategies for each type of wind encountered and allows the planner to flexibly utilise all soaring techniques in the same framework.

Gaussian process regression for wind mapping

Planning soaring paths requires an adequate estimate of the wind field. This thesis proposes a mapping method for generating a wind map from samples taken during flight. Gaussian process regression is a non-parametric Bayesian machine learning method of regression analysis. Applied in a wind mapping context it provides a continuous and differentiable wind map. The method is data driven, model-free and capable of representing features over a range of length scales. Importantly, the GP regression also returns a confidence estimate which can be used to direct future searches of the field for exploration and to maintain map quality in energy-gain regions. A specialised covariance function is proposed for wind fields which allows prediction of drifting features in the GP learning framework. GP regression for wind mapping is demonstrated in both static and dynamic wind fields.

Simultaneous exploration and exploitation of a wind field

The final contribution is the proposed modular system architecture for a small gliding UAV to autonomously explore and exploit wind energy in an unknown wind field. The system is designed to collect wind data in flight, generate a wind map from the data, and plan energy efficient paths to explore the field without propulsive power. The system is data driven and does not require pre-existing models for the wind or pre-defined energy gain flight patterns. The system was demonstrated in simulation with a flight model based on a small gliding UAV. It proved to be capable of exploring and exploiting both static and dynamic wind fields with a range of wind features. The system was capable of building a useful wind map even in the presence of turbulence and demonstrated robust performance when sufficient energy was available for soaring.

7.2 Future Research

As a relatively new research area there is significant scope for further research in autonomous soaring. The application of UAVs has grown considerably in recent years and appears to be accelerating. Like many technologies, whilst UAVs were once purely the domain of military organisations, they have now found applications in civil areas such as surveillance, monitoring, exploration, remote sensing, scientific data collection and search and rescue. As is the case for many applications of robotics, UAVs are ideal for jobs that are too dull, complicated or dangerous for humans. Autonomous soaring has considerable potential for long-duration sensing missions. For example, currently direct sampling of the atmosphere requires either weather balloons or manned aircraft. Balloons are uncontrolled and can not be accurately targeted to sample a particular region. They also only sample each altitude once, since they usually rise until they burst. Manned aircraft have a much greater degree of control but sampling missions are expensive. An autonomously soaring UAV could provide cost-effective data collection over long periods of time with a high degree of controllability.

The first goal of future research would be to demonstrate some of the concepts proposed here on a UAV. The planner presented in this thesis was specifically designed to require sensors which could be carried by a small UAV and to be computationally efficient enough to run on a small computer (such as a PC/104). The baseline design used throughout the thesis (the SBXC remote control cross-country glider) has been demonstrated in previous soaring research as it provides an efficient gliding platform with sufficient payload volume and mass capacity for an autopilot/navigation system, an additional single-board computer and a wind data sensor.

I believe the earliest attempts should focus on practical demonstration of wind field mapping. This thesis presented work which is based on the ability to take observations from a wind field and generate a wind map. However, there is currently no data collected by an aircraft in a relatively small region with consistent revisiting of areas in the field. I think the collection of this data would provide a very useful source

of information for many researchers in this field. This would also provide a good source of data to generate appropriate comparisons of the performance of a variety of mapping methods. Finally, collecting this data need not require a gliding aircraft or even autonomous control. An interesting concept would be to instrument an RC glider piloted by a knowledgeable pilot attempting to soar in thermal lift. This would provide a good analogue to the type of data which could be expected during an autonomous soaring flight. From this data it would be possible to generate more accurate wind fields and to justify the use of a particular mapping method. The next step would be to add some degree of control to attempt autonomous or semi-autonomous soaring control.

A further extension of the current work would be to include consideration for powered aircraft. A powered UAV could utilise the soaring techniques along with propulsive power to extend mission duration. Including propulsive power in the energy equations should not be too difficult and would provide further flexibility for soaring control. Of further interest would be to consider a propulsion system capable of recapturing energy during flight and storing it for later use. This could be possible with an electric folding propeller system, which could be powered to provide propulsion, allowed to free spin to recapture energy, or folded for unpowered glides.

The current work did not focus on computational efficiency. This may be important for the GP regression. To limit the computational load in the current work the number of stored observation points was limited to minimise the size of the covariance matrix (the inversion of which accounts for most of the computational load). However, methods exist for sparse on-line GPs [24] which may allow an increase in the number stored points and map quality without sacrificing computational performance.

It would also be interesting to consider combining soaring flight with solar energy capture. The atmosphere is generally more stable at night and there are fewer opportunities for energy gain. However, an aircraft which collected solar energy could utilise soaring flight during the day whilst simultaneously charging batteries and use battery powered propulsion overnight. Such a system could provide almost endless flight.

This type of system would be especially applicable to exploration missions on other bodies in the solar system. There are a number of scientifically interesting targets in the solar system with atmospheres thick enough to support a flying vehicle. Venus, Mars and the Saturnian moon of Titan have all been considered for autonomous aerial exploration [14, 68]. Titan in particular offers many advantages for flying vehicles including a thick atmosphere with high pressure and density and low surface gravity [64]. A number of concepts have been considered for aerial exploration including balloons, blimps, fixed-wing aircraft and helicopters. Blimps are currently a favoured option as they provide long mission duration and require low propulsive power. However, they are relatively slow and can be heavily affected by wind. A fixed-wing aircraft could provide more control and higher speed but would normally be limited in mission duration by propulsive power. A soaring aircraft, on the other hand, could provide the advantages of an aircraft without being limited by propulsive power. A previous study by the author has shown that wind conditions are believed to exist on parts of Titan which may be sufficient for continuous gliding flight [58].

An interesting extension to the current work would be to examine the possibility of cooperative soaring control across multiple vehicles. It is conceivable that a team of soaring aircraft could coordinate and cooperate to perform a mission using soaring techniques. This would be an interesting problem in terms of team energy management, as cooperating agents could both monitor energy sources and explore a field. There is already considerable literature in the robotics field concerning cooperation of teams of robots, and some of this could be applied to a soaring team. Work such as map maintenance could also be shared through a decentralised network where all aircraft contribute to a shared estimate of the wind field.

Future research could approach the idea of including external sensor information in the wind mapping problem. The work in this thesis focused only on local mapping from direct observations of the wind. However, there are other additional data sources which may aid mapping and/or planning. For example, a vision system could be used to identify features which are likely to be driving thermal formation. Ground features, clouds, and other soaring aircraft could all be used as indicators of soaring conditions.

Larger scale data such as weather data or topographical information could also be included to give prior map estimates or to provide long term planning. Fusing the local, short term planning presented in this thesis with longer horizon planning could provide a system which is capable of travelling much longer distances. Finally, the planner could incorporate a higher level of machine learning between flights to improve prediction for future flights.

Finally, it would interesting to include machine learning in the path planning and control. A machine learning technique at the planning stage could learn actions based on wind conditions to maximise energy gain. This is a natural reinforcement learning (RL) problem since the actual reward can be calculated almost immediately and incorporated into future estimations. Wharington considered the applicability of RL to soaring control in his PhD thesis [105] but concluded that at that time it was too computationally intensive and learnt too slowly for direct learning in flight. With improvements in small computers and developments in RL techniques it would be interesting to revisit this area.

Appendix A

Toroidal thermal model

This section presents the equations for the toroidal thermal model. Background information can be found in §2.2.2.

The basic shape is a torus. A toroidal shell is formed by rotating a circle of radius r and centre $(R, 0, 0)$ in the xy -plane about the z -axis,

$$\left(R - \sqrt{x^2 + y^2} \right)^2 + z^2 = r^2. \quad (\text{A.1})$$

A toroidal thermal would have rising air in the centre core surrounded by sinking air. Having streamlines running around the torus shells simulates this type of flow. The simplest toroidal field has a constant velocity around the shell sections. In this case, the magnitude of vertical flow is constant in the core ($x^2 + y^2 < R^2$) and constant outside the core. However this yields significantly higher downwards volumetric flow than upwards volumetric flow. Ideally the model should have equal volumetric lifting and sinking air, thus making the thermal bubble conservative in its flow.

Firstly, note that the toroidal model is equivalent to a circle rotated about the z -axis to form a toroidal shell. If the thermal is made up of all shells for $r \in (0, R)$ then this defines a filled torus which represents the thermal.

To remain conservative in the lateral direction we can simply show that in any toroidal shell there is no net horizontal flow. This is always true if the flow is aligned parallel

to the shell and is anti-symmetric about the xy plane, since at any point (x, y, z) the lateral flow is equal and opposite to the lateral flow at the corresponding $(x, y, -z)$ point. This remains valid for volumetric flow since the flow volume is a function of the lateral distance $\sqrt{x^2 + y^2}$ which is the same for that pair of points. This can be applied at all points on the lateral shell except when $z = 0$, but in that case the shell is perpendicular to the xy plane so there is no lateral flow. Thus, for streamlines around a toroidal shell there will be no net lateral flow.

However, this does not apply to the vertical flow. In order to solve for a no net vertical flow we have to determine the volumetric flow, since the vertical flow is positive for $\sqrt{x^2 + y^2} < R$ and negative for $\sqrt{x^2 + y^2} > R$. In this case we look at a disk through the centre of the thermal at $z = 0$. The volumetric flow can be considered as the volume swept out by rotating the vertical velocity profile around the z -axis. If the total volume swept is zero, considering the volume swept out for negative vertical velocity as negative volume, then the net vertical flow is zero.

Looking at the xz -plane and taking the vertical speed W_z as a function of the x -distance, we need a function such that

$$2\pi \int_0^{2R} xW_z(x)dx = 0. \quad (\text{A.2})$$

For the toroidal section, $W_z(R) = 0$ since this point is the centre ring of the torus where the vertical speed is zero. The maximum velocity V_{core} should be at the core. Then,

$$W_z(0) = V_{core}, \quad (\text{A.3})$$

$$W_z(R) = 0, \quad (\text{A.4})$$

$$W_z(2R) = 0. \quad (\text{A.5})$$

Also, we consider that the volumetric flow has to be balanced around the $x = R$

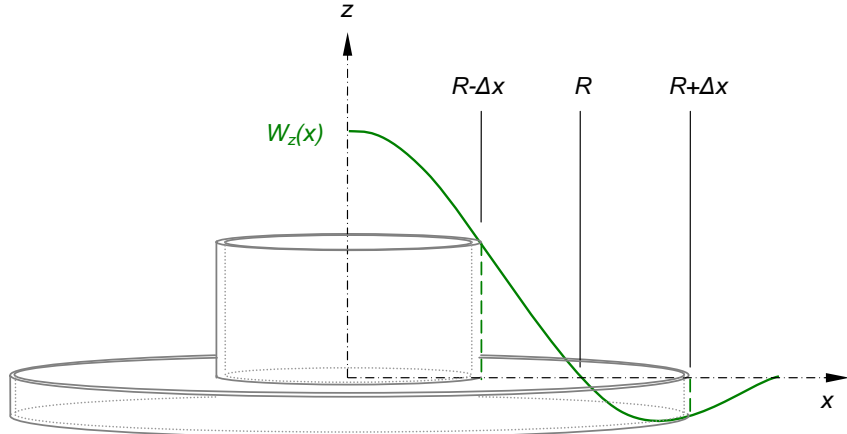


Figure A.1: Balanced vertical volumetric flow for toroidal thermal model

point, such that

$$(R - \Delta x)W_z(R - \Delta x) = (R + \Delta x)W_z(R + \Delta x) \quad (\text{A.6})$$

as shown in Fig. A.1.

A simple solution is a piecewise solution with a linear section for $x \in [0, R]$. Solving for the quadratic for $x \in (R, 2R]$ that meets Eq. (A.6) gives

$$V_w(x) = \begin{cases} V_{core} - \frac{V_{core}}{R}x & \text{for } x \in [0, R], \\ \frac{V_{core}(x-R)(x-2R)}{Rx} & \text{for } x \in (R, 2R]. \end{cases} \quad (\text{A.7})$$

However, this solution gives a peaked core. Ideally, the solution should have a smooth core such that

$$\lim_{x \rightarrow 0^+} \frac{dW_z}{dx} = 0. \quad (\text{A.8})$$

A variable substitution allows easier analysis. Let $\chi = x - R$ such that

$$g(\chi) = xW_z(x). \quad (\text{A.9})$$

Then, from Eq. (A.6) the function $g(\chi)$ needs to be odd around the point $\chi = 0$. The

new set of requirements on g is

$$g(\chi) = -g(-\chi), \quad (\text{A.10})$$

$$g(0) = 0, \text{ and} \quad (\text{A.11})$$

$$g(R) = 0. \quad (\text{A.12})$$

$$(\text{A.13})$$

Making the substitution into the volumetric flow integral (Eq. (A.2)),

$$2\pi \int_{\chi=-R}^R g(\chi) d\chi = 0 \quad (\text{A.14})$$

which is true for all odd functions $g(\chi)$. Solving for the boundary conditions yields

$$\left. \frac{dg(\chi)}{d\chi} \right|_{\chi=\pm R} = RV_{core}. \quad (\text{A.15})$$

There are many solutions to this set of conditions. The simplest polynomial solution is a cubic in $g(\chi)$

$$\begin{aligned} g(\chi) &= \frac{V_{core}}{2R^2} \chi(\chi + R)(\chi - R) \\ \Rightarrow W_z(x) &= \frac{V_{core}}{2R^2} (x - R)(x - 2R). \end{aligned} \quad (\text{A.16})$$

A quintic polynomial can be solved with the smooth core condition

$$\begin{aligned} g(\chi) &= \frac{V_{core}}{8R^4} \chi(\chi + R)(\chi - R)(7R^2 - 3\chi^2) \\ \Rightarrow W_z(x) &= \frac{V_{core}}{8R^4} (x - R)(x - 2R)(4R^2 + 6xR - 3x^2) \end{aligned} \quad (\text{A.17})$$

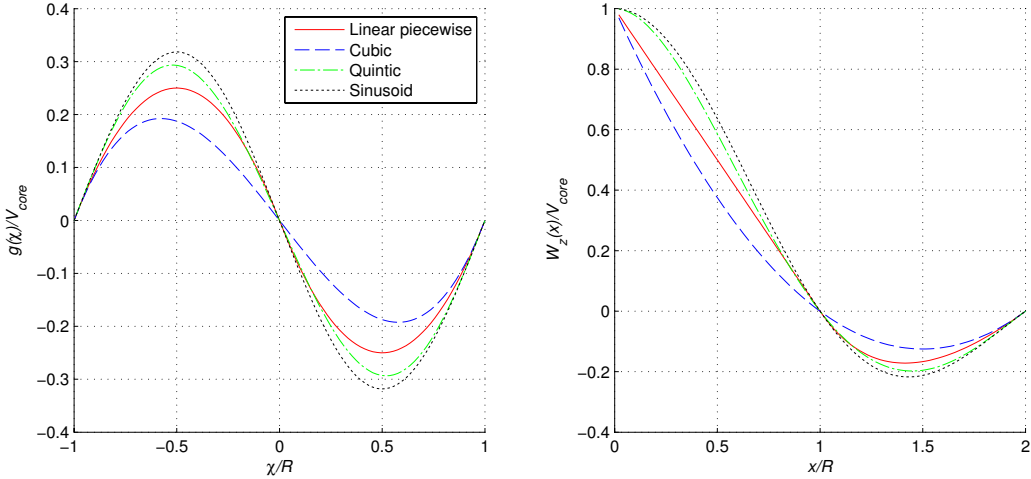


Figure A.2: Generating functions and vertical velocity profiles for toroidal thermal model

Finally, a sinusoidal solution can also be found to meet the conditions

$$g(\chi) = \frac{RV_{core}}{\pi} \sin\left(\frac{\pi\chi}{R}\right)$$

$$\Rightarrow \quad W_z(x) = \begin{cases} \frac{RV_{core}}{\pi x} \sin\left(\frac{\pi x}{R}\right) & x \neq 0 \\ V_{core} & x = 0. \end{cases} \quad (\text{A.18})$$

These generating functions and their corresponding vertical velocity profiles are shown in Fig. A.2.

The quintic and sinusoidal solutions are preferred as they both have smooth core velocities and are continuously differentiable across the domain. The profiles are relatively similar and the toroidal thermal model uses the sinusoidal curve due to the decay outside the domain and the relative ease of implementation.

Using the sinusoidal vertical velocity profile, the required lateral velocities can be solved to yield streamlines which pass around the toroidal sections. A final condition is that the toroidal sections should be elliptical to give the model more flexibility. This allows simulation of column-like thermals with highly elliptical cross sections and degenerates to the pure vertical profile as the eccentricity approaches one, yielding a thermal column similar to existing models.

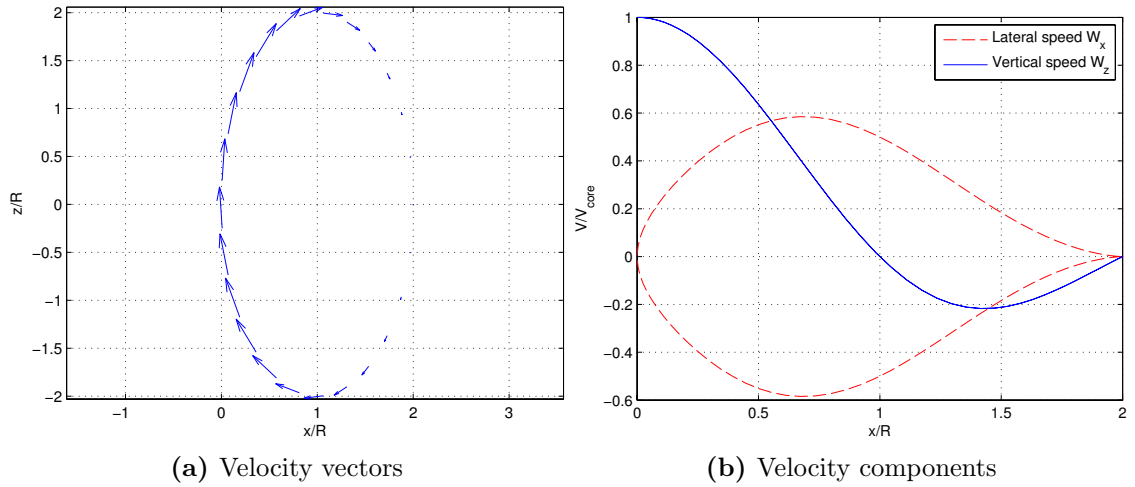


Figure A.3: Velocity profile for an elliptical section with elliptical axis ratio of 2

Figure A.3 shows the velocity field for a single elliptical section with an elliptical axis ratio of 2.

The thermal must have a limited extent. The natural choice is to have a single toroidal thermal bubble defined inside the extent of the torus for $r \leq R$. However, this limitation would mean that there would be significant step changes in velocity between the thermal and the surrounding field. This can be corrected by scaling the vertical velocity with height. Any balanced scaling in z will retain the conservative flow as long as it is symmetric about the centre xy -plane. A cosine scaling is selected with magnitude 1 in the centre and dropping to 0 at the vertical limits ($z = \pm kR$) where k is the elliptical axis ratio. Then, the resulting equations for a toroidal thermal centred at (x_0, y_0, z_0) with an elliptical axis ratio of k are:

$$d = \sqrt{(x - x_0)^2 + (y - y_0)^2} \quad (\text{A.19})$$

$$W_z = \begin{cases} \frac{-V_{core}R}{2\pi d} \sin\left(\frac{\pi d}{r}\right) \left(\cos\left(\frac{\pi(z-z_0)}{kR}\right) + 1 \right) & \text{if } d \neq 0 \\ -V_{core} & \text{if } d = 0 \end{cases} \quad (\text{A.20})$$

$$W_x = \begin{cases} \frac{-W_z(z-z_0)(x-x_0)}{d(d-R)k^2} & \text{if } d \neq \{0, R\} \\ \frac{-V_{core}}{2k^2R} \left(\cos \left(\frac{\pi z}{kR} \right) + 1 \right) & \text{if } d = R \\ 0 & \text{if } d = 0 \end{cases} \quad (\text{A.21})$$

$$W_y = \begin{cases} \frac{-W_z(z-z_0)(y-y_0)}{d(d-R)k^2} & \text{if } d \neq \{0, R\} \\ \frac{-V_{core}}{2k^2R} \left(\cos \left(\frac{\pi z}{kR} \right) + 1 \right) & \text{if } d = R \\ 0 & \text{if } d = 0 \end{cases} \quad (\text{A.22})$$

Figure A.4 illustrates the velocity vector field and vertical velocity profile sections for a toroidal thermal.

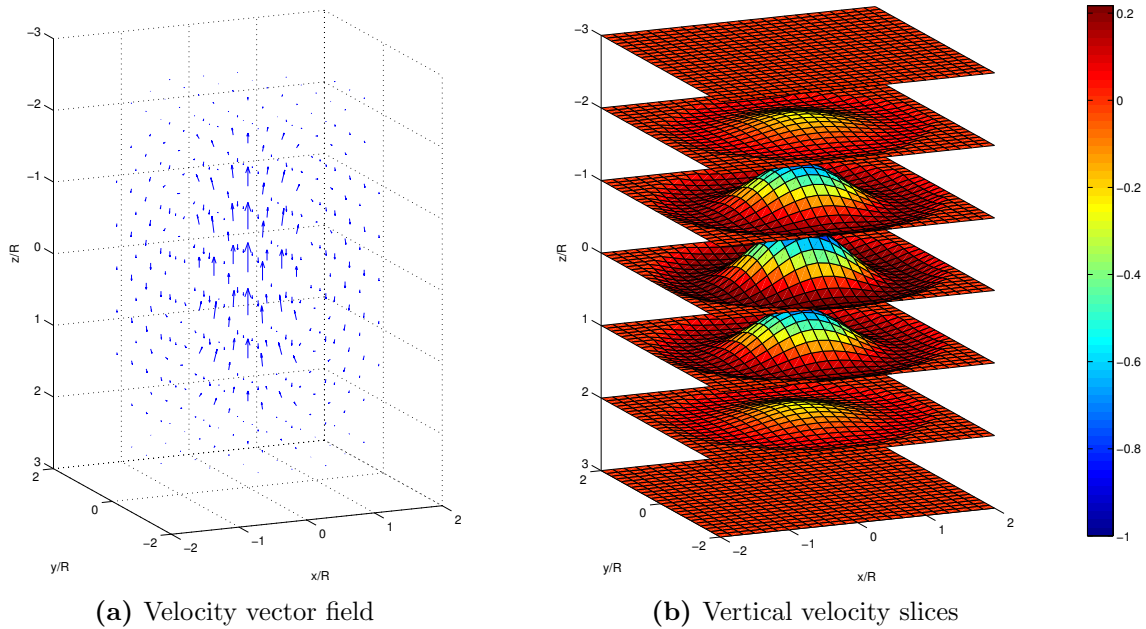


Figure A.4: Velocity vector field and vertical velocity profile sections for a toroidal thermal with elliptical axis ratio $k = 3$

Appendix B

Aircraft models

The SBXC is a radio control cross country glider made by RnR. It is intended to be radio controlled by a human pilot but due to the relatively large payload capacity has been used as a UAV by a number of other researchers [8, 32]. An image of the University of Sydney SBXC model is shown in Fig. B.1.



Figure B.1: The University of Sydney SBXC glider model

B.1 Point mass model for the SBXC glider

The point mass model of the SBXC glider is used in the gilding results in Chapter 3 and the energy planner and reward functions in Chapters 4 & 6.

The physical parameters of wing span, wing area and mass are obtained directly from a model of the aircraft. The aspect ratio is calculated using $\mathcal{R} = b^2/S$.

The main wing section is specified by the manufacturer as the S-2048 section. The maximum lift coefficient was determined to be 1.0 using the airfoil analysis program XFOIL by Mark Drela.

The physical limits (n_{max} , n_{min} , $\gamma_{a,max}$, $\frac{d\phi}{dt}_{max}$) were selected based on discussions with an experienced RC glider pilot.

The parasitic drag coefficient, $C_{D,0}$, is very difficult to estimate without extensive flight and/or wind tunnel testing. The value of 0.017 was selected to yield a peak glide ratio of approximately 28. This value was estimated from tests of the same aircraft by John Ellias [33] and Dan Edwards [30]. The minimum airspeed and sink speeds also agree with Edwards' model.

Table B.1: The aerodynamic and geometric properties of the SB-XC glider model

Parameter	Value	Units	Explanation
$C_{D,0}$	0.017		Parasitic drag coefficient
b	4.32	m	Wing span
S	0.957	m^2	Wing reference area
\mathcal{R}	19.54		Wing aspect ratio
e	0.85		Oswald's efficiency factor
m	5.44	kg	Vehicle mass
n_{max}	2.0		Maximum load factor (positive)
n_{min}	0		Minimum load factor (negative)
$C_{L,max}$	1.0		Maximum lift coefficient
$\frac{d\phi}{dt}_{max}$	30	$^{\circ}/s$	Maximum roll rate
$\gamma_{a,max}$	50	$^{\circ}$	Maximum air relative climb angle
$(\frac{L}{D})_{est}$	25		Approximate glide ratio (for reward function)

B.2 Strip method simulation for the SBXC glider

The strip method model is a high fidelity simulation model for simulation of the SBXC glider. Strip methods are commonly used as relatively computationally efficient methods when a full coefficient model is not available. The strip method model is also applicable to aircraft for which only the physical data is available.

Basically, a strip method model divides the aerodynamic components of the aircraft into strips. Each strip is treated as a section of an infinite wing. This is similar to the common blade-element method used for propeller analysis.

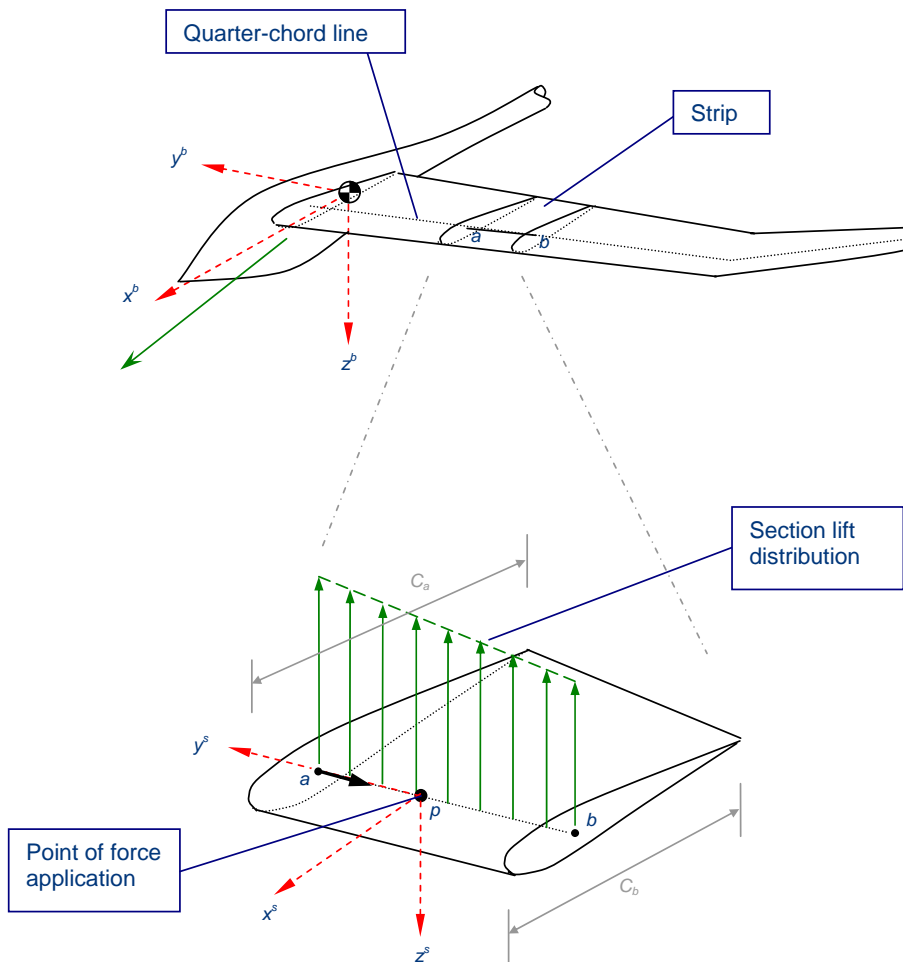


Figure B.2: Strip method component

Figure B.2 illustrates a strip from the strip method simulation. The air relative speed of point p with respect to the wind in the body frame $V_{p/w}$ is

$$\vec{V}_{p/w} = \vec{V}_{cg} + \omega \times \vec{P}_{p/cg} + C_b^i \vec{V}_w \quad (\text{B.1})$$

where \vec{V}_{cg} is the inertial speed of the aircraft with respect to the ground in the body frame, ω is the body rotation rate vector of the aircraft about the CG, $\vec{P}_{p/cg}$ is the vector from the CG to point p , C_b^i is the inertial to body transformation matrix and \vec{V}_w is the speed of the wind in the inertial frame. The component of airspeed perpendicular to the quarter-chord line is assumed to be the air-relative speed of that section. This allows calculation of the effective angle of attack. The resulting lift coefficient is estimated either through a continuous lift function or a lookup table. In the simulation presented here, all wing surfaces are simulated in XFOIL at a range of angles of attack and the tables are stored for linear interpolation to recover lift coefficient from α . The resulting force and corresponding moment on the CG can then be calculated. By repeating this process for all components the total force and moment on the aircraft can be calculated.

This method also includes a neat solution to estimating the effect of control deflections. The control surface is modelled in XFOIL and the results across the range of surface deflections is compiled into a 3 dimensional table allowing interpolation of

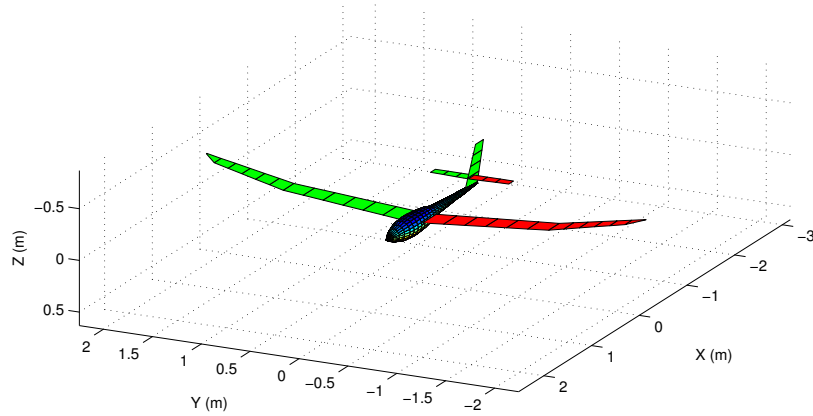


Figure B.3: Strip model SBXC glider

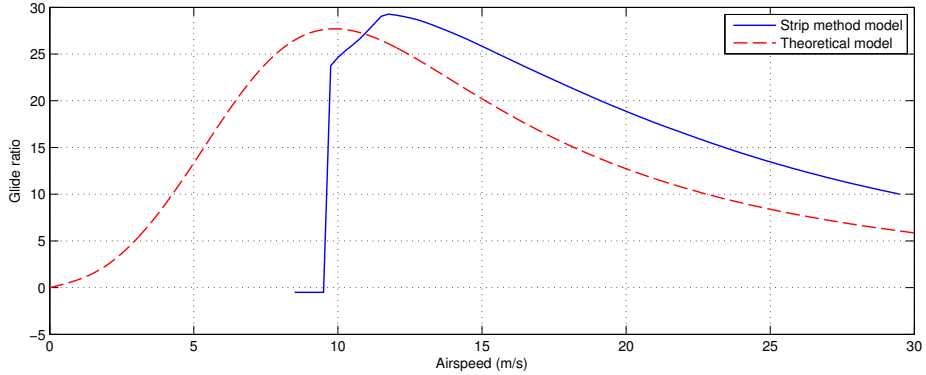


Figure B.4: Glide ratio comparison between strip model and point mass model for the SBXC glider

lift coefficient from angle of attack and surface deflection. In the current simulation, the XFOIL solutions are used until stall, and then a flat plate estimation is used to calculate the post-stall behaviour [97].

The complete model of the SBXC glider is illustrated in Fig. B.3. The aerodynamic components are the wings, vertical stabiliser and horizontal stabilator. Note that the fuselage shown is just for illustrative purposes. The fuselage is actually treated as a cylindrical body with uniformly distributed drag force to estimate the moments.

The resulting simulation is capable of modelling complex flight conditions such as partial wing stall leading to spin, as shown in the attached video of a spin and controller recovery *spin_recovery.avi*. The arrows on the wing surface indicate the force on that strip. Red arrows indicate the section has stalled.

The model is relatively close to the point mass model solution given that the strip method model is entirely driven by wing data and geometry. Figure B.4 illustrates the strip method lift-to-drag ratio for a constant glide against the point mass model. The maximum glide ratio and minimum airspeed values are very similar, but the strip method over-predicts the glide ratio at high speeds. The advantage of the strip method model is the ability to map control actions directly into simulated flight.

Bibliography

- [1] Calibration of spaceage control 100400 mini air data boom. Technical Report X004A(NC), SpaceAge Control, Inc., 2001.
- [2] C. Ahrens. *Meteorology today: an introduction to weather, climate, and the environment*. Brooks/Cole, Cengage Learning, ninth edition, 2008.
- [3] H. Airy. The soaring of birds. *Nature*, 27(703):590–592, 19 April 1883.
- [4] Z. Ákos, M. Nagy, S. Leven, and T. Vicsek. Thermal soaring flight of birds and unmanned aerial vehicles. *Bioinspiration & Biomimetics*, 5(4):045003, 2010.
- [5] M. Alexiadis, P. Dokopoulos, and H. Sahsamanoglou. Wind speed and power forecasting based on spatial correlation models. *IEEE Transactions on Energy Conversion*, 14(3):836–842, 1999.
- [6] M. J. Allen. Autonomous soaring for improved endurance of a small uninhabited air vehicle. In *43rd AIAA Aerospace Sciences Meeting and Exhibit*, Reno, Nevada, 2005. AIAA Paper 2005-1025.
- [7] M. J. Allen. Updraft model for development of autonomous soaring uninhabited air vehicles. In *44th AIAA Aerospace Sciences Meeting*, Reno, Nevada, 2006. AIAA Paper 2006-1510.
- [8] M. J. Allen and V. Lin. Guidance and control of an autonomous soaring UAV. Technical Memorandum NASA/TM-2007-214611, NASA Dryden Flight Research Center, February 2007.
- [9] J. D. Anderson, Jr. *Fundamentals of Aerodynamics*. McGraw-Hill Series in Aeronautical and Aerospace Engineering. McGraw-Hill, New York, New York, fourth edition, 2007.
- [10] K. Andersson, I. Kaminer, and K. D. Jones. Autonomous soaring; flight test results of a thermal centering controller. In *AIAA Guidance, Navigation and Control Conference*, Toronto, Ontario, Canada, 2010. AIAA Paper 2010-8034.

- [11] M. B. Boslough. Autonomous dynamic soaring platform for distributed mobile sensor arrays. Technical Report SAND2002-1896, Sandia National Laboratories, June 2002.
- [12] G. C. Bower, T. C. Flanzer, A. D. Naiman, and S. Saripalli. Dynamic environment mapping for autonomous thermal soaring. In *AIAA Guidance, Navigation and Control Conference*, Toronto, Ontario, Canada, 2010. AIAA Paper 2010-8031.
- [13] P. Boyle and M. Frean. Dependent gaussian processes. In *Advances in neural information processing systems 17: proceedings of the 2004 conference*, pages 217–225. The MIT Press, 2005.
- [14] R. Braun, H. Wright, M. Croom, J. Levine, and D. Spencer. Design of the ARES Mars airplane and mission architecture. *Journal of spacecraft and rockets*, 43(5):1026–1034, 2006.
- [15] R. Brown. The flight of birds. *Biological Reviews*, 38(4):460–489, 1963.
- [16] Bureau of Meteorology. Black and white mean sea level pressure chart, 6 January 2011.
- [17] M. Cavcar. Bréguet range equation? *Journal of Aircraft*, 43(5):1542–1544, 2006.
- [18] S. G. Cayley. On aerial navigation. *Journal of Natural Philosophy, Chemistry and the Arts*, 24, November 1809.
- [19] S. H. Chue. Pressure probes for fluid measurement. *Progress in Aerospace Sciences*, 16(2):147 – 223, 1975.
- [20] N. Clifford, J. French, and J. Hardisty. *Turbulence: Perspectives on Flow and Sediment Transport*. John Wiley & Sons Ltd, 1993.
- [21] J. Cochrane. MacCready theory with uncertain lift and limited altitude. *Technical Soaring*, 23(3):88–96, 1999.
- [22] D. Cornford, L. Csató, D. Evans, and M. Opper. Bayesian analysis of the scatterometer wind retrieval inverse problem: some new approaches. *Journal of the Royal Statistical Society: Series B (Statistical Methodology)*, 66(3):609–626, 2004.
- [23] N. Cressie and H.-C. Huang. Classes of nonseparable, spatio-temporal stationary covariance functions. *Journal of the American Statistical Association*, 94(448), 1999.
- [24] L. Csató and M. Opper. Sparse on-line gaussian processes. *Neural Computation*, 14(3):641–668, 2002.

- [25] M. J. Cutler, T. W. McLain, R. W. Beard, and B. Capozzi. Energy harvesting and mission effectiveness for small unmanned aircraft. In *AIAA Guidance, Navigation and Control Conference*, Toronto, Ontario, Canada, 2010. AIAA Paper 2010-8037.
- [26] I. Damousis, M. Alexiadis, J. Theocharis, and P. Dokopoulos. A fuzzy model for wind speed prediction and power generation in wind parks using spatial correlation. *IEEE Transactions on Energy Conversion*, 19(2):352–361, 2004.
- [27] M. Dank. *The glider gang : an eyewitness history of World War II glider combat*. Cassell, 1978.
- [28] N. T. Depenbusch and J. W. Langelaan. Receding horizon control for atmospheric energy harvesting by small UAVs. In *AIAA Guidance, Navigation and Control Conference*, Toronto, Ontario, Canada, 2010. AIAA Paper 2010-8180.
- [29] DG Flugzeugbau GmbH, Bruchsal, Germany. *Flightmanual for the sailplane DG-808S*, 2003.
- [30] D. Edwards. Performance testing of RNRs SBXC using a Piccolo autopilot, March 2002.
- [31] D. Edwards. Implementation details and flight test results of an autonomous soaring controller. In *AIAA Guidance, Navigation and Control Conference*, Honolulu, Hawaii, 2008. AIAA Paper 2008-7244.
- [32] D. J. Edwards and L. M. Silverberg. Autonomous soaring: The Montague cross-country challenge. *Journal of Aircraft*, 47(5):1763 – 1769, 2010.
- [33] J. Ellias. Performance testing of RnRs SBXC using GPS, Jan. 2002.
- [34] J. Elston, B. Argrow, A. Houston, and E. Frew. Design and validation of a system for targeted observations of tornadic supercells using unmanned aircraft. In *IEEE/RSJ International Conference on Intelligent Robots and Systems*, pages 101–106, Taipei, Taiwan, 2010.
- [35] J. Elston, B. Argrow, A. Houston, and E. Frew. Evaluation of UAS concepts of operation for severe storm penetration using hardware-in-the-loop simulations. In *AIAA Guidance, Navigation and Control Conference*, Toronto, Ontario, Canada, 2010.
- [36] J. Elston and E. Frew. Unmanned aircraft guidance for penetration of pre-tornadic storms. *AIAA Journal of Guidance, Control, and Dynamics*, 33:99–107, 2010.
- [37] Fédération Aéronautique Internationale. Altitude record - world record - class C (aeroplanes) - absolute record of classes C, H and M. Record file n°2825, Jan. 2011.

- [38] R. Froude. On the soaring of birds. In *Proceedings of the Royal Society of Edinburgh*, volume 18, pages 65–72, 1891.
- [39] S. Gage. Creating a unified graphical wind turbulence model from multiple specifications. In *2003 AIAA Modeling and Simulation Technologies Conference and Exhibit*, Austin, Texas, 2003. AIAA Paper 2003-5529.
- [40] C. H. Gibbs-Smith. *The invention of the aeroplane 1799–1909*. Faber and Faber, 1966.
- [41] S. Goldstein. *Modern developments in fluid dynamics : an account of theory and experiment relating to boundary layers, turbulent*. Clarendon Press, Oxford, 1938.
- [42] G. K. Greenhut and S. J. S. Khalsa. Updraft and downdraft events in the atmospheric boundary layer over the equatorial pacific ocean. *Journal of the Atmospheric Sciences*, 39(8):1803–1818, 1982.
- [43] J. Grenestedt and J. Spletzer. Optimal energy extraction during dynamic jet stream soaring. In *AIAA Guidance, Navigation and Control Conference*, Toronto, Ontario, Canada, 2010. AIAA Paper 2010-8036.
- [44] E. A. Haering. Airdata calibration of a high-performance aircraft for measuring atmospheric wind profiles. Technical memorandum NASA-TM-101714, NASA, January 1990.
- [45] M. S. Handcock and J. R. Wallis. An approach to statistical spatial-temporal modeling of meteorological fields. *Journal of the American Statistical Association*, 89(426):368–378, 1994.
- [46] A. Hedenstrom. Migration by soaring or flapping flight in birds: the relative importance of energy cost and speed. *Philosophical Transactions: Biological Sciences*, 342(1302):353–361, 1993.
- [47] P. Henningsson and A. Hedenström. Aerodynamics of gliding flight in common swifts. *Journal of Experimental Biology*, 214(3):382–393, 2011.
- [48] P. Idrac. Experimental study of the “soaring” of albatrosses. *Nature*, 115(2893):532–532, 1925.
- [49] N. Kahveci, P. Ioannou, and M. Mirmirani. Adaptive lq control with anti-windup augmentation to optimize uav performance in autonomous soaring applications. *Control Systems Technology, IEEE Transactions on*, 16(4):691 – 707, 2008.
- [50] J. Kaimal and J. Finnigan. *Atmospheric Boundary Layer Flows - Their Structure and Measurement*. Oxford University Press, Inc., 1994.

- [51] J. C. Kaimal, J. C. Wyngaard, D. A. Haugen, O. R. Cot, Y. Izumi, S. J. Caughey, and C. J. Readings. Turbulence structure in the convective boundary layer. *Journal of the Atmospheric Sciences*, 33(11):2152–2169, 1976.
- [52] J. A. Kyle. *Optimal Soaring by a Small Autonomous Glider*. PhD thesis, Oregon State University, 2006.
- [53] C.-T. E. Lan and J. Roskam. *Airplane aerodynamics and performance*, pages 350–365. Roskam Aviation and Engineering, 1980.
- [54] J. W. Langelaan. Gust energy extraction for mini- and micro- uninhabited aerial vehicles. In *46th AIAA Aerospace Sciences Meeting and Exhibit*, Reno, Nevada, 2008. AIAA Paper 2008-223.
- [55] J. W. Langelaan. Gust energy extraction for mini and micro uninhabited aerial vehicles. *Journal of Guidance, Control, and Dynamics*, 32(2):464–473, 2009.
- [56] J. W. Langelaan, N. Alley, and J. Neidhoefer. Wind field estimation for small unmanned aerial vehicles. In *AIAA Guidance, Navigation and Control Conference*, Toronto, Ontario, Canada, 2010. AIAA Paper 2010-8177.
- [57] B. Laufer. *The Prehistory of Aviation*, volume 18:1 of *Anthropological Series*, pages 31–43. Field Museum of Natural History, 1928.
- [58] N. R. Lawrence and S. Sukkarieh. Autonomous soaring for atmospheric exploration of Titan. In *Proceedings of the 10th Australian Space Science Conference Brisbane 27 – 30 September, 2010*, pages 223–236. National Space Society of Australia Ltd, 2011.
- [59] D. Lawson. Pterosaur from the latest Cretaceous of West Texas: discovery of the largest flying creature. *Science*, 187(4180):947–948, 1975.
- [60] D. Lenschow and P. Stephens. The role of thermals in the convective boundary layer. *Boundary-Layer Meteorology*, 19(4):509–532, 1980.
- [61] P. Ligouri, B. Singer, and L. Baun. Miniature five-hole pressure probe for measurement of three mean velocity components in low-speed flows. *Journal of Physics E: Scientific Instruments*, 22(10):868, 1989.
- [62] M. Likhachev and D. Ferguson. Planning long dynamically feasible maneuvers for autonomous vehicles. *The International Journal of Robotics Research*, 28(8):933–945, 2009.
- [63] O. Lilienthal. *Birdflight as the Basis of Aviation: A Contribution Towards a System of Aviation*. Longmans, Green, and Co., 1911. Translated by A.W. Isenthal.

- [64] G. Lindal, G. Wood, H. Hotz, et al. The atmosphere of Titan: An analysis of the Voyager 1 radio occultation measurements. *Icarus*, 53(2):348–363, 1983.
- [65] P. Lissaman. Wind energy extraction by birds and flight vehicles. In *43rd AIAA Aerospace Sciences Meeting and Exhibit*, Reno, Nevada, 2005. AIAA Paper 2005-241.
- [66] P. Lissaman and C. Patel. Neutral energy cycles for a vehicle in sinusoidal and turbulent vertical gusts. In *45th AIAA Aerospace Sciences Meeting and Exhibit*, Reno, Nevada, 2007. AIAA Paper 2007-863.
- [67] E. Lorenz and W. M. Organization. *The nature and theory of the general circulation of the atmosphere*. World Meteorological Organization, 1967.
- [68] R. Lorenz. Post-Cassini exploration of Titan: Science rationale and mission concepts. *Journal of the British Interplanetary Society*, 53(7/8):218–234, 2000.
- [69] P. B. MacCready. Optimum airspeed selector. *Soaring*, 9:8, March 1954.
- [70] P. B. MacCready. Optimum airspeed selector. *Soaring*, January–February:10–11, 1958.
- [71] I. Nabney, D. Cornford, and C. Williams. Bayesian inference for wind field retrieval. *Neurocomputing*, 30(1-4):3–11, 2000.
- [72] G. Padfield and B. Lawrence. The birth of flight control - an engineering analysis of the Wright brothers' 1902 glider. *Aeronautical Journal*, 107(1078):697–718, 2003.
- [73] S. Peal. Soaring of birds. *Nature*, 23(575):10–11, 4 November 1880.
- [74] C. Pennycuick. Gliding flight of the fulmar petrel. *Journal of Experimental Biology*, 37(2):330–338, 1960.
- [75] C. Pennycuick. Gliding flight of the white-backed vulture *gyps africanus*. *Journal of Experimental Biology*, 55(1):13–38, 1971.
- [76] C. Pennycuick. Soaring behaviour and performance of some east african birds, observed from a motor-glider. *Ibis*, 114(2):178–218, 1972.
- [77] C. Pennycuick. The flight of petrels and albatrosses (Procellariiformes), observed in south georgia and its vicinity. *Philosophical Transactions of the Royal Society of London. B, Biological Sciences*, 300(1098):75, 1982.
- [78] C. Pennycuick. Field observations of thermals and thermal streets, and the theory of cross-country soaring flight. *Journal of Avian Biology*, 29(1):33–43, 1998.

- [79] C. Pennycuick, T. Alerstam, and B. Larsson. Soaring migration of the common crane *Grus grus* observed by radar and from an aircraft. *Ornis Scandinavica*, 10(2):241–251, 1979.
- [80] W. F. Phillips. *Mechanics of flight*, pages 259–270. John Wiley and Sons, Inc., second edition, 2010.
- [81] D. Piggott. *Going solo - A simple guide to soaring*, pages 97–99. A & C Black (Publishers) Ltd, London, UK, first edition, 1978.
- [82] D. Piggott. *Understanding Gliding*, pages 86–94. A & C Black (Publishers) Ltd, London, UK, fourth edition, 2002.
- [83] C. E. Rasmussen and C. K. Williams. *Gaussian Processes for Machine Learning*, pages 7 – 29. Adaptive computation and machine learning. The MIT Press, Cambridge, Massachusetts, 2006.
- [84] L. Rayleigh. The soaring of birds. *Nature*, 27(701):534–535, 5 April 1883.
- [85] H. Reichmann. *Cross-Country Soaring*. Soaring Society of America, Inc., seventh edition, 1993.
- [86] M. Rosén and A. Hedenström. Gliding flight in a jackdaw: a wind tunnel study. *Journal of Experimental Biology*, 204(6):1153–1166, 2001.
- [87] G. Sachs. Minimum shear wind strength required for dynamic soaring of albatrosses. *Ibis*, 147(1):1–10, 2005.
- [88] C. Sequeira, D. Willis, and J. Peraire. Comparing aerodynamic models for numerical simulation of dynamics and control of aircraft. In *44th AIAA Aerospace Sciences Meeting and Exhibit*, Reno, Nevada, January 2006. AIAA Paper No. 2006-1254.
- [89] J. Shamoun-Baranes, Y. Leshem, Y. Yom-Tov, and O. Liechti. Differential use of thermal convection by soaring birds over central Israel. *The Condor*, 105(2):208–218, 2003.
- [90] H. D. Shannon, G. S. Young, M. A. Yates, M. R. Fuller, and W. S. Seegar. American white pelican soaring flight times and altitudes relative to changes in thermal depth and intensity. *The Condor*, 104(3):679–683, 2002.
- [91] H. D. Shannon, G. S. Young, M. A. Yates, M. R. Fuller, and W. S. Seegar. Measurements of thermal updraft intensity over complex terrain using american white pelicans and a simple boundary-layer forecast model. *Boundary-Layer Meteorology*, 104(2):167–199, 2002.

- [92] A. J. Smola and P. Bartlett. Sparse greedy gaussian process regression. In *Advances in Neural Information Processing Systems 13*, pages 619–625. MIT Press, 2001.
- [93] R. Spaar and B. Bruderer. Optimal flight behavior of soaring migrants: a case study of migrating steppe buzzards, *Buteo buteo vulpinus*. *Behavioral Ecology*, 8(3):288–297, 1997.
- [94] B. Stojkovic. Generalized speed-to-fly theory. *Technical Soaring*, XVII(3):77 – 83, 1993.
- [95] R. B. Stull. *An introduction to boundary layer meteorology*. Atmospheric sciences library. Kluwer Academic Publishers, Dordrecht ; Boston, 1988.
- [96] R. Sutton and A. Barto. *Reinforcement learning: An introduction*. The MIT press, 1998.
- [97] J. Tangler and J. Kocurek. Wind turbine post-stall airfoil performance characteristics guidelines for blade-element momentum methods. In *43rd AIAA Aerospace Sciences Meeting and Exhibit*, 2005. AIAA-2005-591.
- [98] V. Tucker. Flight energetics in birds. *American Zoologist*, 11(1):115–124, 1971.
- [99] V. Tucker and K. Schmidt-Koenig. Flight speeds of birds in relation to energetics and wind directions. *The Auk*, 98(1):97–107, 1971.
- [100] V. A. Tucker and G. C. Parrott. Aerodynamics of gliding flight in a falcon and other birds. *Journal of Experimental Biology*, 52(2):345–367, 1970.
- [101] United States Department of Defense. *Military Specification: Flying Qualities of Piloted Airplanes*, November 1980. MIL-F-8785c.
- [102] U.S. Committee on Extension to the Standard Atmosphere. US standard atmosphere, 1976. *US Government Printing Office, Washington, DC*, 1976.
- [103] S. Walkden. Experimental study of the “soaring” of albatrosses. *Nature*, 116(2908):132–134, 25 July 1925.
- [104] H. Weimerskirch, T. Guionnet, J. Martin, S. A. Shaffer, and D. P. Costa. Fast and fuel efficient? optimal use of wind by flying albatrosses. *Proceedings of the Royal Society of London - Biological Sciences*, 267(1455):1869 – 1874, 2000.
- [105] J. Wharington. *Autonomous control of soaring aircraft by reinforcement learning*. PhD thesis, Royal Melbourne Institute of Technology, 1998.
- [106] J. Wharington and I. Herszberg. Control of a high endurance unmanned aerial vehicle. In *21st Congress of International Council of the Aeronautical Sciences*, Melbourne, Australia, September 1998. ICAS-98-3.7.1.

- [107] L. White Jr. Eilmer of Malmesbury, an eleventh century aviator: A case study of technological innovation, its context and tradition. *Technology and Culture*, 2(2):97–111, 1961.
- [108] C. J. Wood. The flight of albatrosses (a computer simulation). *Ibis*, 115(2):244–256, 1972.
- [109] A. Woodcock. Observations on herring gull soaring. *The Auk*, 57(2):219–224, 1940.
- [110] G. S. Young. Turbulence structure of the convective boundary layer. part ii: Phoenix 78 aircraft observations of thermals and their environment. *Journal of the Atmospheric Sciences*, 45(4):727–735, 1988.
- [111] Y. J. Zhao. Optimal patterns of glider dynamic soaring. *Optimal Control Applications and Methods*, 25(2):67–89, 2004.
- [112] Y. J. Zhao and Y. C. Qi. Minimum fuel powered dynamic soaring of unmanned aerial vehicles utilizing wind gradients. *Optimal Control Applications and Methods*, 25(5):211–233, 2004.
- [113] Z. Zhou. The origin and early evolution of birds: discoveries, disputes, and perspectives from fossil evidence. *Naturwissenschaften*, 91(10):455–471, 2004.